DNA-based routes to metal, inorganic and polymer nanowires

Hasan Daw Ashtawi Mohamed

A thesis submitted for the degree of

Doctor of Philosophy in Chemistry

School of Chemistry

Newcastle University

Newcastle Upon Tyne, UK

May 2013

Abstract

This thesis describes the preparation and characterization of conductive nanowires. The synthesis of the nanowires was achieved using a DNA-templating strategy. The chemical identity of the nanowires was characterized using FTIR, XPS and XRD, while the structural character, electronic properties and magnetic behavior were probed using AFM, EFM and MFM, respectively.

The formation of Fe_3O_4 nanowires involved initial association of Fe^{2+} and Fe^{3+} ions to the DNA, and subsequent co-precipitation of the Fe_3O_4 material, upon addition of NaOH. Chemical characterization confirmed the formation of Fe_3O_4 within the product material. AFM data revealed one-dimensional (1-D) nanostructures with diameters up to 30 nm, whilst EFM and MFM showed that the nanowire structures are electrically conducting and exhibit magnetic behaviour.

The preparation of Fe and Rh nanowires, respectively, was achieved by DNA-templating approach in conjunction with either chemical or electrochemical reduction. Chemical characterization confirmed a metal/oxide core/shell structure. AFM data showed 1-D nanostructures with granular character, and diameters up to 26 nm for Fe and 31 and 23 nm for Rh, respectively. The structures were confirmed to be electrically conducting and to display magnetic behaviour as indicated by EFM and MFM, respectively.

Finally, DNA-templating of 2,6-diaminopurine-propyl-2,5 bis-dithenyl pyrrole and thymine-propyl-pyrrole by chemical oxidation using $FeCl_3$ yielded supramolecular polymers. FTIR and XPS studies confirmed the presence and interaction of the component polymer chains. The DNA/CPs nanowires showed smooth and uniform structures with diameters up to 25 and 35 nm, and they were found to be electrically conducting. The attempted formation of larger structures based on the base pair hydrogen bonding between the two types of nanowires was investigated by AFM studies. However, reliable evidence for larger structures formation based on this specific interaction was not found.

Dedication

To my late father Daw Ashtawi Mohamed may *Allah, the Most High and Exalted have mercy on his soul and* grant him the *highest* level of paradise.

A wonderful man and a devout father without whose never-failing encouragement this work would have never been completed.

Acknowledgments

First, I thank *Allah (SW)* for the great help all over my life. I wish to express my sincere gratitude and deep appreciations to my first supervisor Professor Andrew Houlton. Much sincere are due for his continuous supervision, encouragement and support through caring out this work. I would also like to thank my second supervisor Dr. Benjamin Richard Horrocks for his help and advice. Many thanks, gratitude and appreciations go to Dr. Scott Watson for his continuous help, supports and valuable input to my project work.

A sincere gratitude is also expressed to all staff members and colleagues of the Chemical Nanoscience group for their help and advice. I am also indebted to all people in school of chemistry at Newcastle University. Thanks are acknowledged to the XPS and XRD User's service, at Newcastle University, for technical assistance. The Ministry of Higher Education in Libya is acknowledged for the financial support. I also thank all my relatives and friends for their support and encouragement.

Finally, I would like to express my deepest gratitude to my family members (my mother, my father, my wife, my kids: Intisar and Mohamed, my brothers and my sisters) for their prayers, encouragement and support.

Table of contents

1. Chapter 1: Introduction

1.1 Nanoscience and nanomaterials

The word "Nano" refers to one billionth (10^{-9}) and it originates from the word Greek "nanos" (or Latin "nanus"), meaning "Dwarf".[1] Nanoscience is concerned with the study of materials whose size is in the 1 – 100 nm range. Nanotechnology seeks to manipulate, and exploit the properties of materials with structural features bridge the gap between atoms and bulk materials, and have at least one dimension in this size range.[2, 3] The field of nanoscience started in 1959 when Richard Feynman, later to be awarded the Nobel Prize for Physics, gave his now popular talk entitled "there is plenty of room at the bottom". In that lecture, Feynman pointed out the challenges of manipulating and controlling objects on the small scale. He estimated it should be possible to shrink devices down to the atomic level and speculated about moving individual atoms around.[1, 2]

In 1981, Binning and Rohrer developed scanning tunnelling microscopy (STM) with which one can visualise atoms and molecules. The STM is the first instrument used to accurately position atoms.[1] The physicist Don Eligler and Erhard Schweizer have used STM technique to arranged 35 xenon (Xe) atoms on an nickel (Ni) surface as "IBM" letters, see figure 1.1.[4]

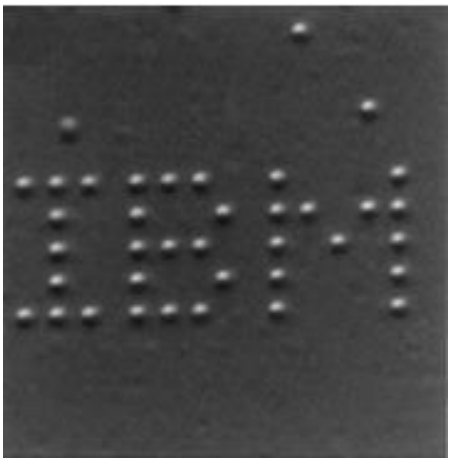

Figure 1-1: Scanning tunnelling microscopy (STM) image of 35 Xe atoms on Ni (110) surface. Grey scale is attributed to the slop of the surface. Each letter is 50 Å from top to bottom.[4]

Nanometer-sized materials can display unique physical, chemical and magnetic properties which may be distinctively different from those exhibited by bulk forms. Appropriate control of the properties of nanostructures can lead to dramatic

technological progress, e.g. as in electronic devices.[5, 6] Alternatively, smaller components can enable further miniaturization of electronic devices. The development of nanotechnology is also driven by decreasing the size of devices in the semiconductor industry and reinforced by the availability of new instruments for characterisation and manipulation of nanostructured materials. The sustained shrinkage in the device sizes has followed the Moore's law.[6] This law predicted by Intel co-founder, Gordon E. Moore, in his 1965 paper, and illustrated in figure 1.2. Gordon Moore predicted that the size of a device shrinks by roughly half every 18 months and by 2020 the size of a transistor will fall in the nanoscale range.[2, 6]

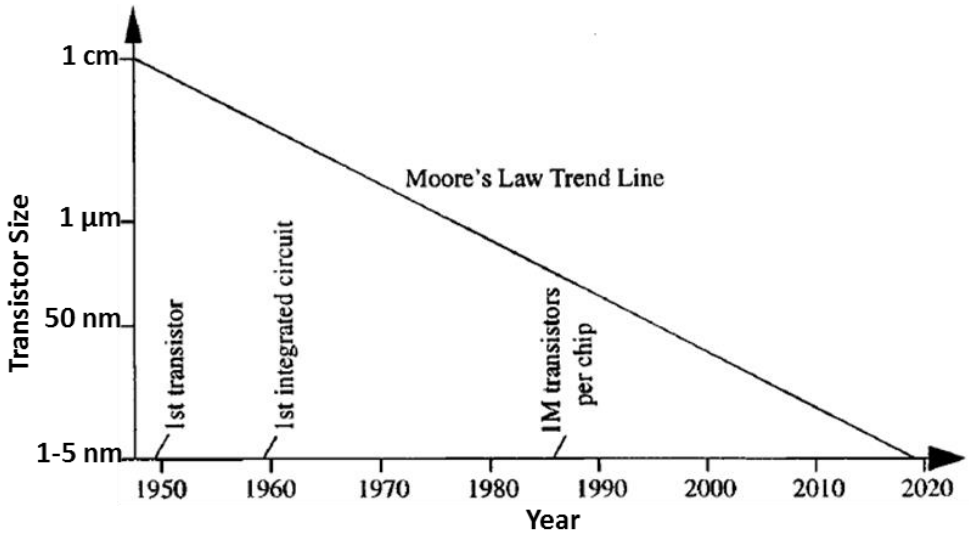

Figure 1-2: A plot of the well-known Moore's law.[6]

With the availability of new instruments for characterisation such small objects, as well as the development of new methods for the preparation of nanomaterials, nanoscale science and technology has become a large field and shown explosive growth during the recent years.[2]

1.2 Size effects

As mentioned earlier, at the nanometere scale, materials can exhibit different properties than the corresponding bulk form. For example, gold in the bulk is yellowish, shiny metal, non-magnetic and melts at 1336 K. However, a nanometre sized pieces of this noble metal is quite different as at 10 nm particles appear red, as well as its melting temperature reducing markedly.[7] Surface effects and quantum effects represent the main factors that make nanomaterials exhibit distinctive properties from the corresponding bulk form. The former one is related to the fraction of atoms at the

surface and the latter one includes the appearance of new features in the electronic structure.[7]

The surface-to-volume ratio increases with decreasing the size, and as a result numerous properties can obey the same scaling law. For example, the melting temperature scales with the inverse size as mentioned for gold.[7] It is found that the melting temperature of a range of materials including metals, semiconductors and insulators decreases with decreasing nanocrystal size. An example of such behaviour is represented by experiments performed on cadmium sulphide (CdS), see figure 1.3. For CdS nanocrystals with sufficient small size, depressions of over 50% in the melting temperature were noticed.[8]

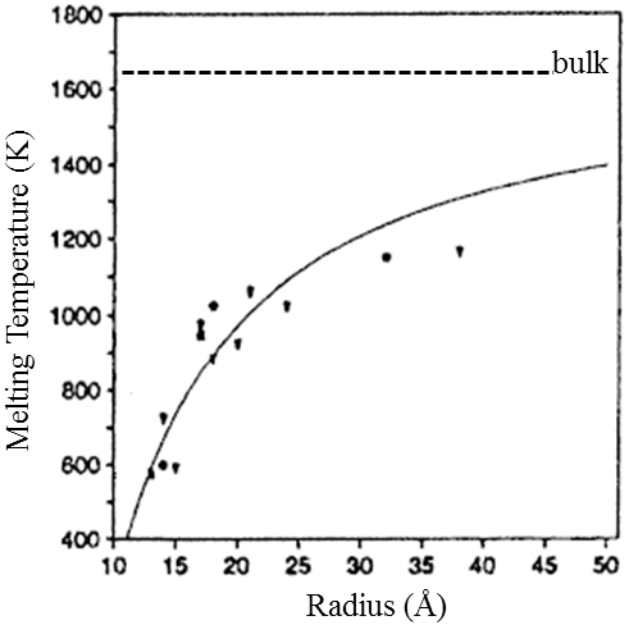

Figure 1-3: Melting temperature of CdS nanocrystals as a function of its size.[8]

Quantum size effects also play an important role in determining the properties of nanomaterials. For example, it is found that by adjusting their size, the fluorescence of CdSe-CdS core-shell nanoparticles can be changed between blue and red for nanoparticles with diameter 1.7 and 6 nm, respectively, see figure 1.4a.[7] Additionally, the quantum confinement in small nanocrystals leads to change in the electronic structure qualitatively which in turn give unique catalytic properties of these systems distinctive from those of bulk metal.[9] An example of this is the absorption of carbon monoxide by copper (Cu) nanoparticles. A bulk Cu surface desorbs CO at temperature > 250 K, while Cu particles binds CO up to higher temperatures, see figure 1.4b. It is

clear from figure 1.4b that, on the surface of bulk Cu, the feature at 268 eV in the C(1s) spectra has disappeared completely at around 250 K, though on the smaller Cu coverage, this feature remains up to ~ 300 K, indicating a dramatic increase in the CO desorption temperature.[9, 10]

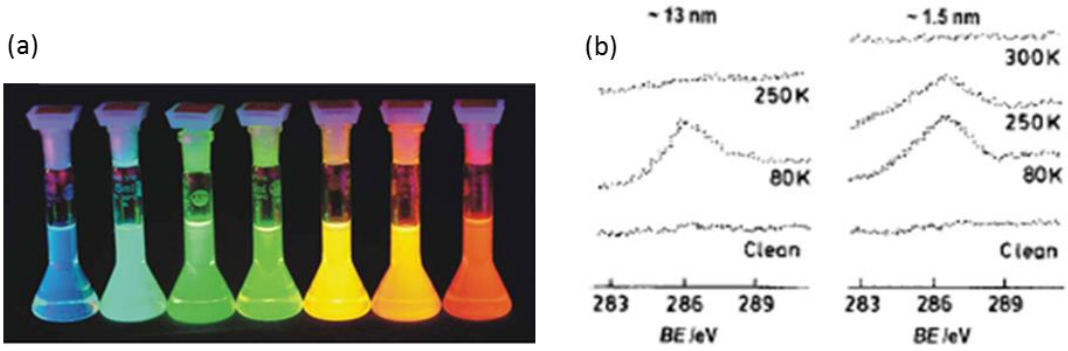

Figure 1-4: (a) Fluorescence of CdSe–CdS core–shell nanoparticles [7], and (b) Change in the C(1s) spectra of CO adsorbed on cupper (Cu).[9, 10]

1.3 Classification of nanomaterials

The number of the nanoscale dimensions of a material plays an important factor in determining their electrical, optical and magnetic properties, hence their potential uses. In order to understand and appreciate the variety of nanomaterials, it is helpful to categorise them.[11] The most typical way of classifying nanomaterials is to identify them according to their dimensions. Nanomaterials can be classified as zero-dimensional (0-D), one-dimensional (1-D), two-dimensional (2-D) and three-dimensional (3-D) [11], see figure 1.5.

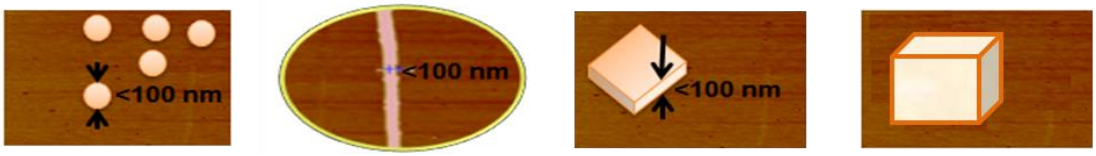

Figure 1-5: Illustration showing classification of nanomaterials according to zero-dimension, one-dimension, two-dimensions and three dimensions.

The first class (0-D) exhibits three-dimensional confinement and represents materials in which all their dimensions are less than 100 nm. Nanoparticles are the most common example of zero-dimensional nanomaterials.[5, 11] 1-D nanomaterials are systems

confined in two dimensions. Therefore, they have one dimension outside the nanoscale. Examples of such nanomaterials include nanowires, nanotubes and nanorods.[5, 11] The third class of nanomaterials which is confined in only one dimensions, are called 2-D systems represents materials with two dimensions outside the nanoscale. These nanomaterials show platelike shapes and include nanofilms and nanolayers.[5, 11] Three-dimensional which also known as bulk materials are materials that do not have any dimension at the nanoscale. However, these systems may have a nanocrystalline structures or comprise of structures at the nanoscale, making them classified as a nanomaterials, e.g. nanoparticle assembly.[11]

In general, nanomaterials have received much attention owing to their unique and important properties. These properties make them attractive for use in a variety of applications and much of modern science and technology relies on the ability for generating nanosized objects. An example of the realization of new prospects by fabrication of nanostructured materials is provided by microelectronics, where miniaturization can improve their performance (e.g., saving energy and cost, and increasing processing speed).[12]

Among the nanostructure materials, conducting one-dimensional (1D) nanostructures, so-called nanowires, have become the focus of intensive studies as they are ideal candidate for use as both interconnects and functional units in fabricating a variety of nanodevices and have potential use in a range of nanotechnology applications.[12-16]

1.4 Nanowires

Nanowires represent the smallest structure for efficient transport of electrons and thus are anticipated for use as critical components, such as interconnect, in nanoscale devices.[14, 16] Nanowires are one-dimensional (1D) structures with two dimensions in the 1 – 100 nm regime.[6, 12] Nanowires of metals and semiconductors possess unique magnetic, electrical, optical, chemical, mechanical and thermoelectric properties which typically differ from those associated with the corresponding bulk material, due to their high aspect (length-to-width) ratio, large surface-to-volume ratio, diameter-dependent bandgap and distinctive density of electronic states.[12, 13]

For instance, semiconductor and metallic nanowires have been demonstrated their potential use in a range of nanoscale devices such as diode logic gates [17-19], nanoscale transistor [20], field effect transistors.[19, 21] Additionally, magnetic

nanowires have also been proposed as important nanostructured material for recording media applications.[13, 19] Nanowires are also ideal candidates for use in future sensor technology, for the detection of trace amounts of biomolecules and chemicals.[19, 22, 23]

In recent years, nanowires have been used as building blocks in the construction of nanodevices via so-called "bottom-up" methods. Semiconductor nanowires for example, have already been demonstrated to be integrated in complex nanosystems to create functioning devices.[24]

1.5 Preparation of nanowires

In comparison with 0-D and 2-D nanostructures, the preparation of 1-D nanostructures with well-controlled dimensions, structure, high purity provides considerable challenges and a variety of methods have been developed to address these challenges.[12] 1-D nanostructures can be prepared using "top-down" or "bottom-up" nanofabrication methods. The advanced top-down high-vacuum based techniques, e.g. X-ray, or extreme-UV lithography, electron-beam (e-beam) or focused-ion beam (FIB) writing, is concerned with the formation of a nanometer-sized materials through macroscale manufacturing operations. However, this method is very costly, slow process, and suffers low throughput.[6, 12]

By contrast, chemical, or bottom-up, approaches like template-based synthesis, is concerned with the preparation of nanometre-sized structures and nanodevices through the self-assembly of atoms and molecules.[25, 26] In this instance, the nanometer-dimension units (atoms or molecules) self-assemble into larger structures through physical and chemical interactions. This method offers an alternative and fascinating approach for fabricating nanomaterials with 1-D form at low cost, high yield and varied materials can be manipulated.[6, 12]

Among the bottom-up fabrication methods, template-directed synthesis is the most common and straightforward route. Templates works as a support within, or around, which various nanomaterials are formed with a morphology complementary to the template.[12] Several template types have demonstrated their use in nanowire fabrication including channels within a porous material and biological molecules, such as DNA.

1.6 Template-directed synthesis

1.6.1 Channels in Porous materials

The use of channels in porous materials as a template in the fabrication of 1-D nanostructures (figure 1.6) was pioneered by Martin and others.[12, 27-29]

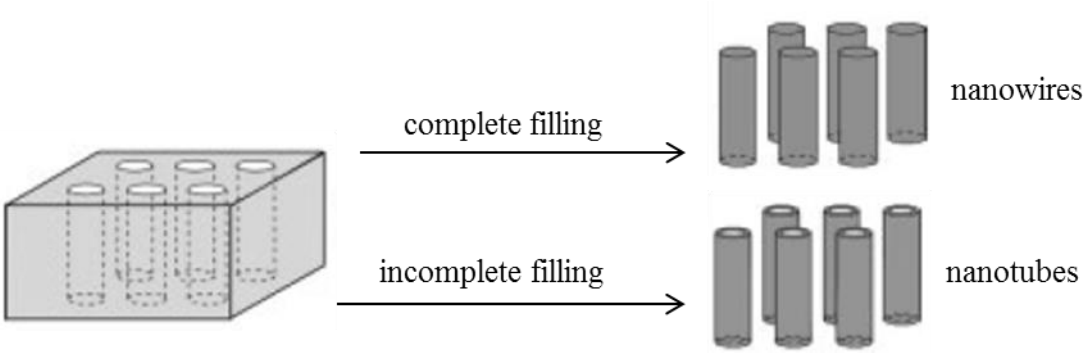

Figure 1-6: Schematic illustrations the formation of nanowires and nanotubes by filling or partial filling the nanochannels of a membrane with the material of interest. [12, 27-29]

The most common porous membranes used in template-directed synthesis are track-etched membranes and anodic-etched alumina films (AAO – anodic aluminium oxide). For the former type, a 6-20 μm thick polymer sheet is bombarded with nuclear fission fragments to generate damage tracks in its surface. Chemical etching of the resulting spots is then carried out to create a membrane with randomly distributed uniform and cylindrical-shaped pores. The orientation of these pores may be as much as 34° from the surface normal.[12, 27] On the other hand, electrochemical oxidation of aluminium metal in an acidic medium is used to prepare porous alumina membranes with uniform and parallel oriented pores which are arranged in hexagonal array in the membrane surface. In comparison with the track-etch membrane, the porous alumina membranes contain highly oriented pores with slight or no angle with respect to the surface normal and high pore density.[12, 27]

The preparation of nanowires using the membrane-based synthesis method produces 1-D nanostructures of the target material complementary to the template, i.e. cylindrical-shaped wires of uniform diameter. [27-29] This type of template-directed synthesis can be used to prepare nanowires composed of metals and polymers.[12, 27-29] The fabrication of nanowires inside the nanochannels of membranes can be achieved through a range of methods such as electrochemical deposition, chemical

polymerisation, electroless deposition, chemical vapour deposition and sol-gel deposition.[13, 27]

Metals with low melting temperature such as bismuth (Bi) can be injected directly into AAO as a liquid and afterward solidified into highly crystalline nanowires.[12, 30] Removal of the alumina template using a solution consists of of 3.5 vol % H_3PO_4 and 45 g/L CrO_3, is needed to extract the Bi nanowires (figure 1.7).[30]

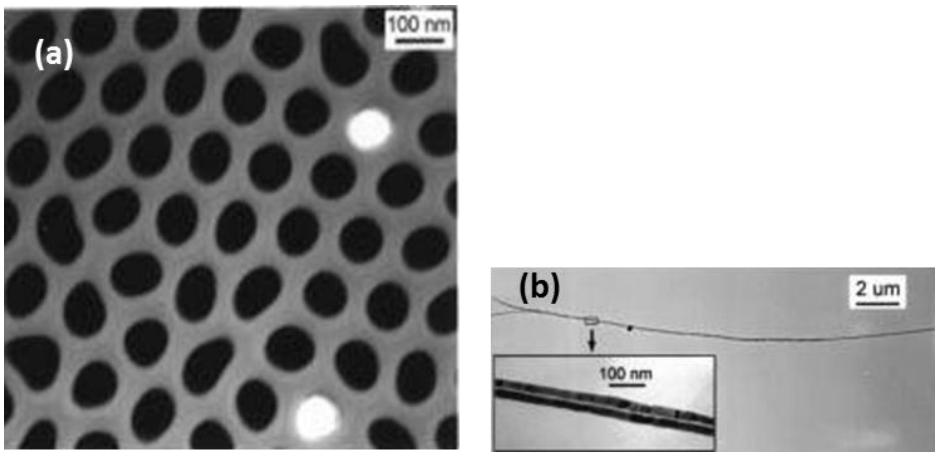

Figure 1-7: (a) TEM image of the cross-section of 65 nm diameter Bi nanowire array (black spots), and the white spots are empty pores. (b) TEM image of free-standing Bi nanowire with diameter of 23 nm.[30]

Metal nanowires are examples that can be prepared through electrochemical reduction of the metal ion located inside the pores of the membrane. Deposition of the desired metal inside the pores of template membrane using the electrochemical reduction approach can be accomplished by coating one face of the membrane with a metal sheet and this metal film used as a cathode for electroplating, see figure 1.8.[27, 29, 31, 32] With the use of this method, a variety of metals can be deposited within the pores of membrane.[27, 29]

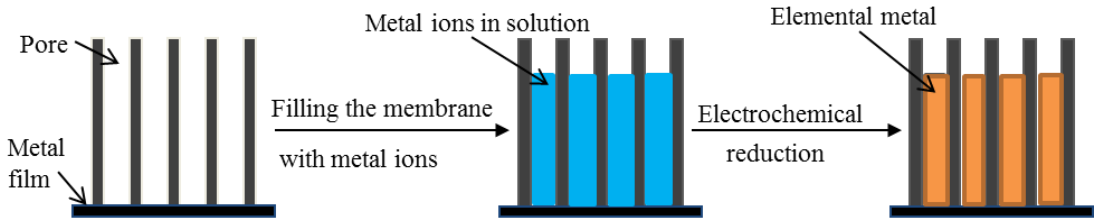

Figure 1-8: Schematic diagram of method used to prepare metal nanowires through electrochemical reduction of metal ion inside the pore of membrane.

For example, gold nanowires were prepared by electrochemical deposition of metallic Au inside the pores of AAO membrane.[32, 33] By varying the quantity of metal deposited, the length of the produced Au nanowires can be controlled.

Membrane-based synthesis can also be used to prepare conductive polymer nanowires such as, polypyrrole, polythiophene and polyaniline.[34-36] This can be accomplished through oxidative polymerisation of the appropriate monomer inside the pores of membrane.[29] The polymerisation can be achieved through either electrochemical method [37] or with the use of a chemical oxidizing agent.[34, 35] The preparation of conducting polymer nanowires using chemical polymerisation involves immersing the membrane in a solution of the desired monomer and subsequently induce its polymerisation.[27, 29] It is found that the polymer nucleates and grows favourably on the walls of pores.[34, 35, 38, 39] This results in formation of tubules at short polymerisation time which close up to form nanowires with increasing the polymerisation period.

1.6.2 Templating using biological nanostructures

Several naturally occurring biological materials have been demonstrated to offer utility as a part of strategies for the fabrication of new nanoscale materials.[40] In particular biology has provided a range of material suitable for the use as templates in the synthesis of 1-D nanostructures, with noticeable examples including peptides, viruses and DNA.[40]

Nanowires of metals and inorganic semiconductor materials have previously been prepared using rod-shaped viruses, such as the M13 bacteriophage and tobacco mosaic viruses.[41] Cellulose nanocrystals (CNC) have also been used to synthesis chains of metallic nanoparticles such as silver (Ag), gold (Au), copper (Cu), and platinum (Pt).[40]

However, among biotemplates, deoxyribonucleic acid (DNA) has emerged as an ideal template for directing the growth of a wide variety of materials into organised 1-D nanostructures due to its chemical and structural features.[26, 42]

1.7 DNA structure and properties

DNA is a polymer of deoxyribonucleotides (figure 1.9a) and each nucleotide contains monophosphate deoxyribose sugar attached with one of four nitrogenated nucleobases at its C-1 carbon atom. These bases are adenine (A) and guanine (G) (purines), and thymine (T) and cytosine (C) which are pyrimidines.[26, 43] The DNA "backbone" is composed of deoxyribose sugars linked together by phosphate groups at the 5' position of the first sugar to the second molecule at the 3' position. The negatively charged phosphate groups of the DNA backbone make DNA stand polyanion.[43]

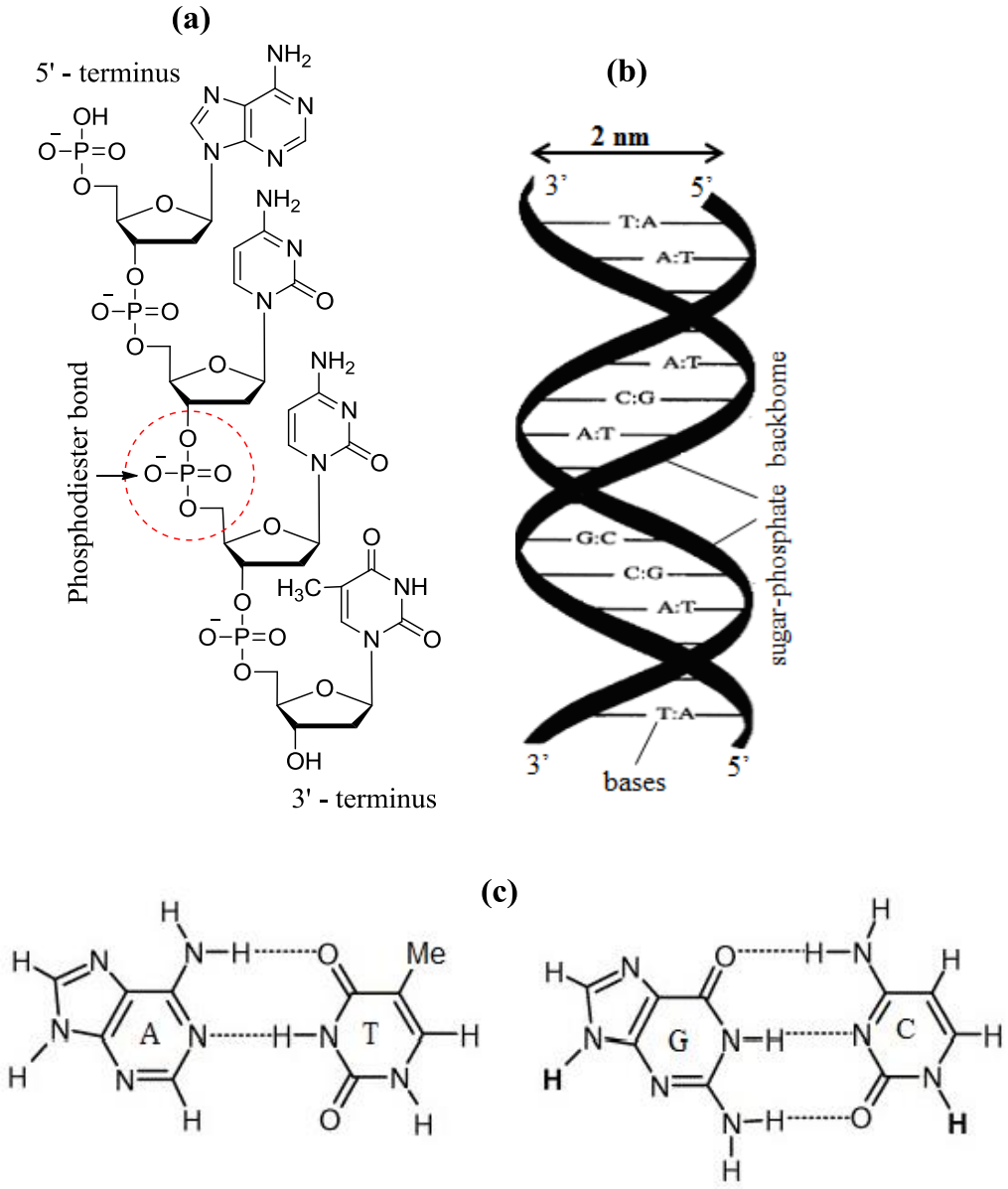

Figure 1-9: (a) Chain of four nucleotides showing the structure of single-stranded DNA molecule. (b) The double helix DNA molecule with diameter of 2 nm. (c) adenine-thymine base pair (left) and guanine-cytosine base pair (right).

Hydrogen bonding between DNA bases holds two complementary single strands together to form a double-stranded DNA (dsDNA) molecule (figure 1.9b). Adenine is paired thymine with two hydrogen bonds, while guanine and cytosine are linked with three hydrogen bonds (figure 1.9c).[43] The hydrogen bonds and aromatic stacking interactions increase the stability of the double helix DNA configuration.

DNA has many unique chemical and structural features that make it well suited as a nanofabrication template. DNA molecules are high aspect ratio structures, being 2 nm in diameter, but ranging from nanometre to micron length scale making it ideal candidate for controlling material growth into 1-D form.[44, 45] Moreover, DNA has a inter base-pair separation of 0.34 nm [46] and its length can be programed by controlling the number of base pairs, which in turn offers the possibility to control the lengths of the nanostructures that can be prepared.[42] More important, DNA has a wealth of chemical functionalities that allow it to bind a range of materials. The anionic phosphodiester backbone and the nucleobases of the nucleosides for example provide routes to seed the DNA with other chemical species. The negatively charged backbone can bind cationic species via electrostatic interactions, whilst the nucleobase groups are capable of coordinating with metal cations. Such interactions are considered of principal importance in the fabrication of DNA-templated nanomaterials.[42, 44]

1.8 Metal ion – DNA interactions

The basic components of nucleic acids comprise nitrogenous base, phosphate group and a ribose sugar.[43] These components together are nucleotides and provide a variety of sites for interactions with metal ions.[47] DNA bases, for example, bind metal ions through coordinate bonds directly to their electron donor sites (e.g. ring nitrogen atoms). Metal ion binding at the phosphate groups can also take place through inner-sphere coordinate bonds directly to the oxygen atoms and/or via outer sphere non-covalent binding, which involves electrostatic interactions and hydrogen bonds between a coordinated ligand molecule and the oxygen atoms of phosphate groups. Selected metal ions can also coordinate bonds with ribose oxygen atoms for ribose ring.[47, 48] For instance, osmate esters can form across the C2′ – C3′ positions in ribose rings (figure 1.10a). This type of interaction is not very general and applies only to RNA.[47] Figure 1 illustrates modes of metal ion binding to sites on nucleic acid.[47]

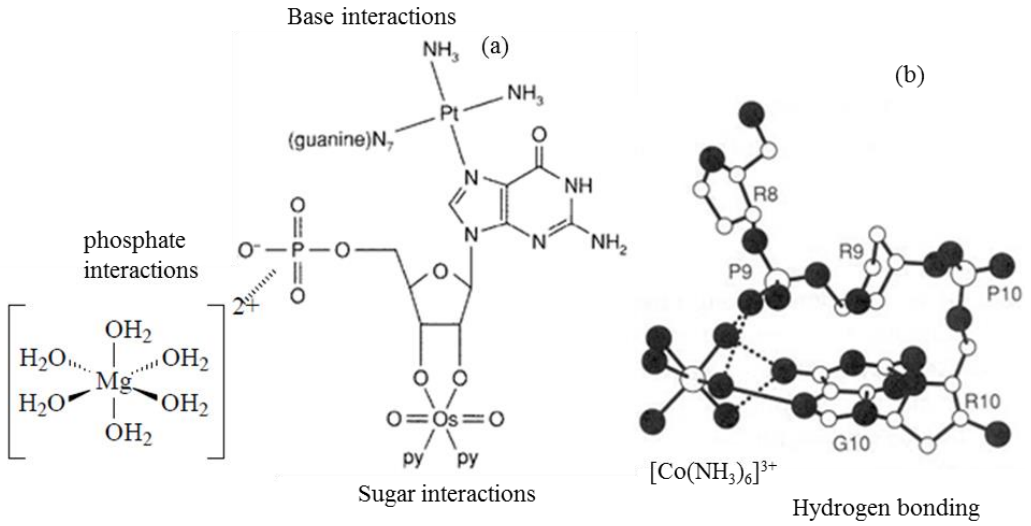

Figure 1-10: (a) An illustration of coordination to the DNA base, and sugar given by the covalent binding of cis-(diammine)platinum to the N7 nitrogen atom of neighbouring guanine residues, the formation of an osmate ester with ribose hydroxyl groups, and the primarily electrostatic association between $Mg(H_2O)_6^{2+}$ and the guanosine phosphate, respectively. (b) An illustration of hydrogen bonding of coordinated ligands. Shown is a partial view of the crystal structure of Z-form $d(CG)_3$ with $Co(NH_3)_6^{3+}$ hydrogen-bonded both to the guanine base (G10) and phosphate backbone (P9).[47]

Common metal ion binding sites on nucleobases are represented diagrammatically in figure 1.11. As illustrated in figure 1.11, the endocyclic nitrogen donors (N7 and N1) represent the most common binding sites of the adenine (A) and guanine (G) bases. Additionally, metal ion binding can also take place at O6 of guanine, though it is less common. On the other hand, interactions with pyrimidines involve N3 position on cytosine and thymine, after deprotonation, are also common.[47, 49, 50]

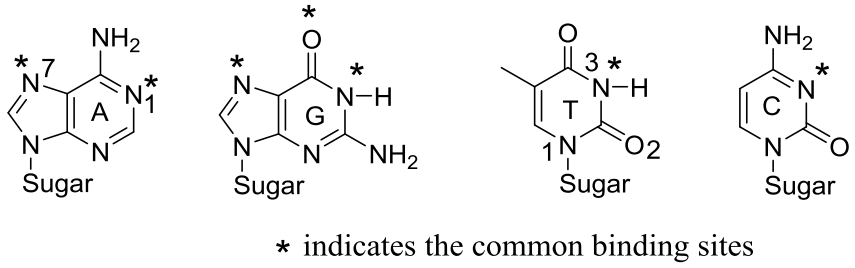

Figure 1-11: The structure of nucleobases with the common metal ion binding sites.

The basic modes of DNA-metal ions interactions can mainly be divided into two types. These are non-covalent interactions and coordinative bonding. The first type of interaction involves electrostatic interaction between the negatively charged phosphate groups and the positively charged metal ions, and 'outer-sphere' binding via hydrogen

bonds between a coordinated ligand molecule and a nucleobase and/or phosphate groups.[48, 49] The second type of interaction between metal ions and nucleic acid is coordinate inner sphere binding. This mode of interaction involves direct interaction between a suitable, empty orbital of the metal ions (acceptor) and nucleophilic positions on the bases (donor atoms), resulting in metal-nucleobase coordinate bond formation.[48, 49] The following sections will outline some examples of interactions between DNA and metal ions.

Alkali metals generally associate via outer sphere interactions with nucleic acids, and these metals do not bind tightly to DNA. The interaction between metal ions and nucleic acids, which are both hydrated, is accompanied with the release of water molecules.[50] Hydrogen bonding between an oligonucleotide and cobalt hexaammine, $[Co(NH_3)_6]^{3+}$, represents another example of outer sphere interactions. This interaction takes place between the ammine hydrogens and both phosphate oxygen atoms and purine bases, see figure 1.10b.[47]

An example of inner sphere binding between a metal ion and nucleic acid is the interaction of cis-diammineplatinum centers, in the drug cis-Platin, with two coordination sites available with DNA. This interaction yields an intrastrand crosslink between neighbouring guanine bases on a strand through coordination of platinum center to the N7 positions, see figure 1.10a.[47] Further example of inner sphere binding is provided by the interaction of mercury (Hg^{2+}) ions with DNA. It is found that Hg^{2+} ions can bring two opposite thymine bases together by substituting hydrogen bonds of the duplex to form strong covalent T-Hg-T crosslinks.[49, 51] In this instant, Hg^{2+} ions were found to form three T-Hg-T base pairs in a small trimer duplex, see figure 1.12.[51, 52]

It is previously reported that at low cation concentration, the interaction of DNA with Fe^{2+} species include binding of guanine N-7 and backbone PO_2^- group of the DNA, while Fe^{3+} cations bind primarily to PO_2^- group of the DNA backbone. At higher cation concentration Fe^{2+} cations bind to adenine N-7 and thymine O-2 of the DNA, whereas Fe^{3+} cations bind to guanine N-7 atom and the backbone PO_2^- group.[53]

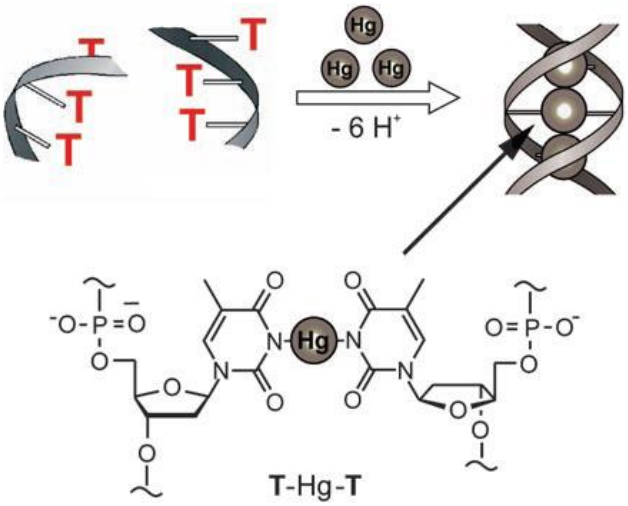

Figure 1-12: Schematic diagram showing formation of three T-Hg-T base pairs in a small trimer duplex upon addition of Hg^{2+} ions.[51]

1.9 DNA for nanoscience and technology

DNA has been shown to be a highly effective material for the design and synthesis of nanoscale objects. This is due to its distinctive molecular recognition properties, combined with the direct methods for modifying DNA.[54] Seeman *et al.*,[55] were first fabricated complex structures based only on DNA by exploiting its molecular recognition properties. They prepared branched junctions (figure 1.13) that work as building blocks for more complex two- and three dimensional DNA structures.

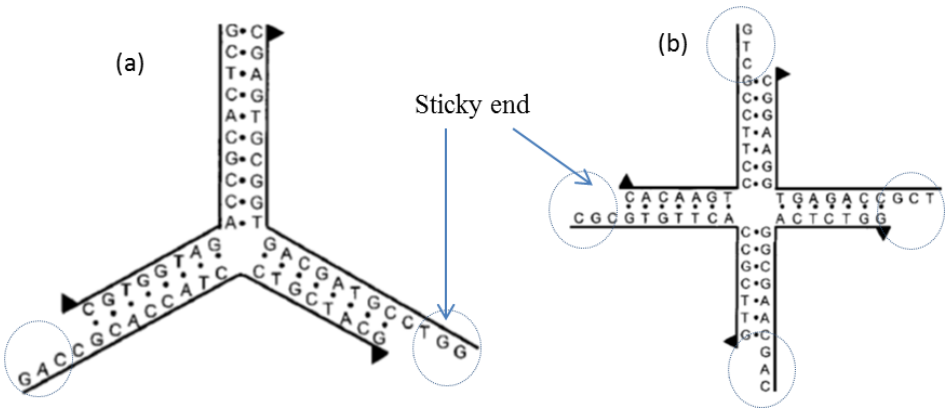

Figure 1-13: Schematic illustration showing (a) three-arm branched junction, and (b) four-arm branched junction, with sticky ends (circled areas). [54]

These branched DNA building blocks can be used to prepare more complex 2-D and 3-D DNA structures, by placing single-stranded "sticky ends" on their arms.[54] A DNA quadrilateral unit was the first structure to be prepared using such method based on the

assembly of four complementary three-arm branched junctions through the association of sequence specific sticky ends, (figure 1.14). The edges of these structures are comprised of double-stranded DNA, whereas the vertices are formed by the junctions. As soon as these structures are formed, the "nicks" in the DNA within these structures can be covalently linked using DNA ligase in order to provide a more rigid material.[54, 56]

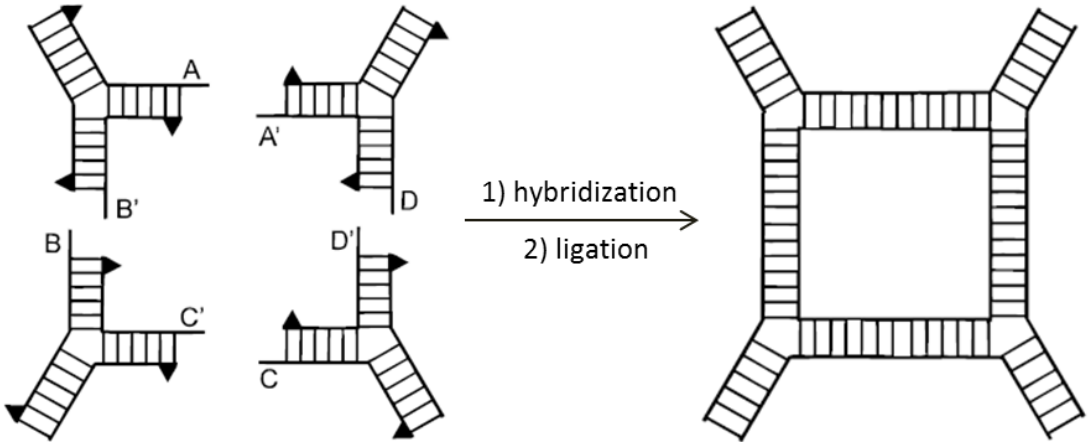

Figure 1-14: Schematic diagram showing the formation of a DNA quadrilateral structure.[54]

In principle, more complex DNA structures can be organized by adjusting the number of "arms" in a given branched DNA structure. Nevertheless, the preparation of more complex three-dimensional structures in solution suffers low yields.[54] In order to address such challenge, Seeman developed a solid support methodology for preparing DNA materials.[57] With the use of such a method, the yield problem was addressed and the preparation of more complex structures became accessible. A DNA truncated octahedron (figure 1.15a), with 2550 nucleotides is an example of complex structures that constructed using a solid support methodology.[58] The DNA truncated octahedron produced is more complex than the DNA cube (figure 1.15b) which comprises only 540 nucleotides and represents the most complex structures prepared in solution.

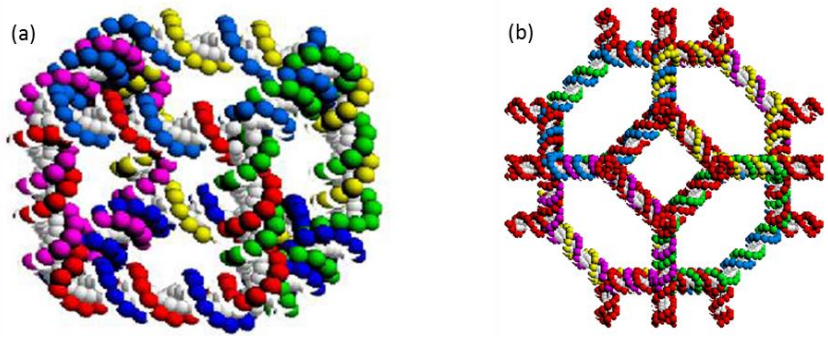

Figure 1-15: Early constructs constructed from DNA (a) A cube-like molecule, and (b) a DNA truncated octahedron. [59]

The cube and the truncated octahedron structures demonstrated that the building of complex structures based on DNA can be accomplished making use of the molecular recognition properties of DNA, combined by enzymatic ligation.[54]

DNA can also be used to organize metallic nanoparticles. Two-dimensional arrays comprising multiple components each carrying a different cargo, have been used to organize complex arrangements of metallic nanoparticles.[60] For this, 5 nm gold (Au) nanoparticles were placed on the end of one of the propagation directions in one of the three-dimensional-double crossover (3D-DX) motif, that used to organise the nanoparticles. In the same place in the other 3D-DX, a 10 nm Au nanoparticles was placed, see figure 1.16a. This results in the elimination of one propagation direction, allowing 2-D arrays to be formed. Transmission electron microscopy image figure 1.16b displays the checkerboard pattern formed by the Au nanoparticles.[59, 60]

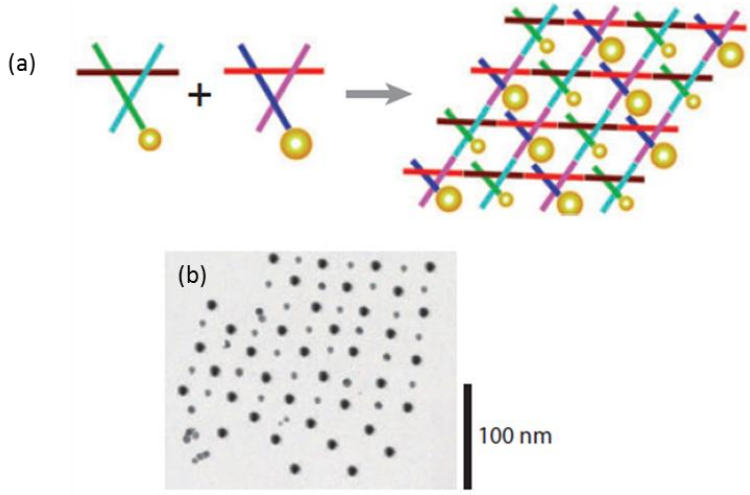

Figure 1-16: (a) Two different three-dimensional-double crossover (3D-DX) motifs and forming a checkerboard nanoparticle array. (b) A transmission electron microscopy image showing a checkerboard array of gold nanoparticles.[59]

1.10 DNA as a template for nanomaterials synthesis

DNA has been used as a template to organize inorganic and organic building blocks.[54] In this regard, the first effort to use DNA as a template to organize inorganic building blocks was reported by Coffer and co-workers.[61] In this work, they used calf thymus DNA as a template for forming cadmium sulfide (CdS) nanoparticles. The CdS nanoparticles were prepared in two steps. The first is the mixing an aqueous solution of calf thymus DNA with Cd^{2+} ions. In the second step, sodium sulfide (Na_2S) was added to the DNA/Cd^{2+} complex solution. This results in the formation of CdS nanoparticles

with an average particle size of 5.6 nm as confirmed by high-resolution transmission electron microscopy (HRTEM).

Coffer and co-workers [62], also developed a method to form CdS nanoparticles with well-defined structures. In this method, Cd^{2+} ions were mixed with a solution containing circular plasmid DNA to form DNA/ Cd^{2+} complex. The resulting DNA/Cd^{2+} complex in the reaction solution were then bound to a polylysine-coated glass surface. The CdS nanostructures were then formed by subsequent treatment of the DNA/Cd^{2+} bound to the modified glass surface with H_2S, see figure 1.17. TEM studies indicated the presence of 5 nm CdS nanoparticles along the DNA backbone.

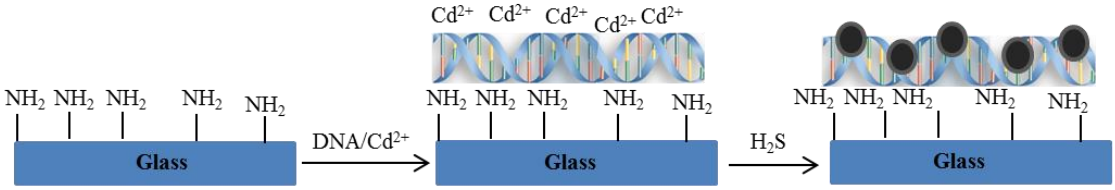

Figure 1-17: Cartoon representation of the preparation of DNA-templated CdS nanoparticles.

It has been demonstrated that DNA can be used as a template to organize nanoparticles of CdS and this method offers great possibility for using DNA as a template to organize the formation of organic/inorganic building blocks.[54]

1.10.1 Metals templated on DNA

The fabrication of DNA-templated metal nanowires relies upon a stepwise process involving initial association of the desired metal ions with the DNA template molecules, followed by their reduction to the zerovalent metal (figure 1.18). The seeding of DNA with metal ions can be performed either by a solution based approach or upon surface-immobilised DNA.[44] Metal ion binding at the polyanionic phosphodiester backbone for example, can take place through the formation of electrostatic interactions involving the hydrating water molecules around the metal ion or through inner-sphere coordinate bonds directly to the DNA phosphate groups.

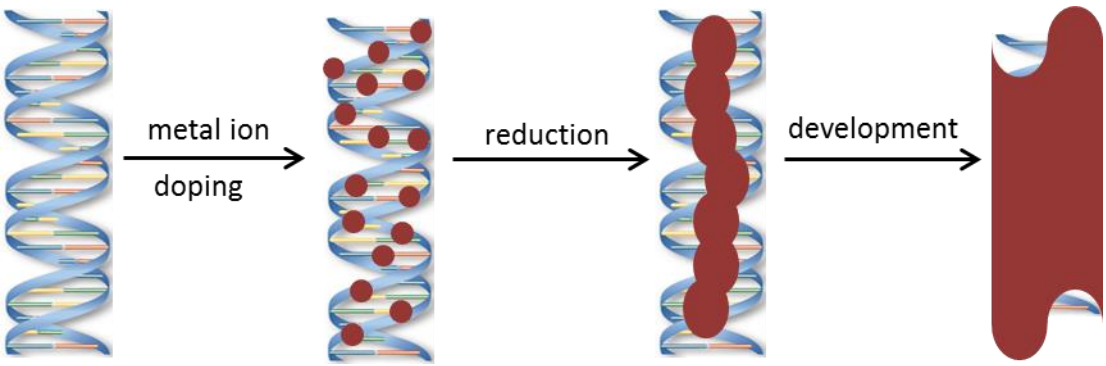

Figure 1-18: Schematic illustration showing the reaction sequence for the fabrication of metal nanowires using DNA as a template.

Alternatively, interactions may also take place through coordination of the metal cations to electron donor sites (*e.g.* ring nitrogen atoms) within the DNA bases.[48, 63] The reduction of DNA-bound metal ions result in formation of nanoparticles of the metal along the duplex DNA strand, which over time, leads to the formation of a continuous coating around the DNA template to give the final metal nanowire.[44] This approach has been used in directing the growth of a range different metals, including silver, palladium, copper and nickel into organised 1-D nanostructures.[44]

The first example of the preparation DNA-templated metal nanowires using this two-step process was reported by Braun *et al.*, [18] describing the formation of silver (Ag) nanowires. In this surface-based approach, λ-DNA molecules were first immobilized between two gold electrodes. The DNA was subsequently treated with a basic aqueous solution of $AgNO_3$ in order to dope the template with Ag^+ ions. The DNA-bound Ag^+ ions were then chemically reduced using a basic solution of hydroquinone to form metallic nanoparticles of silver (Ag^0) along the DNA. The resulting DNA-templated Ag^0 structure was further treated with an acidic solution of Ag^+ and hydroquinone. This results in continuous Ag^0 structure around the DNA template because the Ag^0 aggregates on the DNA act as a catalytic sites for the deposition of further Ag^0 around the templates. Atomic force microscopy (AFM) images of the resulting DNA/Ag^0 nanowires revealed them to exhibit a granular morphology with diameters ranging from 30 to 50 nm (figure 1.19). The electrical characterisation of the silver nanowires using i-V measurements indicated that these are electrically conducting.

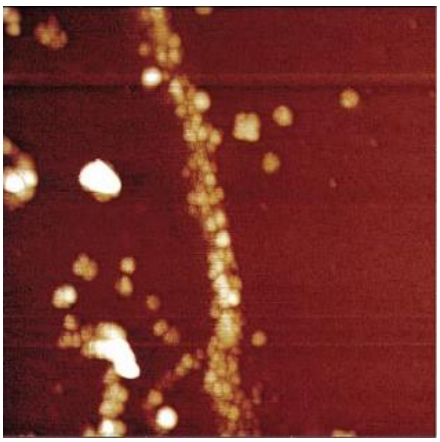

Figure 1-19: AFM image of a silver nanowire with granular structure.[18]

Richter *et al.*, [64] have also used two-step procedures for the preparation of palladium (Pd) nanowires. Here, λ-DNA was doped with Pd^{2+} by mixing with a palladium acetate solution. This was followed by introducing a reduction bath comprising of sodium citrate, lactic acid, and dimethylamine borane to the DNA/Pd^{2+} in reaction solution. This results in formation of clusters of metallic Pd^0 on the DNA templates. Transmission electron microscopy (TEM) and scanning electron microscopy (SEM) studies showed that Pd^0 clusters, with diameter of 3-5 nm, grow along the DNA templates within a few seconds of reduction commencing. However, DNA was coated with quasi-continuous palladium (20 nm in size), after 1 minute reduction time. This indicates that the deposition of Pd^0 on the DNA template taking place through 'nucleation and growth' mechanism[18], in which the Pd^0 clusters which deposited on the DNA at shorter reduction time act as a catalytic sites for deposition of further Pd^0 metal.

DNA-templating strategies have also been used for the fabrication of copper (Cu) nanowires. The earliest example of DNA-templated Cu nanowires was reported by Woolley *et al.*, [65] whereby Cu nanostructures were prepared through association of Cu^{2+} ions with surface-immobilized DNA, followed by their reduction to the zerovalent Cu. For the formation of DNA/Cu^{2+}, DNA modified silicon substrate was treated with aqueous solution of $Cu(NO_3)_2$, and the reduction process was achieved by subsequent addition of ascorbic acid to the reaction solution. AFM studies of the resulting DNA/Cu nanostructures showed irregular coverage of the DNA by the Cu (figure 1.20a) after a single doping/reduction treatment. However, upon repeating the doping and reduction procedures, DNA-templated metal nanowires with more complete coating were able to be produced, see figure 1.20b. In order to improve the deposition of Cu at the DNA

template, a refinement of this method was carried out using dimethylsulfoxide (DMSO) as a solvent. This method results in granular structure with more extensive deposition of Cu along the DNA template. However, although structural characterisation was carried out, there were no electrical studies performed and so the Cu structures could not be confirmed as nanowires.

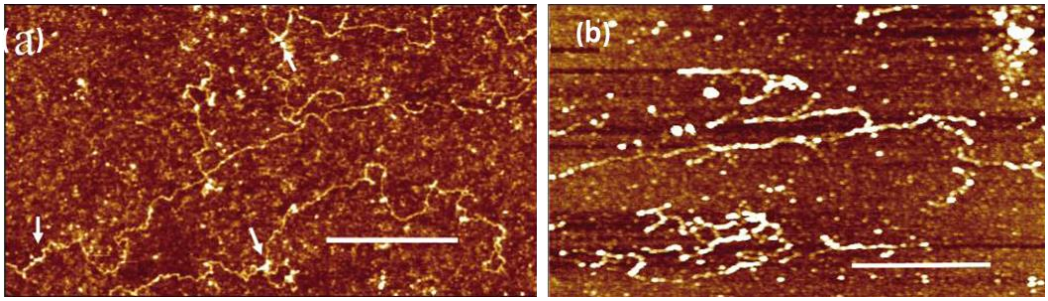

Figure 1-20: AFM images of DNA-templated Cu nanowires after once doping/reduction treatments (a), and after two times $Cu(NO_3)_2$/ascorbic acid treatments (b), scale bare = 1 μm in both images.[65]

As Cu wires are of particular interest with a view to applications as future interconnects, there has been an increasing interest in the fabrication of Cu nanowires using DNA as a template. Recently, Watson *et al.*,[66] have used similar method to that reported by Woolley [65] for the formation of Cu nanowires. In this work, AFM studies of the prepared Cu nanostructures (figure 1.21) indicated that, these nanostructures have a "beads-on-string" morphology and scanned conductance microscopy (SCM) studies demonstrated the structures to be high resistivity. This was proposed to be due to "bead-on-a-string" appearance and size of Cu^0 nanoparticles, which leads to scatter of electrons at the interface between the nanoparticles and at the structure surfaces.

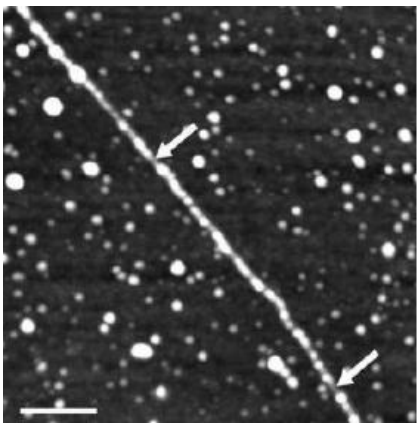

Figure 1-21: AFM image showing "beads-on-a-string" morphology of the Cu nanostructures. The arrows represent a small amount of Cu^0 deposited on the λ-DNA molecule, (scale bare = 200 nm).[66]

1.10.2 Inorganic semiconductors templated on DNA

The ability of DNA molecules to bind metal ions has allowed opportunities to fabricate a range of compound semiconductors as 1-D structures. The method is also a stepwise in which DNA is first doped with a metal ion component of the desired binary material. The DNA-bound metal ions are subsequently treated with an appropriate anion in order to allow the desired compound to nucleate and develop at the DNA template (figure 1.22). Cadmium sulfide (CdS) [61, 67], lead sulfide (PbS) [68], and copper sulfide (CuS) [69] represent some examples of binary materials that have been prepared on DNA.

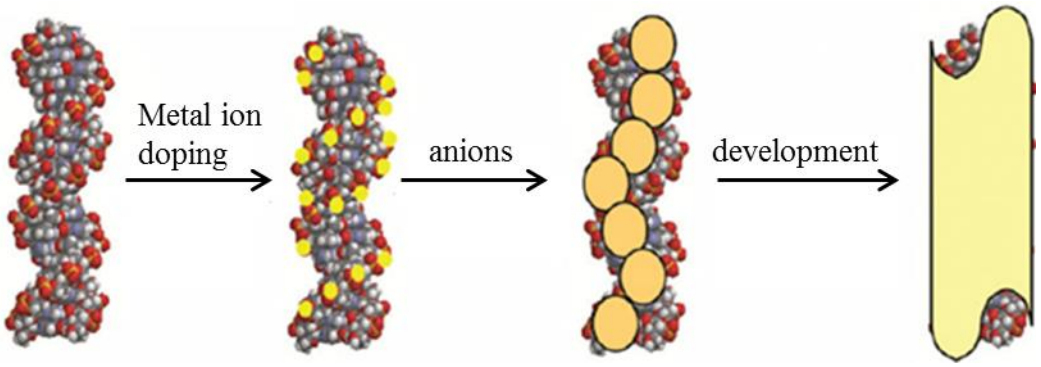

Figure 1-22: Schematic illustration showing general procedure for the formation of compound semiconductors along the DNA molecule.[42]

Coffer *et al.*, [61] first reported the growth of compound semiconductors on DNA, demonstrating the ability of DNA to stabilise CdS nanocrystalls. For the formation of DNA/CdS nanostructures, calf thymus DNA was first mixed with cadmium perchlorate $Cd(ClO_4)_2$ in order to dope the DNA with Cd^{2+} ions. Sodium sulfide (Na_2S) was subsequently added to the reaction mixture to form CdS material directly upon the DNA. High-resolution TEM studies of the product materials displayed zinc blende lattice structure with an average diameter of 5.6 nm.

Recently Dong *et al.*, [67] reported that the synthesis of CdS as either 1D nanoparticles arrays or as continuous nanowires can be accomplished through regulation of the reaction conditions. In their work, templating reactions were performed upon both surface-immobilised DNA and DNA in solution. In both cases the templating reactions were achieved by an initial incubation of the λ-DNA with $Cd(NO_3)_2$ followed by treatment with Na_2S solution. AFM studies of the DNA/CdS material prepared using surface-immobilised method indicated that nanoparticles are formed on the DNA

template, producing a beads-on-a-string morphology, see figure 1.23a. The particles are highly mono-disperse with diameters in the range 11.3-16.7 nm. On the other hand, the templating reactions carried out in solution produced wire-like DNA/CdS structures with little variation in diameter along the length, with the nanowires typically ranging from 11 – 15 nm in size, see figure 23b. The resulting nanowires were subsequently integrated into a two-terminal device (figure 1.23c) to study their electrical behaviour confirmed the structures to be electrically conducting.

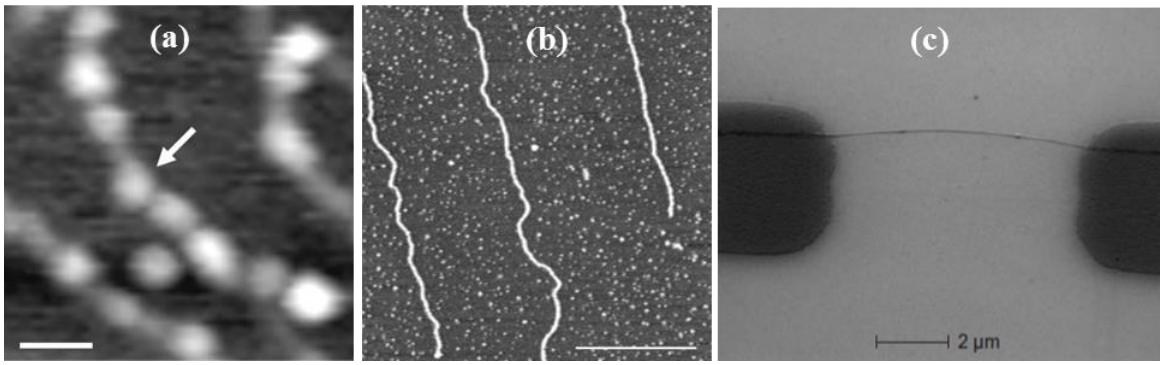

Figure 1-23: AFM image of the DNA/CdS prepared using surface-immobilised method showing a "beads-on-a-string" morphology, white arrow referred to monodispersed particles of the CdS at λ-DNA template. Height scale = 5 nm and scale bar is 25 nm. (b) AFM image of DNA/CdS nanowires prepared in solution, height scale = 3 nm and scale bar is 500 nm. (c) SEM images of DNA/CdS nanowire bridges two gold electrodes. [67]

A number of other compound semiconductors have also template on DNA using this two-step method. For example, Sargent and co-workers reported the preparation of DNA/PbS nanostructures.[68] In this work, calf thymus DNA was exposed to sequential treatment with $Pb(NO_3)_2$ and Na_2S at temperatures ranging from 20-100 °C. These procedures result in formation of efficient infrared photoluminescent PbS nanoparticles directly on the DNA templates.

Copper sulphide has also been subjected to study during the development of DNA-templating strategies. In this instance, templating reactions were performed both via surface-immobilised and solution-based approaches, involving initial incubation of λ-DNA with $CuCl_2$ as source of Cu^{2+}, followed by addition of Na_2S to form CuS directly on the DNA. AFM studies of the material prepared using solution-based approach showed chains of nanostructures, comprised of the DNA templates densely covered with CuS nanoparticles. The surface-immobilised approach produced CuS nanoparticles with diameters up to 10 nm which are larger than those produced by the solution-based approach. [69]

1.10.3 Organic conducting polymers templated on DNA

The templating of conducting polymers (CPs) such as polyaniline (PA), polypyrrole (PPy) and polyindole (PIn) on DNA strands depends on non-covalent interactions between the DNA and the growing CP chains. A simple view of this process is that the conducting polymer, formed as cationic oligomers, binds to the polyanionic biopolymer through a combination of supramolecular interactions, e.g. electrostatics and additional non-covalent bonding, which influences the growth/binding of further polymer along the DNA template. The resulting DNA-templated polymer nanowires comprise of both anionic duplex DNA and cationic synthetic conductive polymer strands.[16, 42, 44] Figure 1.24 displays schematic illustration showing the general procedure for the formation of conducting polymers on DNA. The DNA-templating strategy has been successfully demonstrated for fabrication a variety of different conducting polymer nanowires such as polyaniline (PA) [70], polypyrrole (PPy) [71, 72], polyindole (PIn) [73] and poly2,5-(bis-2-thienyl)-pyrrole (TPT).[16]

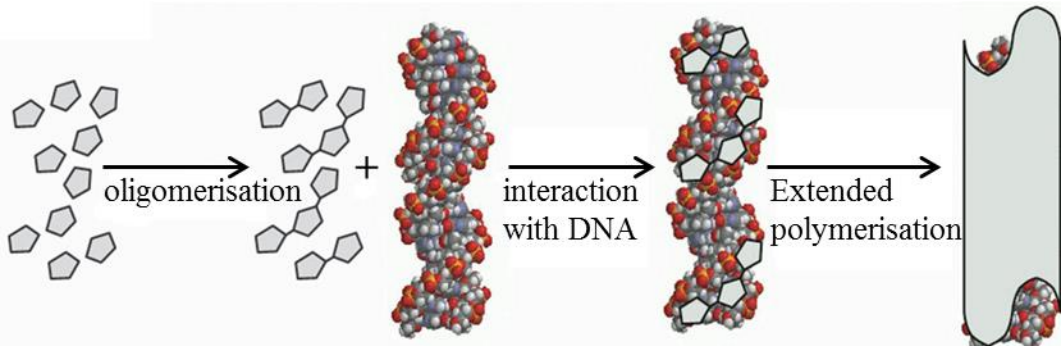

Figure 1-24: Schematic illustration showing general procedure for the formation of conducting polymers at a DNA template. [42]

He and co-workers first reported on the formation of DNA/PA nanowires using DNA molecules immobilised on Si/SiO_2.[70] Here, the substrate surface was first treated with (aminopropyl)triethoxysilane to provide a cationic surface for immobilising the λ-DNA template molecules upon. This was followed by treatment of the DNA-modified surface with an acidic solution of aniline to combine and organize the monomers at the DNA templates. The polymerisation was then induced enzymatically by adding horseradish peroxidase and H_2O_2, to form the DNA/PA nanowires. AFM studies confirmed the presence of material upon the DNA as evident from increase the height structure after the polymerisation procedure. The reaction was also demonstrated to be pH dependent.

For example at pH 5.0 nanoparticles of PA were deposited along the template producing a beads-on-a-string morphology (figure 1.25a), whereas at lower pH (3.2), structures with incomplete polymer coverage of the DNA were observed, see figure 1.25b. The best growth of the prepared DNA/PA nanowires were obtained when the polymerisation was carried out at pH 4.0, see figure 1.25c.

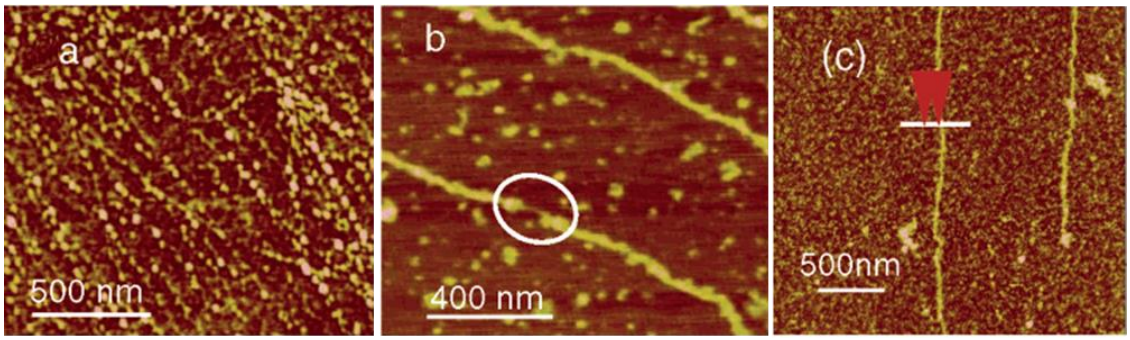

Figure 1-25: AFM images of stretched λ-DNA immobilised on Si substrate after polymerisation at different pH. (a) Polymerisation in pH = 5.0 solution producing PA nanoparticles along the template. (b) Polymerisation in pH = 3.2 solution produced DNA/PA structure with incomplete coverage. (c) Polymerisation in pH = 4.0 solution produced the best structure.[70]

DNA-directed synthesis was also used for the fabrication of DNA/PPy nanowires through oxidation of pyrrole in DNA-containing solution or at surface-immobilised DNA, using $FeCl_3$ as an oxidizing agent.[71] Although both of these procedures result in preferential growth of the conducting PPy along DNA templates, variation in the structure of the resulting DNA-templated PPy nanostructures was observed for templating these materials at surface-immobilised DNA or in solution. AFM studies indicated that the former method produced a bead-on-a-string morphology (figure 1.26a), whereas material isolated from reaction solution showed smooth and continuous DNA-templated PPy nanowires, see figure 1.26b. The DNA/PPy nanowires prepared in solution were aligned between two gold electrodes using molecular combing for fabricating two-terminal electrical devices which confirmed these nanowires to be electrically conducting.

Pruneanu *et al*., [72] have also used aqueous preparations similar to that previously described [71] for the fabrication of DNA/PPy nanowires. Here, the authors demonstrated that over longer incubation time PPy nanowires prepared using DNA as a template undergoes a self-assembly process to produce rope-like structures (figure 1.26c). AFM studies indicated that these nanoropes are formed by twisting individual nanowires around each other. This was evident from the frayed ends of the structure

where individual nanowires were observable. The electrical properties of the resulting DNA/PPy nanoropes were characterised using a combination of electric force microscopy, conductive AFM and two-terminal device, confirming that these nanoropes are conducting.

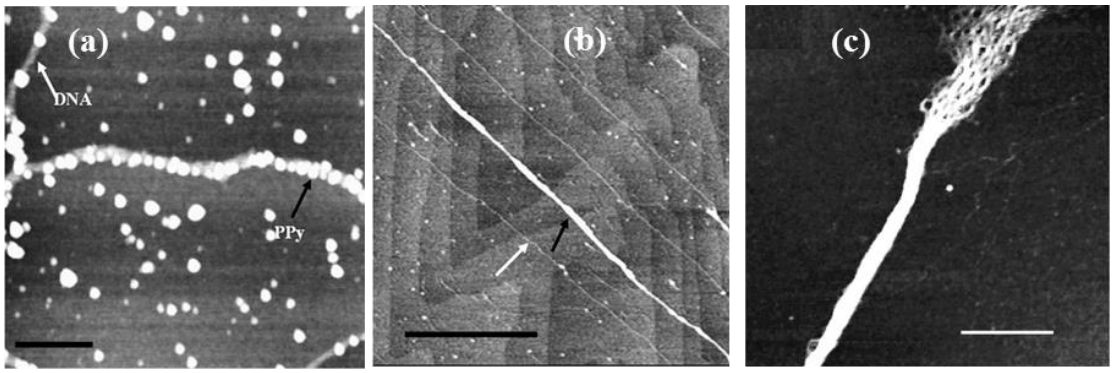

Figure 1-26: AFM image of DNA/PPy nanostructures prepared via polymerisation of pyrrole at surface-immobilised DNA, scale bare is 200 nm and height scale = 4 nm. (b) AFM image showing DNA/PPy nanowires isolated from the reaction solution (black arrow) and bare DNA strands (white arrow). Scale bare = 1 μm and height scale = 4 nm.[71] (c) AFM image of DNA-templated PPy nanoropes aligned upon SiO_2/Si after 48 hours reaction time, scale bare is 500 nm and height scale = 8 nm.[72]

Recently, DNA-templated PIn nanowires have also been prepared in solution by chemical polymerisation of indole using $FeCl_3$ as the oxidizing agent.[73] The resulting DNA/PIn nanowires are found to be photoluminescent, conductive and showed smooth and uniform structures with diameters in the range of 5-30 nm.

More recently, Watson *et al.*, [16] have reported on the formation of supermolecular polymer nanowires via using DNA-templating of 2,5-(bis-2-thienyl)-pyrrole (TPT). In this work, the polymerisation was initiated through the addition of aqueous solution of $FeCl_3$ into a mixed aqueous/organic solvent containing DNA and TPT. FTIR studies indicated that the resulting material is a supramolecular polymer formed via intimate interactions between the DNA template and polyTPT stands. AFM studies of the produced DNA/polyTPT material showed individual nanowires to exhibit smooth and uniform morphologies. These nanowires were judged by a combination of electrostatic force microscopy, conductive AFM and two-terminal device to be electrically conducting.

1.11 Aims and Objectives

This project aims to explore synthetic routes to the growth of metals, inorganic semiconductors and polymers at DNA templates. An example of a semiconductor is iron oxide. The initial focus for this project will be to explore synthetic routes to the growth Fe_3O_4 material at DNA. Such materials have potential use in electronic and magnetic-based devices as well as etch resists in nanoscale pattern formation.

The project is also dedicated to the fabrication of metal-based structures which have not previously been explored as a part of DNA-templating fabrication strategies, such as iron and rhodium. The fabrication of 1-D zerovalent Fe or Rh nanostructures was attempted by chemical and an electrochemical-based, DNA-templating approach. The use of DNA-directed synthesis in conjunction with electrochemical reduction is believed to be the first example of electrochemical growth of an electrically conductive, inorganic material at a DNA template.

Finally, the preparation of supramolecular polymer nanowires via DNA-templating of 2,6-diaminopurine-propyl-2,5-bis-dithenyl pyrrole (DAP-prop-TPT) and thymine-propyl-pyrrole (T-prop-Py) was also explored. These nanowires are expected to interact with each other by means of complementary hydrogen bonding between diaminopurine and thymine substituent groups. This will be explored by AFM studies of mixtures of these individual conducting polymer nanowires in order to investigate changes in morphology upon mixing.

Throughout this project, a range of techniques was used in order to characterize the prepared nanowires, including FTIR and XPS spectroscopy and XRD to confirm the chemical identity of product materials. Additionally, scanning probe microscopy techniques such as atomic force microscopy (AFM), electrostatic force microscopy (EFM), conductive AFM (c-AFM) and magnetic force microscopy (MFM) was used to investigate the structural character, electronic properties and magnetic behavior of the prepared nanowires, respectively.

2. Chapter 2: Analysis Techniques

This chapter describes the main techniques used for characterisation of the DNA-templated nanowires prepared in this project. A series of spectroscopic techniques including Fourier transform infrared (FTIR), and X-ray photoelectron (XPS) spectroscopy, and X-ray diffraction (XRD) have been used in order to establish the chemical composition of the fabricated nanowires. In order to probe structural and physical properties of the nanowires, a range of scanning probe microscopy (SPM) techniques have been in employed. Atomic force microscopy (AFM) has been used to investigate the size and morphology of the nanowires, whilst electrostatic force microscopy (EFM) and conductive AFM (c-AFM) were employed to study their electrical properties. Magnetic force microscopy (MFM) has also been used in order to probe the magnetic behaviour of the nanowires. The details of these techniques will be discussed in the following sections.

2.1 X-ray Photoelectron Spectroscopy (XPS) [74-76]

X-ray photoelectron spectroscopy (XPS), also sometimes referred to as electron spectroscopy for chemical analysis (ESCA) is a surface analysis technique, used to characterise the chemical composition and electronic state of the elements, which is sensitive to a sample surface (usually < 10 nm). This technique is based upon the process of photoemission. In the XPS experiment, the sample is first placed under ultrahigh vacuum environment and then irradiated with X-rays. The X-rays hitting the sample cause a core electron (photoelectron) to be emitted from the atom due to energy transfer from incident photon to the core electron, (figure 2.1). XPS spectra are then recorded by measuring the number of emitted electrons and their kinetic energy.

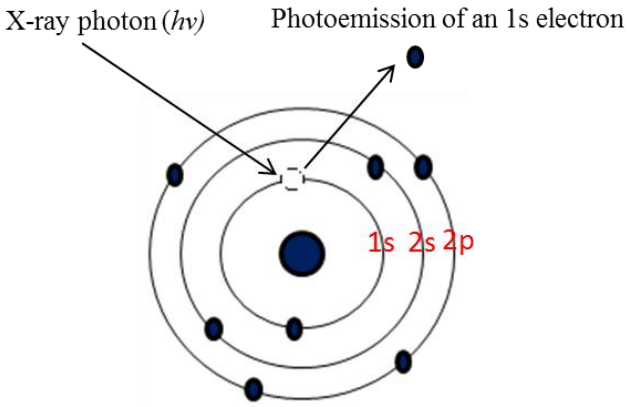

Figure 2-1: Schematic illustration showing the basis of XPS. The energy of X-ray photon is absorbed by a core-level electron, resulting in photoemission process.

The kinetic energy of the ejected electron is described by equation (2.1):[76]

$E_k = h\nu - E_b - \phi$ 2.1

where, E_k is the kinetic energy of emitted electron that is measured in the XPS spectrometer, $h\nu$ is the energy of the X-ray source, E_b refers to the binding energy of the electron, and ϕ is the work function of the spectrometer. As the photon energy and work function are known, this can then give the binding energy which is characteristic of photoelectrons from specific elements in particular states.

It should be noted that the photoemission takes place only when the energy of the excitation photon is higher than or equal to binding energy characteristic of each element. The energy of the X-ray photon is usually sufficient to emit electrons from core energy levels of the target atom. The core electrons are the electrons closer to the nucleus and have binding energies characteristic of their particular elements. Therefore, the binding energy of core electrons can be used as finger print of the constituent atoms of the sample under investigation.

The XPS spectrum is a plot of the intensity of emitted electrons versus the binding energy of these electrons. The energy of the emitted electrons depends on atomic and molecular environment from which they originated and the concentration of the emitting atoms in the sample determines the peak's intensity. A XPS spectrum shows a series of peaks at particular binding energy values which can be related to the photoemission from specific energy levels of specific elements. For instance, XPS survey spectra of DNA/polyTPT nanowires (figure 2.2) indicated the presence of all of the elements in the sample material.[16]

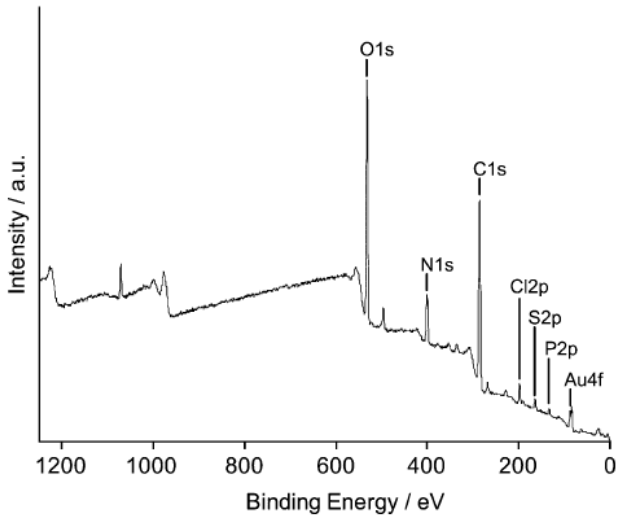

Figure 2-2: XPS survey spectrum of DNA/polyTPT nanowires.[16]

Additionally, the peaks are labelled based on the energy level from which they originated. As it is seen from figure 2.2, peaks are seen due to emission from the O1s, N1s, C1s, Cl2p, S2p, and P2p levels.

Moreover, the energy of the emitted electrons depends on the chemical state of atoms. For example, the presence of a particular element in different chemical state (e.g. oxidation state), its binding energy will be different. Core level XPS spectra of Rh3d region of rhodium nanoparticles (figure 2.3) for example; displays two doublets peaks ($Rh3d_{5/2}$ and $Rh3d_{3/2}$) at different binding energies, indicating that the product material contains rhodium in two different chemical states. In figure 2.3, the dominant doublet peaks with lower binding was assigned to metal Rh(0), while the minor doublet peak is found at higher binding energy and is indicative of the presence of rhodium oxide Rh_2O_3 in the sample material.[77]

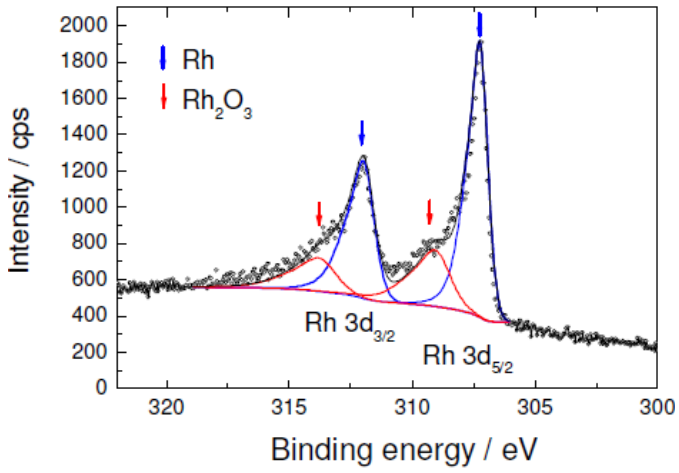

Figure 2-3: Core level XPS spectra of Rh3d region of rhodium nanoparticles.[77]

Figure 2.4 shows the basic components of an XPS spectrometer. These are an X-ray source, sample introduction chamber, lens, energy analyser and a detector mounted in an ultra-high vacuum (UHV). Magnesium (Mg) and aluminium (Al) represent two types of materials that are used as X-ray source. These materials produce X-rays of high energy and narrow linewidth when they are bombarded with high energy electrons. The Mg Kα has energy of 1253.6 eV and a linewidth of 0.7 eV, whereas the line energy of Al Kα is 1486.6 eV and its linewidth is 0.85 eV. In the XPS, sample is radiated with photons of a single energy. This results in emitting electrons from the sample and the emitted electrons are collected by a lens system which in turn directs them into an

energy analyzer where they are resolved by energy. The electrons are then collected and recorded by an electron detector.

In this thesis, all XPS were carried out using a Thermo Scientific K-Alpha X-ray photoelectron spectrometer (Thermo Electron Corp., East Grinstead, UK), equipped with an Al Kα X-ray source (1486.6 eV) with a variable spot size of 30–400 µm. A take-off angle of 90˚ was used during data acquisition, and a charge neutralisation gun used to compensate for surface charging. All spectra were referenced to hydrocarbon C1s peak at 285.0 eV. Survey spectra were acquired using a pass energy of 150 eV, whilst high resolution region spectra were acquired using a pass energy of 50 eV. Data analysis was carried out using CasaXPS software (Casa Software Ltd.).

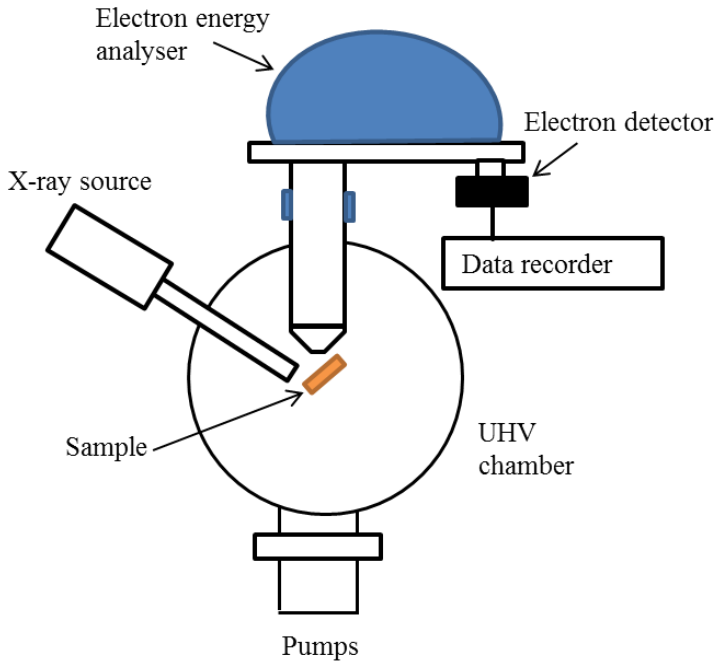

Figure 2-4: Schematic diagram of the major components of an XPS instrument.

2.2 Atomic force microscopy

Atomic force microscopy (AFM) is a type of scanning probe microscopy (SPM) techniques, developed in 1986 by Gerd Binnig and Heinrich.[78] AFM is a powerful tool for visualizing structures with very-high resolutions, approaching the atomic scale. It is classically used for mapping surface topographies.[79] Moreover, conducting atomic force microscopy (c-AFM) can be used to probe quantitatively the electric conductivity of the nanostructures.[73]

The general description of the AFM process, is to use a sharpened tip (typically < 5 μm long and often < 15 nm in diameter) mounted at one end of cantilever upon which a laser beam is focused, to track over the sample surface features. A three-dimensional image of the sample surface can then be obtained by monitoring the motion of the probe in the X, Y, and Z directions. The movement of the tip is achieved using piezeoelectric materials in the scanner. These control movement in the x, y, and z directions are achieved by an appropriately applied bias to the piezeoelectric materials.

The main components of atomic force microscope are illustrated in figure 2.5. These include piezo-scanners which are commonly constructed of piezoelectric materials, such as amorphous $PdBaTiO_3$. It includes also a laser with a set of mirrors, four-segment photodiode to amount the deflection of the cantilever, feedback loop which controls the z-sample place and electronics for a management of scanning procedures and data acquisition.

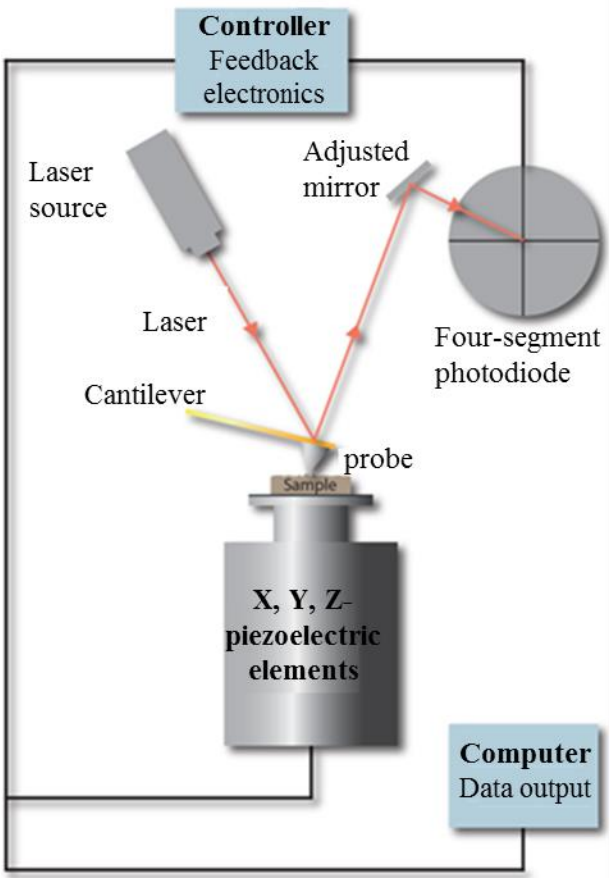

Figure 2-5: Schematic diagram of the major components of atomic force microscopy (AFM).

The tip deflection caused by the sample surface features are monitored through a laser reflecting of the cantilever onto photodiode arrays. The position of the laser on the

photodetector can be used to determine the vertical movement, and deflection of the tip can be interpreted as the surface features. There is also a feedback mechanism to that the height of the tip is adjusted appropriately when the tip is deflected by surface features, in order to keep force of tip on sample constant.

The AFM can be operated in contact mode and tapping, or intermittent contact mode. In contact mode, silicon nitride tips are commonly used. In this mode of operation, the AFM probe remains in close contact with the sample as the scanning proceeds (figure 2.6a). The probe-sample interaction in contact mode is dominated by repulsive forces. This causes a deflection of the AFM tip, and such deflection is used as a feedback signal. It should be noted that contact mode AFM imaging can cause damage to many soft samples such as organic and biological materials, due to high forces exerted by the tip on the samples. Therefore, cantilevers with low spring constant are required for gentle profiling of soft surfaces. On the other hand, in tapping mode operation the tip does not remain in contact the sample surface, but instead it oscillates near the sample surface, (figure 2.6b). In this mode of operation, attractive (mainly due to van der Waal's interaction) forces dominate the inter-atomic force between the cantilever and sample.[79] The tapping mode AFM was used predominantly in this work, in order to elucidate information regarding the size and structural character of the nanowires.

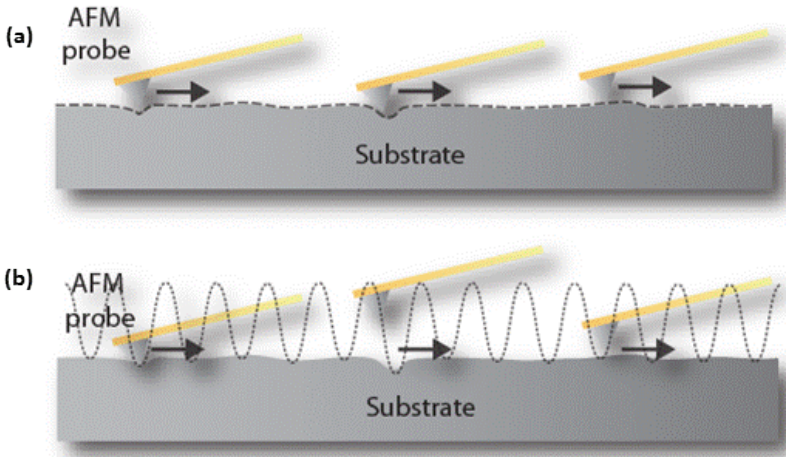

Figure 2-6: Schematic diagram showing (a) contact mode and (b) tapping mode operation of AFM techniques.

The tapping mode is used to map the sample topography by oscillating the probe close to its resonance frequency, mechanically driven by a piezo crystal located in the AFM tip holder (figure 2.7). The oscillating tip movement and its interaction with the sample surface are monitored again by monitoring the position of the laser deflected off the

cantilever onto the photodetector. As the probe encounters surface features, changes in the oscillation amplitude are used to identify and map surface features. In an analogous fashion to maintain a constant vertical force in contact mode, a feedback system maintains constant amplitude, also keeping a constant tip-sample distance. Therefore, in this mode of operation an image can be produced by monitoring the force between the tip and sample surface at the discontinuous contacts. In this mode, shear forces are almost eliminated and the intermittent tip-sample contact takes place at a high frequency that also limits material (both sample and tip) damage. Additionally, tapping mode operation is gentler than the contact mode and therefore it is useful for soft surfaces.

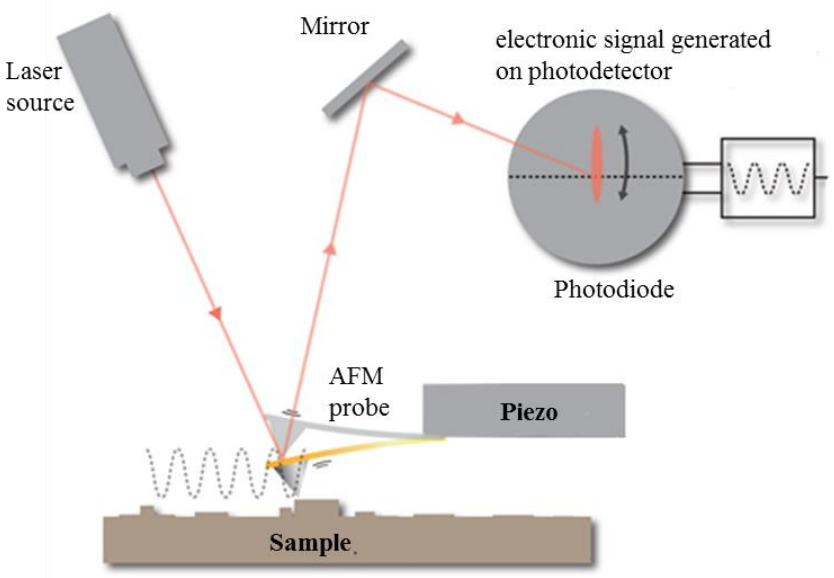

Figure 2-7: Schematic diagram showing tapping mode operation of AFM.

In this work, topographical AFM data was acquired using both a Multimode Nanoscope IIIa and a Dimension Nanoscope V system (Veeco Instruments Inc., Metrology Group, Santa Barbara, CA, USA) in TappingMode^{TM} operation. Etched Si AFM probes (TESP model, n-doped Si cantilevers, f_0 = 230–280 kHz, spring constant = 20–80 N m^{-1}, Veeco Instruments Inc., Metrology Group) were employed during TappingMode^{TM} operation. Data acquisition was carried out using Nanoscope version 5.12b36 and version 7.00b19 software (Veeco Instruments Inc., Digital Instruments) on the Multimode Nanoscope IIIa and Nanoscope Dimension V AFM systems, respectively. To reduce vibrational noise an isolation table/acoustic enclosure was used (Veeco Inc.,Metrology Group).

2.3 Conductive atomic force microscopy

Conductive AFM (c-AFM) is a contact-mode AFM method. It is typically used to characterise differences in conductivity across the sample surface. This technique can deliver simultaneous topographic and current distribution information of the nanostructures under study.[16, 44, 73]

The basic principle of c-AFM is that electrical contact is made to the sample, then the AFM probe acts as the second electrical contact. As the tip scans over the sample, topographical data was collected in contact mode operation, and AFM current image is simultaneously generated by applying a dc bias between a metallised, conductive AFM tip and the sample.[16, 44, 73] The current map can then be used to investigate the electrical conductivity, in which conducting nanowires show bright contrast relative to the background which indicates current flow through the nanowires.[16]

In this work, c-AFM is used to measure the conductance and estimate the nanowires conductivity. For c-AFM measurements, an experimental set-up (figure 2.8) was devised which allows the two electrical contacts to be made to the nanowire under investigation in a relatively straight forward manner.[16, 44, 73]

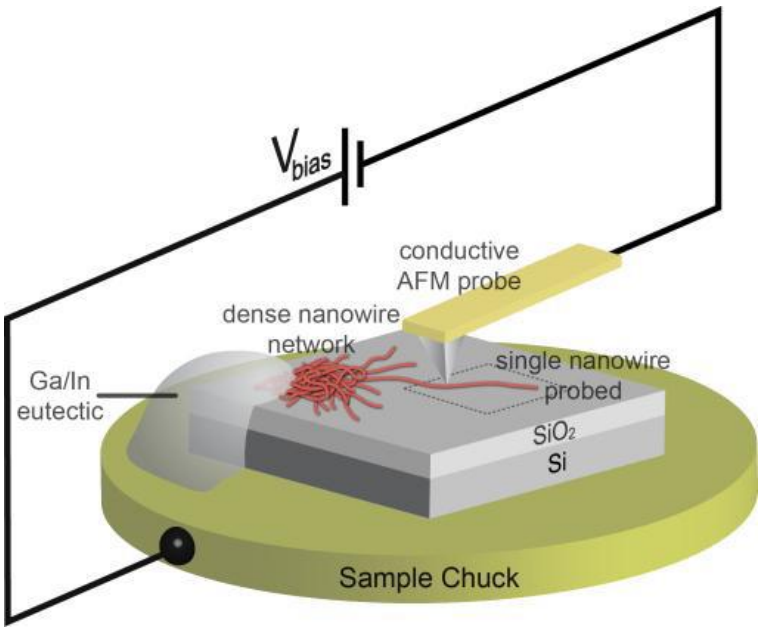

Figure 2-8: Schematic diagram showing c-AFM set-up used to measure the conductivity of nanowires located at the edge of a dense network of the nanowires deposited upon the substrate surface.[16]

This was achieved through drop-casting a sample of nanowires from solution onto the edge of a TMS-modified silicon substrate with dielectric layer of SiO_2 and allowing it to stand at room temperature for ~1 min. Subsequent withdrawal of part of the solution sample (approximately 3 μm) result in a dense network of nanowires on the surface with individual wires protruding out from the periphery of the network. The network acts effectively, as one electrode and electrical contact is made from this network to the sample chuck using Ga/In eutectic. As normal with c-AFM the other contact was provided by the metallic tip of the AFM which was located on the selected nanowire.

It should be considered that the mechanical contact between the tip and nanowire surfaces can cut thin nanowire during the c-AFM measurements. This provides challenges for the use of such techniques in characterising the nanowires conductivity. It is therefore, important to decrease the contact force of the tip on the nanowire under study by decreasing set-point.

After completing the image scan, the closed loop system of the Nanoscope V allows for the AFM tip to be brought into contact with the nanowire at specific points along the nanowire length and i-V measurements were recorded at each single point. The conductance can be estimated from the slope of i-V curve around zero bias for each measurement recorded.[73]

In this thesis, all c-AFM experiments were performed in air with a Dimension Nanoscope V system (Veeco Instruments Inc., Metrology Group), using MESP probes (n-doped Si cantilevers, with a Co/Cr coating, Veeco Instruments Inc., Metrology Group) with a spring constant of 1–5 Nm^{-1}, and SCM-PIC probes (n-doped Si cantilevers, with a PtIr/Cr coating, Veeco Instruments Inc., Metrology Group) with a spring constant of 0.2 Nm^{-1}. Ga/In eutectic was used to make an electrical contact between the nanowires and the sample chuck.

2.4 Scanned conductance microscopy (SCM)

SCM is a variant of electric force microscopy (EFM) which provides a procedurally simple, non-contact means of qualitatively evaluating electronic properties of nanostructures.[80-82] The basic principle of the technique involves probing electronic properties by monitoring the response of a vibrating tip to the influence of electric fields originating from the sample, typically induced by applying an independently applied bias to the sample. This technique has been called scanned conductance microscopy

because conductive objects on a dielectric film modify the capacitance between the tip and the substrate in a manner distinct from that due to polarisable insulators.[80-82]

SCM measurements are conducted using a 'two-pass' method, where the first pass is carried out in TappingMode™ AFM operation in order to collect topographical information. For the second pass, the probe is lifted, and maintained at a constant height above the sample (typically 40–100 nm), where the dominant tip-sample interactions arise from the long-range electrostatic force (figure 2.9). During the second pass, a direct current (dc) bias is simultaneously applied to the sample to generate an electric field. Changes in the phase angle occur as a result of an effective change in the AFM probes cantilever spring constant due to the influence of the electrostatic field gradient upon the oscillating probe. It is known that the phase signal associated with the nanowires provides a direct indication of the structure's electronic properties, with respect to whether they are electrically conducting (dark/negative contrast) or insulating (bright/positive contrast).[72, 80, 81] Further detailed mathematical treatment of the EFM/SCM theory is well-documented.[81]

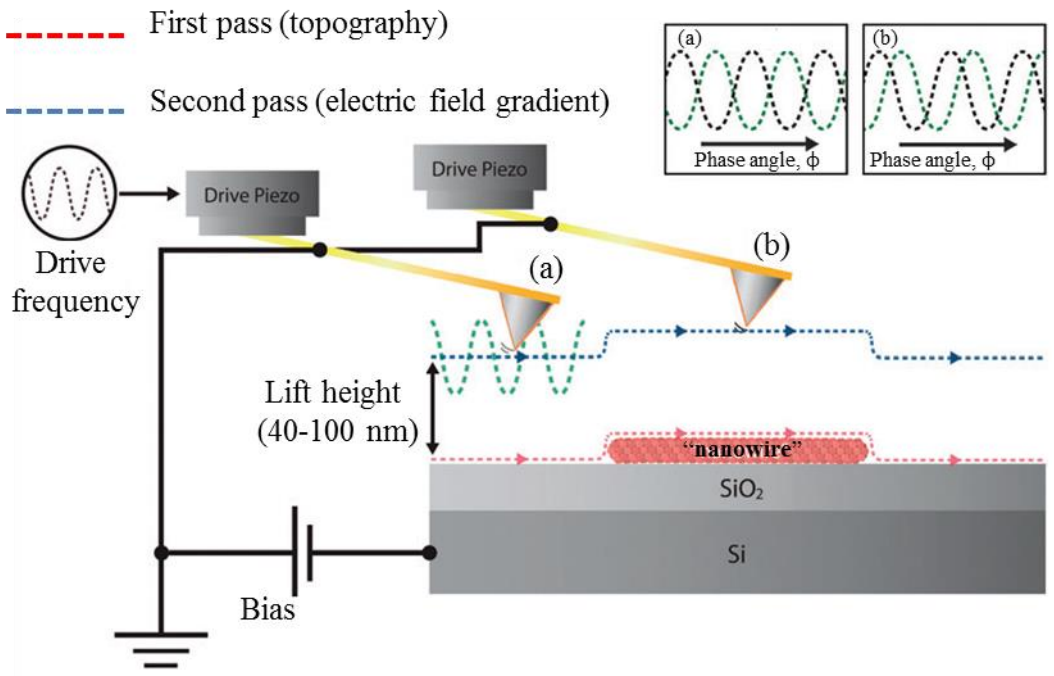

Figure 2-9: Schematic diagram showing the use of the two pass method of scanned conductance microscopy for characterising the electrical conductivity of nanowires supporting on a dielectric film such as SiO_2.[44]

The phase shift is proportional to the second derivative of probe/surface capacitance with respect to the probe–sample separation, where the capacitance is described as the series combination of the probe/nanowire and probe/surface capacitances.[72, 80, 81,

83] The phase shift, $\Delta\phi$, for an insulating object may be estimated using a model geometry in which the nanowire is represented by the area of a thin dielectric strip directly under the tip, itself modelled as a disc of radius, R_{tip}:[81]

$$\tan(\Delta\phi) = \frac{Q}{2k} V_{tip}^2 \left[\frac{2\pi R_{tip}^2 \varepsilon_0}{(h + t/\varepsilon_{ox})^3} - \frac{2\pi R_{tip}^2 \varepsilon_0}{(h + t/\varepsilon_{ox} + d/\varepsilon)^3} \right] \quad \text{.....2.2}$$

In equation 2.2, Q is the quality factor, k the cantilever spring constant, *t* refers to the oxide thickness and d is the diameter of nanowire. The first term of equation 2.2 is originated from the tip/substrate capacitance and the second term derived from tip/nanowire/substrate capacitance. It is clear from equation 2.2 that the phase shift can only be positive for insulating 1-D nanostructures, resulting polarisation of the nanowire region directly under the tip. For this reason, the first term in equation 2.2 is bigger than the second term and the sign of phase shift is positive. On the other hand, if the nanowire is conducting, the charge stored on the nanowire/substrate is able to spread along the whole length (L) of the nanowire. Therefore, the second term of the equation becomes significantly larger, because the nanowire length (L) is used to determine the capacitance instead of R_{tip}, resulting in a negative phase shift. Equation 2.2 also exhibits a parabolic dependence of the tangent of the phase shift on the applied dc voltage. This contrasts with the linear dependence of the phase shift on potential that arises from the electrostatic force caused by trapped charges: the different dependences on applied voltage has been used before to distinguish the effects of static charge and conductance in EFM.[83-85]

In this work EFM was used to demonstrate qualitatively the conductive nature of the nanowires. The resulting data provided is a phase image, where the phase shift associated with the nanowire gives a straight forward means of indicating for the structure is conducting or not.

2.5 Magnetic force microscopy

Magnetic force microscopy (MFM) [86, 87] is an appropriate tool for detecting magnetic fields arising from magnetic nanostructures. MFM is non-destructive technique which uses a magnetic AFM probe in order to map the magnetic structure of a sample. The MFM technique operates in an analogous manner to EFM; in this case a magnetised AFM tip is used which allows for the magnetic force gradients above a

sample to be mapped through monitoring the phase response of the tip during its second pass over each scan line.

Like SCM, MFM also works via a "two-pass", (figure 2.10) in which the first scan of the AFM probe is used to collect topographical information in standard TappingMode operation. The second pass is carried out with the oscillating tip at a defined 'lift height' (10 – 100 nm), where the dominant tip-sample interactions arise from the long-range magnetic forces. The magnetic interactions are monitored in an analogous fashion to electric fields in EFM. That is, changes in the phase lag of the AFM probe, as a result of the influence of the magnetic fields, are recorded as the probe travels above the sample surface. The theory behind the interpretation of the phase shifts is somewhat more trivial in comparison to EFM data, however. Briefly, similar to the influence that an electric field gradient has upon a conductive AFM probe, the presence of a magnetic field will modify the resonance frequency of a magnetic probe, giving rise to a change in its phase lag relative to the drive voltage frequency. If the magnetic moments of the probe and sample are favourably aligned to give an attractive interaction, the probe cantilever effectively becomes "softer", resulting in a decrease in its resonance frequency, and a reduction in the observed phase lag.

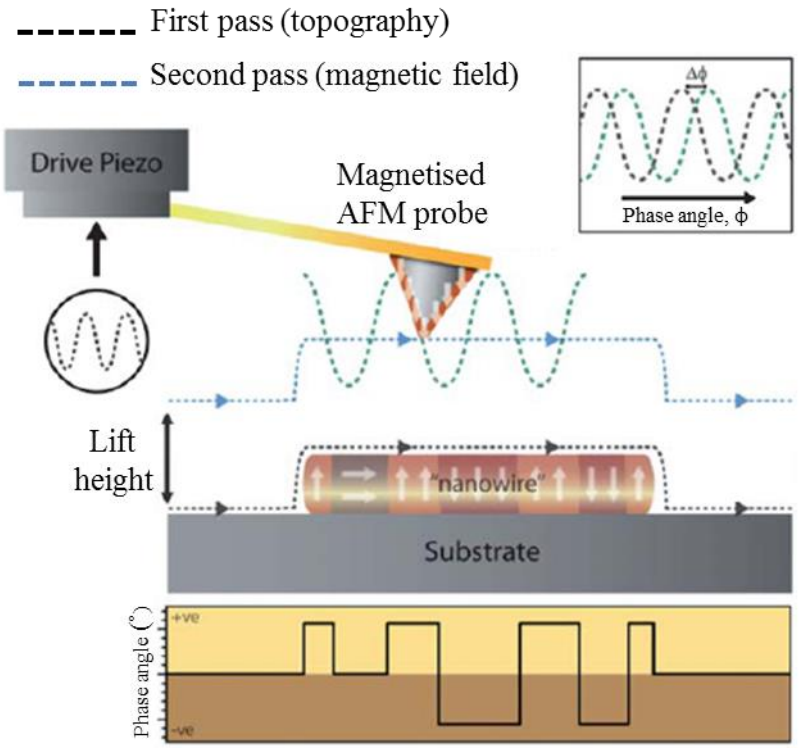

Figure 2-10: Schematic diagram representation outlining the principles of magnetic force microscopy. Magnetic interactions between the AFM probe and sample are monitored through recording changes in the phase lag of the probe relative to the drive voltage signal.

Conversely, repulsive magnetic interactions between the probe and sample cause the cantilever to effectively become “stiffer”, leading to an increase in its resonance frequency and the phase lag recorded. Hence, the contrast observed in the MFM phase images can be used to deduce the relative alignment of the magnetic domains within a sample, where attractive probe–sample magnetic interactions produce dark/negative contrast, and repulsive interactions produce bright/positive contrast.

In this work, both EFM and MFM data were acquired using a Dimension Nanoscope V system, equipped with a conductive/magnetic AFM probe (MESP model, metallic Co/Cr coated n-doped silicon cantilevers, f_0 = 60–100 kHz, spring constant = 1–5 Nm^{-1}, Veeco Instruments Inc., Metrology Group). For MFM measurements, the MESP probes were magnetised by placing them close to a permanent magnet for ~2 minutes immediately prior to data acquisition. An isolation table/acoustic enclosure was again used to reduce Vibrational noise (Veeco Inc. Metrology Group). Data acquisition was carried out using Nanoscope Version 7.00b19 software (Veeco Inc., Metrology Group). Measurements were conducted using a ‘‘two-pass’’ method, with lift heights typically in the range of 40–100 nm and 5–100 nm employed in EFM and MFM experiments, respectively. During EFM measurements, electric fields were generated using an independently controlled direct current (dc) bias applied to the sample, whilst the probe was grounded. A scan rate of 0.5 Hz was typically employed in both EFM and MFM experiments, with the amplitude setpoint and integral/proportional gains adjusted appropriately for optimum image quality.

3. Chapter 3: Preparation of magnetic and conductive magnetite nanowires by DNA-templating

3.1 Introduction

The natural form of iron geologically is an oxide with three types being dominant.[88] These are iron(II) oxide (FeO), wüstite, the mixed valence iron(II,III) oxide (Fe_3O_4) magnetite and an iron(III) oxide (Fe_2O_3).[88, 89] Wüstite, (FeO) contains only divalent iron. It is black in colour and has the sodium chloride (NaCl) structure.[88-90] It can be obtained as a fine black powder by thermal decomposition of iron(II) oxalate (FeC_2O_4), *in vacuo* but the product is unstable toward disproportionation into Fe and Fe_3O_4, therefore it must be cooled rapidly to obtain the metastable Fe(II) oxide phase. Wüstite can also be formed by heating Fe in a low partial pressure of oxygen.[89]

Magnetite, Fe_3O_4 is different from the other iron oxides in that it comprises mixed valence Fe(II) and Fe(III) ions.[88] Magnetite adopts an inverse spinel structure. The formula of this oxide is expressed as $Y[XY]O_4$ where, X refers to Fe(II), Y points to Fe(III) and brackets indicate octahedral sites.[88] In this structure, tetrahedral sites are occupied by half of the Fe(III), while other half of the Fe(III) ions and the Fe(II) ions are occupying octahedral sites.[88, 89] Fe_3O_4 is a black, ferrimagnetic material, naturally exists as the mineral magnetite or lodestone. It can be produced by partial oxidation of FeO or, by heating Fe_2O_3 at high temperature (> 1400 °C).[89] Moreover, magnetite can be obtained by precipitation from a mixture of Fe(II) and Fe(III) solution using alkaline systems.[88]

Fe_2O_3 exists in a variety of forms such as α-Fe_2O_3 (hematite), γ-Fe_2O_3 (maghemite), β-Fe_2O_3, and ε-Fe_2O_3. However, hematite and maghemite represent the most important forms of iron(III) oxide as the β-Fe_2O_3 and ε-Fe_2O_3 are rare.[88] The hematite phase is a red-brown solid or grey-black crystals [88, 90] and can be prepared in two steps.[89] The first is treatment of an aqueous solution of Fe(III) with alkali to produce the hydrated oxide (FeO(OH)). In the second step, the hydrated oxide is heated to 200 °C to give the red-brown α-Fe_2O_3. This phase of Fe(III) oxide has the corundum (α-Al_2O_3) structure with octahedral sited Fe(III) centres.[88-91]

Maghemite, γ-Fe_2O_3 also has a red-brown colour and structure similar to that of magnetite. It is ferromagnetic and has application in magnetic recording tapes.[88, 89]

This form of Fe_2O_3 can also be obtained by careful oxidation by heating Fe_3O_4 in air.[89]

Iron oxides have potential use in a broad variety of applications. These compounds are used as pigments in paints, coatings, rubber fillers, and ceramic glaze. Additionally, they are used as catalysts, materials for magnetic recording devices and gas sensors. The properties of a particular iron oxide material that make it suitable for use in such variety of applications depend on its particle size, shape, crystallinity and porosity.[92]

In recent years there has been an increasing interest in the use of magnetic nanostructures in a wide range of applications due to their important physical properties.[93, 94] Magnetite (Fe_3O_4) nanoparticles in particular have already been received much attention because of their size and low toxicity which make them attractive material for a variety of biomedical application such as, drug delivery and biosensor.[95-99] The production of iron oxide nanowires may offer similar potential for exploitation, and could even provide additional benefits in use over their nanoparticle counterparts, due to their unique combination of structural, magnetic and electronic properties.[100, 101] However, the organisation of nanoparticles into precise 1D form where it is possible to exploit these properties is a major challenge for nanofabrication.[102] Therefore, it is desirable to develop methods that induce such anisotropic growth. The templating strategy is one such method for the construction of well-defined forms and can produce low-dimension structures quickly and at low cost.[103, 104]

The biomolecular polymer DNA has become an attractive candidate for use as a template for assembling materials into organised 1D nanostructures because of its chemical and structural features, as out lined in chapter 1.[26, 42] Examples of the assembly of Fe_3O_4 upon DNA have previously been reported, though these involved the interaction of preformed nanoparticles with DNA stands.[86, 105] In one example, a solution of pre-formed Fe_3O_4 nanoparticles was mixed with DNA solution and incubated for 30 minutes at room temperature.[86] TappingMode AFM studies showed stretched DNA templates coated with magnetite nanoparticles, see figure 3.1a.[86]

In another example, two different methods were used to template DNA with pre-formed Fe_3O_4 nanoparticles. In the first, the templating is performed in solution similar to that described in first example.[86] AFM studies of material isolated from this

method showed a "network" structures, see figure 3.1b. The second method involved two-step templating in which DNA is first stretched on the surface, and then treated with an aqueous solution of magnetite nanoparticles. This two-step method produced 1-D wire-like structures of DNA/Fe_3O_4 with incomplete coverage of the template. These structures showed some uncoated regions as the DNA can be visualised (figure 3.1c).[105]

During the work for this thesis, the direct growth of magnetite on DNA was reported by Sarkar *et al*.,[95] using a co-precipitation method, similar to that adopted in the work presented here.[106] The resulting templated structures showed morphologies, appearing to consist of a series of coalesced nanoparticles encapsulating the DNA, see figure 3.1d. Interestingly, individual strands of DNA/Fe_3O_4 were not notably evident in the presented data.

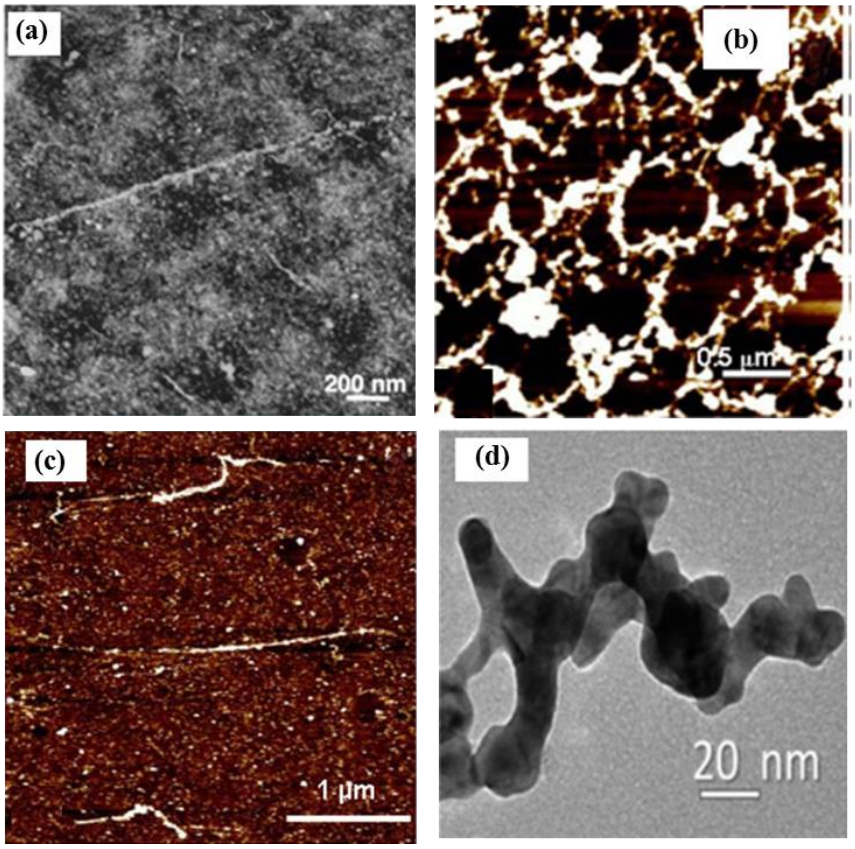

Figure 3-1: (a) AFM height image shows the Fe_3O_4 nanoparticles with single stranded DNA core, height scales is 8 nm.[86] (b) AFM image of DNA-templated Fe_3O_4 nanoparticles prepared in solution, height scale is 10 nm, and (c) AFM image shows DNA-templated Fe_3O_4 nanoparticles prepared by the two-step process, height scale is 15 nm.[105] (d) TEM micrograph of DNA-templated chain-like Fe_3O_4 nanoparticle.[95]

This chapter describes the formation and growth of Fe_3O_4 directly upon the DNA templates through co-precipitation of Fe^{2+} and Fe^{3+} in alkaline solution. The product material was then analysed using a combination of FTIR, XRD, XPS, and Raman spectroscopy, which together confirmed the iron oxide formed is present in Fe_3O_4 crystal phase. The structures produced were investigated by AFM and show regular morphologies in which the DNA templates are coated with a continuous coverage of metal oxide material. The uniformity of these coatings represents a notable improvement to that observed in previous examples of DNA/Fe_3O_4 structures.[86, 95, 105] The resulting DNA-templated Fe_3O_4 nanostructures were also characterised using scanning probe techniques (EFM and MFM), which confirmed the structures to be electrically conducting and to have room temperature magnetic properties.

3.1 Experimental section

3.1.1 Materials

Ferric chloride ($FeCl_3$, 97%), sodium hydroxide (NaOH, > 99%), calf thymus DNA (CT-DNA) (highly polymerized, 6 % sodium), herring testes DNA (HT-DNA) (type XIV, sodium salt) and chlorotrimethylsilane (Me_3SiCl) were purchased from Sigma-Aldrich Company Ltd. (Gillingham, Dorset, UK) and used as received. Lambda DNA (λ-DNA, Cat. no. N3011S) was purchased from New England Biolabs UK Ltd. (Hitchin, Hertfordshire, UK). Ferrous sulfate heptahydrate ($FeSO_4.7H_2O$, 99%) was purchased from BDH Chemicals Ltd. (Poole, dorset, UK).

Si<n-100> wafers (phosphorous doped, 525 ± 50 μm thickness, 1-10 Ω cm resistance, single side polished), were used as substrate supports for standard AFM imaging. Si<n-100> wafers with a thermally grown SiO_2 layer, 200 nm thick, on top (arsenic doped, 500 ± 25 μm, <0.005 Ω cm resistance, thermal oxide layer 200 nm ± 10 % thickness, double side polished) were used in scanned conductance microscopy and magnetic force microscopy experiments. All Si wafers were purchased from Compart Technology Ltd. (Peterborough, Cambridgeshire, UK).

NANOpure® deionized water (18 MΩ cm resistivity) was obtained from a NANOpure® DIamond™ Life Science ultrapure water system equipped with a DIamond™ RO Reverse Osmosis System (Barnstead International).

3.1.2 Cleaning, oxidation and modification of silicon substrates

Si<n-100> wafers (~1×1 cm^2) were treated in freshly prepared "piranha" solution (4:1 H_2SO_4/H_2O_2) for 45 minutes to both clean and chemically oxidize the substrate surface *(Caution! Piranha solution should be handled with extreme care; it is a strong oxidant and reacts violently with many organic materials. It also presents an explosion danger).* After this period of time, the wafers were rinsed with NANOpure® water, and dried in a gentle stream of N_2 before further drying in a clean oven for 5 – 10 minutes. Surface modification of the cleaned Si<n-100> wafers was performed through vapour deposition of a trimethylsilane (TMS) self-assembled monolayer (SAM): briefly, a specimen bottle containing 100 µL of chlorotrimethylsilane (Me_3SiCl) was placed in a larger specimen bottle. The Si<n-100> wafers was placed on the top of the inner specimen bottle (polished side facing up) and exposed to the Me_3SiCl vapour for 10 minutes at room temperature. Static contact angle measurements performed upon "piranha-cleaned" Si<n-100> wafers, following TMS-modification under the experimental parameters stated, give contact angle values of ~71°.[16]

For Si<n-100> wafers (~1x1 cm^2) with a 200 nm thick, thermally grown SiO_2 layer on top, the SiO_2 layer was first removed from one side of the wafer by applying a drop of HF solution (48% in H_2O, Sigma-Aldrich Company Ltd.) onto the wafer surface. The HF solution was left on the wafer until a change in the surface wetting was observed (hydrophilic to hydrophobic), indicated by a sudden "beading" of the HF solution. The HF solution was then removed and the wafer rinsed with copious amounts of NANOpure® water. Subsequent piranha treatment and TMS modification were carried out as previously described for the Si<n-100> wafers.

3.1.3 Preparation powder samples of DNA-templated Fe_3O_4 material for spectroscopic characterisation

In order to ensure the DNA/Fe_3O_4 product material could be produced in sufficient quantities which allowed for meaningful spectroscopic data to be acquired, "powder" samples were prepared as described herein. Synthesis of the Fe_3O_4 was carried out using a similar method as that described by Guo *et al.,* [107] but whilst in the presence of DNA in this instance. An aqueous solution containing $FeCl_3$ (7.5 mM) and $FeSO_4 \cdot 7H_2O$ (5 mM) was added to a solution of HT-DNA (1 mg mL^{-1}) in a ratio of 2:1 (v/v). Under continuous stirring, and at a maintained temperature of 30 °C, NaOH solution (75 mM)

was slowly added until the solution pH was ~11. Upon completion, a black precipitate of the DNA/Fe_3O_4 product material was observed in the reaction solution. Magnetic separation was used to isolate the product from the reaction solution, and was subsequently washed with NANOpure® water until the washings were ~pH7.

3.1.4 Fourier transform infra-red spectroscopy

FTIR spectroscopy of the DNA/Fe_3O_4 powder samples was carried out using a Varian 800 Scimitar series spectrometer (Varian Inc.) fitted with an ATR attachment. Spectra were recorded over the 500–4000 cm^{-1} range, with 128 scans and at 4 cm^{-1} resolution.
In order to compare the DNA/Fe_3O_4 material to unmodified DNA, FTIR spectra of samples of "bare" DNA (i.e. prior to any templating) were also acquired. Samples were prepared by depositing 80 µL of a CT-DNA solution (1 mg mL^{-1}) upon a piranha-cleaned Si<n-100> wafer, and allowing to dry at room temperature. Spectra were acquired using a Bio-Rad Excalibur FTS-40 spectrometer (Varian Inc., Palo Alto, CA, USA), equipped with a liquid nitrogen cooled deuterated triglycine sulphate detector, and recorded over the 500–4000 cm^{-1} range, with 128 scans, and at 4 cm^{-1} resolution.

3.1.5 Powder X-ray diffraction

Samples of DNA/Fe_3O_4 material were prepared for powder X-ray diffraction (XRD) analysis in the same manner as described above, section 3.2.3. A PAN-alytical X'Pert Pro diffractometer equipped with a Cu $K\alpha_1$ radiation source (λ = 1.540 Å) was used for powder XRD data collection.

3.1.6 X-ray photoelectron spectroscopy

X-ray photoelectron spectroscopy (XPS) was carried out upon samples of DNA/Fe_3O_4 material prepared in the same manner as described for the previous spectroscopic studies (section 3.2.3). The sample material was deposited from solution onto a piranha-cleaned Si<n-100> wafer and allowed to dry at room temperature. XPS was performed using a Kratos Axis Ultra 165 (Kratos Analytical Ltd., Manchester, UK), equipped with an Al Kα X-ray source (1486.6 eV), and using a take-off angle of 90°. Samples were mounted on copper sample stubs with carbon tape. To compensate for surface charging, a charge neutraliser gun was used. All binding energies were referenced to the

hydrocarbon C1s core level at 285.0 eV. Kratos Vision software (Kratos Analytical Ltd.) was used for data acquisition.

3.1.7 Raman spectroscopy

Raman spectroscopy was carried out upon samples of DNA/Fe_3O_4 material prepared in the same manner as described for all other spectroscopic experiments (section 3.2.3). The sample material was deposited from solution onto a glass coverslip, and allowed to dry at room temperature.

Raman spectroscopy was also carried out upon samples of DNA/Fe_3O_4 material prepared for use in SPM characterisation. In this case, samples were prepared by depositing approximately 60 μL of DNA/Fe_3O_4 solution (prepared as described in section 3.2.8) upon a glass coverslip, and allowed to dray at room temperature.
Raman spectra were acquired using a CRM200 confocal Raman microscope (Witec GmBH, Ulm, Germany) equipped with a cooled CCD detector, an Ar+ laser (λ = 488 nm) as the excitation light source, and a Raman edge filter to remove elastically scattered light.

3.1.8 Preparation and alignment of λ-DNA-templated Fe_3O_4 nanowires for scanning probe microscopy (AFM, EFM and MFM) studies

The preparation of DNA/Fe_3O_4 samples for scanning probe microscopy (SPM) studies was carried out using a modified version of the previous method used for producing ‘‘powder’’ samples (section 3.2.3). These adjustments were introduced due to the benefits they provided in improving the structural quality of the DNA/Fe_3O_4 nanostructures produced. Initial AFM studies of DNA/Fe_3O_4 nanostructures isolated from the powder samples (prepared as described in section 3.2.3) revealed that the Fe_3O_4 coatings around the DNA were of high surface roughness due to excessive, uncontrolled Fe_3O_4 formation, see section 3.3.5. Improved control over the growth of the Fe_3O_4 upon the DNA was offered through further regulation of the NaOH treatment stage of the preparation (i.e. using a precisely defined quantity of NaOH solution), yielding smoother Fe_3O_4 coatings.

Based upon these findings, preparation of the DNA/Fe_3O_4 nanowire structures for SPM characterisation was carried out as follows: A 12 μL stock solution of λ-DNA (500 mg

mL^{-1}, 10 mM tris–HCl, pH8, 1 mM EDTA) was diluted down to a concentration of 300 mg mL^{-1} using NANOpure® water. 5 µL of the diluted λ-DNA solution was mixed with 10 µL of an aqueous solution of $FeCl_3$ (2.25 mM) and $FeSO_4.7H_2O$ (1.5 mM), and incubated for 20 minutes at room temperature. 5 µL of NaOH solution (1.32 mM) was then added, and the reaction solution incubated for a further 1 hour at room temperature. Raman spectroscopy carried out upon sample material prepared in this manner confirmed the successful formation of Fe_3O_4, see section 3.3.4. The resulting DNA-templated Fe_3O_4 structures formed in the reaction solution were aligned upon TMS-modified Si<n-100> and Si<n-100>/200 nm SiO_2 wafers as follows: 5 mL of the DNA/Fe_3O_4 solution was applied to a TMS-modified wafer whilst spun at 125 rpm. The wafer was then spun for a further 2 minutes at 250 rpm before the residual DNA/Fe_3O_4 solution was withdrawn from the surface by micropipette. The wafer was left to dry at room temperature for 20 minutes before analysis using scanning probe microscopy techniques.

3.2 Results and Discussion

The formation of magnetite (Fe_3O_4) nanowires is based upon the growth of Fe_3O_4 at duplex DNA strands (figure 3.2). This method involves initial mixing of DNA with a solution containing Fe^{3+}/Fe^{2+} cations in order to allow the cations to associate with the duplex DNA through DNA/metal ion complex formation. In the second step, the formation of Fe_3O_4 was initiated via chemical co-precipitation of the Fe^{3+}/Fe^{2+} through addition of NaOH. In this preparation method, it is suggested that the formation of DNA/metal ion complexes plays an important role in the control of the Fe_3O_4 formation, confining its growth in two dimensions to produce structurally well-defined, high aspect ratio Fe_3O_4 nanowires.

It should be noted that, for chemical characterisations, powder samples were prepared as described in section (3.2.3). In this case, HT-DNA was used and the product isolated from the reaction solution by magnetic separation. Due to the possibility for iron oxide to be formed in several phases, such as hematite (α-Fe_2O_3), maghemite (γ- Fe_2O_3), and magnetite (Fe_3O_4) amongst others [88], the product material was characterised using a combination of FTIR, XRD, XPS, and Raman spectroscopy in an effort to distinguish the product.

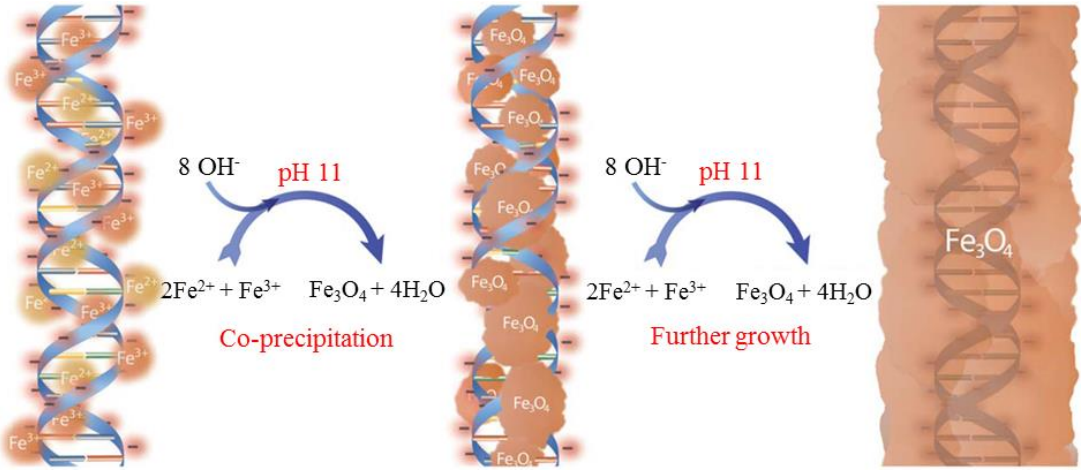

Figure 3-2: Representation of the preparation of DNA-templated Fe_3O_4 nanowires, involving initial association of Fe^{2+} and Fe^{3+} cations to the DNA template molecules, followed by subsequent co-precipitation of the Fe_3O_4 material upon increasing the reaction solution pH.

Samples for SPM studies were prepared using a modified version of the method used for producing powder samples. For this, further regulation of the NaOH treatment stage was used to yield smoother Fe_3O_4 coatings. Additionally, λ-DNA with suitable length (~ 16 μm) was used in order to facilitate individual nanowires measurements.

3.2.1 Fourier transform infra-red (FTIR) spectroscopy studies

FTIR spectroscopy was applied in order to confirm the formation of iron oxide upon the DNA 'template' molecules. For purpose of comparison FTIR spectroscopy was carried out upon films of both DNA and powder samples of the final DNA/iron oxide material. The FTIR spectrum of the DNA/iron oxide shown in (figure 3.3) shows the successful formation of iron oxide, as evident from the intense broad band located at 562 cm^{-1}, arising from the Fe-O bond vibration of iron oxide material.[95, 107, 108]

The characteristic bands from the DNA structure are still apparent in the spectrum after sequential treatments with Fe^{3+}/Fe^{2+} ions and NaOH, though several notable shifts in their peak positions and intensities are observed as a consequence of the interactions between the DNA and iron oxide material which take place, see Table 3.1. All the DNA vibration bands were assigned according to literature.[109-111] For example, the symmetric PO_2^- vibration at 1097 cm^{-1}, the P-O or C-O stretches of the phosphate backbone at 1071 cm^{-1} and the asymmetric PO_2^- vibration at 1246 cm^{-1} are all shown to be reduced in the intensity and shifted by 16, 6 and 34 cm^{-1} to lower frequency, respectively.

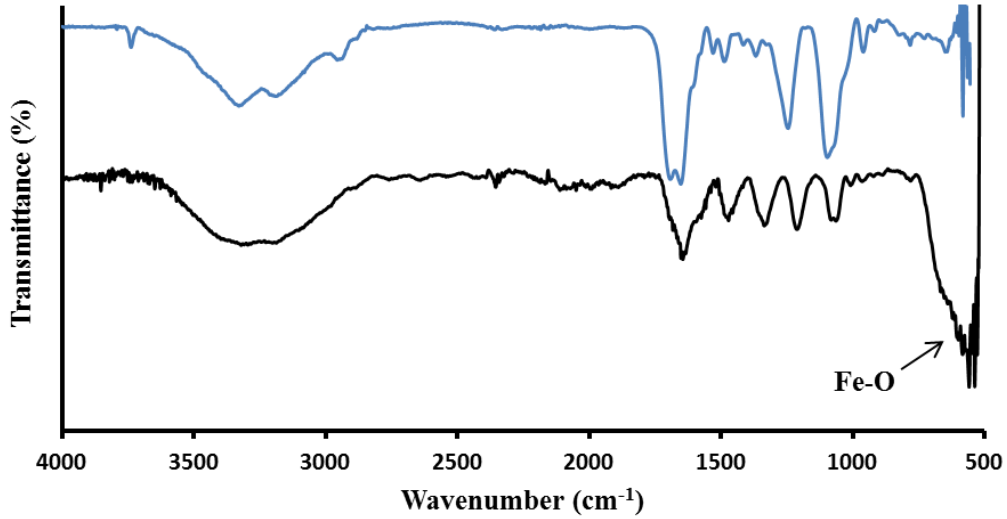

Figure 3-3: FTIR spectra of DNA-templated Fe_3O_4 material (black spectrum), along with bare CT-DNA (blue spectrum). The DNA/Fe_3O_4 material was prepared as a powder, whilst the bare DNA was deposited as a film from solution on a silicon substrate.

These spectral changes of the DNA backbone-related bands (900-1300 cm^{-1}) in the spectrum of DNA/iron oxide material indicate interactions between the iron oxide material and deoxyribophosphodiester backbone. [109-111]

There are also several visible changes in the DNA nucleobase region (1300-1800 cm^{-1}) of the spectra: a guanine ring vibration at 1488 cm^{-1} and C-N stretch of guanine and cytosine at 1368 cm^{-1} are shifted to 1472 and 1336 cm^{-1} respectively. An in-plane vibration of adenine, thymine and guanine bases at 1653 is shifted 10 cm^{-1} to lower frequency. In addition, the in-plane cytosine/guanine vibration at 1529 cm^{-1} is no longer observed following Fe_3O_4 templating. Additionally, the carbonyl stretch at 1653 and 1692 cm^{-1} is replaced by one band at 1643 cm^{-1} upon DNA/iron oxide formation. These changes in the peak position and intensity in the 1300-1800 cm^{-1} region of spectrum provide evidence for the interaction of iron oxide material with DNA nucleobases.[109-111]

Wavenumber (cm^{-1})		**Assignment**
CT-DNA	**CT-DNA/Fe_3O_4**	
960	964	C-C deoxyribose stretch
1033[a]	1006[a]	C-O deoxyribose stretch
1071	1065	P-O/C-O deoxyribose stretch

1097	1081	PO_2^- symmetric stretch
1246	1212	PO_2^- asymmetric stretch
1368	1336	C-N stretch of cytosine/guanine
1416	-	C-H /N-H deformation; C-N stretch
1488	1472	Ring vibration of cytosine/guanine
1529	-	In-plane vibration of uanine/cytosine
1603[a]	1581[a]	In-plane vibration of adenine
1653	1643	C=O stretch of cytosine/thymine; In-plane vibration of thymine
1692	-	C=O stretch of guanine/thymine; N-H thymine
2850–3750	2850–3500	C-H/N-H /O-H stretches

Table 3-1: Assignment and comparison in FTIR spectra (500–4000 cm^{-1}) of calf thymus DNA, and calf thymus DNA-templated iron oxide material. [a] Peak appeared as a shoulder.

3.2.2 X-ray diffraction studies

X-ray diffraction (XRD) studies were carried out upon powder samples of the DNA/iron oxide material in order to confirm the formation of iron oxide as well as to estimate its crystallite size. These studies provide evidence of the formation of iron oxide under the reaction conditions employed. Figure 3.4 presents the powder XRD pattern obtained from the DNA/iron oxide material. The product material displays five main peaks at 2θ = 30.1º, 35.5º, 43.4º, 57.3º and 62.9º, respectively, which can be indexed to the (220), (311), (400), (511) and (440) reflections of the magnetite (Fe_3O_4) phase of iron oxide.[95, 96, 112-114] However, this pattern is also consistent with a cubic, inverse spinel crystal structure of the maghemite (γ-Fe_2O_3) phase which shows similar XRD patterns to that of the Fe_3O_4 phase.[93, 115-117] The γ-Fe_2O_3 phase has few low-intensity diffractions [117], as well as marginally smaller lattice spacing (lattice parameter a: γ-Fe_2O_3 = 8.351 Å, Fe_3O_4 = 8.396 Å), which leads to a slight difference in the scattering angles.[115] However, the broadening of the diffraction

peaks that is seen here as a result of the small crystallite size of the product material, makes it difficult to distinguish in this instant between the two phases from the diffraction pattern alone. It should be noted however, that the product material was produced as a black powder, characteristic of the appearance of Fe_3O_4. In contrast, γ-Fe_2O_3 is well-known to exist as a reddish-brown substance.

The line broadening of the diffraction peaks was used to calculate the average crystallite size of the metal oxide material through applying the Scherrer equation ($D = k \cdot \lambda / [\beta \cdot \cos\theta]$). Using a line broadening parameter (β) of 0.365°, determined from the full-width-at-half-maximum of the (311) reflection, and a Scherrer constant (k) value of 0.89, a mean crystallite size of 23 nm was determined.

However, although the XRD data did confirm the formation of iron oxide under the synthetic method used, this technique cannot distinguish between Fe_3O_4 and γ-Fe_2O_3 phases because of their similar XRD pattern. Therefore, further characterisations were carried out upon the product material using both X-ray photoelectron and Raman spectroscopies in order to establish the phase crystal of the produced iron oxide nanostructures with more certainty.

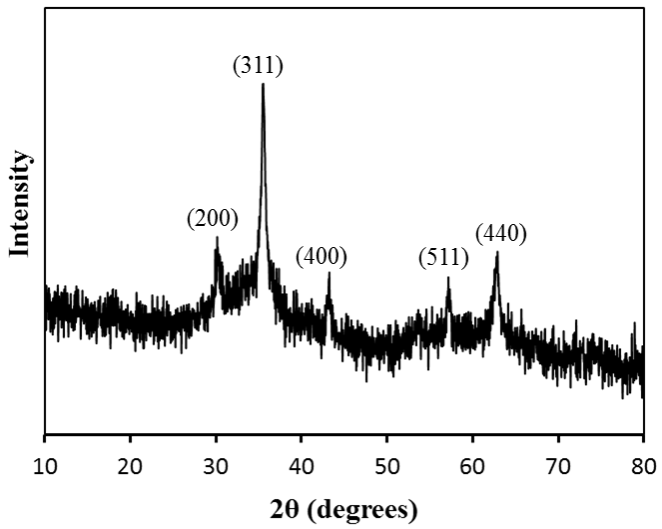

Figure 3-4: XRD pattern obtained from a powder sample of DNA-templated Fe_3O_4 material.

3.2.3 X-ray photoelectron spectroscopy

X-ray photoelectron spectroscopy (XPS) is one of the most powerful techniques for studying the electronic structure of solids.[118] Therefore, XPS was used here in an effort to distinguish between iron oxides in the γ-Fe_2O_3 and Fe_3O_4 phases because of its

sensitivity to the iron valence state.[93] Furthermore, the chemical composition of the product material can be examined using this surface analysis technique. The XPS survey spectrum of the DNA/iron oxide material (figure 3.5), displays signals arising from both DNA such as P2p and N1s, and iron oxide material e.g. Fe2p. The remaining elements appeared in XPS survey spectrum, such as O, S, and Si originated from adsorbed oxygen from air and/or DNA, the $FeSO_4.7H_2O$ starting material and silicon wafer used as a substrate.

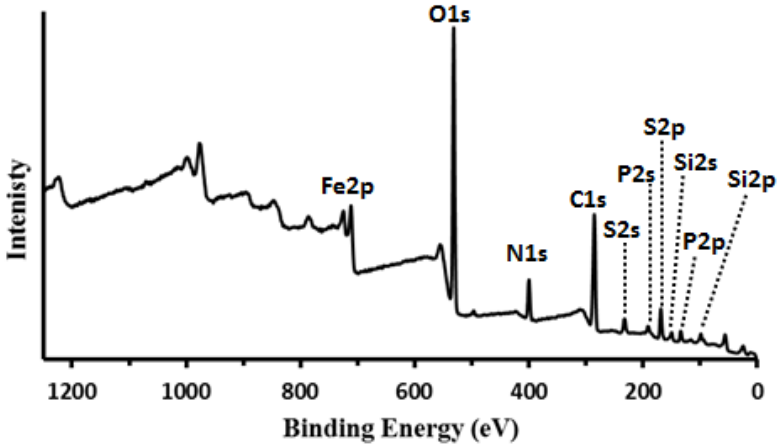

Figure 3-5: XPS survey spectrum of a film sample of calf thymus DNA-templated Fe_3O_4 material immobilised upon a Si/native SiO_2 substrate.

Initial confirmation of the presence of DNA in sample material is obtained from the observation of N1s signal. Two peaks centred at binding energies of 399.1 and 400.4 eV are revealed upon curve fitting of N1s spectrum of the DNA/iron oxide material (figure 3.6). The former emission at 399.1 eV with lower intensity can be ascribed to sp^2-bonded N atoms in the DNA aromatic rings, while the more intense peak at 400.4 eV is consistent with sp^3-bonded N atoms present in exocyclic amino group ($-NH_2$).[119-122]

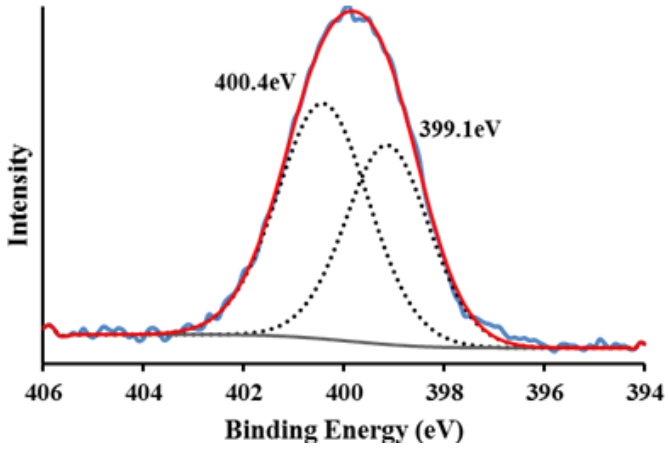

Figure 3-6: High resolution XPS spectrum of N1s region of calf thymus DNA-templated Fe_3O_4 material immobilised upon a Si/native SiO_2 substrate. Blue solid line, represents raw data, total fits is indicated by red line and black dashed lines are for component peaks.

Moreover, curve fitting of the P2p signal provides further evidence for the presence of the DNA in the product. XPS spectrum of P2p region (figure 3.7) reveals P2p doublets at binding energies of 133.6 and 134.4 eV for $P2p_{3/2}$ and $P2p_{1/2}$, respectively, arising from the phosphorus atoms in the DNA backbone.[119, 121, 123, 124]

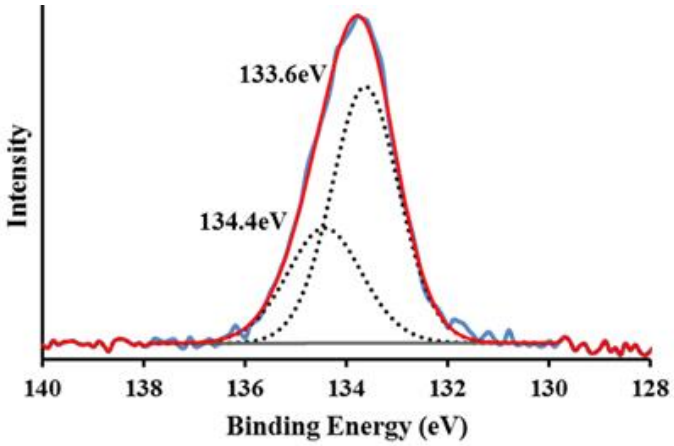

Figure 3-7: High resolution XPS spectrum of P2p region of calf thymus DNA-templated Fe_3O_4 material immobilised upon a Si/native SiO_2 substrate. Blue solid line represents raw data, total fits is indicated by red line and black dashed lines are for component peaks.

As mentioned earlier, XPS can readily distinguish between iron oxides in the γ-Fe_2O_3 and Fe_3O_4 phases due to the techniques sensitivity to the iron valence state.[93] The satellite structures associated with XPS spectra of iron oxides, can be used to identify the iron oxide phases as they are very sensitive to the electronic structure of the compounds.[118] The Fe2p signal from γ-Fe_2O_3 is known to show the main Fe2p doublet at binding energies of ~711 eV ($2p_{3/2}$) and ~724 eV ($2p_{1/2}$). This is also accompanied by a shake-up satellite peak at ~719 eV, arising from the Fe^{3+} species.[116, 125] In comparison, the Fe2p doublet in Fe_3O_4 tends to give a broader structure due to the coexistence of Fe^{2+} and Fe^{3+} species within the crystal structure, whilst the satellite peak around 719 eV becomes less resolved due to the increasing intensity of another satellite at ~716 eV, resulting from the presence of the Fe^{2+} species.[114, 118, 126, 127]

High resolution XPS spectra of the Fe2p core level from the DNA/iron oxide material show the Fe2p band to be relatively broad, whilst there is no evidence of the presence of the Fe^{3+} shake-up satellite at 719 eV, see figure 3.8. These findings indicate that the iron oxide material is present in Fe_3O_4 phase rather than γ-Fe_2O_3.

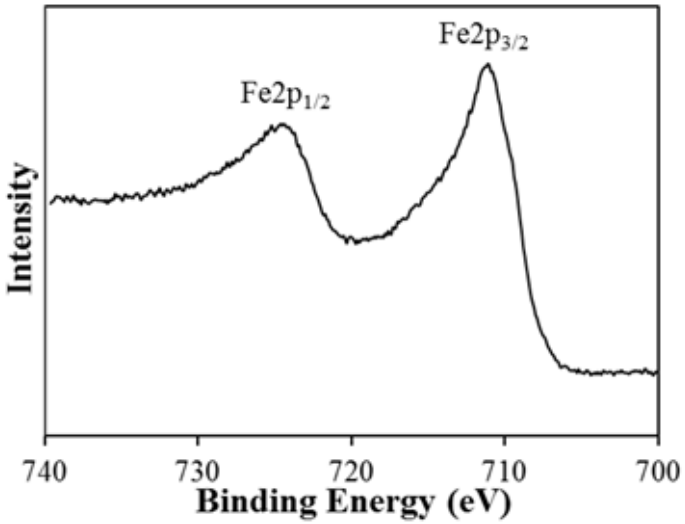

Figure 3-8: High resolution XPS spectrum of the Fe2p region of calf thymus DNA-templated Fe_3O_4 material immobilised upon a Si/native SiO_2 substrate.

Inspection of the O1s spectra (Figure 3.9) reveals that at least two distinct peaks can be identified in the O1s envelope, centred at 529.6 and 531.8 eV, respectively. The peak at higher binding energy can be assigned to the SiO_2 of the substrate support.[128, 129] This peak is the dominant feature in the spectrum due to the large amount of native SiO_2 at the substrate surface. On the other hand, a smaller, less intense peak appeared at 529.6 eV, assigned to oxygen present in the Fe_3O_4 is in good agreement with previously reported values for this material.[114, 118] The latter is providing further evidence for the iron oxide to be present in the magnetite crystal phase.

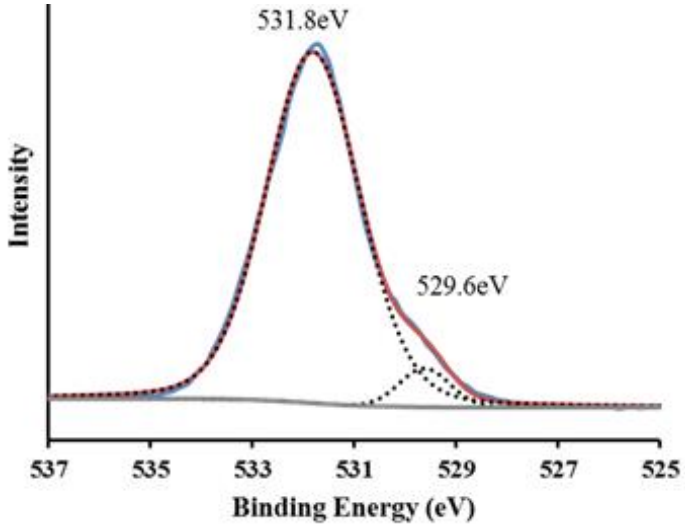

Figure 3-9: High resolution XPS spectrum of the O1s region of calf thymus DNA-templated Fe_3O_4 material immobilised upon a Si/native SiO_2 substrate. Blue solid line represents raw data, total fits is indicated by red line and black dashed lines are related to component peaks.

3.2.4 Raman spectroscopy studies

Raman spectroscopy studies were carried out upon samples of the produced DNA/Fe_3O_4 material, in order to provide further confirmation of the Fe_3O_4 crystal phase of the iron oxide material. This technique can readily differentiate Fe_3O_4 and γ-Fe_2O_3 phases of iron oxide material.[115, 117] As previous Raman spectroscopy studies of both magnetite and maghemite have reported that the former phase of iron oxide has a main band (A_{1g} mode) at 668 cm^{-1} [115, 117, 130-132], while the maghemite phase reveals broad bands at 700, 500 and 350 cm^{-1}.[115, 117] A representative Raman spectrum of the produced DNA/Fe_3O_4 material prepared for use in spectroscopic characterisation (as described in section 3.2.3) is predicted in figure 3.10. This spectrum shows a band at 665 cm^{-1}, characteristic of the A_{1g} transition of Fe_3O_4, and no bands related to γ-Fe_2O_3 was observed, indicating that there was no γ-Fe_2O_3 impurities present in the product material.

Therefore, from the XPS and Raman spectroscopy data, it can be concluded that the iron oxide produced in presence of DNA is in the Fe_3O_4 phase with little or no evidence for the presence of any maghemite impurities. Moreover, there is an indication that the product material has nanoscale structure as evident from the broadening of the XRD diffraction peaks.

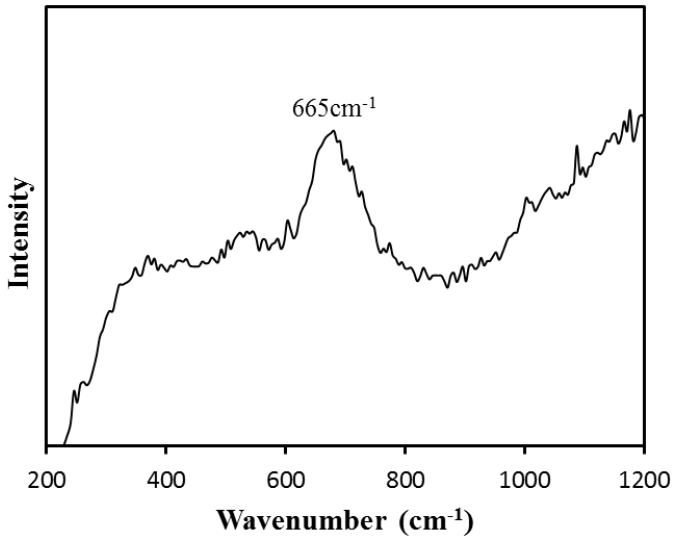

Figure 3-10: Raman spectrum of a sample of DNA-templated Fe_3O_4 nanowires. The peak at 665cm^{-1} confirms the Fe_3O_4 phase of iron oxide material.

Raman spectroscopy studies were also carried out upon sample material prepared for use in SPM studies (as described in section 3.2.8). The sample material was prepared by

depositing approximately 60 µL of NA/Fe_3O_4 solution upon a glass coverslip, and allowed to dray at room temperature. Raman spectra of samples prepared for use in spectroscopic analysis and SPM measurements are depicted in figure 3.11. Both samples show a band in the 665-680 cm^{-1}, characteristic of the A_{1g} transition of iron oxide in the Fe_3O_4 phase.[115, 131, 132] The broad nature of this band in both spectra is due to the small particle sizes of the Fe_3O_4 material produced.

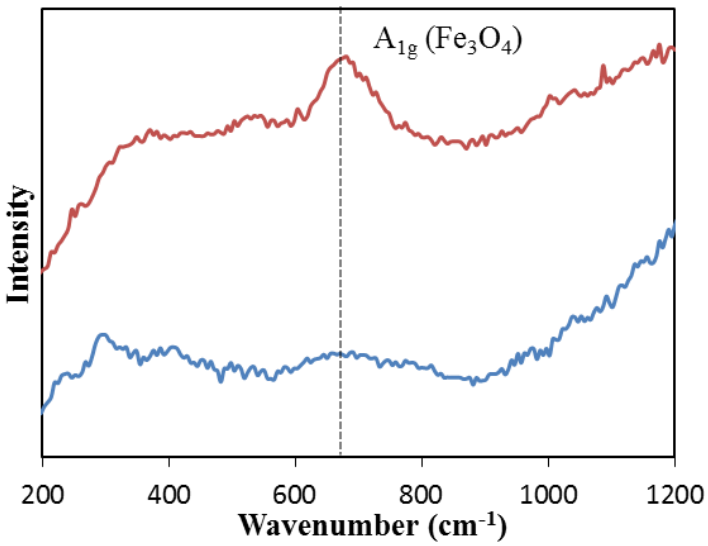

Figure 3-11: Comparison of Raman spectra of samples of DNA/Fe_3O_4 material prepared for use in spectroscopic analysis (red spectrum) and in scanning probe microscopy studies (blue spectrum). The spectra have been normalised and offset for clarity.

3.2.5 Atomic force microscopy (AFM) studies of the DNA/Fe_3O_4 nanostructures

AFM measurements were carried out upon samples of the DNA/Fe_3O_4 material in order to elucidate information regarding their size and structural character. Samples for AFM measurements were prepared using λ-DNA which has a well-defined length of ~16.2 µm.[16] In AFM studies it was important to be able to isolate and probe individual structures in order to evaluate their structural morphologies. To address this need, molecular combing methods [133, 134] were employed as a means of aligning the DNA-templated Fe_3O_4 structures directly from the reaction solution onto a substrate support. The combing process was carried out upon Si/SiO_2 substrates which had been modified with a trimethylsilane (TMS) self-assembled monolayer (SAM). This increases the surface hydrophobic character of the substrate, giving typical static contact angle values in the region of ~71˚.[16] Tailoring the substrate surface properties in this fashion has a significant impact upon the densities of DNA-based materials subsequently deposited. The experimental parameters used to achieve the TMS-

modifications here, were established to provide surfaces which demonstrate the desired balance of hydrophilic/hydrophobic character in order to facilitate alignment of the DNA-templated Fe_3O_4 structures in sufficient densities that they could be readily located by AFM, but whilst also allowing them to be individually addressed.

Initial AFM studies were carried out upon samples of DNA/Fe_3O_4 nanostructures isolated from the powder samples (prepared as described in section 3.2.3). These studies revealed that the Fe_3O_4 coatings around the DNA were of high surface roughness due to excessive, uncontrolled Fe_3O_4 formation. For AFM measurements, the DNA/Fe_3O_4 nanostructures were immobilized upon TMS-modified Si/SiO_2 substrates. Figure 3.12 shows AFM height images of some examples of structures isolated from the powder samples.

These images display parallel chains of DNA/Fe_3O_4 structures with a great variation in the structure height along their length, where metal oxide deposition has taken place to varying extent upon the DNA template. Moreover, the nanoscale coverage of Fe_3O_4 material around DNA strands is found to show high surface roughness likely because excessive, uncontrolled metal oxide formation.

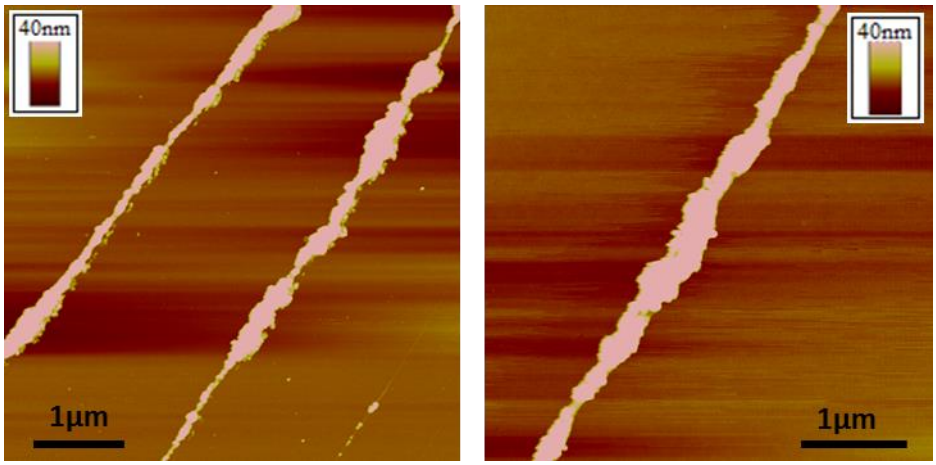

Figure 3-12: TappingMode™ AFM height images showing DNA-templated Fe_3O_4 structures isolated from a DNA/Fe_3O_4 powder sample initially prepared for use in spectroscopic studies.

AFM studies were also carried out upon samples of DNA/Fe_3O_4 nanostructures prepared as described in section 3.2.8, for use in SPM studies and where the synthesis was optimised to produce smooth, regular nanowires. In this instance, AFM images show a range of structures with different sizes (diameters range from 2 – 32 nm), where metal oxide deposition has taken place to varying extents upon the DNA templates

(figure 3.13a-d). The deposition of Fe_3O_4 material upon DNA is evident by comparing the theoretical diameter of an individual DNA molecule (≤ 2 nm) measured by AFM [135], and the diameters of the isolated DNA/Fe_3O_4 "nanowires" which show thicker (> 2 nm) structures.

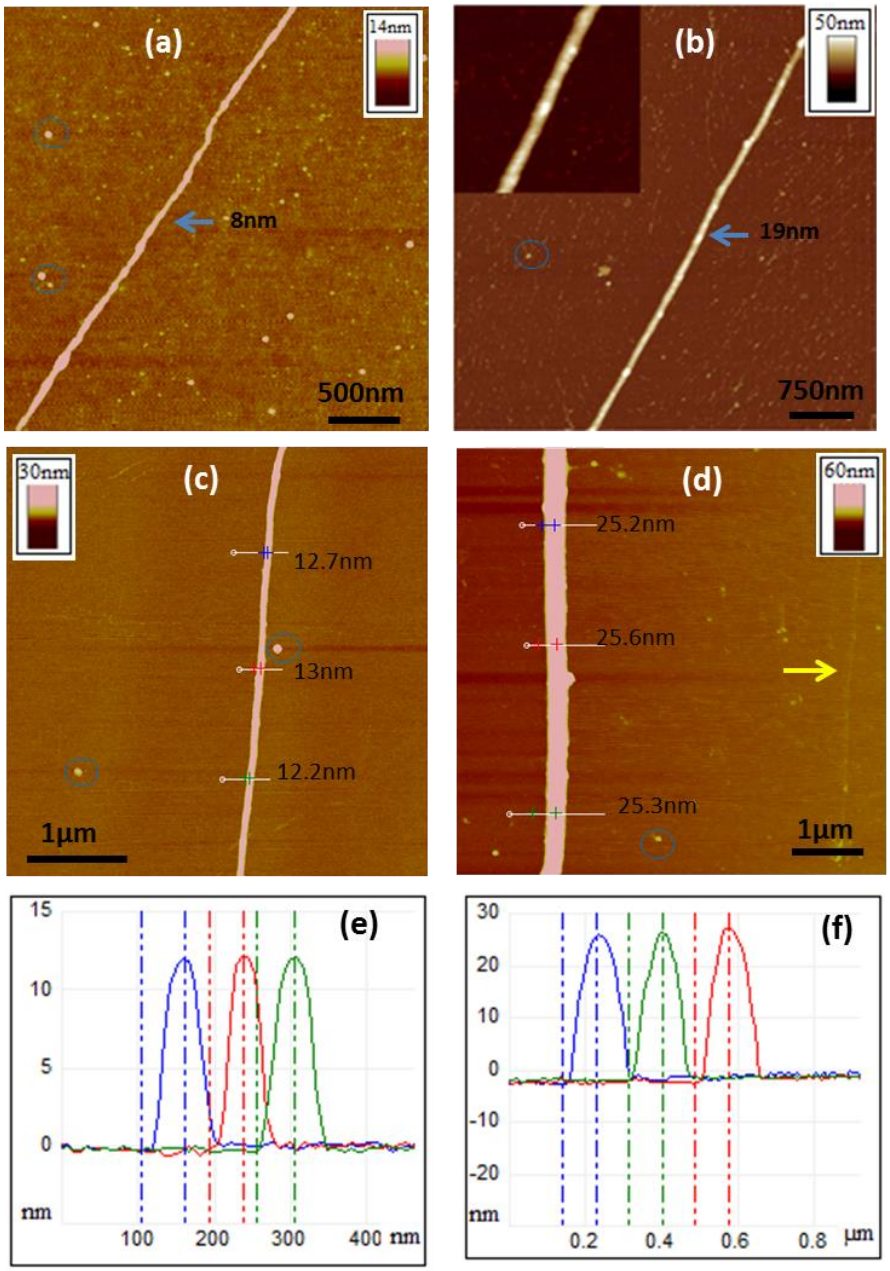

Figure 3-13: Selected TappingMode AFM images of the DNA-templated Fe_3O_4 "nanowires" aligned upon a TMS-modified Si/native SiO_2 substrate. (a) AFM image shows a nanostructure with average diameter of 8 nm and relatively granular character of the metal oxide coverage. (b) This image represents also a "nanowires" with structure height of 19 nm, and a zoomed-in region of the nanowire is also shown (inset), with the image contrast adjusted to highlight the granular character associated with the morphology of the Fe_3O_4 coating. (c) and (d) AFM images reveal two parallel "nanowires" represent regular structure with little variation in the diameter size along their length. (e) and (f) are cross sections of (c) and (d), respectively.

Figure 3.13a shows a nanostructure with average diameter of 8 nm and relatively granular character of the metal oxide coverage. This image displays also some of metal oxide nanoparticles deposited on the substrate surface (circled areas). Figure 3.13b shows nanostructure with structure height of 19 nm, and a zoomed-in region of the nanowire is also shown (inset), with the image contrast adjusted to highlight the granular character associated with the morphology of the Fe_3O_4 coating. Figure 3.13c and d reveal two parallel nanostructures with regular structure and little variation in the diameter size along their length as shown in figure 3.13e and f, which are cross sections of (c) and (d), respectively. It is clear form figure 3.13 that the Fe_3O_4 nanoparticles are templated effectively the DNA as little bare DNA strands (yellow arrows in figure 3.13d), and a low frequency of nonspecific deposition of Fe_3O_4 nanoparticles (circled areas in figure 3.13) are observed on the substrate surfaces.

The DNA/Fe_3O_4 nanostructures typically consist of good uniform morphologies, with a continuous coverage of the DNA templates by the metal oxide material. The uniformity of metal oxide coatings represents a notable improvement to that observed in previous example of DNA/Fe_3O_4 structures reported by Sarkar [95], using a similar co-precipitation strategy. In that work, the produced DNA/Fe_3O_4 material was found to show structures which displayed a more distinctive, granular appearance (figure 3.14a). This was suggested to be a consequence of the growth mechanism behind the Fe_3O_4 formation, which was proposed to take place via the gradual, step-wise growth of a series of discrete Fe_3O_4 particles along the DNA.

Upon closer inspection of the structures produced in the studies described here, a small degree of granular character associated with the Fe_3O_4 coatings can also be identified, see Fig. 3.13a and b (inset), indicating that a similar “nucleation and growth” mechanism may also be involved in their formation. Further supporting evidence for this growth mechanism was also provided by a small number of DNA/Fe_3O_4 structures which showed irregular and incomplete coverage of the DNA template by the Fe_3O_4 material (figure 3.14c and d). These structures with a series of distinct nanoparticles bound along individual DNA strands can be regarded as examples where the Fe_3O_4 growth upon the template has not gone to completion. These help provide some insight into the growth mechanism by which the DNA/Fe_3O_4 structures was formed.

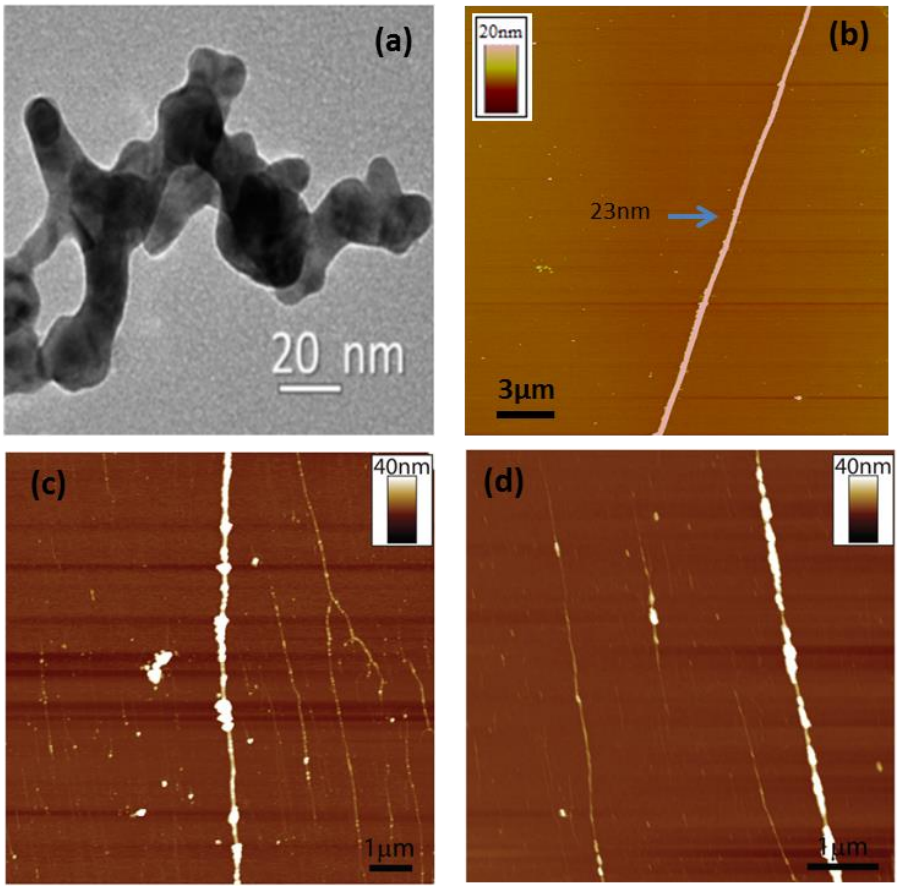

Figure 3-14: (a) TEM micrograph of DNA-templated chain-like Fe_3O_4 nanoparticle (reprinted from reference [95]). (b) AFM height image of DNA-templated Fe_3O_4 "nanowire" produced in the studies described here, showing smooth and regular structure with 23nm height and > 25µm in length. (c) and (d) AFM height images showing examples of partially formed λ-DNA-templated Fe_3O_4 "nanowires", where the metal oxide growth has not reach maturity during the reaction period.

Formation of the Fe_3O_4 on the DNA is proposed to take place through the DNA initially being 'seeded' with Fe^{2+}/Fe^{3+} ions upon exposure to the $FeCl_3/FeSO_4$ solution. The Fe^{2+}/Fe^{3+} can readily bind to the DNA through the formation of electrostatic interactions with the DNA's polyanionic phosphate backbone as well as through coordination the DNA nucleobases. The Fe cations are rapidly converted to nanoparticlate Fe_3O_4 upon exposure of the seeded DNA to a basic solution [107], which can then act as sites for further growth to take place. As a consequence of this process, the early stages of DNA-templated Fe_3O_4 formation is expected to yield a series of discrete nanoparticles of Fe_3O_4 along the DNA templates, as is observed in Figure 3.14c and d. Over time, further growth of the Fe_3O_4 particles leads to them coalescing, and the structure 'ripening' into a continuous coating encapsulating the whole DNA molecule (figure 3.13). Growth of the Fe_3O_4 upon the DNA in this manner is perhaps not surprising, with several previous examples of metallised DNA structures having been reported to exhibit

similar granular morphologies, resulting from metal deposition taking place via a series of nucleation and growth steps.[18, 66]

However, whilst the DNA/Fe_3O_4 "nanowires" have showed constant heights along the whole length of any individual "nanowires" (figure 3.13 c and d), AFM analysis revealed also a great variation in the mean diameters (1-30 nm) of the isolated DNA/Fe_3O_4 "nanowires". Due to the wide range of DNA/Fe_3O_4 structure sizes observed, a statistical treatment of the structures was carried out. For this, the average heights of > 100 DNA/Fe_3O_4 structures were measured using AFM line profiles, and the frequency plotted as a function of diameter, see Figure 3.15. A quite broad size distribution with structures up to 30 nm in diameter was observed. The data appears also to show a distinctive trimodal distribution with modal values of 5.0 – 6.0 nm, 15.0 – 16.0 nm, and 24.0 – 25.0 nm, respectively.

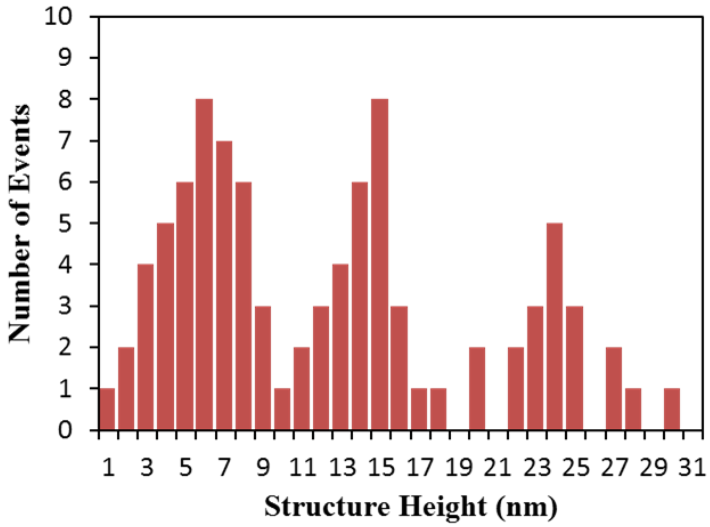

Figure 3-15: Histogram of the size (diameter) distribution of the of the DNA-templated Fe_3O_4 "nanowires".

It is also found that the largest of these DNA/Fe_3O_4 nanostructures as measured by AFM, are reasonably consistent with the estimated Fe_3O_4 crystallite size that was determined from the powder XRD data (23 nm). This suggests that the Fe_3O_4 crystalline grains assemble themselves in linear "beads-on-a-string" type arrangement along the DNA stands, resulting in the 1D appearance of the isolated DNA/Fe_3O_4 structures. However, AFM data cannot be used to investigate whether the magnetite nanoparticles are merged to produce a single, continuous coverage around the DNA, or they remain as a sequence of discrete nanoparticles. Further SPM (EFM and MFM) studies were carried out for evaluating the "nanowires" electronic and magnetic properties.

3.2.6 Electrical characterization of the DNA/Fe_3O_4 nanostructures using electrostatic force microscopy (EFM) technique

It has been reported that Fe_3O_4 phase of iron oxide has room temperature electrical conductivity of the order of 10^2 S cm^{-1} [136], and the conduction is suggested to be due to a hopping of the electrons between octahedral Fe^{2+} and Fe^{3+} sites within the Fe_3O_4 crystal structure.[137, 138] In order to investigate the electrical properties of the DNA/Fe_3O_4 "nanowires", 'electrostatic force microscopy' (EFM) [80, 81] was used. For EFM measurements, the DNA/Fe_3O_4 nanowires were aligned upon a silicon substrate which has an insulating SiO_2 layer (typically of the order of 10^2 nm thick) on top. Samples can then be probed using a metal-coated, conductive AFM tip, whilst a direct current (dc) bias is applied to the substrate. Further details of the technique are given in chapter 2.

EFM data of the produced DNA-templated Fe_3O_4 "nanowires" is depicted in figure 3.16. This figure shows a height image (figure 3.16a) of a "nanowire" with average diameter of approximately 10 nm, and a series the corresponding EFM phase images (3.16 b-e) recorded at dc potentials of +7, -7, +5 and -5 volts, respectively. These phase images show a uniform dark line (negative phase shift) across regions of the substrate surface which correspond to the position of the aligned DNA/Fe_3O_4 "nanowires", and confirm the structure to be electrically conductive. The larger lateral feature sizes of the DNA/Fe_3O_4 nanowire's phase shift is due to the diffuse nature of the electric fields originating from the sample. Plotting of the tangent of the nanowire's phase shifts as a function of the applied dc potential gives a parabolic curve (figure 3.16f). This relationship has previously been established as the expected result when the interactions between probe and sample are dominated by capacitance effects.[66, 72, 73]

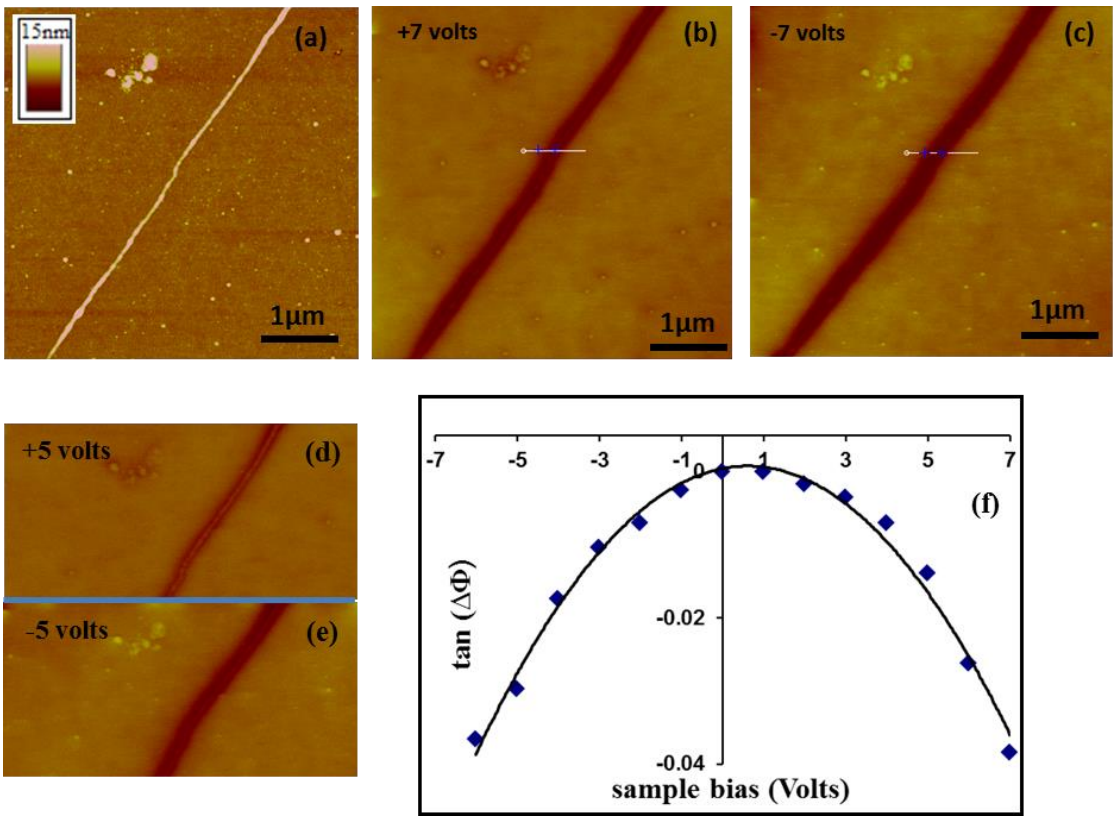

Figure 3-16: Electrostatic force microscopy (EFM) studies of DNA-templated Fe_3O_4 nanowire aligned upon a Si/SiO_2 substrate. (a) AFM height image of a nanowire with structure height of 10 nm. (b - e) the corresponding EFM phase images of the nanowire in (a) at different sample biases, phase scale of 4°. (f) Plot of the tangent of the nanowire phase shift as a function of applied voltage.

3.2.7 Magnetic characterization of the DNA/Fe_3O_4 nanowires using magnetic force microscopy (MFM) technique

The magnetite phase of iron oxide in its bulk form is a ferrimagnetic material, though it may exhibit superparamagnetism if the particle size is smaller than that of a single magnetic domain. In this instant, Fe_3O_4 nanoparticles with particle sizes smaller than the single domain limit (20 nm), show superparamagnetic behaviour at room temperature.[107, 139-142] Whilst ferrimagnetic materials tend to possess a net magnetic moment, superparamagnetic materials are subject to thermal fluctuations which prevent stable magnetisation being observed. In the presence of an external magnetic field however, the magnetic moments of such superparamagnetic particles will align with the field to give a strong net magnetisation which will remain as long as the external field is applied.

Here, initial confirmation of the room temperature magnetism of the DN/Fe_3O_4 material was provided during preparation of the powder samples for use in spectroscopic studies,

where magnetic separation was successfully used to isolate the product material from the reaction solution. However, the magnetic behaviour of nanostructures can be different from those of the corresponding bulk form.[95] It is therefore of interest to probe the magnetic behaviour of individual DNA/Fe_3O_4 nanowires to investigate if the produced DNA/Fe_3O_4 nanowires exhibit superparamagnetic behaviour similar to reports on smaller Fe_3O_4 nanoparticles (< 20 nm in size) [107, 139-142], or they mimic the bulk counterparts in which ferromagnetic character is exhibited.

In order to study the magnetic behaviour of individual DNA-templated Fe_3O_4 nanowires, MFM was required to be used. MFM [86, 87] is an appropriate tool for detecting magnetic fields arising from magnetic nanostructures. MFM experiments here were carried out upon DNA/Fe_3O_4 nanowires, immobilized upon a Si/SiO_2 substrate, and a range of different lift heights (10 nm and above) were implemented, until the phase shifts were no longer observed. Figure 3.17b-f, reveals a series of MFM phase images of a DNA-templated Fe_3O_4 nanowire recorded at a range of lift heights (10–40 nm), along with the corresponding height image (figure 3.17a). The latter reveals a nanowire with distinctive break in the Fe_3O_4 coating. The uncoated region of the nanowire (blue arrow) has a diameter of 1.2 nm as measured by AFM line profile, which is in reasonable agreement with the measured height (1.0-1.5 nm) of λ-DNA by AFM.[66] Therefore, this section of structure is suggested to be bare DNA. On the other hand, the coated regions of the nanowire had an average diameter of 17 nm. Moreover, the height image also reveals a bare or a very thin, irregular Fe_3O_4 coating DNA strand, see Figure 3.17a (red arrow).

The corresponding MFM phase images visibly display negative contrast associated only with the Fe_3O_4 coated regions of the DNA. This is particularly well highlighted here, with the negative contrast clearly seen to be absent at the break in the Fe_3O_4 coating, where the bare DNA template is exposed. At lift heights of ≤ 10 nm, bright contrast can be seen associated with the uncoated DNA portion of the nanowire, as well as the λ-DNA molecule with a very thin, irregular Fe_3O_4 coating (Figure 3.17b). The appearance of such phase signals in MFM phase image at lift heights of ≤ 10 nm is likely to be due to the short-range forces (e.g. Van der Waals force). Similar findings relating to other non-magnetic materials have previously been commented upon in MFM studies reported by other groups.[86, 102, 126]

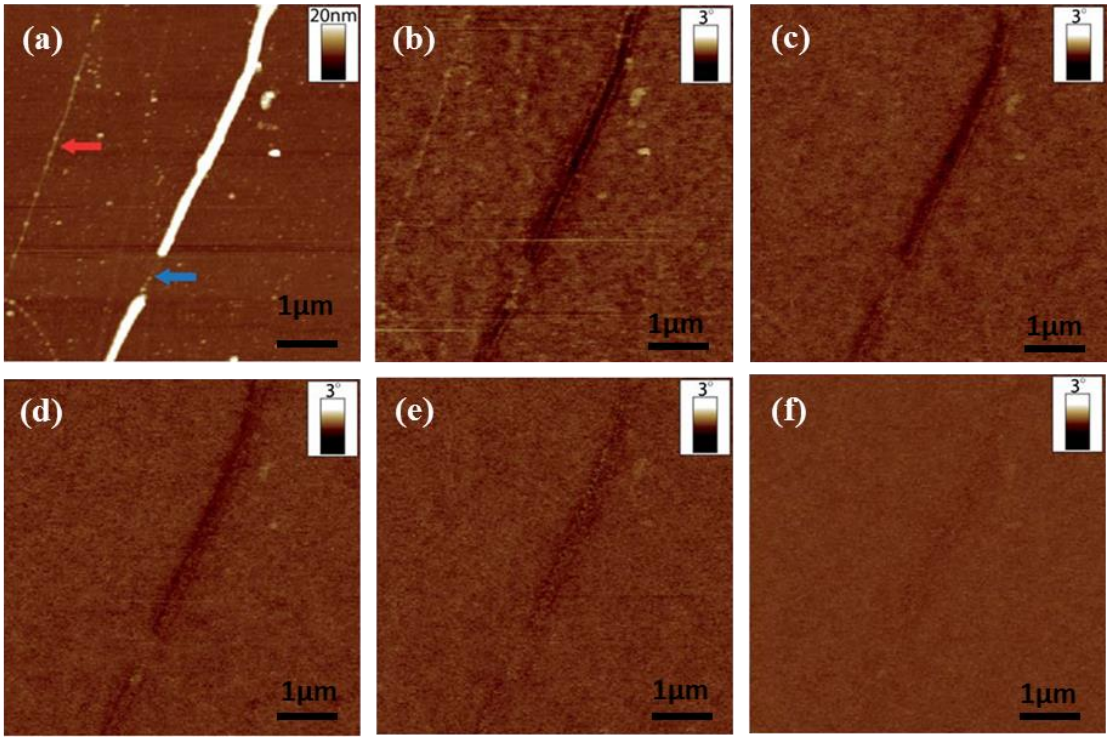

Figure 3-17: (a) AFM height image of a DNA-templated Fe_3O_4 nanowire aligned upon a Si/SiO_2 substrate, showing a break in the metal oxide coverage where the DNA template is exposed (blue arrow), and a bare DNA strand (red arrow). the corresponding MFM phase images of the nanowire are shown, recorded at lift heights of (b)10 nm, (c) 20 nm, (d) 30 nm, (e) 35 nm, and (f) 40 nm, respectively.

These weak phase signals (positive contrast) characteristic of uncoated DNA regions were found to be eliminated completely when the lift height was increased > 10 nm above the sample surface. In contrast to this, however, Fe_3O_4-coated parts of DNA produce negative phase shifts, which remain distinguishable from the surface background up to lift heights of 35 nm. The persistence of this negative contrast at increased lift heights confirms these features arise because of long-range magnetic interactions between the probe and sample. This indicates the room-temperature magnetic behaviour of the Fe_3O_4 when prepared in such a nanostructured form. The magnitude of this negative phase shift is clearly seen to decrease gradually with the increasing tip-sample separation, becoming almost negligible at lift heights of 40 nm and above.

Further MFM experiments were conducted in an effort to distinguish the type of magnetic behaviour exhibited by the Fe_3O_4 nanowires. For these MFM measurements, a strong permanent magnet involved to orientate the nanowire magnetisation perpendicular to the substrate surface prior to MFM data being collected. The MFM phase images then recorded also showed a negative phase signal associated with the

nanowires. The same outcome also resulted when the direction of the AFM probe's magnetisation was changed instead of the nanowire magnetisation. The occurrence of negative phase signals associated with the nanowires, irrespective of the orientation of the probe/sample magnetisation, is indicative of the nanowire's magnetic domains aligning with the AFM probes magnetic field. This indicates superparamagnetism of the DNA-templated Fe_3O_4 nanowires, (figure 3.18a). These findings demonstrate that the metal oxide coating around the DNA can be considered to consist of a series of discrete superparamagnetic nanoparticles, the magnetic moments of which align with the AFM probe's magnetic field as it passes over them, resulting in the attractive probe–sample interactions recorded in the MFM data. This is in contrast to the predicted result if the nanostructured Fe_3O_4 had exhibited ferrimagnetic behaviour (figure 3.18b), where an inversion in the nanowire phase signals would be expected upon reversal of the magnetisation of either the probe or sample.

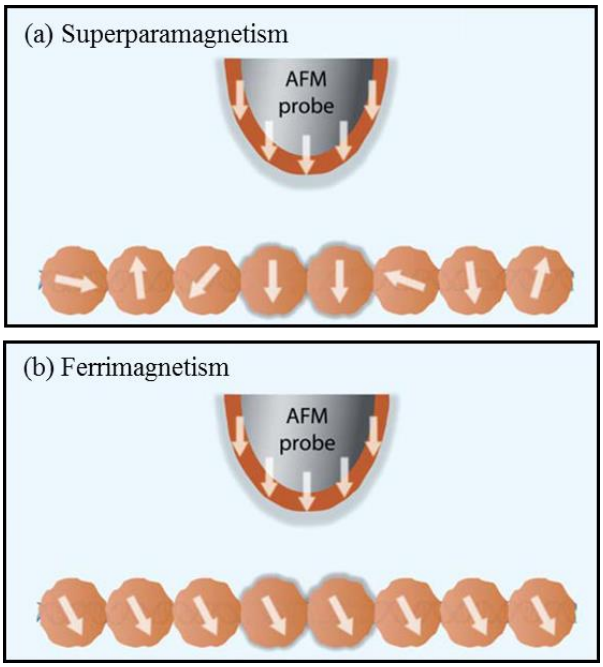

Figure 3-18: Illustration of the two possible types of magnetic behaviour which may be expected for the Fe_3O_4 nanostructures. (a) superparamagnetism – the Fe_3O_4 material behaves as a series of superparamagnetic nanoparticles, and no net magnetisation is observed. (b) Ferrimagnetism – the magnetic moments of the Fe_3O_4 material are locked into alignment with one another, to give a net magnetisation. Reversing the magnetisation (of either the probe or sample) in this scenario would result in the MFM phase signal inverting.

3.3 Conclusion

A simple solution-based DNA-templating approach has been used for the preparation of iron oxide nanowires in the magnetite (Fe_3O_4) phase. In this approach DNA is shown to

be a highly effective template for directing the growth of Fe_3O_4 material in one dimension, yielding nanowires with diameters up to 30 nm. The coverage of metal oxide typically appears to be highly continuous along the DNA templates. Upon closer inspection of the nanowire morphology a small degree of granular character can be identified, indicating that the Fe_3O_4 formation is likely to involve a "nucleation and growth" mechanism.[18, 66, 143] Moreover, EFM studies were used to evaluate qualitatively the electronic properties of the produced nanowires, confirming them to be electrically conducting, whilst MFM data indicated the structures to exhibit room temperature magnetic behaviour. Additional MFM studies revealed the nanowires to be superparamagnetic. This indicates the Fe_3O_4 coatings around the DNA templates to consist of a series of paramagnetic nanoparticles of the metal oxide material.

4. Chapter 4: Preparation and characterization of electrically conductive magnetic DNA-templated Fe nanowires

4.1 Introduction

Iron is a silvery-white in color, pyrophoric if it is very finely divided, while in dry air bulk iron is oxidised when heated.[90] Iron is one of the best examples of a ferromagnetic material and it is also electrically conducting with a resistivity at 293 K of $9.71X10^{-8}$ Ω cm.[144] Chemical reduction of the iron oxides with hydrogen is used to produce metallic iron, or alternatively by thermal decomposition of iron pentacarbonyl $Fe(CO)_5$.[90] Iron has continued in wide use and played an important role in the start of the industrial revolution.[89]

In recent years, there has been an increasing interest in the fabrication of well-defined materials with nanoscale dimensions due to their attractive chemical and physical properties. The unique properties of the nanomaterials makes them ideal candidate to use in a variety of applications, particularly their projected role as building blocks for the construction of nanoscale devices. Much attention has already been paid to the development of a variety of Fe-based nanomaterials due to their potential for exploitation in numerous fields such as catalysis, data storage, biotechnology, spintronics, and sensor technologies.[145-149] Iron nanoparticles, for example display unique chemical and magnetic properties and therefore they have potential for use in magnetic (e.g. magnetic recording media), electric (electric components e.g. transformers), biochemical (e.g. drug delivery and MRI contrast enhancement), and catalytic applications.[148]

Iron nanoparticles can be prepared through many chemical synthesis methods. Among these, thermal decomposition [150-153] and chemical reduction [154-157] are the most important routes.[158] The former method can produce small and uniform Fe nanoparticles in high purity by dissolving $Fe(CO)_5$ in organic solvent, and heating the resulting solution to ~ 200 °C. However, this method requiring high temperature, as well as costly and highly toxic precursors, makes it an uneconomical process. On the other hand, preparation of iron nanoparticles using the chemical reduction method is less costly. In such a method, metallic iron nanoparticles can be obtained by reducing an aqueous solution containing iron salt, such as $FeCl_3$, with hydrazine hydrate

($N_2H_4.H_2O$) or sodium borohydride ($NaBH_4$) which are most common materials used as reducing agents.[158]

Electrochemical growth is amongst the most common approaches to the fabrication of 1-D nanostructures. Such method provides advantages such as, low cost, it can be carried out under ambient conditions and it affords considerable control over material formation. Electrochemical methods have also been shown to offer good adaptability with a wide variety of material types being produced, including metals (*e.g.* Fe, Ni, Co, Pt), semiconductors (*e.g.* CdSe, ZnO), and organic conducting polymers (*e.g.* polyaniline, polypyrrole).[145, 159-167] The fabrication of nanowires using electrochemical methods commonly involves the use of a porous membrane such as anodically etched aluminium oxide (AAO) [145, 159, 160] polycarbonate track membranes [161] or porous silica [163, 164], supported upon an electrode during the electrodeposition process. In this way the porous membrane confines the material growth from the electrode surface to individual channels resulting in 1-D growth.

The use of DNA-templating strategy for the fabrication of 1-D Fe-based nanostructures has to date, focused upon oxide-based structures. Chain-like magnetite (Fe_3O_4) phase iron oxide nanoparticles has recently prepared using co-precipitation and in presence of DNA.[95] More recently, magnetic and conductive magnetite nanowires have also been achieved using DNA as a template to direct the growth of metal oxide into 1-D form (chapter 3).[106] No examples of the preparation of alternative Fe-based nanostructures through direct DNA-templating have been described to date.

This chapter describes the formation of 1-D zerovalent Fe nanostructures via an electrochemical-based, DNA-templating approach. It is believed that this represents the first example of electrochemical growth of an electrically conductive, inorganic material at a DNA template in nanoscale form. The use of DNA to direct material growth during the electrochemical process provides a relatively straight-forward route to nanowire fabrication, avoiding the need for an additional post-synthetic step for removal of the template, as required when using porous membranes.

4.2 Experimental section

4.2.1 Materials

Sigma-Aldrich Company Ltd., of Analar grade or equivalent, and used as received. Ferrous sulphate heptahydrate ($FeSO_4 \cdot 7H_2O$, 99%) was obtained from BDH Chemicals Ltd. Lambda DNA (λ-DNA, Cat No. N3011S) was purchased from New England Biolabs (UK) Ltd. Calf thymus DNA (CT-DNA, highly polymerised, 6% sodium) was purchased from Sigma-Aldrich Company Ltd. and used as received. n-Si <100> wafers (3 inch diameter, 525±50 µm thickness, polished on one side, phosphorus doped, 1–10 Ωcm resistance) were used as the working electrode in electrochemistry experiments and as substrate supports for AFM imaging of samples. n-Si <100> wafers with a thermally grown SiO_2 layer on top (3inch diameter 500±25 µm, double side polished, arsenic doped, <0.005Ωcm resistance, thermal oxide layer 2000 Å±10% thickness) were used in scanned conductance microscopy (SCM) and magnetic force microscopy (MFM) experiments. All Si wafers were purchased from Compart Technology Ltd.

NANOpure® deionised water (18 MΩ cm resistivity) was obtained from a NANOpure® DIamond™ Life Science ultrapure water system equipped with a DIamond™ RO Reverse Osmosis System (Barnstead International).

4.2.2 Fourier transform infra-red spectroscopy of DNA/Fe^{2+}

All samples for FTIR spectroscopy were prepared as films upon Si wafers in order to ensure sufficient material was present to obtain useful data. Prior to preparation of the samples, the Si wafers were treated with Piranha solution as previously described (chapter 3, section 3.2.2), but were not subject to TMS modification.

Samples of bare DNA (i.e. prior to exposure to the Fe^{2+} solution) were prepared by depositing 80 µL of an aqueous solution of CT-DNA (1 mg mL^{-1}) upon a n-Si<100> wafer and allowing the solvent to evaporate at room temperature. Samples of DNA/Fe^{2+} were prepared by adding 60 µL of an aqueous solution of $FeSO_4 \cdot 7H_2O$ (1 mM) to 30 µL of an aqueous solution of CT-DNA (1mg mL^{-1}), and left to stand for 10 minutes. 80 µL of the resulting DNA/Fe^{2+} solution was deposited upon a n-Si<100> wafer, and the solvent allowed to evaporate at room temperature. FTIR spectra were acquired using a

Bio-Rad Excalibur FTS-40 spectrometer (Varian Inc.). Spectra were recorded in the range 400–4000 cm^{-1}, with 128 scans at 4 cm^{-1} resolution.

4.2.3 Preparation of DNA/Fe material for X-ray diffraction and X-ray photoelectron spectroscopy studies

The DNA/Fe material for X-ray diffraction (XRD) and X-ray photoelectron spectroscopy (XPS) was required to be prepared in a manner which ensured sufficient product material could be obtained to allow for meaningful data to be acquired. Samples were prepared by adding 200 µL of an aqueous solution of $FeSO_4 \cdot 7H_2O$ (1 mM) to 100 µL of an aqueous solution of CT-DNA (500 $\mu g mL^{-1}$) and leaving to stand for 10 minutes. 40 µL of the resulting DNA/Fe^{2+} reaction solution was then drop-cast onto a TMS-modified n-Si<100> substrate (TMS modification was carried out similar to what was described previously, see chapter 3, section 3.2.2) for electrochemical reduction of the Fe^{2+} species to be carried out.

The electrochemical process was carried out using a cyclic voltammetry (CV) approach, in which the TMS-modified n-Si<100> substrate was used as the working electrode, and the counter and reference electrodes were tungsten wire (diameter = 0.25 mm) and Ag/AgCl, respectively. The hydrophobic nature of the TMS-modified substrate results in "beading" of the deposited DNA/Fe^{2+} solution, enabling the counter and reference electrodes to be easily inserted into the solution droplet without contacting the substrate surface. CV measurements, and electrochemical reduction of the Fe^{2+}, was performed using a computer-interfaced SECM CHI 900 electrochemical microscope system (CH Instruments), sweeping the potential between E = +0.3 V and E = –3.3 V, with a scan rate of v = 0.1 Vs^{-1}, quiet time of t = 2.0 seconds, and sweep segments = 2.

Following the electrochemical process, the reaction solution was allowed to dry upon the working electrode at room temperature in order to maximise the amount of product material present for subsequent analysis. In the case of samples prepared for XRD, this procedure was repeated a further two times on the same Si substrate in order to provide sufficient of the product material for diffraction pattern to be acquired.

4.2.4 Preparation and alignment of DNA-templated Fe nanowires for scanning probe microscopy studies

Whilst CT-DNA was used in the preparation of the DNA-templated Fe where large amounts of material were required for investigation (FTIR, XRD, XPS), λ-DNA was employed as the templating agent in the preparation of Fe nanowires fabricated for SPM studies. Molecules of λ-DNA are of a consistent length (16.2 μm) [16], allowing for the formation of well-defined nanowire structures, highly suited for investigation by SPM. Samples were prepared by adding 10 μL of an aqueous solution of $FeSO_4 \cdot 7H_2O$ (1 mM) to 5 μL of an aqueous solution of λ-DNA (500 μgmL^{-1}), which was left to stand for 10 minutes. 5 μL of the DNA/Fe^{2+}solution was subsequently deposited upon a TMS-modified n-Si<100> wafer. CV was subsequently carried out at the surface of the wafer as previously described. Following the electrochemical process, the reaction solution was removed from the Si working electrode by micropipette. The resulting DNA-templated Fe nanowires present in the reaction solution were isolated by immobilisation upon a fresh TMS-modified n-Si<100> wafer using a process based upon spin-coating methods. In this method, the DNA/Fe solution was applied to a TMS-modified n-Si <100> wafer whilst spun at 125 rpm. The substrate was spun for a further 2 minutes at 250 rpm before the residual solution was withdrawn from the substrate surface by micropipette.

4.2.5 X-ray diffraction

XRD data was acquired using of a PANalytical X'Pert Pro diffractometer (PANalytical) using Cu K_α radiation source (λ = 1.540 Å).

4.2.6 X-ray photoelectron spectroscopy

XPS was carried out using a Thermo Scientific K-Alpha X-ray photoelectron spectrometer (Thermo Electron Corp., East Grinstead, UK), equipped with an Al Kα X-ray source (1486.6eV) with a variable spot size of 30–400 μm. A take-off angle of 90˚ was used during data acquisition, and a charge neutralisation gun used to compensate for surface charging. All spectra were referenced to hydrocarbon C1s peak at 285.0 eV. Survey spectra were acquired using a pass energy of 150 eV, whilst high resolution region spectra were acquired using a pass energy of 50 eV. For depth profiling

experiments, an Ar^+ ion gun (200 eV) was used for sputter etching of samples. Data analysis was carried out using CasaXPS software (Casa Software Ltd.).

4.3 Results and Discussion

For the preparation of DNA/Fe nanowires, an electroreduction of Fe^{2+} was carried out in aqueous solution containing the duplex DNA strands according to the experimental setup illustrated in Figure 4.1. This electrochemical-based DNA-templating method involves initial association of the Fe(II) cations with the DNA through DNA/Fe^{2+} complex formation. In the second step and for electrochemical reduction to be carried out, the DNA/Fe^{2+} in the reaction solution was supported upon an n-Si<100> which modified with a TMS self-assembled monolayer in order to improve the hydrophobic properties of the substrate surface.

The hydrophobic nature of the TMS-modified substrate results in "beading" of the deposited DNA/Fe^{2+} solution, enabling the counter and reference electrodes to be easily inserted into the solution droplet without contacting substrate surface. The conversion of the DNA-bound Fe^{2+} species into the metallic phase took place by performing cyclic voltammetry measurements upon the reaction solution supported on TMS-modified Si substrate which acts as working electrode.

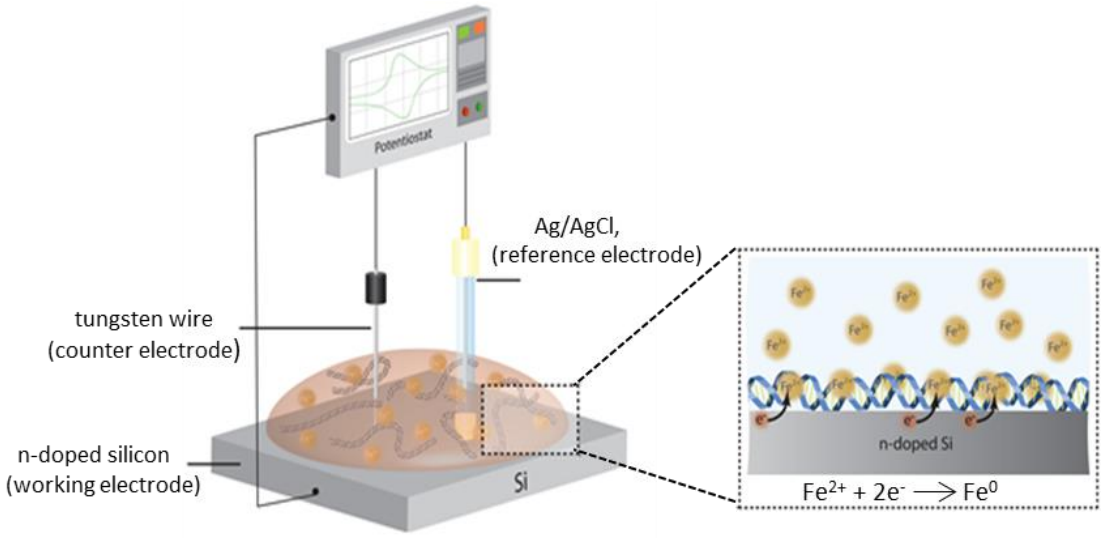

Figure 4-1: Design describing the electrochemical process of the DNA-bound Fe^{2+} ions during the preparation of DNA-templated Fe nanowires.

It is suggested that the nanowire fabrication using such novel method relies upon two distinct stages. The first one is the formation of DNA/Fe^{2+} complex which has

fundamental role in the preparation process, directing subsequent formation of the Fe material to take place along the axis of the DNA molecules. The electrochemical reduction of the DNA-bound Fe^{2+} cations to zerovalent is the second significant stage for the nanowire formation. This process results in the growth of Fe coating around the DNA template molecule to give the final metal nanowire.

The DNA-templated Fe produced using DNA-templating strategy in conjugation with electrochemical reduction method, was characterised using XRD and XPS studies in order to confirm the formation of Fe within the product material. AFM measurements were used to investigate the effectiveness of the DNA in directing the growth of Fe material into one dimensional form and establish the material's structural character.

4.3.1 Fourier transform infra-red (FTIR) spectroscopy studies

FTIR spectroscopy was carried out in order to confirm the formation of the interactions between the Fe^{2+} cations and the duplex DNA strands. The rich chemical functionality presented by the DNA offers several different types of site for metal ion interaction. Metal ion binding at the polyanionic phosphodiester backbone for example, can take place through the formation of electrostatic interactions involving the hydrating water molecules around the metal ion or through inner-sphere coordinate bonds directly to the DNA phosphate groups. Alternatively, interactions may also take place through coordination of the metal cations to electron donor sites (*e.g.* ring nitrogen atoms) within the DNA bases.[48, 63] Previous FTIR studies of the DNA/metal ions interaction have reported that the metal ions attach to the DNA structure mainly at guanine (N7, O6) and adenine (N-7, N-1) of purines bases and at the N3 of the pyrimidine.[50] Moreover, it is reported that at low cation concentration, Fe^{2+} species bind guanine N-7 and the backbone PO_2^- group of the DNA, while at higher cation concentration they bind to adenine N-7 and thymine O-2 of the DNA.[53]

Here, FTIR spectra of samples of DNA before and after treatment in solution containing Fe^{2+} cations are depicted in figure 4.2. The spectrum of the DNA following $FeSO_4$ treatment (black spectrum) shows several spectral changes in the DNA-related bands (see figure 4.2 and table 4.1), indicative of interactions between the DNA and Fe^{2+} species. These changes are evidently observed in the 900-1300 cm^{-1} region of spectra, thereby indicating interaction of the Fe^{2+} cations with the DNA phosphodiester backbone. The P-O/C-O stretches at 1071 cm^{-1} and PO_2^- symmetric stretches located at

1097 cm^{-1} of the phosphate backbone are shifted upon Fe^{2+} association to be observed at 1066 and 1103cm^{-1}, respectively. This was combined with a relative increase in intensity of these bands upon metal binding.

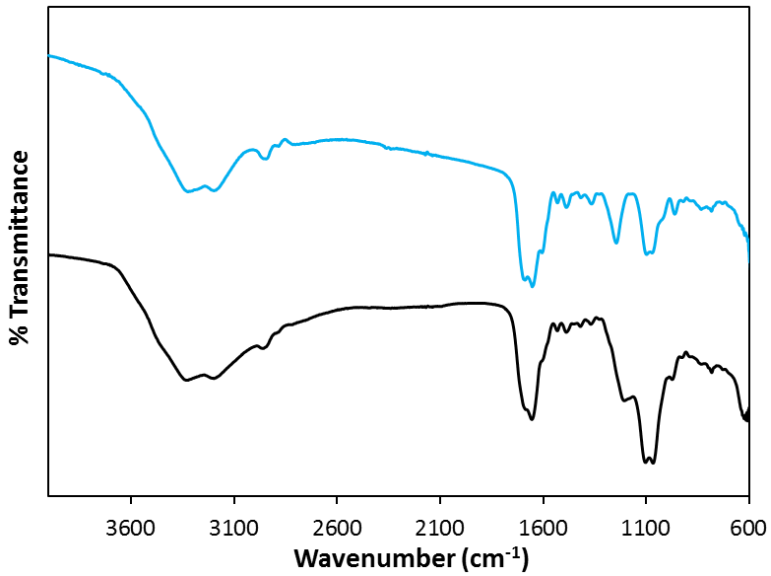

Figure 4-2: FTIR spectra of "bare" DNA (blue spectrum) and DNA following exposure to an aqueous solution of $FeSO_4$ (1mM) (black spectrum).

Moreover, the PO_2^-asymmetric stretch at 1244 cm^{-1} showed a noticeable shift toward lower frequency to 1205 cm^{-1} following Fe^{2+} treatment. Similarly changes in IR-band positions can also be identified in the nucleobase region (1300–1800 cm^{-1}), indicating the Fe^{2+} cations also interact with the DNA through coordination to the DNA nucleobases. The carbonyl stretch at 1688 cm^{-1}, for example has shifted -7 cm^{-1} following DNA/Fe^{2+} binding. All the DNA vibration bands were assigned according to literature.[109-111]

Wavenumber (cm^{-1})		**Assignment**
CT-DNA	**CT-DNA / Fe^{2+}**	
961	973	C-C deoxyribose stretch
1021[a]	-	C-O deoxyribose stretch
1071	1066	P-O/C-O deoxyribose stretch
1097	1103	PO_2^- symmetric stretch

1244	1205	PO_2^- asymmetric stretch
1364	1368	C-N stretch of cytosine/guanine
1417	1419	C-H /N-H deformation; C-N stretch
1487	1487	Ring vibration of cytosine/guanine
1530	1531	In-plane vibration of uanine/cytosine
1605	1602[a]	In-plane vibration of adenine
1652	1654	C=O stretch of cytosine/thymine; In- plane vibration of thymine
1688	1681	C=O stretch of guanine/thymine; N-H thymine
2850–3500	2850–3500	C-H/N-H /O-H stretches

Table 4-1: Assignment and comparison of FTIR spectra (600–4000 cm^{-1}) of calf thymus DNA, and calf thymus DNA following association of with Fe^{2+} cations in aqueous solution. [a] Peak appeared as a shoulder.

4.3.2 Cyclic voltammetry

Electrochemical reduction of the DNA-bound Fe^{2+} species was carried out via a CV approach. For CV measurements, the experimental setup was adopted as previously described, see Figure 4.1. A typical voltammogram curve obtained from CV measurements during the DNA/Fe nanowires preparation is illustrated in figure 4.3. This curve displays a single broad cathodic peak at approximately E = -1.4 V, which is in reasonable agreement with the reported cathodic peak (-1.49 V) of the electrodeposition of iron on gold disk electrodes.[168] It is obvious from the CV recorded for the DNA/Fe^{2+} solution system that, there was no peak in the anodic sweep. This indicates a single irreversible reductive process was carried out, corresponding to the two-electron reduction of the Fe^{2+} cations at the n-Si<100> wafer surface.

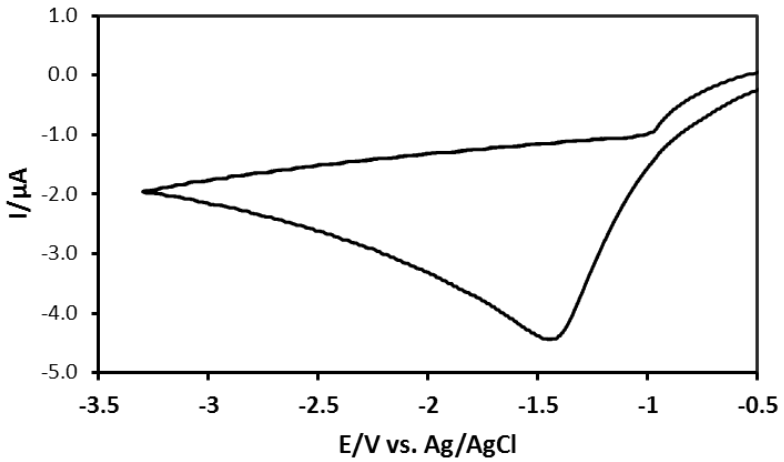

Figure 4-3: Cyclic voltammogram of the reduction of Fe^{2+} in a $FeSO_4$ (1 mM) /CT-DNA (500 µg mL^{-1}) aqueous solution at an n-Si<100> electrode.

4.3.3 X-ray diffraction studies

In order to verify the chemical identity of the material produced during the CV experiments, XRD analysis was performed. For XRD studies, a sample solution was left to dry upon the Si wafer (working electrode) following the electrochemical reaction, and the fabrication process then repeated two further times on the same wafer in order to ensure sufficient material was present in the samples to acquire a diffraction pattern. XRD data provide evidence for the formation of metallic iron following the electroreduction process within the product material. Figure 4.4 illustrates the XRD diffraction pattern obtained of the film sample of DNA/Fe material.

The predominant peaks in the XRD pattern recorded for the sample material appeared within 2θ = 10–35° range, and are very likely due to unreacted starting material ($FeSO_4 \cdot 7H_2O$) which is present in the sample as a consequence of the manner in which it is required to be prepared in order to obtain meaningful XRD data. More significantly, a small peak at 2θ = 45° can also be identified, which is consistent with the (110) reflection of the α-Fe phase (body-centred cubic).[158, 169] Despite a poor signal to noise ratio of such small peak (2θ = 45°), the average crystallite size of the iron was estimated through applying the Scherrer's equation ($D = k \cdot \lambda / [\beta \cdot \cos\theta]$). Using a line broadening parameter (β) of 0.23°, determined from the full-width-at-half-maximum of the (110) reflection, and a Scherrer constant (k) value of 0.89, a mean crystallite size of approximately 37 nm was determined.

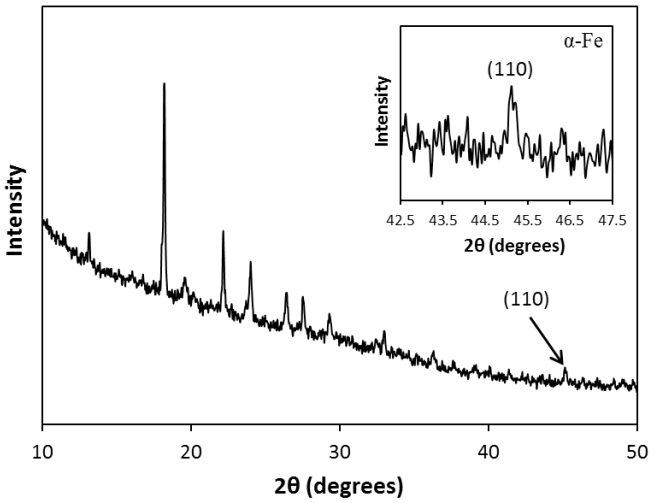

Figure 4-4: XRD pattern of DNA-templated Fe nanowires, showing (inset) the characteristic α-Fe (110) reflection at 2θ = 45˚. The series of peaks present at lower 2θ values are attributed to unreacted $FeSO_4 \cdot 7H_2O$ starting material present in the sample.

Moreover, from the XRD pattern recorded for the sample material, no peaks characteristic of any iron oxide phases were observed, suggesting the product material is predominantly metallic α-Fe. It should be noted that, despite XRD pattern indicated the product material is predominantly metallic α-Fe, it is still expected that the possibility of the α-Fe to be coated with an oxide layer at its surface to which XRD is insensitive. For this reason, the product material was also characterised using X-ray photoelectron spectroscopy (XPS) in order to establish the existence of any oxide species at the surface of the product material.

4.3.4 X-ray photoelectron spectroscopy (XPS) studies

XPS studies were carried out upon the product material in order to provide further evidence for the presence of zerovalent metallic Fe to support XRD data, as well as to allow for the surface/core chemical structure of the Fe material to be elucidated. This was achieved through depth profile analysis of the material, which allowed for the chemical composition both at the surface and within the core of the Fe material to be probed. The XPS survey spectrum of the DNA/Fe material is depicted in Figure 4.5. This spectrum shows signals arising from both DNA e.g. P2p and N1s, and Fe material e.g. Fe2p and Fe3p. The additional peaks, such as O (originated from contributions of air, DNA and/or the $FeSO_4.7H_2O$), C (appeared due to DNA and/or organic contaminants), S (which indicates the presence of the $FeSO_4.7H_2O$ starting material)

and Si (originated from silicon wafer used as a substrate) also appeared in the spectrum of the product.

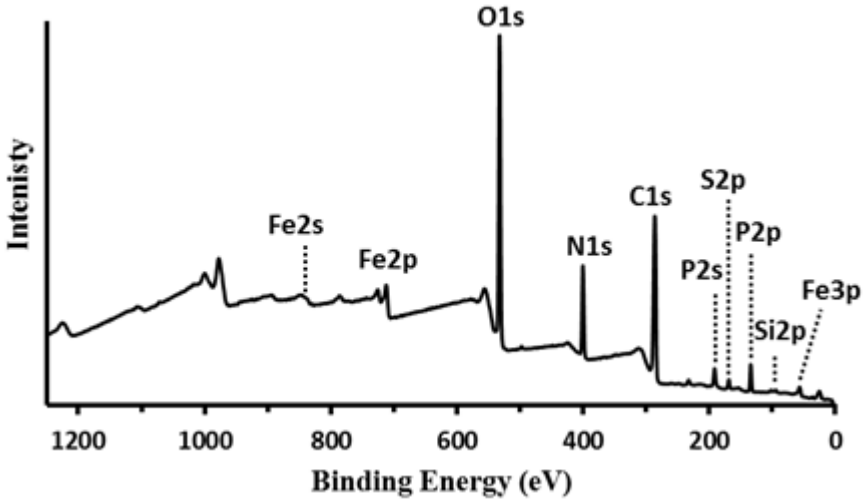

Figure 4-5: XPS survey spectrum of a film sample of calf thymus DNA-templated Fe material immobilised upon a Si/native SiO_2 substrate.

Evidence for the presence of the DNA in the product material is provided by the P2p signal. Curve fitting of the P2p region (figure 4.6a) displays a doublet structure with binding energies at $P2p_{3/2}$ = 133.7 eV, and $P2p_{1/2}$ = 134.5 eV, respectively. Such a doublet arises from the phosphorus atoms in the DNA backbone.[53, 119, 121, 124]

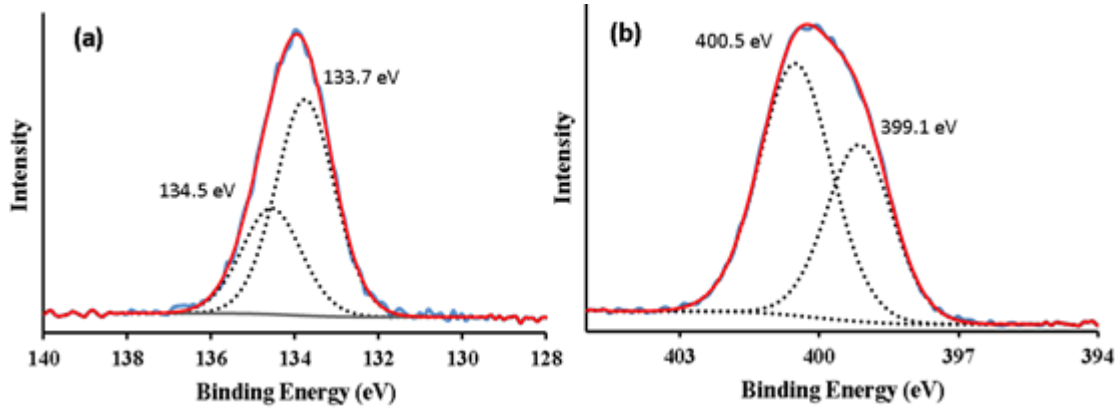

Figure 4-6: Curve fitting of high resolution XPS spectra of the P2p region (a) and the N1s region (b) of a film sample of calf thymus DNA-templated Fe nanowires immobilised upon a Si/native SiO_2 substrate. Blue solid line represents raw data, total fits is indicated by red line and black dashed lines are referred to component peaks.

Further confirmation of the presence of DNA in sample material is obtained from the examination of N1s signal. Curve fitting of the N1s region (figure 4.6b) is consistent with two components at binding energies of 399.1 and 400.5 eV, respectively. The lower energy peak with lower intensity is consistent with the reported value of

sp^2-bonded N atoms, and the more intense emission at higher binding energy can be assigned to sp^3-bonded N atoms present in exocyclic amino group ($-NH_2$) of DNA.[119-122]

On the other hand, the presence of the Fe in the product material is confirmed by observation of Fe2p region. Figure 4.7 shows a high resolution XPS spectrum of the Fe2p region of the DNA/Fe material. This spectrum reveals a broad doublet structure with binding energy at approximately $Fe2p_{3/2}$ = 711.2 eV, and $Fe2p_{1/2}$ = 723.9 eV. Curve-fitting of the spectrum has not been carried out due to the complex and unreliable nature of accurately assigning Fe2p spectra which potentially contain several different Fe species; as well as requiring to fit each Fe species present. The curve-fit would be further complicated by multiplet splitting of the components due to electrostatic and spin-orbit interactions between the 2p core hole and the unpaired 3d electrons of the photoionised species (characteristic of high-spin Fe^{2+} and Fe^{3+} species).[170, 171]

However, despite these apparent complexities, several distinctive features of the spectrum can be identified which allow for different Fe species in the sample to be distinguished. Firstly, the doublet structure has a broad appearance and distinctive shape, characteristic of that previously seen for Fe^{2+} species present in $FeSO_4 \cdot 7H_2O$.[172, 173] A broad tail can be identified to the higher binding energy side (~713–717eV) of the $Fe2p_{3/2}$ peak, characteristic of a satellite peak arising from Fe^{2+} species.[171-175]

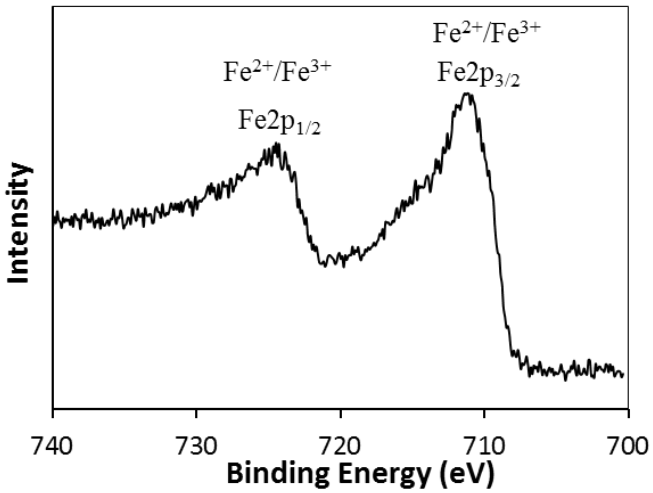

Figure 4-7: High resolution XPS spectra of the Fe2p region, recorded from a sample of DNA-templated Fe nanowires immobilised upon a Si/native SiO_2 substrate.

The presence of $FeSO_4 \cdot 7H_2O$ in the sample material was further verified by the S2p peak around 168.7 eV, consistent with sulfur present in the form of SO_4^{2-} species, [176, 177], see figure 4.8. These findings are similar to those of the XRD data discussed earlier, which showed several peaks in the diffraction pattern relating to unreacted $FeSO_4 \cdot 7H_2O$ due to the manner in which the sample material was prepared.

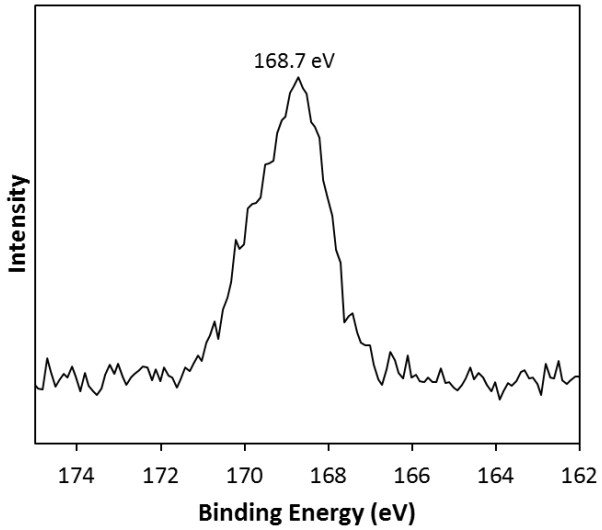

Figure 4-8: High resolution XP spectra of S2p region acquired from a sample of DNA-templated Fe nanowires.

The broad nature of the Fe2p spectrum also suggests a second Fe component to be present in addition to Fe^{2+}. This is also evident from the presence of a shoulder on the lower binding energy side of the $Fe2p_{3/2}$ peak, which can be attributed to the Fe^{2+} ($Fe2p_{3/2}$) signal overlapping with the Fe2p spectrum of a second Fe component at higher binding energy. The position of this component, relative to the Fe^{2+}, is consistent with the presence of Fe^{3+}.[173] A shake-up satellite around 719 eV would typically be expected to be observed in the Fe^{3+} spectrum, but is difficult to distinguish in this instance as a result of the overlapping with the Fe^{2+} spectrum.[118, 127, 173]

The presence of Fe^{3+} is most likely the consequence of surface oxidation of the Fe product material forming an oxidized layer around the metallic Fe. The formation of such coatings is generally known to take place at the surface of nanostructured α-Fe materials, typically in the form of an oxide such as Fe_2O_3 or Fe_3O_4 for example, or as oxyhydroxide (FeOOH).[178-181] However, the similar binding energies of the Fe2p core level in these two materials, along with the complexities of having multiple components present in the Fe2p envelope, makes it difficult to confidently confirm in which phase the oxide layer exists in this instance.

Another important feature of the spectrum in Figure 4.7 is the absence of a doublet peak arising from the zerovalent metallic Fe, expected around 706–708 eV ($Fe2p_{3/2}$). This confirms there to be no Fe present in the surface layers of the fabricated structures. When it is also considered that the XRD data indicated the product material to be predominantly composed of α-Fe, this suggests that the DNA/Fe structures do indeed possess an iron/oxide core-shell structure. In order to verify this, depth profile XPS analysis was also carried out. Figure 4.9 shows a series of XPS spectra of the Fe2p region from the DNA/Fe material following etching by Ar^+ sputtering for a defined period of time (0–1200 s).

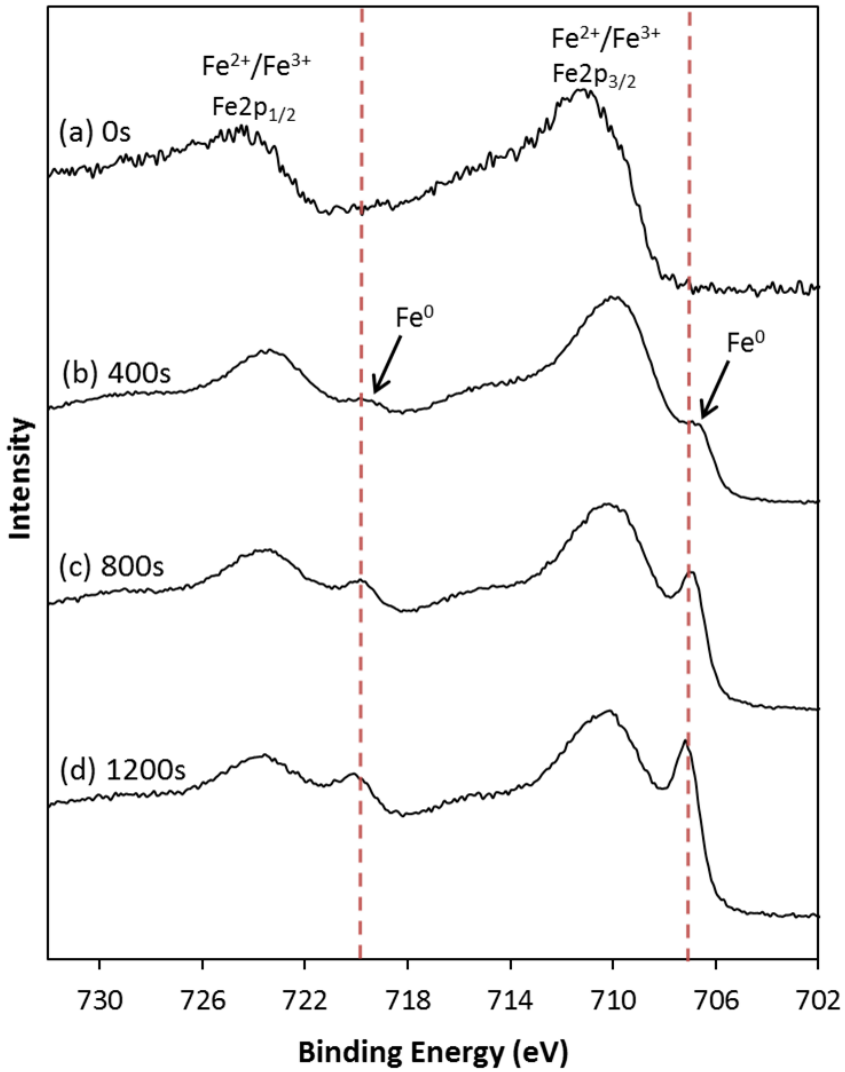

Figure 4-9: High resolution XPS spectra of the Fe2p region, recorded from a sample of DNA-templated Fe nanowires. The spectra were recorded following etching of the sample material by Ar^+ sputtering for (a) 0s, (b) 400s, (c) 800s, and (d) 1200s, respectively.

The appearance of an additional doublet at lower binding energy ($Fe2p_{3/2}$ = 706.9 eV, and $Fe2p_{1/2}$ = 719.8 eV) relative to the Fe^{2+}/Fe^{3+} signal is observed in the spectra upon

etching, which increases in intensity as a function of the etching time. The binding energy of this doublet is consistent with zerovalent Fe [158, 175] confirming that the core of the Fe-based structures are composed of metallic Fe, in agreement with XRD data.

It is also noted that the Fe2p signal from the oxide material is still observed following etching, as the sample is not deposited as a homogenous film, and will consist of a multilayer network of DNA-templated Fe nanostructures. From XPS depth profile studies of the DNA-templated Fe material, it could be concluded that, the electro-deposited Fe to possess a core-shell structure comprised of a metallic Fe core encased by a surface oxide layer. In order to provide further evidence for the core-shell structure of the produced DNA/Fe material, curve-fitting of the O1s spectra was attempted.

The product material contains several different oxygen types, such as oxygen present in iron oxide/hydroxide, DNA, $FeSO_4 \cdot 7H_2O$. Therefore, it is not straightforward to make an accurate fitting of the O1s spectra. A simple approach has been used, in which a minimum of three components are required in order to accurately reproduce the shape of the O1s spectra, shown in 4.10. It should be noted that each component is the sum of several contributions. For example, the component at highest binding energy (532.9 eV) is attributed to oxygen atoms in the DNA phosphate groups.[119, 122] This is consistent with the observation of P2p region (figure 4.6a) which confirmed the presence of the DNA in the sample material. Other contributions to this component of the O1s envelope are expected from the sulfate groups of unreacted $FeSO_4 \cdot 7H_2O$ starting material present in the sample.[172, 176] The presence of sulfate groups was also indicated from the S2p signal observed around 168.7 eV, see figure 4.8. Additionally, there will also be a contribution from H_2O adsorbed at the surface of the Fe structures to this peak (532.9 eV).[178, 179]

The second component in the O1s envelope (531.5 eV), of similar intensity to the first, can be assigned to oxygen atoms present in the sugar and nucleobase units of the DNA.[119, 122] A contribution from the SiO_2 substrate to the spectrum within the region of these first two components may also be present, though this is not expected to be significant due to the considerable amount of sample material present on top of the substrate (this is supported by the XPS survey scan which showed only a weak Si2p signal). The final component fitted within the O1s envelope (530.2 eV) is in reasonable agreement with the expected binding energy for O^{2-} species found in iron oxides.[172,

178, 179] This is at least consistent with the Fe nanostructures possessing an oxide layer at their surface.

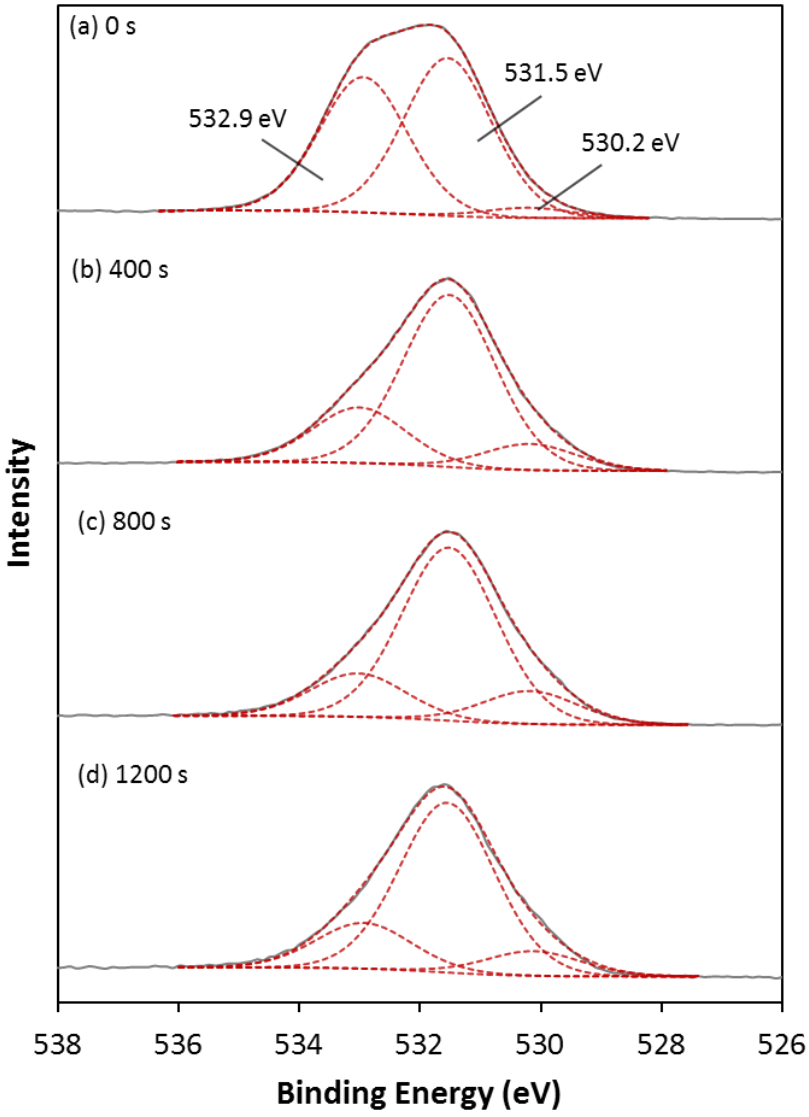

Figure 4-10: Curve-fitting of high resolution XPS spectra of the O1s region from DNA-templated Fe nanowires, prepared via electrochemical reduction of Fe^{2+} in the presence of DNA. The spectra were acquired following etching of the nanowires by Ar^{+} sputtering for a period of (a) 0s, (b) 400s, (c) 800s, and (d) 1200s.

4.3.5 Atomic force microscopy (AFM) studies of the DNA/Fe nanostructures

The structure and morphology of individual DNA-templated Fe nanowires prepared using electrochemical reduction of DNA-bound Fe^{2+} ions has been probed by AFM. For the AFM measurements, samples were prepared by stretching the DNA-templated Fe "nanowires" on a TMS-modified Si/SiO_2 substrate. The treatment of the silicon wafers with a TMS self-assembly monolayer is a very important initial step to improve the hydrophobic properties of the substrate surface, giving typical static contact angles

~71˚.[16] This facilitates alignment of the produced DNA-templated Fe "nanowires" upon the substrate surface via molecular combing in adequate density,[133, 134] allowing individually structures to be probed by AFM. Selected AFM height images of the produced DNA/Fe "nanowires" aligned upon a TMS-modified Si substrate are illustrated in figure 4.11.

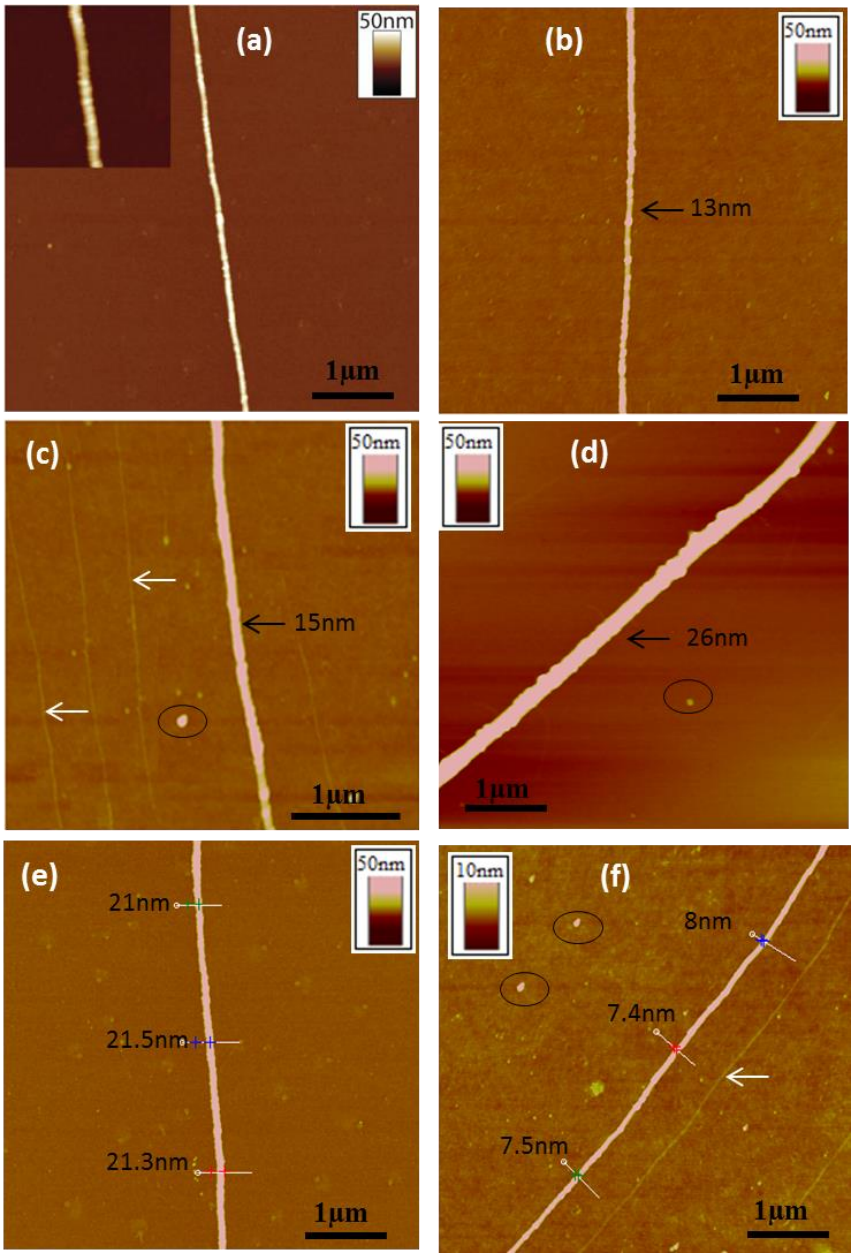

Figure 4-11: Selected TappingMode AFM images of the DNA-templated Fe "nanowires" aligned upon a TMS-modified Si/native SiO_2 substrate. (a) AFM image shows a nanostructure with average diameter of ~22 nm. The inset image shows a zoomed-in region of the nanowire with the image contrast adjusted to highlight the nanowire morphology, which consists of linear arrangements of metal particles packed along the DNA template. (b) AFM image shows granular character of the 15 nm height of DNA/Fe "nanowire". (c) This image represents also a "nanowire" with structure height of 15 nm, along with bare DNA molecules, which denoted with white arrows. (d) AFM image reveals thicker (26 nm in diameter) structure. (e and f) represent regular structure with little/or no variation in the diameter size along their length.

These images display structures with different sizes, as the Fe electrodeposited has occurred to variable levels upon the duplex DNA templates. Thickening of all observed structures except those indicated by white arrows (figure 4.11c and f) is obviously evident relative to the DNA itself (≤ 2) [135], indicating that the Fe is successfully electrodeposited upon DNA.

The influence of the DNA upon the growth of the electrodeposited Fe is evident from the observed 1D form of the resulting DNA-templated Fe nanostructure, indicating that DNA templates the growth of the Fe material along in its own direction. Moreover, the substrates show a low level of globular features which are expected to be non-templated Fe material (circled areas in figure 4.11). A number of structures with diameters < 2 nm (figure 4.11c and f, white arrows), are also observed which are very likely to be bare DNA molecules.

It is clear from figure 4.11 that for the DNA/Fe structures, the Fe appears to form a continuous coating around the DNA with little evidence of breakages in its structure. Upon closer inspection however, the metal coating can be seen to exhibit a granular morphology (see Figure 4.11a, inset), consisting of a linear arrangement of nanoparticles densely pack together along the DNA, as illustrated in Figure 4.12b.

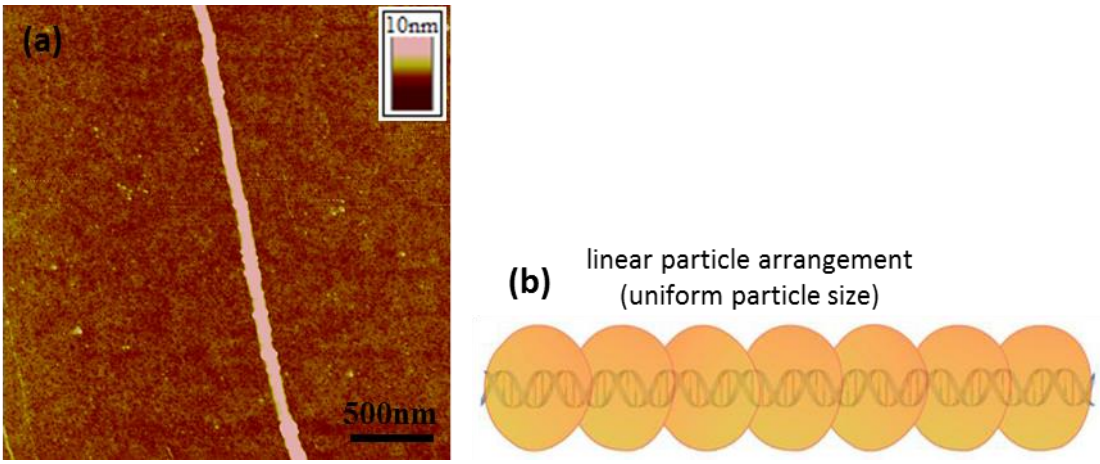

Figure 4-12: (a) AFM height image of the produced DNA-templated Fe "nanowire" aligned upon a TMS-modified Si/native SiO_2 substrate, showing granular character of the Fe coatings around DNA with uniform size. (b) Illustration showing the morphology exhibited by the DNA-templated Fe nanowires.

The morphology associated with the metal coating is most likely a consequence of the Fe formation taking place through a series of nucleation and growth processes on the template, similar to that previously reported in the preparation of other DNA-templated

metal structures.[18, 66, 182] For example, AFM studies of Cu^0 nanostructures prepared using chemical reduction of DNA-bound Cu^{2+} ions with ascorbic acid,[66] showed a distinctive "beads-on-a-string" appearance (figure 4.13a), indicating that the growth of Cu^0 nanoparticles at DNA templates had took place via a "nucleation and growth" mechanism. Such a growth mechanism of the Fe material is supported by a minority of DNA-templated Fe "nanowires" which presented incomplete coverage of the DNA template by the Fe material (figure 4.13b). This image shows parallel chains of structures with a series of distinct nanoparticles being bound along the DNA. These structures are regarded as examples where the growth of Fe material upon the template has not gone to completion and help provide a useful insight into the growth of the Fe material at DNA template during the DNA/Fe "nanowire" formation.

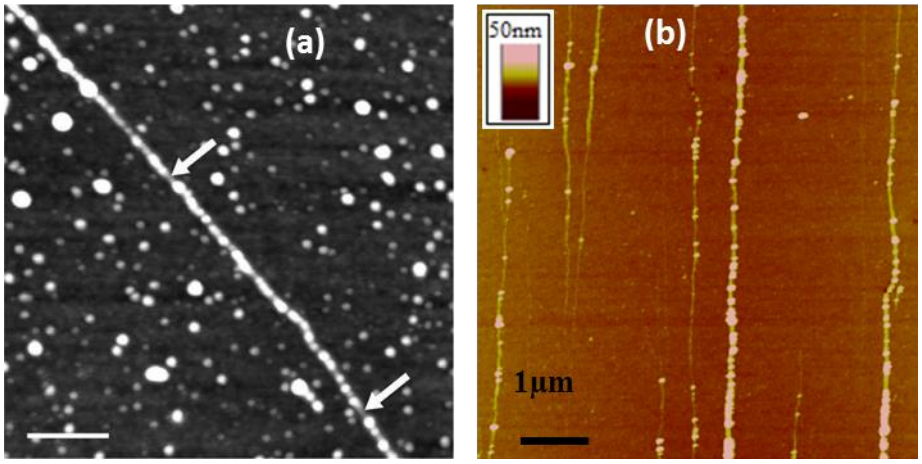

Figure 4-13: (a) AFM height image of DNA/Cu nanostructure with "beads-on-a-string" morphology, the arrows indicate regions between Cu^0 nanoparticles on the DNA stands, where less substantial Cu^0 deposition has taken place, (scale bar=200 nm, height scale=8 nm).[66] (b) Example of partially formed λ-DNA-templated Fe "nanowires", where the metal growth has not reach maturity during the reaction period.

It can also be noted from the AFM images of the DNA/Fe "nanowires" that the constituent Fe nanoparticles of the metal coating appear highly monodisperse in size. This is in contrast to morphologies seen in previously reported examples of DNA-templated nanostructures, which have typically displayed one of two general types of structure. The first of these can be described as linear arrangements of nanoparticles along the DNA (figure 4.14a), similar to that shown by the current DNA-templated Fe nanowires, but with much larger variation in the constituent particle sizes.[66, 67, 134] One such structure illustration of this has been observed for metallic palladium nanowires prepared via chemical reduction of the DNA-absorbed Pd^{2+}.[134] These showed continuous structures of nanowires which are composed of nanoparticles.

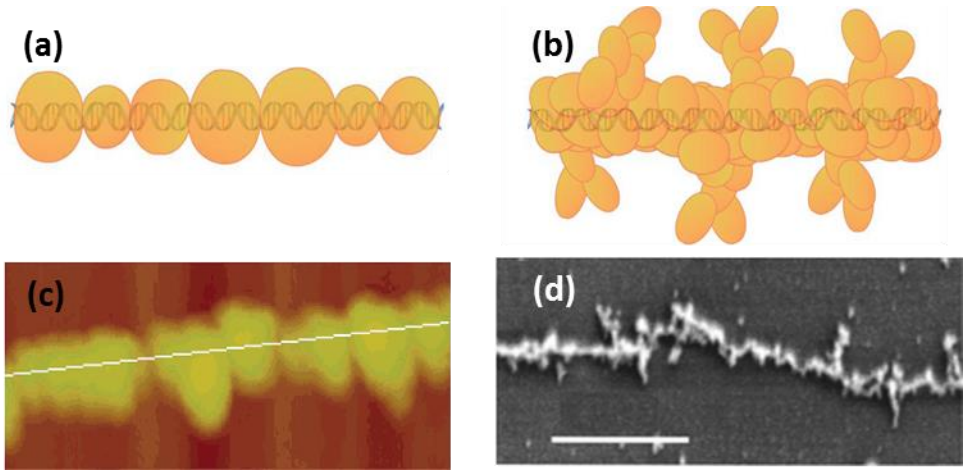

Figure 4-14: (a and b) Illustration showing two general morphology types that have previously been reported of various DNA-templated nanowires which are (a) linear particle arrangement (variablr particle size) and (b) cluster formations.(c) AFM image with high-magnification of a DNA/Pd nanowire, showing morphology behaviour similar to illustrated in (a). (d) Scanning electron microscope image of Pd nanowire with small dendrites perpendicular to the strand.[143]

However, section analysis showed a variation in the diameters of these nanoparticles along the whole length of any single nanowire, see figure 4.14c. The second morphology type involves the templated material binding in a much less linear fashion, forming clusters of particles around the DNA (figure 4.14b), which in some instances produce structures with a dendritic appearance.[18, 64, 143] An example of such morphology behaviour is revealed by the Pd nanowires prepared through two-step chemical deposition of Pd on DNA templates.[143] Scanning electron microscope image of the produced nanowires showed thicker structure (40 nm) with dendrites perpendicular to the main structure's body, see figure 4.14d.

It has been suggested that there are two factors which may be responsible for the uniform particle growth seen in the DNA-templated Fe "nanowires" described here. These are: (i) at the high driving forces of the electrochemical experiment, resulting in instantaneous nucleation on the template being favoured over progressive nucleation; (ii) confinement of nuclei to a 1-D template results in inhibition of the growth of larger particles because they experience overlap with their neighbours sooner. Both factors are likely to narrow the size distributions of particles nucleating and growing on DNA in comparison with the cases of nucleation at a surface or in a bulk phase.[183]

Whilst there is a relatively narrow size distribution of the constituent particles associated with any individual nanowire, AFM analysis revealed considerably more

variation in the mean diameter between different nanowires in the product material; height measurements showed the structures to range in size from 1–26 nm in diameter. In order to evaluate the size distribution of the structure heights of the DNA-templated Fe "nanowires" produced, a statistical treatment of the structures was carried out. For this, the average heights of 100 DNA/Fe "nanowires" were measured using AFM line profiles. A histogram of the nanowire diameters (figure 4.15) displays moderately wide size distributions with structures up to 26 nm in diameter were observed. This histogram showed a large peak value at < 2 nm, indicating that a number of the DNA did not involve in the templating process and remain free in the reaction solution.

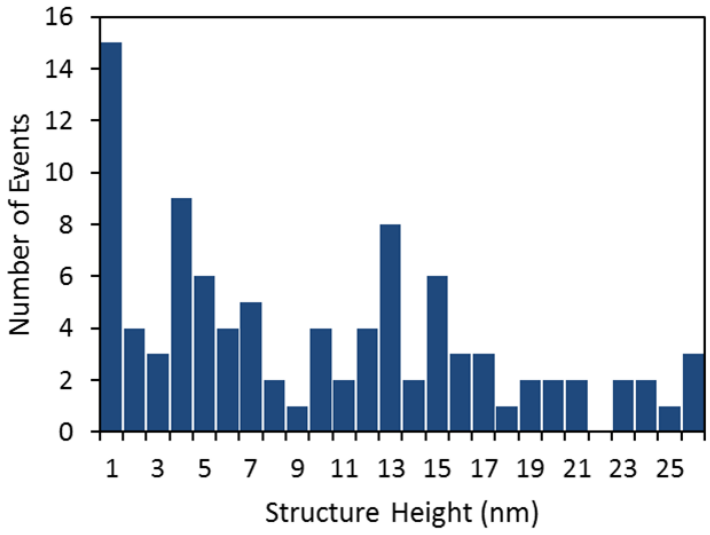

Figure 4-15: Histogram of the size (diameter) distribution of the of the DNA-templated Fe "nanowires".

4.3.6 Electrostatic force microscopy (EFM) studies of the DNA/Fe nanostructures

The electrical properties of the DNA-templated Fe nanostructures were qualitatively probed using the EFM method.[72, 80, 81] For EFM measurements, samples were prepared by transferring the reaction solution comprising DNA/Fe "nanowires" from the Si working electrode following electrochemical reduction process to a TMS-modified Si wafer with a thermally grown dielectric layer of SiO_2. The "nanowires" were subsequently aligned upon the substrate using a process based upon spin-coating methods as described earlier in this chapter, section 4.2.4.

EFM data recorded of the DNA-templated Fe "nanowires" are depicted in figure 4.16. The height image (figure 4.16a) shows two main "nanowires" with main diameters of 4.7 nm (left) and 12 nm (right), along with a number of structures with diameters of < 2

nm (denoted by yellow arrows). Such thinner structures are suggested to be bare DNA as their heights are consistent with the theoretical diameter of single DNA molecule (≤ 2 nm) measured by AFM.[109] Information relating to the electrical behaviour of such structures can be elucidated from the phase contrast associated with them in the phase images (figure 4.16b-e). Specifically, a negative/dark contrast is observed if the nanostructure is electrically conducting, whilst dielectric structures produce only positive/bright contrast.[72, 80, 81]

It is clear from the corresponding phase images (b, c, d and e) recorded with applied bias potentials of +7, -7, +5 and -5 V, respectively, that the two main DNA-templated Fe nanowires shown in the AFM height image correspond to the prominent negative/dark contrast seen in the phase images. This was found to be the case over the range of bias potentials used (between -7 V and +7 V), confirming that the structures are electrically conductive, *i.e.* the metal coatings provide a continuous electron conduction pathway.

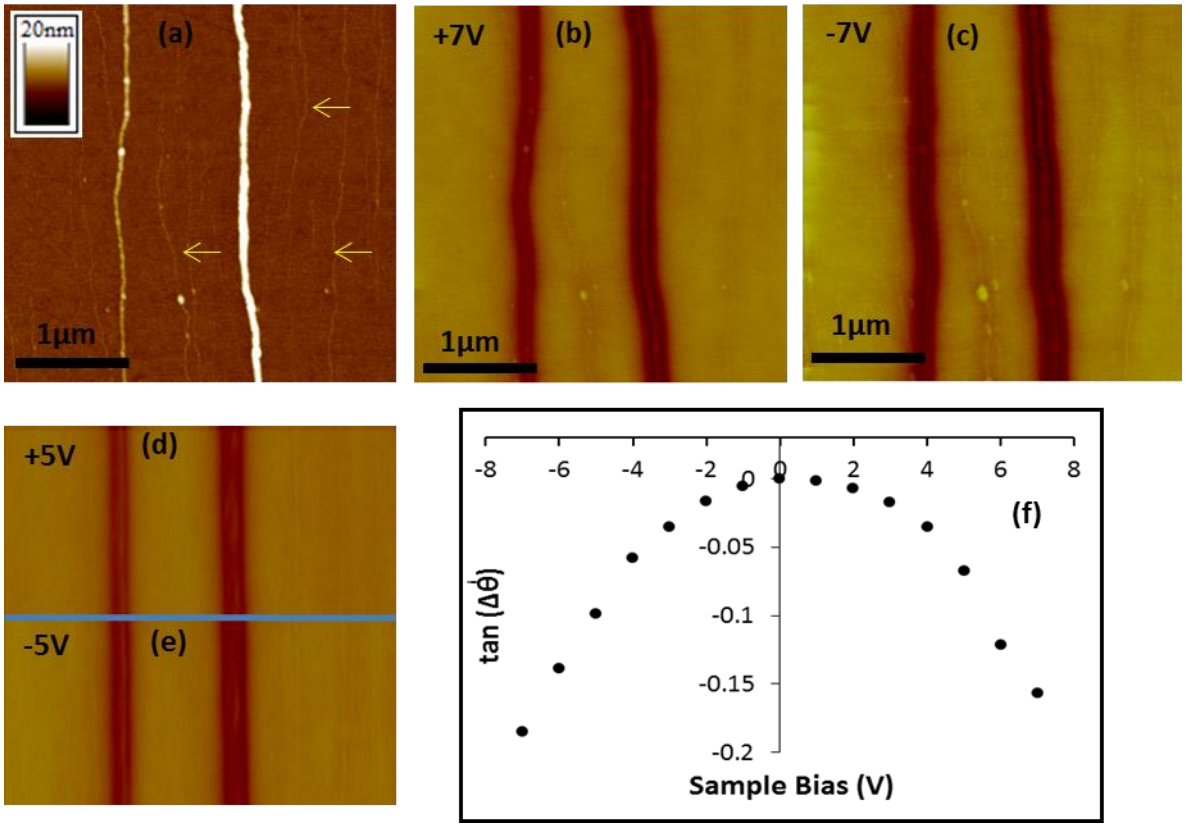

Figure 4-16: Electrostatic force microscopy (EFM) data of DNA-templated Fe nanowires aligned upon a Si/SiO_2 substrate. (a) AFM height image of two main nanowires with main diameters of 4.7 (left) and 12 nm (right), respectively, along with thinner structures (< 2 nm), which indicated by yellow arrows. (b, c, d and e) The corresponding EFM phase images of the nanowires featured in (a) at an applied bias potential of +7, -7, +5 and -5 V, respectively, phase scale of 20°. (f) Plot of the tangent of the nanowire phase shifts (measured from the 12 nm diameter wire) against the bias potential applied to the sample.

The magnitude of the phase shifts associated with the nanowires (relative to the substrate background) were dependent upon the applied bias, as can be seen by the parabolic trend displayed when plotting the tangent of the phase shifts as a function of the applied bias (Figure 4.16f). This relationship between the phase shifts and applied bias is characteristic of the probe–sample interactions is dominated by capacitance effects rather than electrostatic interactions, which are expected to show a linear relation.[81, 83-85] This confirmation that the phase shifts are predominantly influenced by the tip/substrate capacitance, rather the presence of static charges on the wire, verifies that the indicative of the conductive nature of the nanowire.[81]

4.3.7 Magnetic force microscopy (MFM) studies of the DNA-templated Fe nanowires

One of the best examples of a ferromagnetic material is metallic Fe^0 in its bulk form. However, magnetic properties are known to be size-dependent [139, 184], which can make nanomaterials display quite different magnetic behaviour relative to the corresponding bulk. An example of this is the transition from a bulk ferromagnetic to superparamagnetic behaviour when in nanoparticle form, where the particle volume is smaller than the size of a single magnetic domain.[139, 184] This change is because of the magnetic anisotropy energy is overcome by the thermal energy, and results in randomisation of the magnetic spin direction, leading to a net magnetisation of zero in the absence of any external magnetic field. Moreover, due to its high sensitivity towards anisotropic effects, the geometry of nanostructured materials also plays an important role in determining their magnetic character.[185, 186] Hence the nanostructured form in which a material is prepared (*e.g.* nanoparticles, nanowires/nanorods) can also dictate magnetic character. It was therefore of interest to probe the magnetic behaviour of the Fe structures produced here. In order to achieve this, magnetic force microscopy (MFM) was used.[106]

For MFM studies, samples were prepared using similar a method to that previously described for EFM studies, in which the nanowires were aligned upon a Si/SiO_2 substrate following the electrochemical reduction process. MFM measurements were then recorded at different tip-sample separations ranging from 10 to 110 nm. Figure 4.17b-g, shows a series of MFM phase images of a DNA-templated Fe nanowire recorded at a range of lift distance, along with the accompanying AFM height image (figure 4.17a). The height image displays a 17.4 nm diameter nanowire with branches

leading off the nanowire's main body. In the MFM phase images, when the lift height is increased, a dark contrast relative to the background was clearly observed to be associated with the main DNA/Fe nanowire. This indicates the Fe structure to exhibit a room temperature magnetic response to the probe.

In addition, the dark contrast indicates that the magnetic interaction between the probe and nanowire is an attractive one, *i.e.* the magnetic moments of the nanowire and probe are in alignment with one another. It should be noted that the magnitude of the produced negative phase shift is clearly seen to decrease gradually with the increasing tip-sample separation, becoming almost negligible at lift heights of > 90 nm. Plotting of the measured phase shift of the DNA/Fe nanowire as a function of the lift heights gives a logarithmic curve (Figure 4.17h), indicating that phase shifts decay regularly in response to the increase of the tip-sample distance. Additional evidence for confirming that the recorded signal in MFM scans is due to magnetic interactions between the magnetised probe and nanowire is provided by control experiments which carried out using non-magnetic Si probes. No phase signal was recorded from such control measurements, indicating that the previous phase signals observed must be a result of magnetic interactions between the magnetised probe and nanowire.

In order to establish the type of magnetic behaviour displayed by the nanowire, additional MFM experiments were performed in which the direction of the probe's magnetisation was reversed. If the Fe nanowire is ferromagnetic in character (as Fe is in its bulk form) reversing the direction of the probe's magnetisation would be expected to result in the phase signal inverting, *i.e.* changing from dark contrast to bright contrast, as any probe–nanowire interactions will now be repulsive. However, the dark phase contrast associated with the nanowire was found to persist regardless of the direction of the probe's magnetisation. This behaviour is consistent with the magnetic field of the AFM probe inducing alignment of the magnetic moments within the region of the nanowire over which the probe is positioned at any given time, indicating that the nanowire structure is composed of a series of superparamagnetic Fe particles packed along the DNA template.

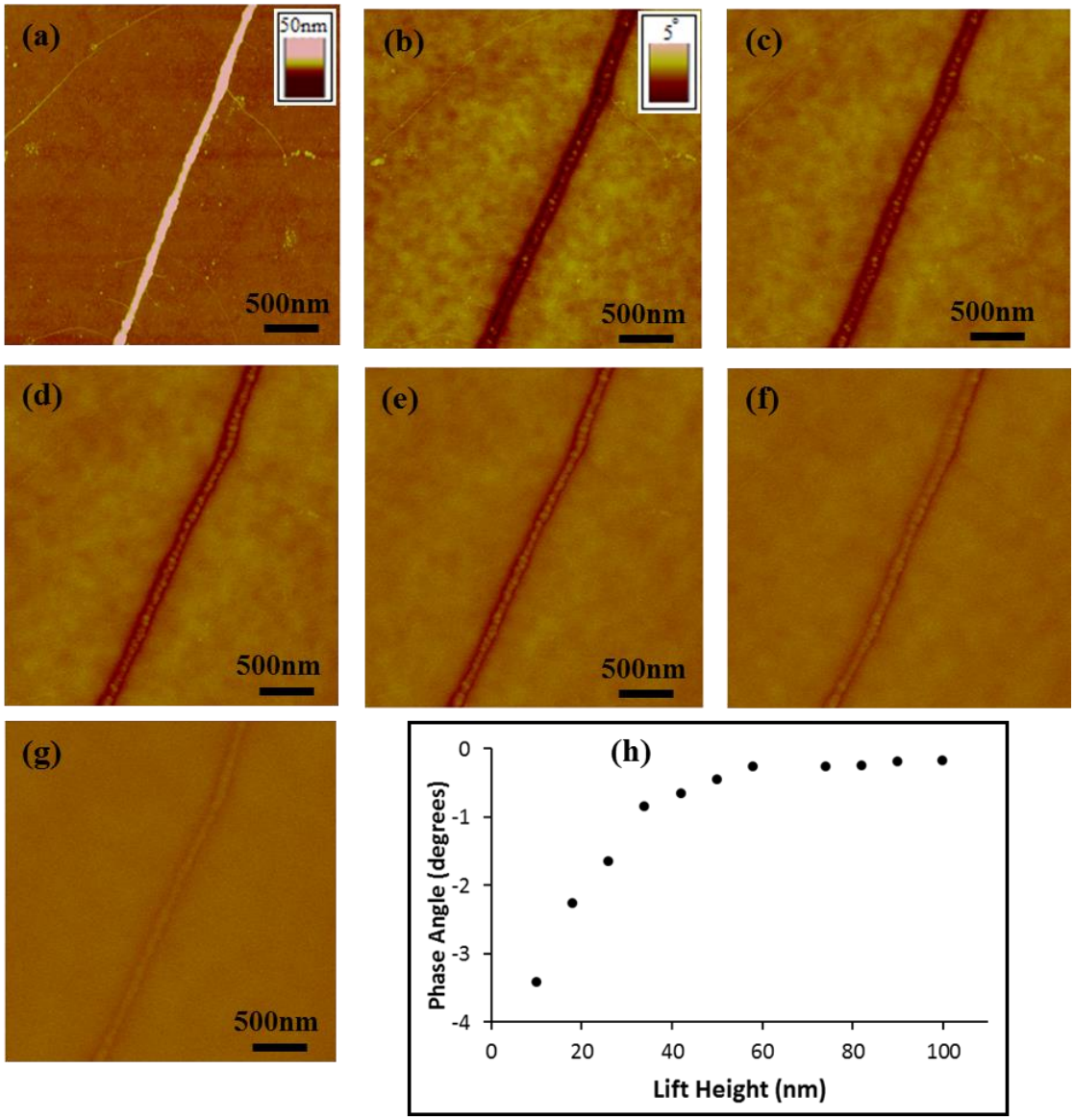

Figure 4-17: (a) AFM height image of a DNA-templated Fe nanowire supported upon a n-Si<100>/200 nm SiO_2 wafer, showing 17.4 nm diameter nanowire. The corresponding MFM phase images of the nanowire are shown, recorded at lift heights of (b)18 nm, (c) 26 nm, (d) 34 nm, (e) 32 nm, 50 nm (f) and (g) 50 nm, respectively. Phase scale in all MFM phase images is 5°. (h) Plot showing the magnitude of the measured nanowire phase shifts as a function of the lift height of the probe.

The proposed structure here is also supported by the morphology of the nanowires, *i.e.* linear arrangements of Fe nanoparticles, densely packed along the DNA. This finding is similar to the magnetic behaviour reported for DNA-templated magnetite (Fe_3O_4) nanowires, where superparamagnetism was displayed in contrast to the ferrimagnetism observed in the bulk phase.[106]

4.4 Conclusion

The preparation of Fe nanowires has been achieved for the first time using a DNA-templating approach in conjunction with electrochemical reduction. The chemical composition of the resulting DNA/Fe nanowires was determined by XRD and XPS to consist of a core-shell structure, where an oxide sheath encapsulates the Fe core. AFM data indicated that DNA templates directed the growth of the electrodeposited Fe material as organised 1D structure, with diameters of up to 26 nm. The metal coatings around the DNA stands are continuous and show granular character consisting of a linear arrangement of nanoparticles with uniform particle size. Furthermore, EFM and MFM studies were used to evaluate the electronic and magnetic properties of the resulting DNA/Fe nanowires, respectively, confirming them to be electrically conducting and to exhibit room temperature magnetism.

5. Chapter 5: Preparation and Characterization of DNA/Rh nanowires

5.1 Introduction

Nanoscale forms of transition metals are expected to show new and unique chemical and physical properties distinct from the equivalent bulk material.[187] For instance, the magnetic properties of metals are known to be dramatically altered when scaling the material down to the nanoscale.[188] For rhodium the bulk form is non-magnetic, but magnetic behaviour can be displayed in low-dimensional systems.[188-190] Rhodium is one of transition metals which already has many industrial applications, and the development of stable low-dimensional forms of this metal, may extend its use to further.[191] For instance, Rh nanoparticles have already demonstrated their possible applications, as a catalyst in C-C coupling reactions.[192]

Well-dispersed Rh nanoparticles in the size range 2-8 nm, have been synthesised on carbon nanotubes (CNTs) using a simple one-step sonochemical method.[193] In this work, the preparation of CNT-supported metallic Rh nanoparticles was achieved through the addition of an aqueous solution of $RhCl_3$ and boron-containing reducing agent to an ethanol solution containing carboxylate functionalized multiwalled carbon nanotubes (MWNTs). This method produced well-dispersed Rh nanoparticles of different size which are uniformly attached to the surface of the MWNTs.

Rh nanoparticles were also prepared on one-dimensional titania nanostructures.[194] In this instance, titanate nanowires and nanotubes were impregnated with a solution of $RhCl_3$. The Rh nanoparticles on the titania nanostructures were characterised by XPS, SEM and FT-IR spectroscopy, which confirmed the formation of metallic Rh nanoparticles on the surface of nanowires and nanotubes.

There are rather few examples of 1-D nanoscale Rh reported in the literature. Fukuoka, *et al.,* [187] for example, used organic-inorganic hybrid mesoporous materials (HMM) as a template to prepare metallic nanowires which included rhodium. In this instance the Rh nanowires were formed via photoreduction of the $RhCl_3.3H_2O$ inside the mesoporous medium (HMM-1) and had a bead-on-a-string morphology. Moreover, Rh nanowires have also prepared by using an anodic aluminum oxide (AAO) as a template. Here, electrodeposition of metal from Rh plating solution inside the AAO template

produced Rh nanowires with diameter ~ 300 nm. The length of nanowires can be controlled by varying electrodeposition time, and the nanowires were extracted by dissolving the template in a 3.0 M NaOH solution.[195]

Although metallic Ag [18], Pd [64, 143], Pt [196] and Cu [65, 66], nanowires have all previously been fabricated through chemical reduction of the DNA-bound metal ions, to the best of our knowledge, no work has been reported to date on preparation of Rh-based nanowires using DNA as a template.

In this chapter, the preparation of Rh nanowires using the DNA-templating approach in conjunction with either chemical or electrochemical reduction is described. Rh nanowires were prepared through chemical reduction of Rh^{3+}, using $NaBH_4$ in the presence of DNA. The preparation of DNA/Rh nanowires through electrochemical reduction method is also described. In this method, cyclic voltammetry measurements were applied upon a droplet of DNA/Rh^{3+} systems deposited on TMS-modified Si (n-100) wafer which acts as working electrode during electrochemical reduction process. Chemical characterisation of the product material using XRD and XPS techniques is then described. This is followed by interpretation of the AFM (to investigate the structural character of the nanowires), EFM and c-AFM (to investigate the electrical properties) and MFM studies to probe the magnetic behaviour of the nanowires. Finally, the main findings in both preparation methods were summarised.

5.2 Experimental section

5.2.1 Materials

Rhodium(III) chloride hydrate ($RhCl_3.xH_2O$) (Rh 38.40 %) and calf thymus DNA (CT-DNA) (highly polymerised, 6 % sodium), were purchased from Sigma-Aldrich Company Ltd. (Gillingham, Dorset, UK) and used as received. Lambda DNA (λ-DNA, Cat. No. N3011S) was purchased from New England Biolabs UK Ltd. (Hitchin, Hertfordshire, UK). Sodium borohydride ($NaBH_4$, 98%) was purchased from Alfa Aesar.

Si<n-100> wafers (phosphorous doped, 525±50 μm thickness, 1–10 Ω·cm resistance, single side polished), were used as substrate supports for TappingMode™ AFM imaging. Si<n-100> wafers with a 200nm thick, thermally grown SiO_2 layer on top (arsenic doped, 500±25 μm, <0.005 Ω cm resistance, thermal oxide layer 200 nm±10%

thickness, double side polished) were used in scanned conductance microscopy and magnetic force microscopy experiments. All Si wafers were purchased from Compart Technology Ltd. (Peterborough, Cambridgeshire, UK). NANOpure® deionised water (18 MΩ cm resistivity) was obtained from a NANOpure® DIamondTM Life Science ultrapure water system equipped with a DIamondTM RO Reverse Osmosis System (Barnstead International).

5.2.2 Large-scale preparation of DNA/Rh material using chemical reduction method

Samples for XRD and XPS studies were prepared through addition of 10 mL of an aqueous solution of $RhCl_3.xH_2O$ (2.5 mM) to 5 mL of a solution of CT-DNA (500 μg mL^{-1}). The mixture was left to stand for approximately 10 days at room temperature, before adding a freshly prepared $NaBH_4$ (10 mL; 25 mM) solution in water. The reaction solution turned brownish-black in colour and the resulting colloidal solution was then centrifuged and concentrated in order to extract the DNA/Rh final material. The collected black powder was allowed to dry at room temperature prior to X-ray diffraction (XRD) analysis.

The sample material for X-ray photoelectron spectroscopy (XPS) was deposited from the colloidal solution onto a piranha-cleaned Si<n-100> wafer and allowed to dry at room temperature.

5.2.3 Preparation of λ-DNA/Rh samples using chemical reduction method

5 μL of an aqueous solution of λ-DNA (500 μg mL^{-1}) was mixed with 10 μL of an aqueous solution of $RhCl_3.xH_2O$ (2.5 mM), and incubated for 10 days at room temperature. Then, a freshly prepared $NaBH_4$ (10 μL; 25 mM) solution in water was added. The resulting DNA-templated rhodium nanostructures formed in the reaction solution was allowed to stand for further 10 min before being aligned on the TMS-modified Si<n-100> or Si<n-100>/200 nm SiO_2 wafers for AFM and EFM/MFM measurements, respectively. For nanowires alignment, 5 μL of the DNA/Rh solution was applied to a TMS-modified wafer (TMS modification was carried out similar to what was descried previously, see chapter 3, section 3.2.2) whilst being spun at 125 rpm. The wafer was then spun for a further 2 minutes at 250 rpm before the residual solution was withdrawn from the surface by a micropipette. Finally, nanowires-

modified wafer was left to dry at room temperature before performing scanning probe microscopy measurements.

5.2.4 Large-scale preparation of DNA/Rh material using an electrochemical reduction method

For XPS studies, it is important to produce sufficient materials for meaningful spectroscopic data to be recorded. For this, 40 µL of an aqueous solution of $RhCl_3.xH_2O$ (2.5 mM) was mixed with 20 µL of an aqueous solution of CT-DNA (500 µg mL^{-1}) and incubated for 10 days at room temperature. Then, 40 µL of the reaction solution was applied to a chemically oxidized Si<n-100> substrate modified with a TMS SAM as descried previously in chapter 3, section 3.2.2. The modified Si substrate was used as the working electrode during the electrochemical reduction process, while the counter and reference electrodes were a tungsten wire with diameter of 0.25 mm, and Ag/AgCl, respectively. The hydrophobic nature of the modified Si substrate results in 'beading' of the deposited DNA/Rh^{+3} solution enabling the counter and reference electrodes to be easily inserted into the solution droplet without contacting the substrate surface.

Cyclic voltammetry measurements were performed using a computer-interfaced SECM CHI 900 electrochemical microscope system (CH Instruments, Austin, Texas, USA), sweeping the potential between E = 0.3 V and E = –0.3 V, with a scan rate of v = 0.1 Vs^{-1}, quiet time, t = 2.0 seconds, and sweep segments = 2.

After completion of the electrochemical reduction, the reaction solution was removed from the Si working electrode by micropipette and transferred to a fresh TMS-modified Si<p-100> substrate. The solvent was allowed to evaporating at room temperature in order to produce a thin film of the product materials for XPS analysis.

5.2.5 Preparation of λ-DNA/Rh samples using an electrochemical reduction method

For the AFM, EFM and MFM measurements, DNA/Rh samples were prepared using λ-DNA. Here, samples were prepared by mixing 10 µL of an aqueous solution of $RhCl_3.xH_2O$ (2.5 mM) and 5 µL of an aqueous solution λ-DNA (500 µg mL^{-1}). The resulting DNA/Rh^{3+} solution system was allowed to stand for 10 days at room temperature before performing any electrochemical reduction process. Cyclic voltammetry measurements were subsequently carried out upon a 5 µL of the

DNA/Rh^{3+} solution system deposited on Si working electrode, in the same manner as previously described in section 5.2.4.

Following the CV measurements, the resulting DNA/Rh nanowires in the reaction solution were transferred by micropipette into a new TMS-modified n-Si<100> wafer, and then aligned upon it using a process based upon spin-coating methods as described in section 5.2.3.

5.3 Results and Discussion of DNA/Rh materials prepared using chemical reduction method

Preparation of the conducting 1D nanostructures of metallic Rh^0 material was attempted using DNA as a template to direct the anisotropic growth of the material (figure 5.1).

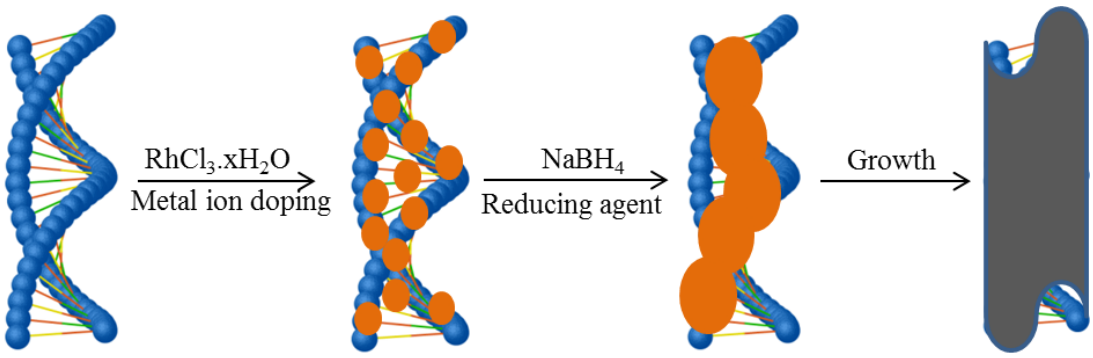

Figure 5-1: Scheme presenting the chemical reduction method used for the preparation of the DNA-templated Rh nanowires.

For this, chemical reduction of DNA-bound Rh^{3+} ions using $NaBH_4$ as a reducing agent was carried out in an aqueous solution containing $RhCl_3.xH_2O$ and DNA molecules. In this preparation method, mixing of DNA with Rh^{3+} species is carried out as first step, in order to allow the metal cations to associate with the duplex DNA through metal-ligand complex formation (DNA/Rh^{3+}). The DNA/Rh^{3+} binding have previously reported to take place at both of phosphate backbone and aromatic bases.[197, 198] Here, FTIR studies (appendix C.1), indicated that Rh^{3+} cations are associated with the DNA structure via interactions with the nucleobases and phosphate backbone. The DNA/metal ion complex formation plays a key factor in organizing the growth of zerovalent Rh(0) formed upon addition of $NaBH_4$, as 1D nanostructures.

However, as the reduction of Rh^{3+} in an aqueous solution under ambient condition may result in the formation of a mixture of Rh^0 and rhodium oxides, it was important to

elucidate the chemical composition of the produced material. In order to address this, characterisation of the product material was carried out by powder XRD and XPS methods.

5.3.1 Powder X-ray diffraction studies

In order to confirm the formation of metallic rhodium material and estimate its crystallite size, powder X-ray diffraction (XRD) studies were carried out. The XRD pattern (figure 5.2) obtained from the product material showed three prominent peaks at 2θ values of 41.06°, 45.07° and 69.24°. These peaks can be indexed to the (111), (200) and (220) reflections of the metallic Rh^0, respectively, and are well-matched with the values previously reported for rhodium nanoparticles.[199-202]

It can also be noted that the diffraction peaks in the XRD data appear broadened, indicating that the prepared Rh associated with the DNA templates are nanocrystalline in nature.[203] With the use of line broadening of the diffraction peaks (β) of 2.67° (defined from the full-width-at-half-maximum of the (111) reflection), the average crystalline size was estimated using Scherrer's equation to be 3 nm. It is also worth mentioning that, according to XRD finding no further peaks were observed, indicating that metallic Rh^0 nanostructures have successfully formed in high purity under the method used.

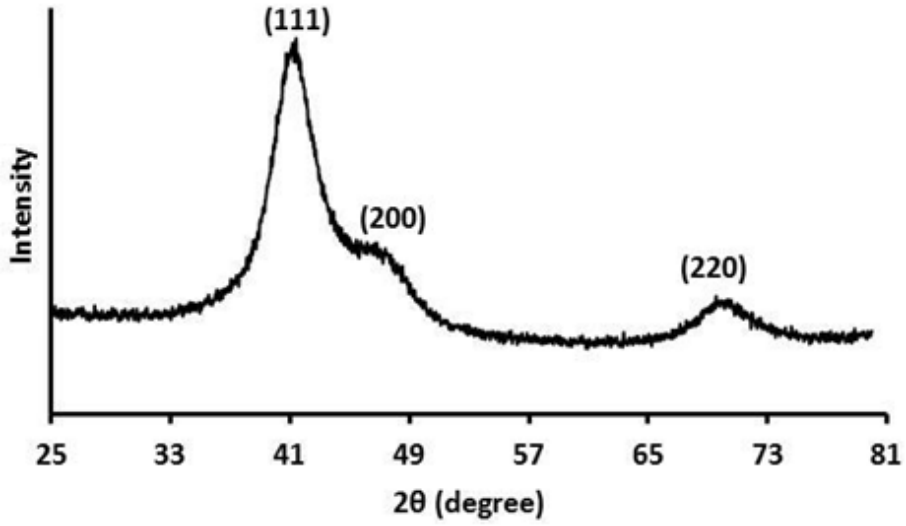

Figure 5-2: XRD pattern obtained from a powder sample of DNA-templated Rh material.

However, although XRD confirms the product material to consist primarily of Rh^0, one may still expect the metal to be susceptible to oxidation upon exposure to ambient

conditions, i.e. formation of an oxide coating at the surface of the Rh^0 may form which is beyond the detection limits of XRD. Therefore, X-ray photoelectron spectroscopy (XPS) has also been used to establish the presence of any oxide species at the surface of the prepared material.

5.3.2 X-ray photoelectron spectroscopy (XPS) studies

The XPS survey spectrum of the DNA/Rh sample (figure 5.3) displays peaks arising from both DNA and rhodium materials. The O1s, N1s, C1s and P2p signals can be attributed to the presence of DNA in the sample, whereas Rh3d and Rh3p peaks are from the template metal material present. Additional peaks can also be identified arising from, Na2s, likely due to $NaBH_4$, used as the reducing agent in the reaction and Cl2p peak which is most likely to originate from the $RhCl_3.xH_2O$ start material.

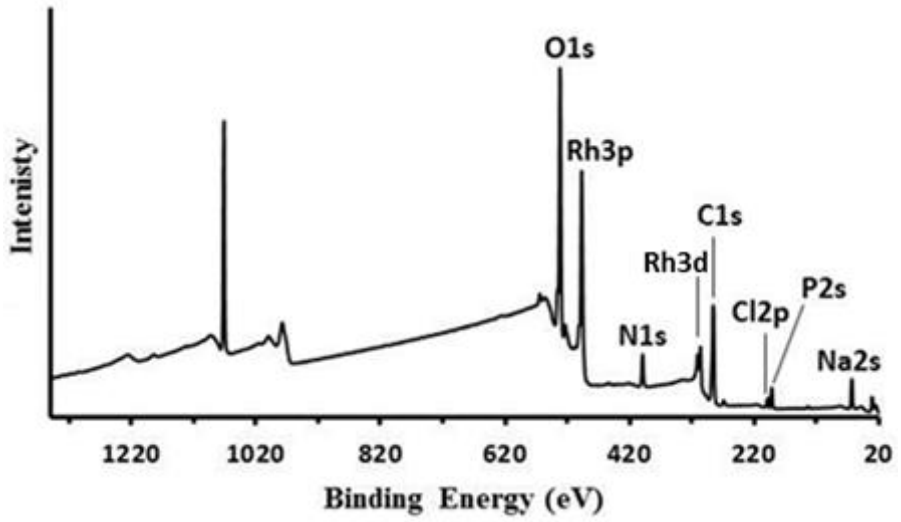

Figure 5-3: XPS survey spectrum of calf thymus DNA-templated Rh nanowires deposited upon a Si/native SiO_2 substrate.

The high resolution N1s region spectrum (figure 5.4), provides evidence for the presence of DNA in the product. Curve fitting of the N1s region is consistent with two peaks at 399.4 and 400.6 eV. The most intense peak is at lower binding energy, and can attributed to sp^2-bonded N atoms in the aromatic rings, whereas the peak at higher binding energy is consistent with sp^3-bonded N atoms present exocyclic amino group ($-NH_2$).[119-121]

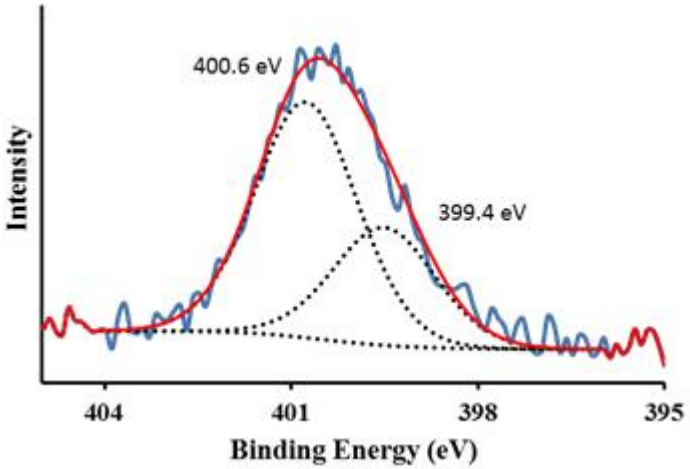

Figure 5-4: High resolution XPS spectrum of N1s region of calf thymus DNA-templated Rh nanowires immobilised upon a Si/native SiO_2 substrate. Blue solid line with dots represents raw data, total fits is represented by red line and black dashed lines is for component peaks.

Figure 5.5 illustrates the XPS spectra of Rh3d region of the DNA/Rh sample. Two sets of doublets peaks ($Rh3d_{5/2}$ and $Rh3d_{3/2}$) can be identified upon curve fitting of Rh3d region, indicating that the product material contains rhodium in two different chemical states. The dominant doublet peaks are found with a binding energy of $3d_{5/2}$ = 306.1 eV; $3d_{3/2}$ = 310.8 eV, which falls in reasonable agreement with previous values for this element.[193, 203-209] The doublet separation value is also in good agreement with the $3d_{3/2}$-$3d_{5/2}$ splitting value of the standard Rh metal.[207, 210] The minor doublet peak is found at higher binding energy ($3d_{5/2}$, 308.3; $3d_{3/2}$, 313.1 eV) and is indicative of the presence of rhodium oxide (Rh_2O_3) in the sample material.[204, 211]

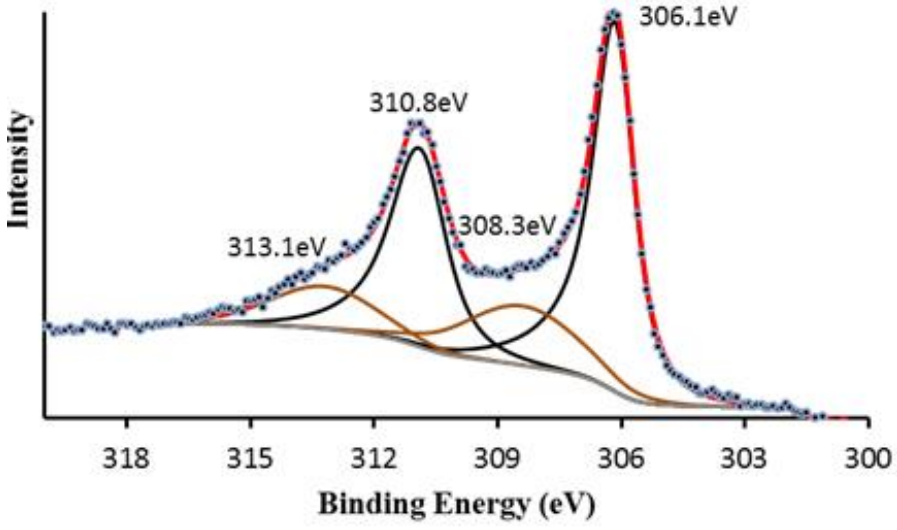

Figure 5-5: High resolution XPS spectrum of Rh3d region of calf thymus DNA-templated Rh nanowires immobilised upon a Si/native SiO_2 substrate. Black dots represent raw data, total fits is represented by red solid line and black and brown solid lines are for component peaks.

A simple approach has been used for curve fitting of the O1s region, in which minimum of three components are required in order to accurately reproduce the shape of the O1s spectra, see figure 5.6. The component at highest binding energy (532.6 eV) may be due to the oxygen atoms in the DNA phosphate groups.[119, 122] The second feature at binding energy of 531 eV can be assigned to oxygen atoms present in the sugar and nucleobase units of the DNA.[119, 122] A contribution from the SiO_2 substrate to the spectrum within the region of these first two components may also be present. The final component with lowest intensity is at 529.5 eV and can be assigned to the oxygen in the rhodium oxide (Rh_2O_3) [204], which provide further evidence for the presence of oxide layer of Rh_2O_3 in the product material.

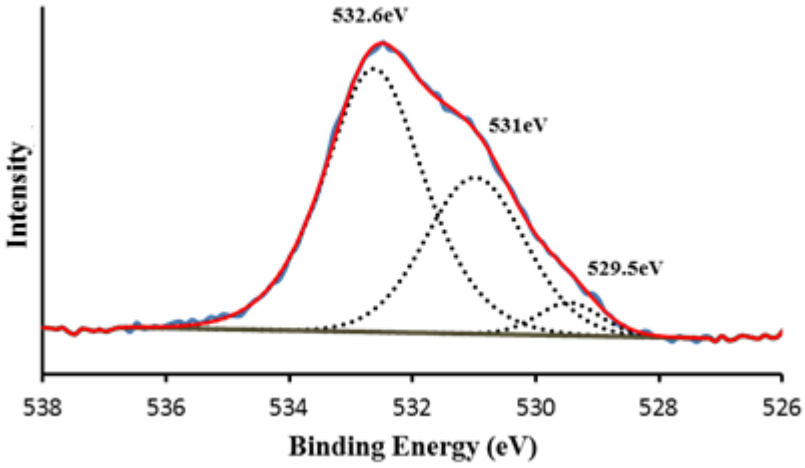

Figure 5-6: High resolution XPS spectrum of O1s region of calf thymus DNA-templated Rh nanowires immobilised upon a Si/native SiO_2 substrate. Blue dots represents raw data, total fits is represented by red solid line and black dashed lines is for component peaks.

The results of the XPS studies show that both rhodium metal and rhodium oxide are present in the product material. However, the XRD pattern, showed only a pure metallic Rh^0 peaks and no rhodium oxide peaks were observed. Therefore, it can be concluded that Rh/DNA nanostructures consist of a core-shell structure comprised of a thin layer of Rh_2O_3 encasing the metal Rh core.

5.3.3 Atomic force microscopy (AFM) characterisation of DNA/Rh nanostructures

AFM studies were carried out upon samples of DNA/Rh nanostructures in order to evaluate their morphology. Prior to the alignment of DNA/Rh materials from the reaction solution upon Si/SiO_2 substrates for AFM imaging, the substrate was modified with a trimethylsilane (TMS) self-assembly monolayer. This step is an essential

preliminary step to increase the hydrophobic character of the silicon substrate. For modification, contact angle values of ~71˚ were typically achieved. Hydrophobic surfaces of this nature allow nanowires to be stretched and aligned upon the substrate surface via molecular combing methods [133, 134], in sufficient density to allow individual structures to be probed by AFM.

Figure 5.7 shows AFM height images of some typical examples of the DNA/Rh nanostructures fabricated using the chemical reduction method. These images reveal the 1-D nanowire-like structure of the produced DNA/Rh material, indicating the effectiveness of DNA as a template to direct the growth of the Rh materials into organised 1-D nanostructure. The resulting structures were found to range in diameter from 3-31 nm, and thickening of these structures is clearly evident relative to the DNA itself (≤ 2) [135], demonstrating that the Rh is successfully deposited upon DNA.

The DNA/Rh nanostructures are observed to show uniform morphologies with the DNA templates coated with continuous coverage of Rh materials along the length of their structure. The uniformity of these DNA/Rh nanostructures present a significant improvement to that observed for other metal nanowires e.g. Ag [18], Pd [64, 143], Pt [196] and Cu [65, 66], prepared through chemical reduction of the DNA-bound metal cations. For example, AFM studies of Ag^0 nanowires prepared using chemical reduction of DNA-bound Ag^+ ions with a basic solution of hydroquinone revealed them to exhibit a granular morphology with diameters ranging from 30 to 50 nm (figure 5.7f).[18] The granular character associated with the Ag^0 coating was suggested to be due to the growth of metal upon the DNA template via a “nucleation and growth” mechanism.

Upon closer inspection of the DNA/Rh structures, a small degree of granular appearance associated with the Rh coatings can also be identified, see Figure 5.8b (inset) and structure indicated by black arrow in figure 5.7d. This indicates that these structures result from may be a series of nucleation and growth steps.[143] Further supporting evidence for such growth mechanism was also provided by a small number of DNA/Rh structures which displayed irregular and incomplete coverage of the DNA template by the Rh material; see (figure 5.7d and e). In figure 5.7d, structures denoted by yellow arrows display bead-on-a-string structures with a very thin, irregular Rh coating, and figure 5.7e shows also bead-on-a-string structure with very low density of Rh material at DNA stand.

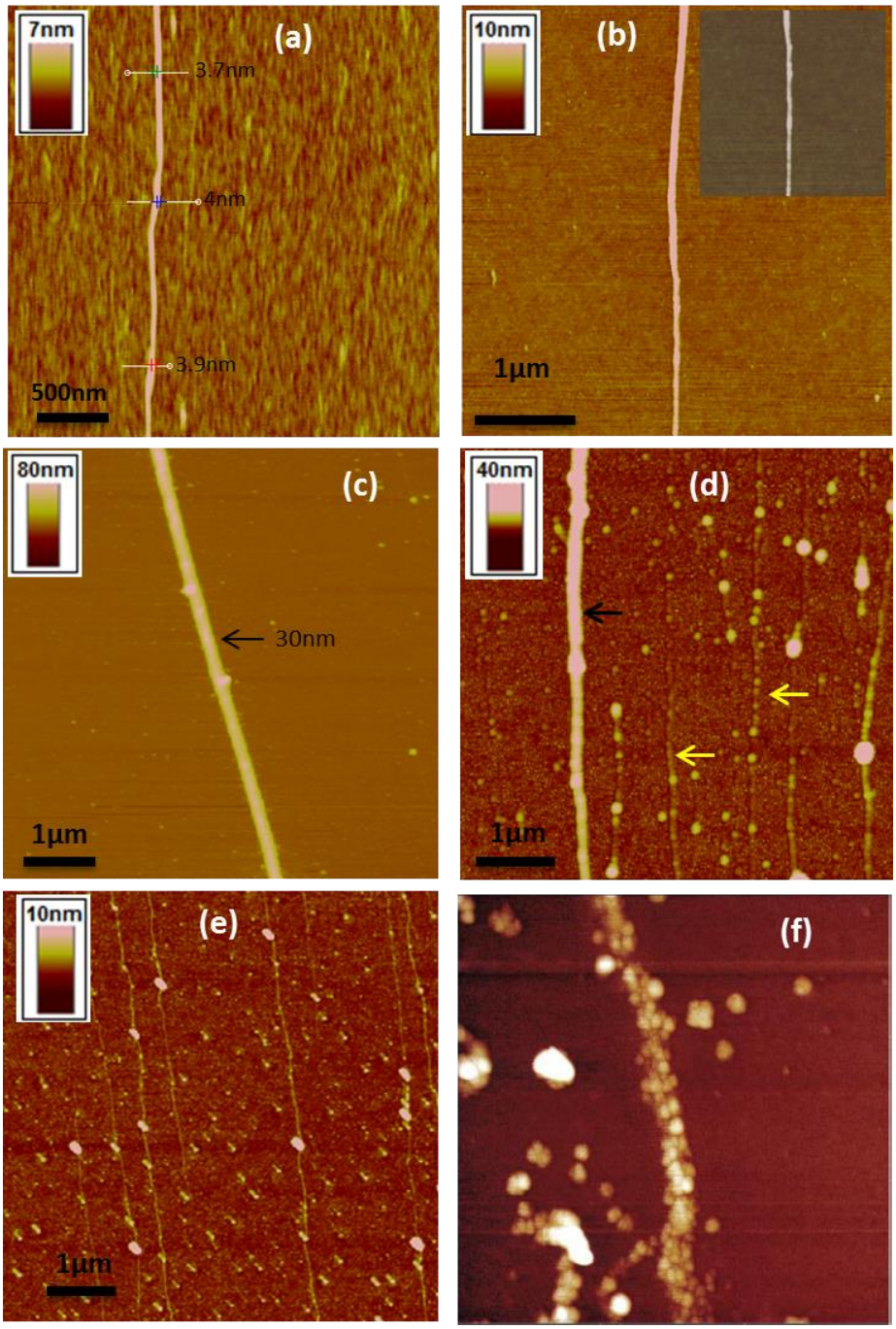

Figure 5-7: Selected TappingMode AFM images of the DNA/Rh "nanowires" immobilised upon a Si/native SiO_2 substrate. (a) AFM image shows a nanostructure with average diameter of 3.8 nm and relatively granular character of the Rh material coverage. (b) This image represents nanostructure with different packing density of the Rh material along the length of DNA template, a zoomed-in region (inset) of "nanowire" with the image contrast adjusted to show the granular character of the Rh material coverage. (c) AFM image shows thicker structure with diameter of 30 nm. (d) AFM image display structure with granular character of the Rh material coverage (black arrow), along with some DNA strands with a very thin, irregular Rh coating (yellow arrows). (e) Chains of λ-DNA molecules with very low intensity of metal nanoparticles, representing earlier stage of nanowires formation, where the metal growth has not reaches maturity during the reaction period. (f) AFM image of a silver nanowire with granular structure bridging two gold electrodes.[18]

In general, these structures can provide information regarding the growth mechanism by which DNA/Rh structures were formed. Formation of the Rh material on the DNA is suggested to take place through the DNA being doped with Rh^{3+} ions upon exposure to $RhCl_3$ solution. The Rh ions associated with the DNA structure are then converted to metallic Rh^0 nanoparticles upon addition of $NaBH_4$. These nanoparticles can then act as sites for further growth to take place. Therefore, the early stages of DNA-templated Rh formation are expected to yield a series of discrete nanoparticles of Rh along the DNA templates, as is observed in Figure 5.7e. Over time, further growth of the Rh particles leads to a continuous coating encapsulating the whole DNA molecule (figure 5.7a, b and c).

However, although the DNA/Rh nanostructures prepared using chemical reduction, were found to show constant diameter along the whole length of any single nanostructure, a great variation of structure heights (3-31 nm) was also observed by AFM studies. For evaluating the size distribution of the structure heights of the prepared DNA/Rh nanostructures, a statistical analysis of the average diameters was applied upon > 100 metallized DNA molecules. The structure heights were measured using AFM line profile measurements of randomly selected nanostructures. A histogram of the nanowire diameters (figure 5.8) shows moderately wide size distributions (2-31 nm) with modal value of 6 nm identified from the statistical analysis.

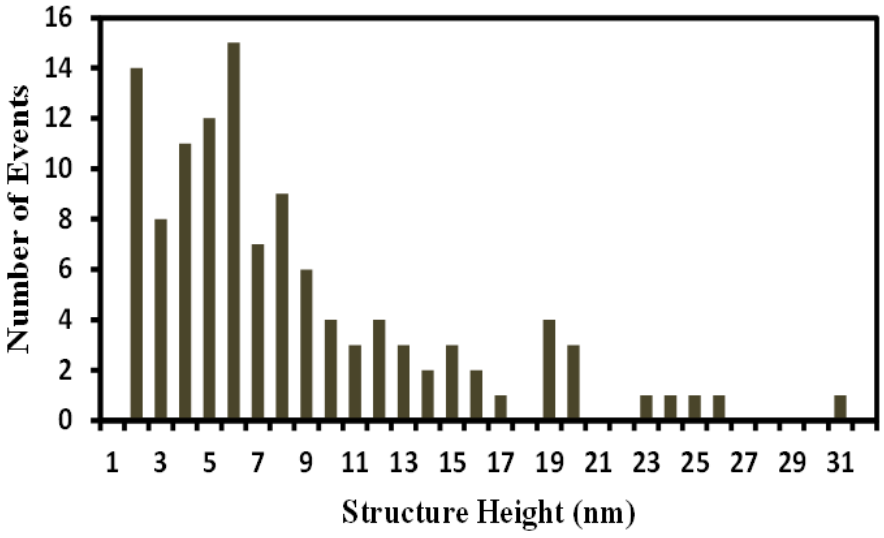

Figure 5-8: Histogram of the size distribution of the DNA/Rh "nanowires".

5.3.4 Electrical characterization of DNA/Rh "nanowires" using electrostatic force microscopy (EFM) investigation

For the investigation of the electrical conductivity of the prepared DNA/Rh "nanowires", initially EFM [80, 81] was used to qualitatively probe their electrical behaviour. For these measurements, the DNA/Rh "nanowires" were aligned upon a silicon substrate coated with dielectric layer of SiO_2. Samples can then be probed using a metal-coated, conductive AFM tip, whilst a direct current (dc) bias is applied to the substrate.

During the EFM measurements, the first scan of the tip is carried out in TappingMode to acquire topographical data regarding the sample. In the second pass (lift mode) the tip is lifted and maintained at 60 nm above the sample surface where the dominant tip-sample interactions arise from the long-range electrostatic forces. Figure 5.9 illustrate the height image (figure 5.9a) along with the corresponding EFM phase images (figure 5.9b-e). The height image showed a 1D nanostructure of DNA/Rh material with average diameter of ~ 9 nm. The corresponding EFM phase images were recorded at different dc potentials typically between +7 and -7 V volts. These showed a uniform dark line across regions of the substrate surface, which correspond to the position of the aligned DNA/Rh nanostructure. The appearance of such dark contrast (negative phase shift), regardless of the magnitude or sign of the applied bias, indicates DNA/Rh nanostructure to be electrically conductive.[16, 73, 212]

Additionally, the magnitude of the phase shifts showed a parabolic dependence upon the dc bias applied to the sample, see Figure 5.9f. These observations confirm that capacitance effects dominate the tip-sample interactions and trapped charge makes no significant contribution to data.[72, 73] It also of worth noting here that the negative phase shift characteristic to the conducting 1-D structures associated with the whole structure of the DNA/Rh nanowire, suggests that the produced nanowires comprise an essentially continuous nanoscale coverage of metallic Rh material around DNA templates and the structures can be considered as genuine nanowires.

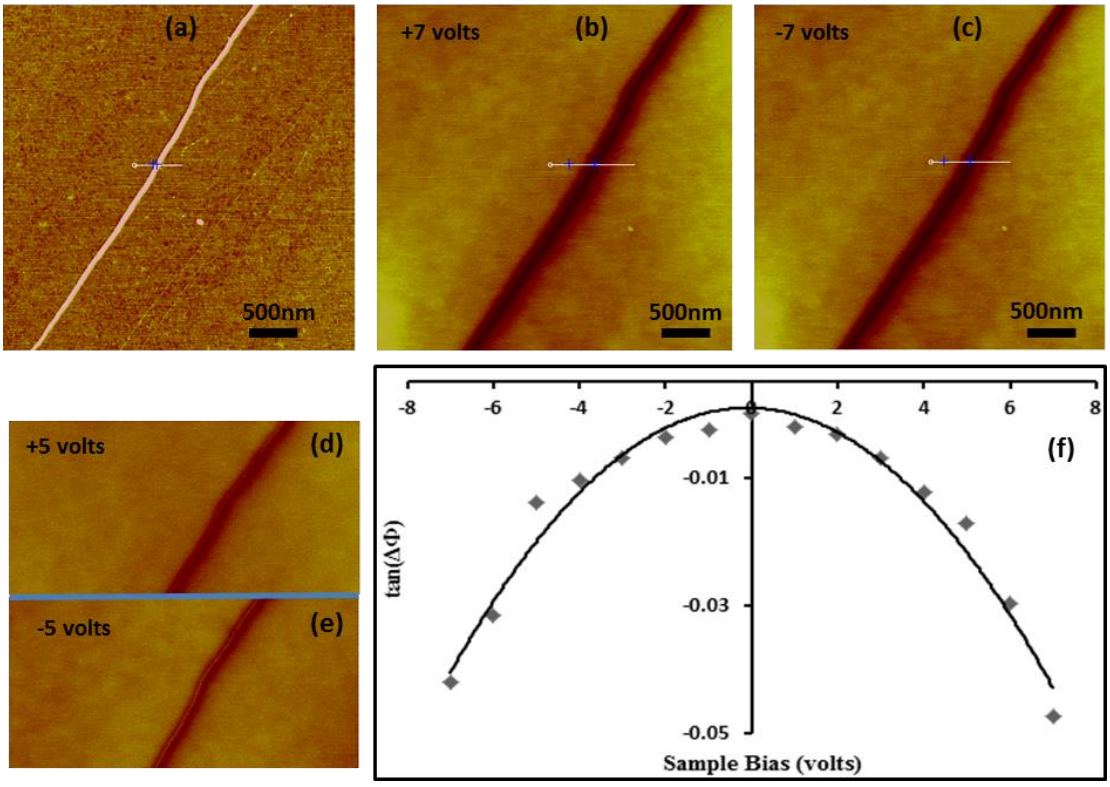

Figure 5-9: Electrostatic force microscopy (EFM) studies of DNA/Rh nanowire aligned upon a Si/SiO_2 substrate. (a) AFM height image of a nanowire with structure height of 9 nm, height scan is 7 nm. (b, c, d and e) the corresponding EFM phase images of the nanowire in (a) at different sample biases, phase scale of 4°. (f) Plot of the tangent of the nanowire phase shift as a function of applied voltage.

Although, the EFM technique has successfully used to demonstrate that the DNA/Rh nanowires are conductive, it is not possible so far to determine a quantitative value for the nanowire conductivity with the use of this non-contact technique. For this reason, and in order to obtain quantitative information relating to the electrical properties of single DNA/Rh nanowire, conductive AFM (c-AFM) technique has also been used.

5.3.5 Conductive atomic force microscopy (c-AFM) studies

This technique is a useful method for investigating the DNA/Rh nanowires electrical properties taking advantage from the c-AFM measurements as only one electric contact needs to be fabricated. Prior to the c-AFM measurements, an experimental set-up was devised which allows for the two electrical contacts to be made to the nanowire under investigation in a relatively straight forward manner.[16, 73, 213] This was achieved through applying 5µl of a DNA/Rh solution onto the edge of a TMS-modified silicon substrate with dielectric layer of SiO_2 and allowing it to stand at room temperature for ~1 min. Subsequent withdrawal of the solution sample (approximately 3 µm) result in a

dense network of nanowires on the surface with individual wires protruding out from the periphery of the network. The network acts effectively, as one electrode and electrical contact is made from this network to the sample chuck using Ga/In eutectic. As normal with c-AFM the other contact was provided by the metallic of the AFM tip which was located on the selected DNA/Rh nanowire extending from periphery of the dense body mass as shown in figure 5.10a.

With the use of such procedures, c-AFM measurements can be performed to detect electrical currents passing through the nanowire. Figure 5.10b and c illustrate an example of the c-AFM data recorded for a DNA/Rh nanowire. The contact mode AFM image (figure 5.10b) shows a 1-D structure with average diameter of approximately 40 nm. The corresponding current map (figure 5.10c), shows bright contrast relative to background, which appears only where the nanowire is located on the substrate. This indicates current flow through the DNA/Rh nanowire, confirming it to be electrically conducting.

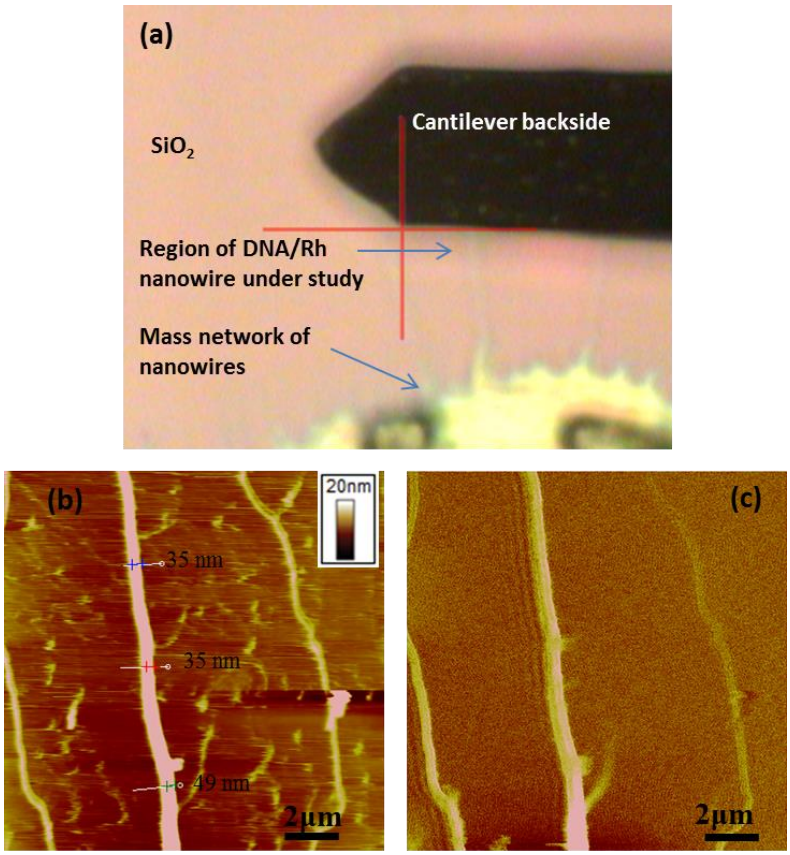

Figure 5-10: (a) Optical image of AFM cantilever with metallic tip positioned on a selected DNA/Rh nanowire. (b and c) C-AFM measurements of the DNA/Rh nanowires aligned upon a Si/SiO_2 substrate. (b) A contact mode AFM image. (c) Current map image recorded at 0.5V tip-sample bias and the data scale corresponds to a current of 100 nA.

After completing the image scan, the closed loop system of the Nanoscope V allows for the AFM tip to be brought into contact with the nanowire at specific points along the wire length and i-V measurements were recorded over the range of -5 to +5 V. The conductance was estimated from the slope of the i-V curve at zero bias and the resistance was then plotted against the relative distance of the cantilever along the nanowire in a direction away from the network (figure 5.11).

It is known that the circuit resistance obtained from c-AFM measurements is equal to the sum of the tip-nanowire contact (R_{tip}) resistance, the resistance between the external circuit and nanowire (R_{ext}), and the resistance of the nanowire portion located between the tip and the dense material deposited on the substrate (R_{wire}).[73, 213] As it can be seen, the circuit resistance approximately increases as the relative distance is increased (figure 5.11). This is because the electric current travels a longer distance through the nanowires, thus increasing the resistance in the circuit. The resistance of DNA/Rh nanowires per unit length was calculated from the slope to be $2x10^{11}$ Ω cm^{-1}.

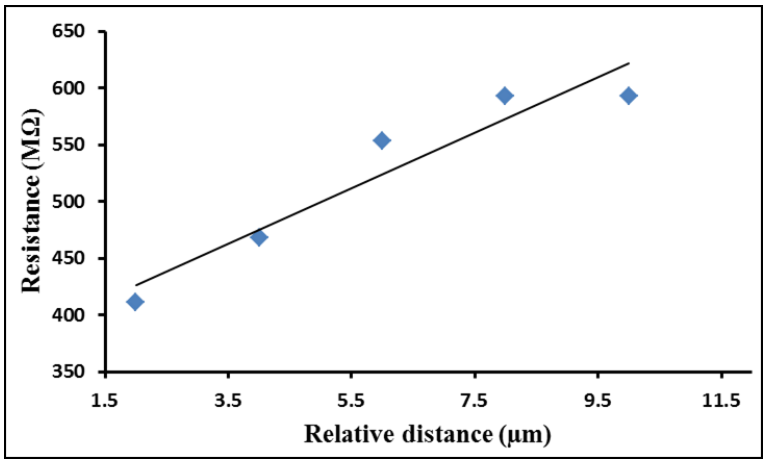

Figure 5-11: Resistance of DNA/Rh nanowires as a function of relative distance at deflection set-point of 0.5V.

Moreover, in order to estimate the nanowire resistivity, the cross-section area (assumed elliptical) was calculated using the diameter and width of the DNA/Rh nanowire under study. Based on these calculations, the conductivity of the DNA/Rh nanowire prepared using chemical reduction method was estimated to be 0.015 S cm^{-1}, and the resistivity was calculated to be 65 Ω cm. This resistivity is significantly greater than the resistivity reported for rhodium in bulk form (4.7×10^{-6} Ω cm).[214, 215]

The large reduction in the conductivity is likely to be due to the combination of two main factors. These are: (1) the granular character associated with the nanowires, and (2) the formation of an oxide layer on the surface of the nanowires. AFM data indicated that the Rh coating around the DNA templates can be considered to be made of a series of nanoparticles closely packed along the DNA strands. Moreover, high resolution XPS spectrum of Rh3d region of the DNA/Rh nanowires showed a doublet peak at binding energy of ($3d_{5/2}$, 308.3; $3d_{3/2}$, 313.1 eV) and is indicative of the presence of rhodium oxide (Rh_2O_3) in the sample material.[204, 211] These factors can therefore constitute a substantial tunnelling barrier to electron transport between particles, consequently increasing the resistivity of nanowire.

5.3.6 Magnetic characterization of DNA/Rh nanowires using magnetic force microscopy (MFM)

As mentioned in the introduction section of this chapter, rhodium metal is non-magnetic in its bulk form, but can display magnetic behaviour in low-dimensional systems.[188-190] In order to determine if the DNA/Rh nanowires prepared here show magnetic behaviour, magnetic force microscopy (MFM) measurements were carried out. For the MFM studies, nanowires were first aligned upon a silicon substrate coated with dielectric layer of SiO_2 using the same procedures described for AFM and EFM samples, and MFM measurements were subsequently recorded at a range of lift heights (typically 12, 14 and 16 nm). Recording the MFM images at sufficiently large tip-sample separations where short-range forces (e.g. van der Waals forces) are negligible is important to ensure the resulting phase shifts are a consequence of long-range forces (i.e. magnetic interactions) alone.

Figure 5.12 shows a height image (a) along with the corresponding MFM phase images (b-d) of the DNA/Rh nanowire prepared using the chemical reduction method. The height image reveals a uniform DNA/Rh nanowire with average structure height of approximately 10 nm. In MFM scans, where the magnetic AFM probe is lifted at fixed distance above the sample surface, the nanowire appears as a uniform dark line relative to the substrate background.

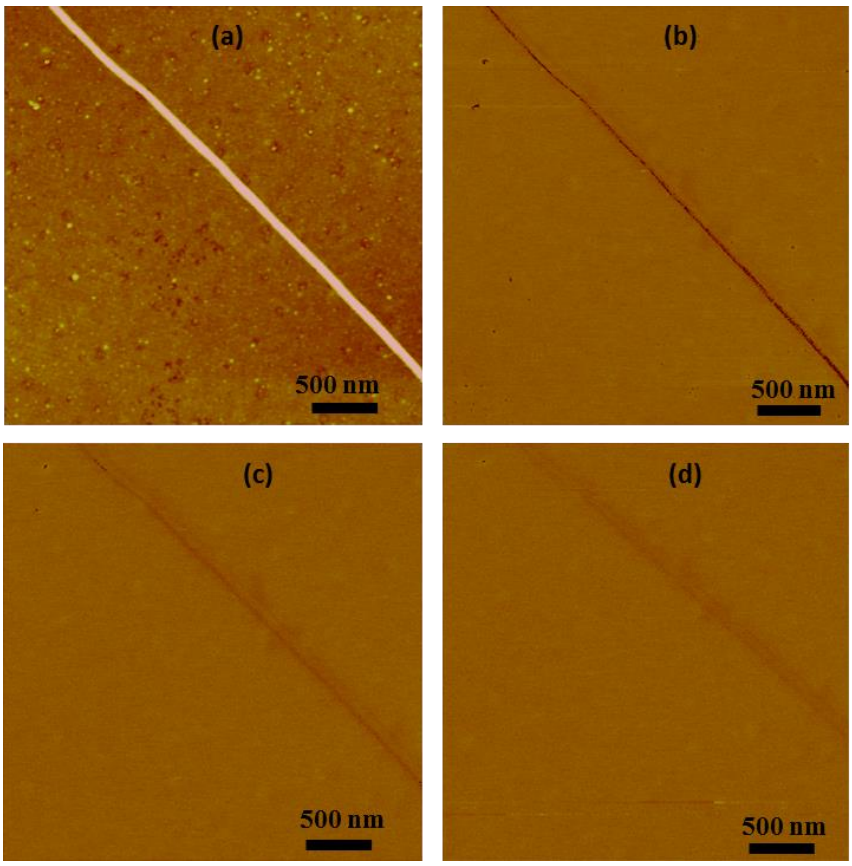

Figure 5-12: Height and MFM phase images of a DNA/Rh nanowire prepared using chemical reduction method, immobilised upon Si/SiO_2 substrate. (a) Height image of the nanowires with average diameter of 10 nm (height scale is 10 nm). The corresponding MFM phase images of the same nanowires, recorded at lift heights of (b) 12 nm, (c) 14 nm and (d) 16 nm, respectively, colour scale corresponds to a phase angle of 4°.

This dark contrast associated with the nanowire can be distinguished from the substrate background up to tip-sample separations of 16 nm. Whilst the appearance of this negative contrast was observed over lift heights of 12-16 nm, the signal was found to reduce gradually with increasing separation. The observation of such negative contrast at large lift heights mean that these features arise as a result of long-range magnetic interactions between the tip and nanowire [106], and confirm a room-temperature magnetic behaviour of the Rh when fabricated as one-dimensional nanostructures.

Further evidence that the contrast observed in MFM phase images is the result of the tip-sample magnetic interactions is provided by recording additional MFM images of the same sample using non-magnetic Si probes. In this control experiment, no phase shift was observed for the nanowires, indicating the absence of long-range magnetic interaction.

Additional MFM images were recorded of the same sample, where the magnetization of the AFM probe was reversed, in order to elucidate further information about the type of magnetic behaviour displayed by the DNA/Rh nanowires. MFM phase images recorded of the DNA/Rh nanowires after switching the magnetisation direction of the AFM tip, were found to also show dark phase contrast. This behaviour is indicative of the magnetic domains of the nanowire region located under the probe aligning with the AFM probe magnetic field, during the imaging. Based upon this finding, these DNA/Rh nanowires should be considered to have superparamagnetic behaviour. This is because if the sample was ferromagnetic in character, changing the magnetisation direction of the probe is expected to change the sign of the phase contrast (from dark to bright contrast) as the interactions between the probe and sample would be repulsive. The magnetic behaviour of the prepared DNA/Rh nanowires is consistent with what was seen for Rh clusters which also behaved superparamagnetically [216], as well as with the magnetic behaviour reported for DNA/Fe_3O_4 nanowires [106] (chapter 3), and DNA/Fe nanowires (chapter 4). The magnetic behaviour for the iron-containing nanowires (DNA/Fe_3O_4 and DNA/Fe) was explained by the nanowire's structure comprising a series of superparamagnetic nanoparticles around DNA template; the proposed structure was supported by the observed close packed "bead-on-a-string" morphology. AFM data of the DNA/Rh nanowires also showed such morphology and support the MFM finding in which the Rh coating around the DNA templates can be considered to be made of a series of superparamagnetic nanoparticles packed along the DNA strands.

5.4 Results and Discussion of DNA/Rh materials prepared using an electrochemical reduction method

DNA/Rh nanowires were also synthesised using an electrochemical-based DNA-templating method. In this novel method, Rh(III) cations were allowed to associate with DNA templates in order to direct the growth of Rh material as 1-D form as for chemical reduction method. The subsequent conversion of the Rh^{3+} species into the metallic phase took place by performing cyclic voltammetry measurements upon an aqueous solution containing DNA/Rh^{3+} system using n-Si<100> wafer as a working electrode. In order to achieve this, an experimental procedure was developed (figure 5.13) similar to that described for preparation of DNA/Fe nanowires (chapter 4).

In these procedures, a silicon substrate used as a working electrode, was modified with TMS to make a more hydrophobic surface. This produces beading of a reaction solution, consequently allowing the counter and reference electrode to be inserted into reaction solution for electrochemical reduction to be carried out. It is believed that there are two fundamental processes behind the nanowire fabrication process used here. The first one is the DNA-metal ions interactions which enable for metallic Rh to be formed predominantly upon the DNA templates. The second factor is associated with the electrochemical reduction of the Rh^{3+} cations, the atoms then act as seeds sites for further metallic nanoparticle growth upon the DNA strands, resulting in continuous Rh^{3+} coating around DNA molecules.

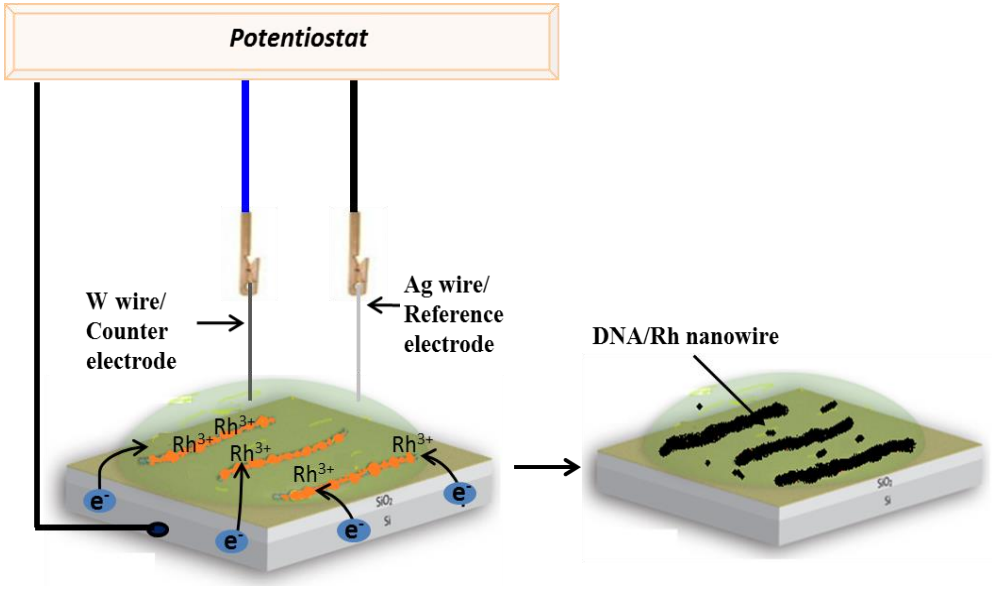

Figure 5-13: Design representing the electrochemical method used for the preparation of the DNA-templated Rh nanowires.

The produced DNA/Rh material was characterised using XPS studies in order to establish the chemical identity of the product material. AFM studies were carried out upon samples of DNA/Rh nanostructures in order to investigate their structural character. Additional scanning probe microscopy studies (EFM and MFM) studies were used to study the electronic and magnetic properties of the DNA/Rh nanowires, respectively.

5.4.1 Cyclic voltammetry

Electrochemical reduction of the DNA-bound Rh^{3+} ions using a CV approach was carried out in an aqueous solution. For CV measurements, the experimental setup

(figure 5.14) was adopted as described earlier. Figure 5.14 illustrates a typical current-potential curve obtained from CV measurements during the DNA/Rh nanowires preparation. This curve shows a broad peak in the cathodic sweep located around E = -0.49 V, which is close to the reported reduction potential value of the $RhCl_3$ at aluminium (Al) electrodes.[217] Reduction of Rh^{+3} ions to metallic Rh^0 is likely to take place in one step involving a three electron transfer process. The one-step reduction process of the Rh may be indicated by the absence of additional cathodic peak relating to any further intermediate oxidation state. Moreover, the cyclic voltammogram recorded for the solution system of DNA/Rh^{+3} is characterised by a single wave as no peak has been observed upon the reverse scan (anodic scan).

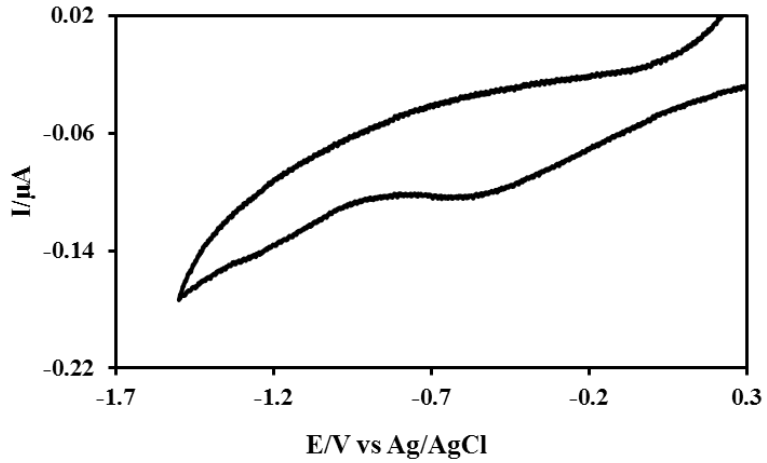

Figure 5-14: Cyclic voltammogram for an aqueous solution containing (500 μg/mL) calf thymus DNA and $RhCl_3.xH_2O$ recorded on n-doped Si substrate as working electrode.

5.4.2 XPS studies

In order to examine the effectiveness of the electrochemical reduction method for reducing the DNA-bound Rh^{3+} ions, and to determine the chemical composition of the product material, XPS studies were used. XPS data of the DNA/Rh nanostructures samples prepared using electrochemical reduction method reveals similar findings to that obtained from DNA/Rh nanowires prepared using $NaBH_4$ as reducing agent. Figure 5.15 illustrates the XPS survey scan spectrum of the DNA/Rh nanostructures prepared by electrochemical templating approach. This spectrum indicates that both of DNA and rhodium features are present in the product materials. These are peaks for O1s, N1s, C1s and P2p arising from DNA and (Rh3d and Rh3p) due to the presence of Rh. Additional, Cl2p peak indicates the presence of chlorine most likely from the $RhCl_3$ start material.

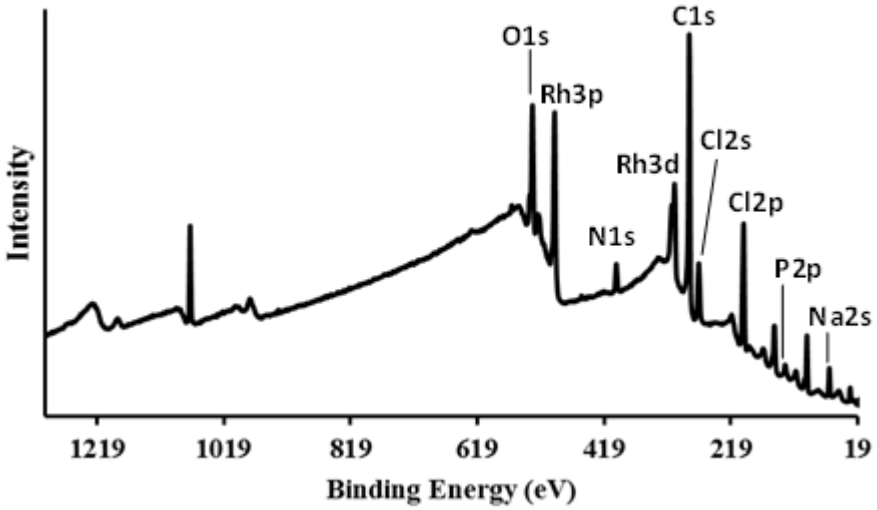

Figure 5-15: XPS survey spectrum calf thymus DNA-templated Rh nanowires prepared using electrochemical method, immobilised upon a Si/native SiO_2 substrate.

The high resolution N1s region spectrum provides evidence for the presence of DNA in the product. Curve fitting of the N1s XPS spectrum (figure 5.16) shows two peaks at 399.3 and 400.4 eV. The position of these peaks falls in the reported values of the N1s core level of the DNA molecules. Peak at 399.3 eV with low intensity is likely to arise due to sp^2-bonded N atoms, and second peak at 400.4 eV with higher intensity is consist with the literature value of sp^3-bonded N atoms in the nucleobase rings and amino group.[119-121]

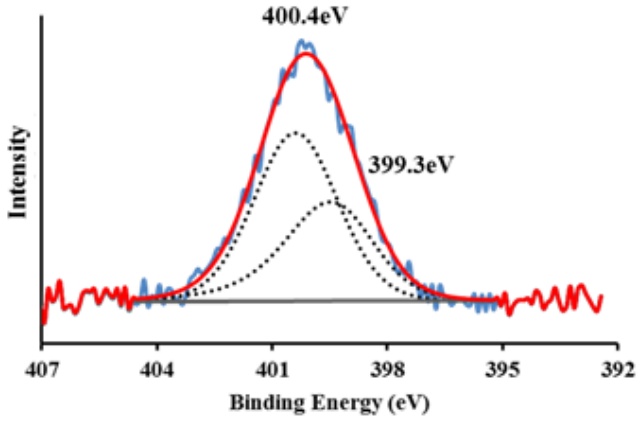

Figure 5-16: High resolution XPS spectrum of N1s region of calf thymus DNA-templated Rh nanowires, prepared using electrochemical templating method, immobilised upon a Si/native SiO_2 substrate. Blue solid line represents raw data, total fits is represented by red solid line and black dashed lines is for component peaks.

Confirmation that the metallic phase of Rh materials deposited upon DNA templates prepared via electrochemical method was found in the Rh3d region of the spectrum. The

corresponding XPS region of Rh3d was fitted to show two different oxidation states (figure 5.17). These are zerovalent Rh^0 formed upon electrochemical reduction of the Rh (III) species and the presence rhodium oxide (likely due to oxidation of some Rh material due to air exposure during the DNA/Rh sample preparation). The major component, with low-binding energies at 307.1 and 311.8 eV for $3d_{5/2}$ and $3d_{3/2}$ respectively, is in good agreement with the reported values of metallic Rh^0.[206, 218, 219] The higher binding energies doublet at ($3d_{5/2}$, 309.2eV; $3d_{3/2}$, 313.5 eV) is attributed to an oxide layer (mainly Rh_2O_3).[206, 218, 219]

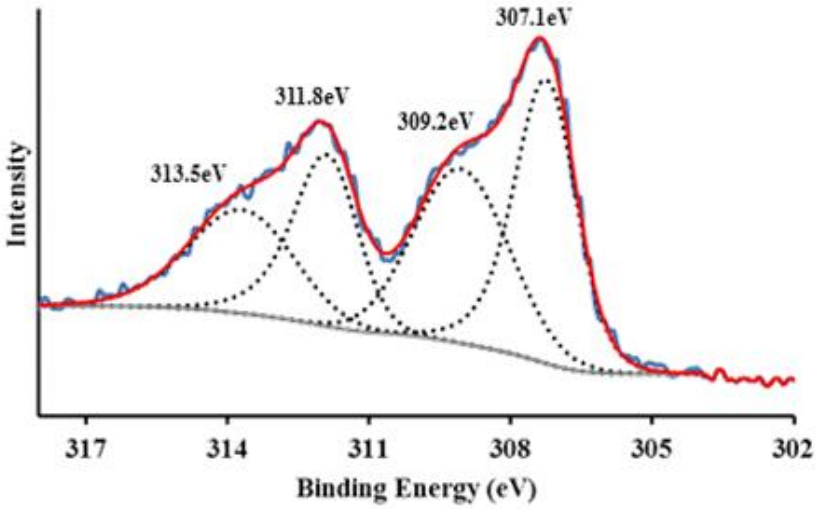

Figure 5-17: High resolution XPS spectrum of Rh3d region of calf thymus DNA-templated Rh nanowires immobilised upon a Si/native SiO_2 substrate. Blue solid line represents raw data, total fits is represented by red solid line and black dashed lines is for component peak.

It can be concluded that the chemical composition of the DNA/Rh material produced using this electrochemical reduction approach is very similar to that prepared using $NaBH_4$ as reducing agent, in which the metallic Rh^0 core material is encapsulated by an oxide (Rh_2O_3) sheath.

5.4.3 AFM characterisation of DNA/Rh nanostructures

The structural character of the DNA/Rh nanostructures synthesised using electrochemical reduction of DNA-bound Rh^{3+} ions was investigated by AFM. Selected AFM images of the resulting 1-D nanostructure are depicted in figure 5.18 a-d.

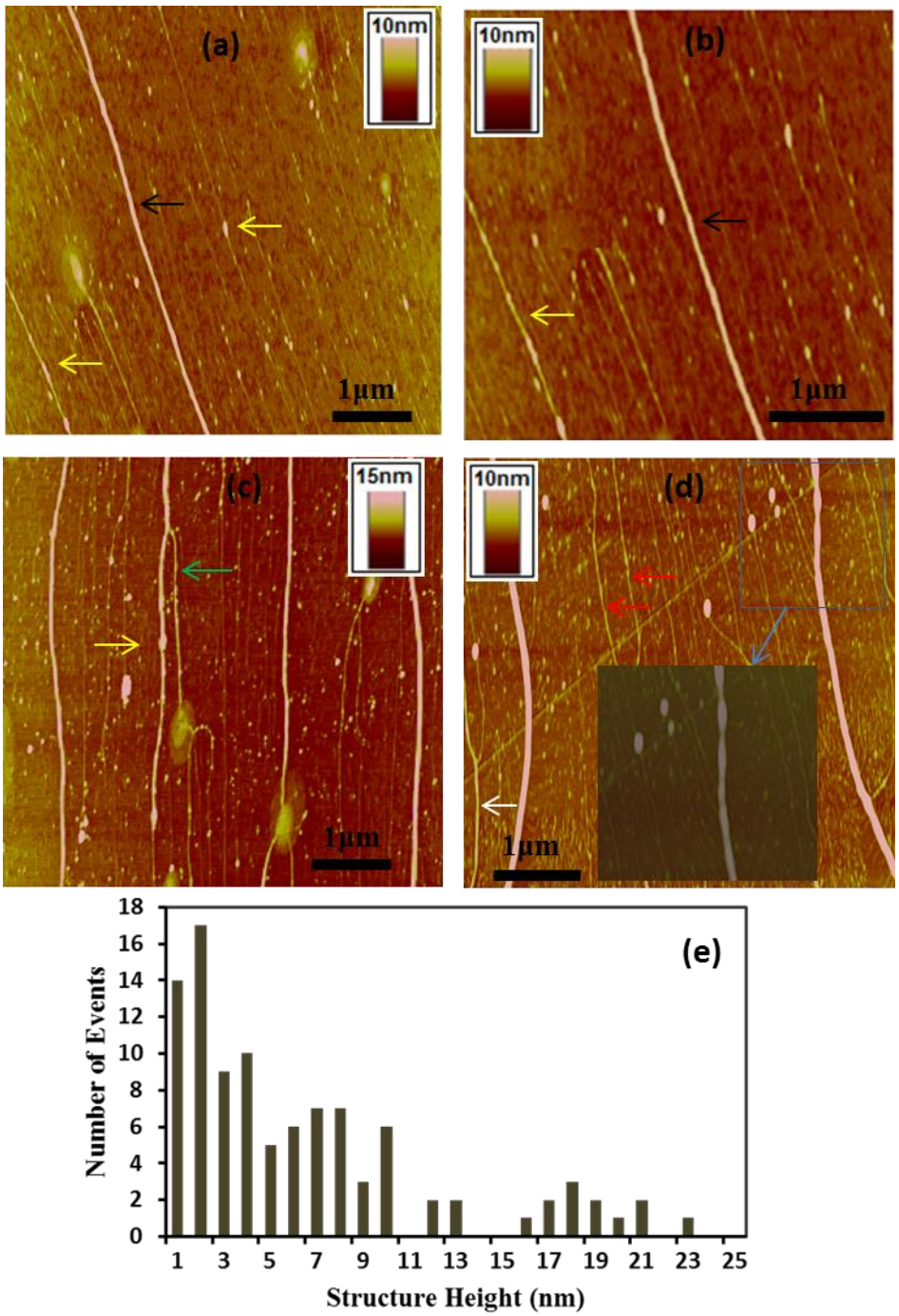

Figure 5-18: Typical examples of TappingMode AFM images of the DNA/Rh "nanowires" prepared using electrochemical reduction method, immobilised upon a Si/native SiO_2 substrate. (a) AFM image shows uniform nanostructure of DNA/Rh material (denoted by black arrow) along with some DNA strands with a very thin, irregular Rh coating (yellow arrows). (b) This image represents also uniform structure (black arrow), and another structure with bead-on-a string morphology (yellow arrow). (c) AFM image reveals four main structures with different diameter. This image show also relatively granular character of the Rh material coverage (indicated by yellow arrow). (d) AFM images reveals a uniform structures of DNA/Rh material, along with some bare DNA molecules (denoted by red arrows), the inset image is a zoomed-in part of the nanostructure with the image contrast used to highlight the granular character of the Rh material coverage. (e) Histogram of the size distribution of the DNA/Rh nanostructures formed using this electrochemical method.

These images show DNA/Rh “nanowires” with diameters up to 23 nm, along with a number of bare DNA molecules as indicated by structure heights < 2 nm (figure 5.18d, red arrows). The observed 1-D form of the produced nanostructures indicates DNA templates the growth of the Rh material along its length, producing the nanowire-like form. Moreover, the rhodium material on many strands was found to be uniform and continuous around the DNA strands.

A granular morphology characteristic of the structure of DNA/metal nanowires prepared by other groups [18, 66, 143], and which was also observed for DNA/Fe nanowires prepared using a similar electrochemical method, is also observed here. Such granular character of the Rh coatings is supported by some structures which displayed irregular Rh coating; see structures denoted by yellow arrows in figure 5.18a and b. These structures contain a series of discrete nanoparticles attached to DNA template, which can be considered as examples of nanostructures where the growth of Rh material has not reached maturity.

Although, the DNA/Rh “nanowires” formed by this electrochemical templating method are found to show uniform structures in many instances, as with the chemical reduction a great variation in the mean diameters of the produced “nanowires” was observed. Statistical analysis of the average diameters of > 100 DNA/Rh nanostructures shows a broad size distribution ranging from 1 and 23 nm (figure 5.18e). Structures with diameters < 2 nm are likely due to bare DNA molecules which remain bare in the reaction solution [16], whereas thicker structures > 2 nm are predominately DNA-templated Rh nanowires.

The variation in the structure height of the DNA-templated Rh nanowires, may be attributed to the formation of ‘bundles’ of DNA molecules in solution upon which the templating reaction takes place, yielding nanowires of larger diameters. The formation of such bundles is evident from some branches (indicated by green arrow in figure 5.19c) which are found to be extending out from the main DNA/Rh nanowires body. Moreover, some structures (indicated by white arrow in figure 5.18d) showed very smooth morphology with main diameter of 3.5 nm, which is larger than the reported value of the single λ-DNA molecule (1-1.5 nm).[66] Therefore, it is suggested that thicker DNA/Rh nanowires may in part be due to the growth of Rh material upon DNA “ropes” instead of single DNA molecule.

In summary, AFM studies reveal that the electrochemical templating strategy allows the fabrication of DNA/Rh "nanowires" with highly continuous and granular coatings of Rh material along the DNA templates. However, the effectiveness in terms of conversion of DNA is low.

5.4.4 Electrical characterization of the DNA/Rh "nanowires" using Electrostatic Force Microscopy (EFM) technique

The electrical properties of the DNA/Rh nanostructures were qualitatively investigated using the EFM method. For this, samples were prepared by transferring the reaction solution containing DNA/Rh "nanowires" from the Si working electrode to a TMS-modified Si wafer with a thermally grown oxide layer. The nanowires were subsequently aligned upon the substrate using a process based upon spin-coating methods as described before.

EFM data of the DNA/Rh nanostructures produced using electrochemical were illustrated in figure 5.19. The height image (figure 5.19a) reveals two main structures with diameters of 11 and 4.1 nm for nanowires denoted with yellow and green arrows, respectively. Moreover, DNA molecules (red arrow) can also be observed with structure heights (< 2 nm). The corresponding EFM phase images of the nanowires, collected during the second pass of the tip at a maintained tip-sample separation, with applied bias potentials of between +7 and -7 V, are shown in figure 5.19 b and c, respectively. These images show negative phase shift associated only with the larger two structures.

The negative phase shifts associated with nanowires over the bias potentials range typically between +7 and -7 volts, indicates that these are electrically conductive. This is because the negative/dark phase contrast is characteristic only for conducting nanostructures as the insulators produce bright/positive phase contrast, as discussed previously.[72, 80, 81] Furthermore, the tangent of the phase shift of nanowire (indicated with yellow arrow in height image) when plotted against the applied voltage (figure 5.219d) shows a parabolic curve, indicating that the tip-sample interactions are dominated by capacitance effects.

In conclusion, the uniform and negative phase shift observed in EFM phase images provide evidence that the metallic Rh^0 nanowires formed by electrochemical reduction as a part of DNA-templating strategy are conductive.

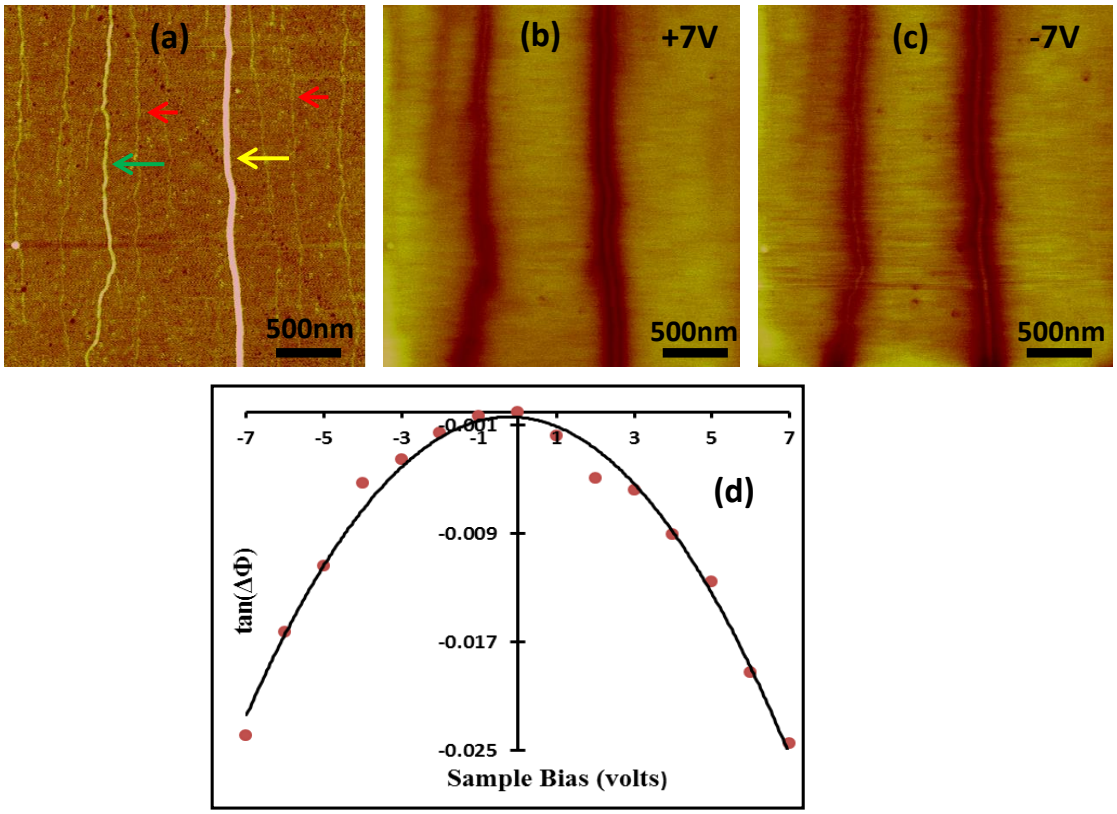

Figure 5-19: Height and EFM phase images of DNA/Rh nanowires prepared using electrochemical reduction method, immobilised upon Si/SiO_2 substrate. (a) Height image of the nanowires with different diameters (height scale is 10 nm). (b and c) The EFM phase images of the nanowires in (a) at sample biases of +7 and -7 Voltas, respectively, phase scale is 4°. (d) Plot of the tangent of the nanowire phase shift as a function of applied voltage.

5.4.5 Electrical characterization of the DNA/Rh nanowires using conductive atomic force microscopy (c-AFM)

As discussed in the preceding section, EFM studies indicate that the DNA/Rh nanowires prepared using electrochemical reduction is electrically conducting. However, EFM does not yet allow the action of determine the nanowire's conductivity. Therefore, to further probe the electronic properties using conductive AFM (c-AFM) experiments were performed. In order to achieve this, a similar manner to that described earlier in this chapter, (see section 5.3.5), was used in which a network of nanowires was connected to the sample.

Figure 5.20 displays c-AFM images of the DNA/Rh nanowires. The contact mode AFM height image (figure 5.20a) reveals two DNA/Rh nanowires with average diameters of approximately 43 nm (white arrow) and 47 nm (yellow arrow). In the c-AFM current map image (figure 5.20b), bright contrasts relative to background can only be observed where the nanowires are located on the substrate. The appearance of such contrast when

the tip is in connection with the DNA/Rh nanowires indicates an electrical current is flowing through the nanowires, consequently confirming their electrical conductivity. As the image scan was completed, the tip was placed on the DNA/Rh nanowire indicated by white arrow in figure 5.21a, at defined points and then I-V curves were recorded over the range of -5 to +5 V.

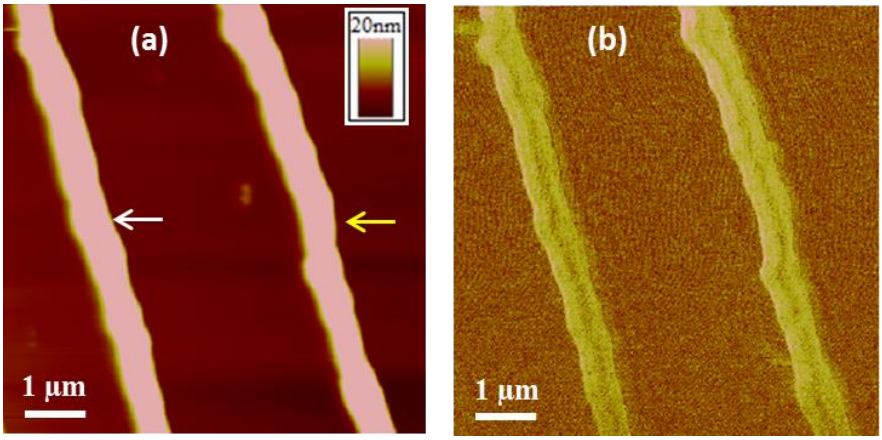

Figure 5-20: C-AFM measurements of the DNA/Rh nanowires aligned upon a Si/SiO_2 substrate. (a) a contact mode AFM image. (b) Current map image recorded at 0.5V tip-sample bias and the data scale corresponds to a current of 100 nA.

The conductance was calculated from the slope of the I-V curve at zero bias, and the resistance was plotted against the relative distance of the tip along the nanowire in the direction away from the network (figure 5.21). It is clear from figure 5.21 that the circuit resistance increases in an approximately linear manner as the relative distance is increased. This is because the electric current must cross a longer distance through the nanowires which has the largest resistance in the circuit.

The DNA/Rh nanowire resistance per unit length was calculated from the slope to be 1×10^{11} Ω cm^{-1}. In order to estimate the nanowire conductivity, their diameter and width were determined by AFM in order to calculate the cross-section area (assumed elliptical). Based on these calculations, the conductivity of the DNA/Rh nanowire prepared using electrochemical reduction method was estimated to be 0.024 S cm^{-1}, and the resistivity was calculated to be 41 Ω cm. It is also considerably greater than the resistivity reported to the Rh in bulk form (4.7×10^{-6} Ω cm).[214, 215] Such reduction in the nanowire conductivity can also be attributed to the granular morphology as indicated by AFM and formation of oxide layer on the nanowires surface as indicated by XPS data.

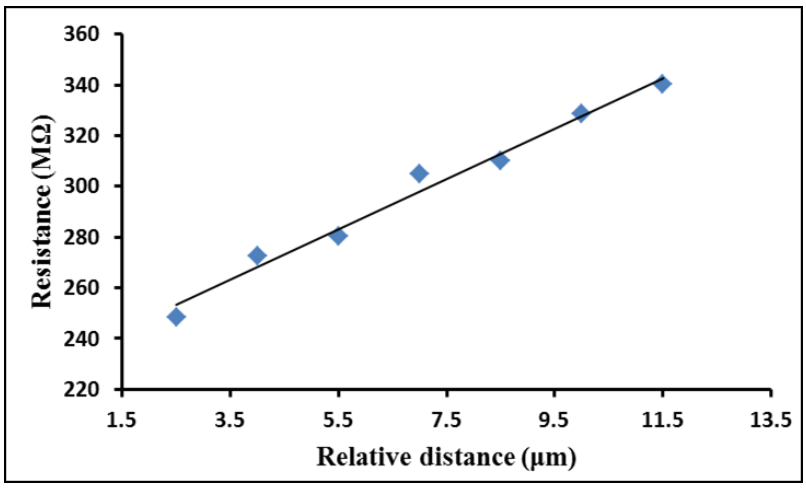

Figure 5-21: Resistance of DNA/Rh nanowires as a function of relative distance at deflection setpoint of 0.5V.

5.4.6 Magnetic characterization of the DNA/Rh nanowires using magnetic force microscopy (MFM)

As discussed earlier in this chapter, MFM studies show DNA/Rh nanowires formed using $NaBH_4$ as reducing agent to be superparamagnetic at room temperature, when prepared in this nanostructured form. It was therefore worthwhile to explore if the nanowires produced here show similar magnetic behaviour or if they display distinct properties. MFM measurements were again performed upon DNA/Rh nanowires aligned upon Si/SiO_2 substrates.

The topography image (figure 5.22a) collected in the first MFM scan reveals two DNA/Rh nanowires with structure heights of 25 and 14 nm (yellow and green arrows), respectively. The height image shows also a noticeable number of thinner structures (red arrows) with heights < 1.5 nm, indicating them to be bare DNA. The corresponding MFM phase images (figure 5.22 b-d) were recorded over a range of tip-sample separation (typically 12, 14 and 16 nm) to avoid any short-range forces which can produce misleading results.

In the MFM scans, dark contrast was observed only for the two prominent DNA/Rh nanowires (yellow and green arrows in figure 5.22a). Such contrast is seen to be absent for bare DNA (red arrow in figure 5.22a) which does not exhibit any MFM phase contrast due to a lack of magnetic properties. The appearance of dark contrast at increased lift heights indicates a room temperature magnetic behaviour of the prepared DNA/Rh nanowires.[106]

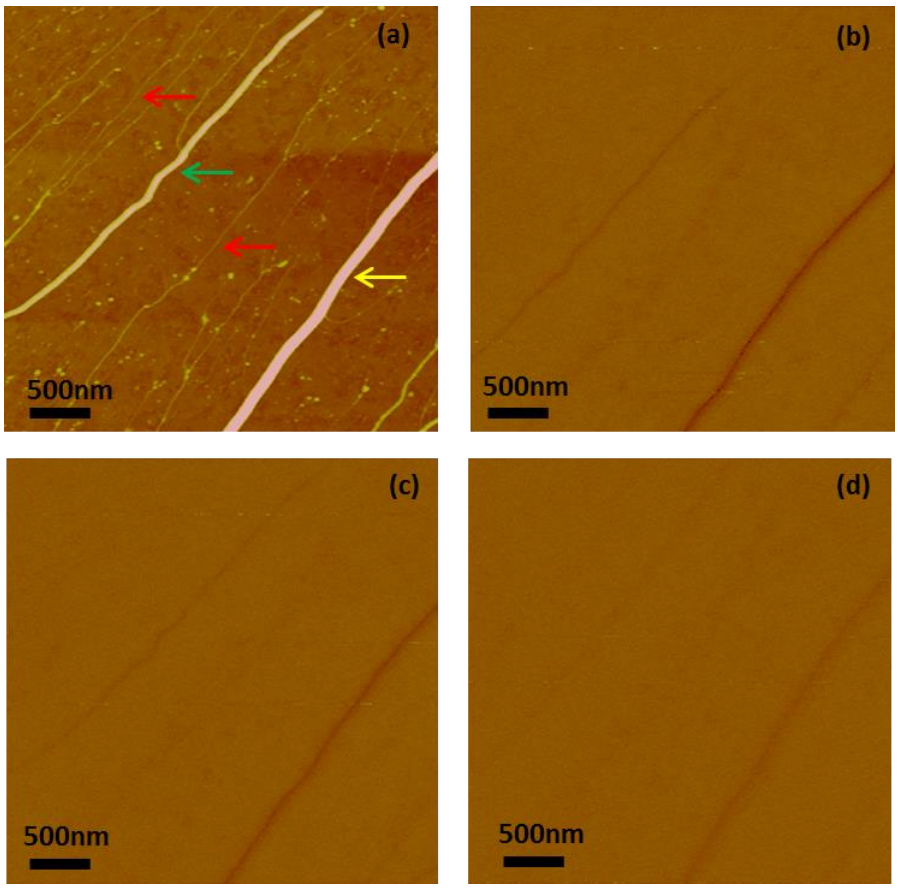

Figure 5-22: Height and MFM phase images of DNA/Rh nanowires prepared using electrochemical reduction method, immobilised upon Si/SiO_2 substrate. (a) Height image of the nanowires with different diameters (height scale is 30 nm). The corresponding MFM phase images of the same nanowires, recorded at lift heights of (b) 12 nm, (c) 14 nm and (d) 16 nm, respectively, colour scale corresponds to a phase angle of 7°.

Moreover, the sign of MFM phase contrast (dark contrast/negative phase shift) indicates attractive tip-sample interactions, where the nanowires magnetic domains and magnetic fields from the probe are in favourable alignment with one another. It is also found that thicker nanowire (25 nm heights) shows stronger contrast than the nanowire with structure height of 14 nm. Moreover, the phase signals associated with both structures gradually decreased with increasing lift height becoming difficult to distinguish from the substrate background when the tip-sample separation is >16 nm lift height.

To establish the type of magnetism of the produced nanowires, further MFM measurements were carried out upon the same sample, whilst the magnetisation direction of the probe was reversed. These measurements also show dark contrast associated with the nanowires, indicating that the DNA/Rh nanowires prepared using electrochemical reduction method presenting also superparamagnetism and magnetic field of the AFM probe inducing alignment of the magnetic moments within the region

of the nanowire over which the probe is placed at given time. Such magnetic behaviour is similar to that observed for DNA/Rh nanowires prepared using chemical reduction method, DNA/Fe_3O_4 nanowires [106], (chapter 3) and DNA/Fe nanowires (chapter 4).

5.5 Conclusion

Rhodium nanowires have been successfully produced using DNA-templating approaches in conjunction with either chemical or electrochemical reduction. The association of the metal cations with DNA templates directs the subsequent growth of the metallic Rh material formed during reduction step to give 1-D nanostructures. For nanowires prepared using $NaBH_4$ as reducing agent, XRD data reveals that these nanostructures are made of Rh in zero-valence state. However, XPS data indicates that the metallic Rh^0 core in the nanowires is coated with layer of oxide (probably, Rh_2O_3). The chemical nature of the DNA/Rh nanowires fabricated using electrochemical templating was confirmed by XPS studies to comprise of a metallic Rh^0 core coated with oxidised Rh species (Rh_2O_3).

AFM studies indicated that both chemical and electrochemical methods allow the fabrication of DNA/Rh "nanowires" with complete coverage of the DNA templates by the Rh material. Closer inspection of the structures produced showed a small degree of granular character associated with Rh coatings, indicating that the growth of Rh upon DNA template was took place via nucleation and growth mechanism. It is worth mentioning that the chemical reduction method is suggested to be more effective in terms of templating DNA with Rh material. That is because statistical analysis of the average diameters of nanowires indicated that the electrochemical method produced large number of DNA molecules which remain untemplated in the reaction solution relative to those produced by chemical reduction method.

The qualitative investigation of electric conductivity using the EFM technique indicates that the nanowires are electrically conducting. However their room temperature conductivity value, calculated from i-V curves recorded by c-AFM, was very similar and low at 0.015 S cm^{-1} and 0.024 S cm^{-1}, for nanowires prepared using chemical and electrochemical reduction, respectively. Furthermore, MFM measurements have confirmed the nanowires exhibit room temperature magnetic behaviour and additional MFM studies revealed the nanowires exhibit superparamagnetic behaviour.

6. Chapter 6: Preparation and Characterization of polymer-based nanowires

6.1 Introduction

In 1963 D.E. Weiss and co-workers reported high conductivity in polypyrrole,[220] however, the field of conductive polymers (CPs) really started in 1977 when Alan J. Heeger, Alan G. MacDiarmid and Hideki Shirakawa reported on high conductivity of polyacetylene.[221] For this discovery, they were awarded the 2000 Nobel Prize in chemistry for the discovery and development of CPs.[222]

In contrast to conventional polymers, which are electrically insulating, CPs have received much interest since their discovery and have been exploited in a range of devices like solar cells, transistors, capacitors, memory and bio/chemical sensors, due to their electronic and optical properties which are similar to metals and semiconductors.[16, 223] Moreover, fabrication of CPs with nanoscale dimensions can improve the performance of organic devices. Organic transistors fabricated from conducting polymer nanostructures for example, are suitable for use in ultrathin panel displays.[223, 224] Additionally, because of their high specific surface areas, conducting polymer nanomaterials can enhance the response and sensing rate of the sensors made of conducting polymers.[223, 225] Therefore, attention has been paid to the preparation of CPs in low-dimensional forms particularly as nanowires which have been synthesised and demonstrated for potential use in nanoelectronics.[226]

CPs have been formed as nanowires by various techniques, including formation in porous templates [29] and on DNA. Examples of this latter approach include DNA/polyaniline [70], DNA/polypyrrole [71, 72], and DNA/polyindole [73], and all these are examples of supramolecular polymers. The ability for conducting polymer to be templated on DNA strands depends on the complementarity nature of the two polymer types as outlined in chapter 1, section 1.10.3.

In the work described in this chapter, the formation of supramolecular polymer nanowires via DNA-templating of 2,6-diaminopurine-propyl-2,5-bis-dithenyl pyrrole (DAP-prop-TPT) and thymine-propyl-pyrrole (T-prop-Py) is explored (figure 6.1). The resulting materials were characterised using a combination of FTIR and XPS spectroscopy in order to characterize their chemical structural properties, while

structural character and electronic properties were studies using AFM and EFM, respectively.

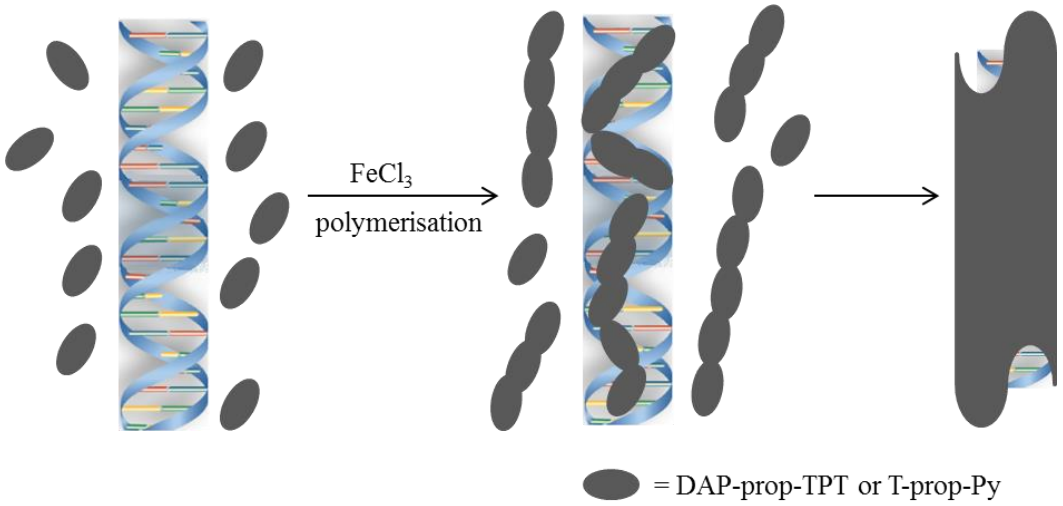

Figure 6-1: Representation of the use of DNA as a template for controlling the growth of poly(DAP-prop-TPT) and poly(T-prop-Py) toward organised one-dimensional structures. Polymerisation of the DAP-prop-TPT and T-prop-Py monomers produces cationic oligomers, which bind to the template through supramolecular interactions. Further growth produces the final hybrid polymer-based nanowires.

The attempted formation of larger structures based on the hydrogen bonding between two types of nanowires which bear functional groups with base pairing capability is investigated by AFM studies. It is known that adenine (A) can pair with thymine (T) via two hydrogen bonds (figure 6.2a) [227], whereas 2,6 diaminopurine, which is a derivative of adenine, can form a total of three hydrogen bonds, two N-H…O and one N-H…N hydrogen bonds with thymine, see figure 6.2b.[227] It is found that the DAP-T pairs in DNA exist as Watson-Crick pairs stabilized by three hydrogen bonds with structural parameters mimicking those of A-T pairs.[228]

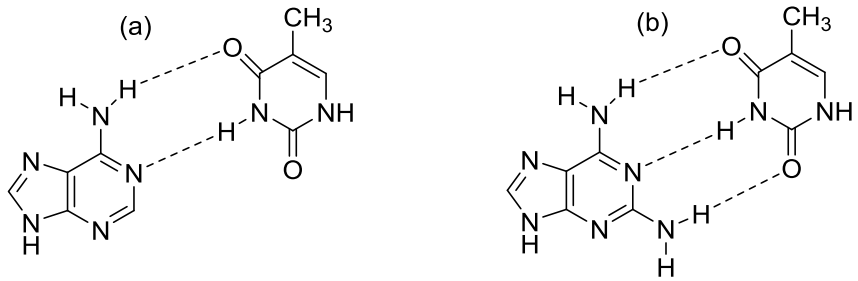

Figure 6-2: Chemical structures of (a) adenine-thymine and (b) 2,6-diaminopurine-thymine base pairs.

As the 2,6-diaminopurine forms three hydrogen bonding with thymine, the stability of DAP-T base pairs is expected to be increased. It is found that by incorporating of DAP into short oligomers of DNA, the thermal stability of the duplex is increased by 0 – 2 °C per DAP-T base pair.[229, 230] It has also been shown that the substitution of adenine by DAP in peptide nucleic acid (PNA) increases the thermal stability of the complexes formed between PNA and complementary DNA, RNA, and PNA oligomers. Additionally, such substitution in PNA produces oligomers that bind both more efficient and most often with improvement sequence specificity to complementary DNA, RNA or PNA oligomers.[230]

The DNA/poly(DAP-prop-TPT) and DNA/poly(T-prop-Py) nanowires are expected to have free hydrogen bonds sites provided by 2,6 diaminopurine unit and thymine ring of the DNA/poly(DAP-prop-TPT) and DNA/poly(T-prop-Py) nanowires, respectively. It is therefore possible that the nanowires produced can be considered as complementary strands with potential hydrogen bonding between their functional groups. In this way they may be used as building blocks for the assembly of these nanowires, producing larger structures of hybrid polymer-based nanowires. Figure 6.3 illustrates the purposed scheme for the fabrication of larger structures based on hydrogen bonding formation between two complementary nanowires.

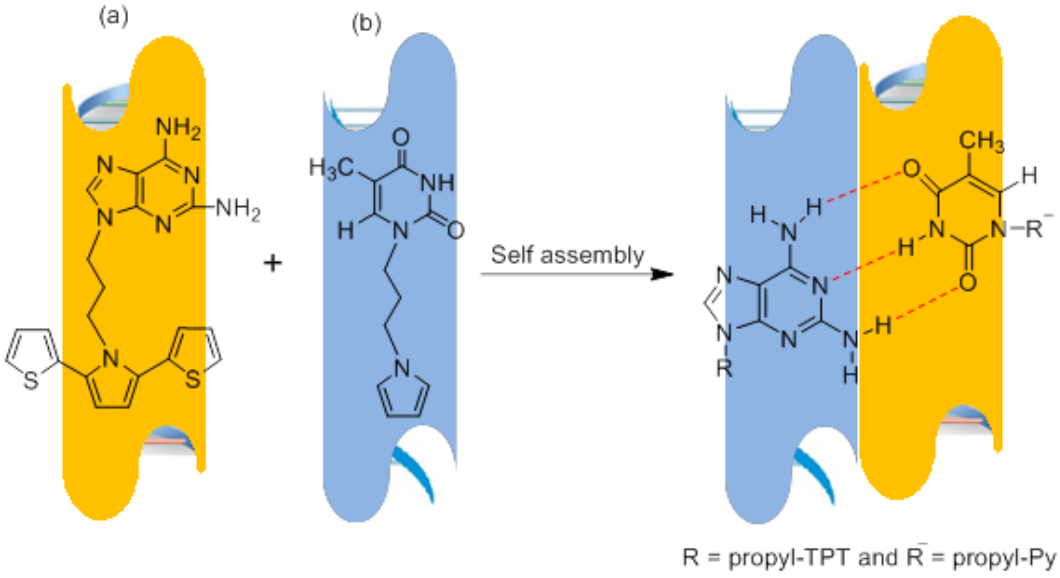

Figure 6-3: Representation of the fabrication of larger structures of polymer–based material via hydrogen bonding interactions between two complementary nanowires. (a) DNA/poly(DAP-prop-TPT) nanowire, (b) DNA/poly(T-prop-Py) nanowire.

It is expected that, despite the probability for the functional groups attached both DNA/poly(DAP-prop-TPT) and DNA/poly(T-prop-Py) nanowires to be involved in templating with DNA during nanowires preparation, a number of them are expected to be free and therefore able to form H-bonds with the complementary partner.

6.2 Experimental section

6.2.1 Materials

Lambda (λ) DNA (48502 base pairs in length, 500 μg mL^{-1}, 10 mM Tris-HCl, 1mM EDTA, pH8 at 25°C) was purchased from New England Biolabs (cat no. N3011S, New England Biolabs UK Ltd. Hitchin, United Kingdom). DNA sodium salt from calf thymus (Type I, highly polymerized, fibrous preparation, 16.7 A260 units mg-1, 6% sodium), $MgCl_2.6H_2O$ (99.0%), $FeCl_3$ (>97%), dimethylformamide $HCON(CH_3)_2$ (99.8%) and HF (48% in H_2O) were purchased from Sigma-Aldrich (Sigma-Aldrich Company Ltd., Dorset, United Kingdom). Si<p-100> wafers (3 inch diameter, boron doped, 525±50 μm thickness, single side polished, 1-10 Ω cm resistance) and Si<n-100> wafers (3 inch diameter, arsenic doped, 525±25μm thickness, double side polished, ≤0.005 Ω cm resistance, coated with a thermally grown SiO_2 layer, 200 nm±10% thick) from Compart Technology Ltd, Peterborough, Cambridgeshire, U.K. NANOpure® deioinized water (18 MΩ cm resistivity) was supplied from a NANOpure® DIamondTM Life Science ultrapure water system equipped with a DIamondTM RO Reverse Osmosis System (Barnstead International). The 2,6-diaminopurine-propyl-2,5-(bis(di-2-thienyl)-pyrrole (DAP-prop-TPT) and thymine-propyl-pyrrole (T-prop-Py) were prepared by Dr. Galindo and used as received.

6.2.2 Preparation of poly(DAP-prop-TPT) and poly(T-prop-Py) materials for spectroscopic studies

A freshly prepared aqueous solution of $FeCl_3$ (50 μL; 3 mM) was added to a solution of DAP-prop-TPT (50 μL; 3 mM) in dimethylformamide (DMF) and incubated for a period of 1 hour at room temperature. After 1 hour had elapsed, 80μL of the resulting solutions were deposited upon a "piranha-treated" Si<n-100> wafer and allowed to dry at room temperature. A similar procedure was used to prepare the poly(T-prop-Py) materials.

6.2.3 Preparation of DNA/poly(DAP-prop-TPT) and DNA/poly(T-prop-Py) materials for spectroscopic studies

Samples of DNA/poly(DAP-prop-TPT) nanowires were prepared for FTIR and XPS studies by addition of an aqueous solution of calf thymus DNA (200 μL; 0.5 mg mL^{-1}) to a solution of DAP-prop-TPT (50 μL; 3 mM) in DMF. Then, a freshly prepared aqueous solution of $FeCl_3$ (50 μL; 3 mM) was added to start the polymerisation. The product material in the reaction solution was allowed to stand at room temperature for a period of 1 hour. 80 μL of the resulting solutions were then deposited upon a "piranha-treated" Si<n-100> wafer and the solvent was allowed to evaporate at room temperature prior to FTIR and XPS analysis. A similar procedure was used to prepare the DNA/poly(T-prop-Py) nanowires.

6.2.4 Preparation and alignment of λ-DNA/poly(DAP-prop-TPT) and λ-DNA/poly(T-prop-Py) nanowires for scanning probe microscopy (AFM and EFM) studies

10 μL of aqueous $MgCl_2.6H_2O$ solution (0.5 mM) was mixed with an aqueous solution of λ-DNA (40 μL; 500 μg mL^{-1}). Following this, 10 μL of DAP-prop-TPT solutions in DMF (3 mM) was added to the λ-DNA/$MgCl_2$ mixture solution before addition of a freshly prepared aqueous solution of $FeCl_3$ (10 μL; 3 mM) to induce the polymerisation, as before. The resulting solutions were incubated for approximately 1 hour at room temperature. After this period of incubation, the reaction solutions were centrifuged at 6000 rpm for about 5 minutes. After 5 minutes, 5 μL of the lower part of the reaction solution was deposited and aligned upon the TMS-modified Si substrate prepared as described in chapter 3, section 3.2.2.

6.2.5 Fourier transform infra-red spectroscopy

A Bio-Rad Excalibur FTS-40 spectrometer (Varian Inc., Palo Alto, CA, USA), equipped with a liquid nitrogen cooled deuterated triglycine sulphate detector, was used for recording FTIR spectra of the product material DNA/poly(DAP-prop-TPT) and DNA/poly(T-prop-Py) and control samples of "bare" DNA, and the polymers poly(DAP-prop-TPT) and poly(T-prop-Py). Samples were prepared by depositing 80 μL of a CT-DNA solution (500μg mL^{-1}), polymer materials or the product materials upon a piranha-cleaned Si<n-100> wafer, and allowing the solvent to evaporate at room

temperature. Spectra were recorded over the 600–4000 cm^{-1} range, with 128 scans and at 4 cm^{-1} resolution.

6.2.6 X-ray photoelectron spectroscopy

XPS spectra were acquired using X-ray photoelectron spectrometer (Thermo Electron Corp., East Grinstead, UK), equipped with an Al Kα X-ray source (1486.6 eV) with a variable spot size of 30–400 µm. A take-off angle of 90˚ was used during data acquisition, and a charge neutralisation gun used to reduce surface charging. All spectra were referenced to hydrocarbon C1s peak at 285.0 eV. Survey spectra were acquired using a pass energy of 150 eV, whilst high resolution region spectra were acquired using a pass energy of 50 eV. Analysis of XPS data was carried out using CasaXPS software.

6.3 Results and Discussion

The synthesis of DNA/poly(DAP-prop-TPT) and DNA/poly(T-prop-Py) nanowires were attempted using a similar method to that described for previous examples of DNA-templated conducting polymer nanowires.[16, 71-73] This method involves chemical oxidation of the monomer unit using $FeCl_3$ in an organic, aqueous or a mixture of organic/aqueous solution containing DNA molecules. In this study, both DAP-prop-TPT or T-prop-Py monomers (figure 6.4) are dissolved in DMF as they are not water soluble.

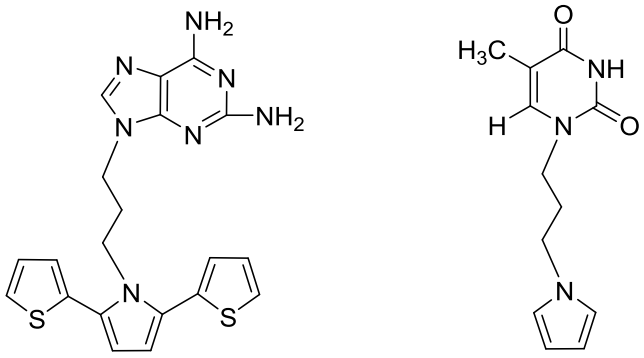

DAP-prop-TPT T-prop-Py

Figure 6-4: (Left) structure 2,6-diaminopurine-propyl-2,5-(bis(di-2-thienyl)-pyrrole (DAP-prop-TPT) and (right) thymine-propyl-pyrrole (T-prop-Py).

The organic solutions of these monomers in DMF were mixed with the aqueous solution containing DNA molecules. For chemical characterisations, which require a larger amount of the product material to be produced, calf thymus DNA was used, whereas λ-DNA with suitable length (~ 16 μm) was used in preparations where the analysis of single nanowire structures was desirable such as AFM.

The polymerisation of the monomer is then induced by addition of an aqueous solution of freshly prepared $FeCl_3$ which acts as an oxidant. This step forms conducting polymer chains, some of which bind to duplex DNA through electrostatic and hydrogen bonding interactions. The formation of such non-covalent interactions are supported by previous FTIR data [16], which indicate intimate interaction between DNA template and CPs chains, producing a supramolecular hybrid polymer comprising both strand types. The DNA/polymer binding is very important step for controlling the growth of these conducting polymers along a single axis. The product material in the reaction solution was allowed to incubate for 1 hour at room temperature.

The product materials were isolated and characterised using a combination of FTIR and XPS spectroscopy in order to confirm their chemical identity. Moreover, scanning probe microscopy studies were conducted using AFM and EFM in order to investigate the structural morphology and electrical properties of the resulting polymer-based nanostructures, respectively.

6.3.1 FTIR studies of DNA/poly(DAP-prop-TPT) and DNA/poly(T-prop-Py) material

In order to establish that the product did contain both the template DNA, and the CP, FTIR spectroscopy was initially used. Spectra were recorded for the isolated DNA-templated CP materials as well as DNA, and pure CP materials as controls. FTIR spectra of the isolated DNA/poly(DAP-prop-TPT) material along with the controls spectra are shown in figure 6.5. These data provide evidence for the formation of the desired hybrid supramolecular polymer containing both DNA and poly(DAP-prop-TPT) chains. The product does not appear to be a simple mixture but instead the two types of polymer interact.

One of the significant indications of this is provided by displacement of water molecules from DNA upon interaction with polymer material. This displacement is indicated by the reduction in the intensity of the broad band centred around 3300 cm^{-1}.

This is due to contributions of both O-H stretching vibrations from water bound to DNA and N-H stretches in the DNA nucleobases. Upon DNA/polymer interaction, this band is reduced in comparison to the corresponding band in the spectrum of bare DNA. FTIR studies of previous examples of DNA-templated polymer nanowires have also reported this water displacement upon interaction of DNA with polymer materials.[16, 71, 73] Assignment and comparison in FTIR spectra of calf thymus DNA and calf thymus DNA-templated poly(DAP-prop-TPT) material is shown in table 6.1.

The presence of the poly(DAP-prop-TPT) in the product material is indicated by bands at 783, 833 and 1404 cm^{-1} due to C-H out of plane bending of pyrrolyl, C-H out of plane bending of thiophenyl, and C-N and C=C stretches of pyrrolyl unit, respectively.[16, 231-234] These bands are absent in the spectrum of DNA itself (blue spectrum), while they are found to be shifted relative to the corresponding bands in the spectrum of pure poly(DAP-prop-TPT) (black spectrum). Indeed, C-H out of plane bending of pyrrolyl observed at 764 cm^{-1}, C-H out of plane bending of thiophenyl at 844 cm^{-1}, and C-N and C=C stretches of pyrrolyl unit at 1412 cm^{-1} in the pure polyDAP-prop-TPT, shifts of +19, -11 and -8 cm^{-1}, respectively, upon DNA/poly(DAP-prop-TPT) formation. These shifts in the position of polymer-related bands add further evidence for the DNA/poly(DAP-prop-TPT) interactions, and that the material is not simple mixture.

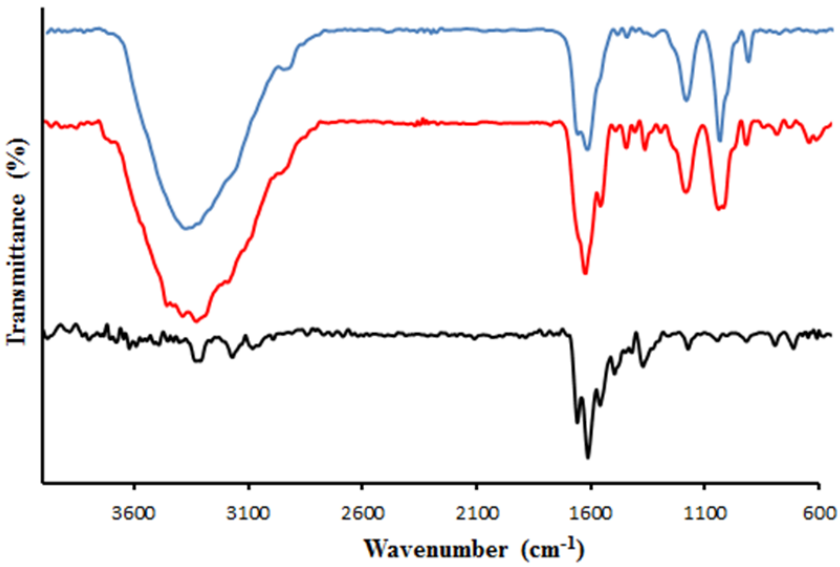

Figure 6-5: FTIR spectra of DNA/poly(DAP-prop-TPT) material (red curve) vs control samples of bare CT- DNA (blue curve) and poly(DAP-prop-TPT) (black), in the 600 – 4000 cm^{-1} region.

Furthermore, several bands were observed in the 900-1750 cm^{-1} region of spectrum which is confirmed the presence of the DNA in the product material. These bands are likely to be due to both phosphodiester backbone (900-1300cm^{-1}) and the nucleobases (1300-1800cm^{-1}) of DNA.[16, 71, 110, 235] However, although in this region of spectra DNA itself and the DNA/poly(DAP-prop-TPT) material showed similar spectral features, one still can see some spectral changes (see figure 6.5 and table 6.1), supporting the interaction of poly(DNA-prop-TPT) with DNA. Evidence for the interactions of poly(DAP-prop-TPT) with the DNA backbone is provided by the change in the relative intensity between PO_2^- symmetric stretching (ca. 1090 cm^{-1}) and C-O deoxyribose stretching (1064 cm^{-1}) vibrations for bare DNA in comparison with the spectrum of the product material. This change is combined with a slight shift toward lower wavenumber of the PO_2^- symmetric stretching (1084 cm^{-1}) upon DNA/polymer formation. Additionally, the PO_2^- asymmetric stretching at 1234 cm^{-1} in the DNA itself is centred at lower frequency (1228 cm^{-1}) in the spectrum of DNA/poly(DAP-prop-TPT) material.

There are also several changes in the DNA nucleobase region (1300-1800 cm^{-1}) of the spectra upon DNA/polymer formation which may indicate that polymer material also interacts with the nucleobases. C-N stretches of the cytosine and guanine bases at 1375 cm^{-1}, as well as the a cytosine or guanine ring vibration at 1493 cm^{-1}, for example are shifted to lower frequency 1367 and 1484 cm^{-1}, respectively. Additionally, the latter band also shows a noticeable increase in intensity relative to the corresponding band in the spectrum of bare DNA. Moreover, the C=O stretch of guanine at 1702 cm^{-1} in the spectrum of DNA itself, was not evident, likely due to being shifted, providing further evidence for involving DNA nucleobases in the DNA/poly(DAP-prop-TPT) interactions.

In summary, FTIR data have provided evidence for the formation of a supramolecular hybrid polymer material by intimate interactions between DNA and poly(DAP-prop-TPT) strands. This was indicated by numerous spectral changes of DNA-related bands (in the FTIR region between 900 and 1700 cm^{-1}), along with the loss of intensity of water-related band. The presence of thiophenyl and pyrrolyl related bands in FTIR spectrum of the final product are also shifted relative to their position in the spectrum of pure poly(DAP-prop-TPT).

DNA wavenumber	DNA/poly(DAP-prop-TPT) wavenumber	Assignment[a]
-	783 cm^{-1}	C-H out of plane bending of pyrrolyl ring β-hydrogen in polyDAP-prop-TPT
-	833 cm^{-1}	C-H out of plane bending of thiophenyl ring β-hydrogen in polyDAP-prop-TPT
967 cm^{-1}	969 cm^{-1}	C-C deoxyribose stretch
ca. 1022cm^{-1}	1021 cm^{-1}	C-O deoxyribose stretch[b]
ca. 1064cm^{-1}	1065 cm^{-1}	C-O deoxyribose stretch
1090 cm^{-1}	1084 cm^{-1}	PO_2^- symmetric stretch
1234 cm^{-1}	1228 cm^{-1}	PO_2^- asymmetric stretch
-	1336 cm^{-1}	C-N stretch of guanine and cytosine
1375 cm^{-1}	1367 cm^{-1}	C-N stretch of guanine and cytosine
-	1404 cm^{-1}	C-H, N-H deformation; C-N stretch
1493 cm^{-1}	1484 cm^{-1}	C8-N stretch, coupled with a ring vibration of guanine
1531 cm^{-1}	1531 cm^{-1}	In-plane vibration of guanine and cytosine
ca. 1609 cm^{-1}	1594	In-plane vibration of adenine
1661cm^{-1}	1661 cm^{-1}	C=O stretch of cytosine/thymine
1702 cm^{-1}	-	C=O stretch of guanine
ca. 3300 cm^{-1}	*ca*. 3300 cm^{-1}	O-H stretch

Table 6-1: Assignment and comparison in FTIR spectra (600-4000 cm^{-1}) of calf thymus DNA and calf thymus DNA-templated poly(DAP-prop-TPT) material.[a] Assignments of DNA bands were made with reference to literature.[16, 71, 110, 235]

For the investigation of the interactions between the DNA and poly(T-prop-Py) in DNA/poly(T-prop-Py) material, FTIR spectroscopy studies were carried out upon samples of the produced DNA/poly(T-prop-Py) material, as well as upon control

samples of CT-DNA and pure poly(T-prop-Py). FTIR spectrum of the product material (figure 6.6, red curve) can indicate that the product material is a hybrid supramolecular polymer containing both DNA and poly(T-prop-Py). The presence of the poly(T-prop-Py) can be indicated by the band at 738 cm^{-1} is assigned to C-H out of plane bending of pyrrolyl ring in the poly(T-prop-Py).[236] This band is observed at higher frequency (742 cm^{-1}) in the spectrum of pure poly(T-prop-Py) (black spectrum in figure 6.6), while it is absent in FTIR spectrum of CT-DNA itself.

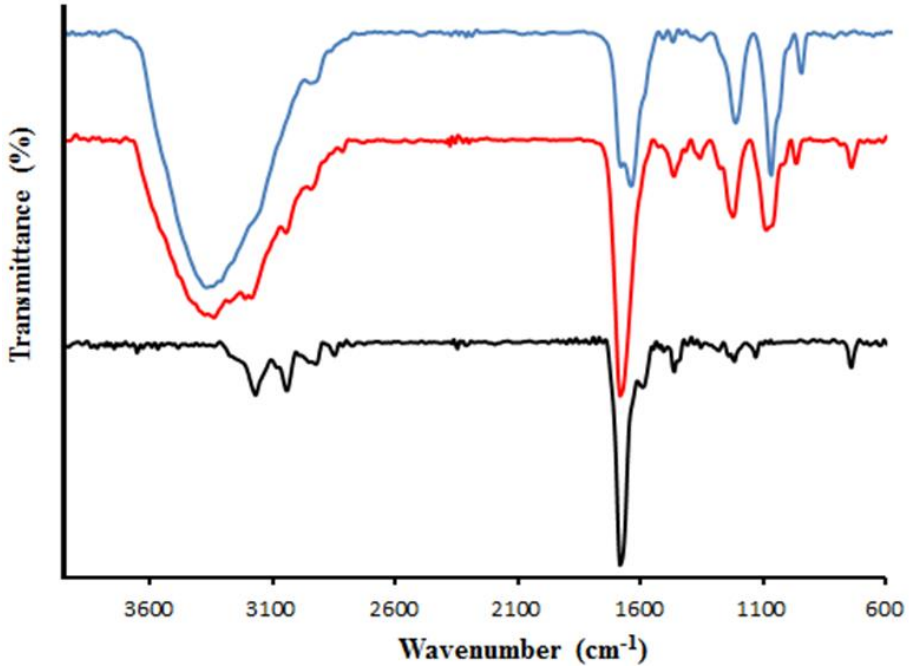

Figure 6-6: FTIR spectra of DNA/poly(T-prop-Py) material (red curve) vs spectrum of bare CT- DNA (blue curve) and poly(T-prop-Py) (black curve), in the 600 – 4000 cm^{-1} region.

Moreover, in the spectrum of the product material a large band around 3300 cm^{-1} related to O-H stretching vibrations from water bound to DNA and N-H stretches in the DNA nucleobases is also present, however, the intensity of this band is decreased relative to the corresponding band in the spectrum of CT-DNA itself (blue curve in figure 6.6). This indicates that the water molecules bound to DNA is displaced upon DNA/polymer interaction as noted previously for DNA/poly(DAP-prop-TPT). This can be judged by comparison the relative intensity with the band at ~ 1700 cm^{-1} in the spectra of DNA and the product.

That DNA in the product material is evident from several bands observed in the 900-1750 cm^{-1} region of spectrum of the isolated DNA/poly(T-prop-Py) material. These features can be assigned to both phosphodiester backbone (900-1300 cm^{-1}) and the

nucleobases (1300-1800 cm^{-1}) of DNA molecules.[16, 71, 110, 235] However, although in this region of spectrum (900-1750 cm^{-1}) DNA itself contains similar spectral features, careful inspection shows some changes of the DNA-related peaks upon interaction of DNA with poly(T-prop-Py); see figure 6.6 and table 6.2.

In the spectrum of CT-DNA itself, the bands related to the PO_2^- symmetric stretching (ca. 1090 cm^{-1}) and C-O deoxyribose stretching (1064 cm^{-1}) were found to show a change in their intensities relative to one another upon DNA/poly(T-prop-Py) interaction. Furthermore, the PO_2^- asymmetric mode of vibration at 1234 cm^{-1} in the DNA itself is shifted toward lower frequency (1227 cm^{-1}) and appears with a shoulder at 1274 cm^{-1} in the DNA/poly(T-prop-Py) hybrid material. The polymer material has also three peaks in the 1000-1300 cm^{-1} region of spectrum, typically at 1076, 1138 and 1283 cm^{-1} which can be attributed to C-H and C-N in-plane deformation of the PPy unites [237], breathing mode of vibration of the PPy [237] and C-H or C-N in-plane deformation mode of vibration of the PPy rings [71, 237], respectively.

Moreover, C-N stretches of the thymine and adenine bases (1375 cm^{-1}) in the spectrum of CT-DNA, is increased in intensity and appeared at lower frequency (1366 cm^{-1}) in the spectrum of the DNA/poly(T-prop-Py) material. The enhancement in the intensity of such band may be due to the contribution of thymine of the polymer material, as the spectrum of pure polymer material also showed a band at 1360 cm^{-1} which is likely related to deformation vibration of C-H of the thymine rings.[238-240] Additionally, CT-DNA itself displays three peaks at 1418 cm^{-1} (due to C-H, N-H deformation and C-N stretch), 1493 cm^{-1} (related to C-N stretch, coupled with a ring vibration of guanine) and 1531 cm^{-1} corresponds to in-plane vibration of guanine and cytosine bases. In the pure polymer sample four peaks at 1417, 1463, 1515 and 1555 cm^{-1}, were observed. These peaks can be assigned to N-H and C-H deformations and C-N stretch vibrations of the thymine rings [240, 241], C-N stretch vibration of PPy rings [71, 237, 242] and/or deformation vibration of CH_3 in the thymine unites [238-240], C=C stretch mode of vibration of the pyrrole rings [234, 236], and C-C stretch mode of vibration of pyrrole rings [237, 243], respectively. However, In the 1400-1560 cm^{-1} region of spectra, the product material showed only one band at 1472 cm^{-1} which appeared as a relatively broad intense band with shoulders at lower and higher frequency of 1416 and 1527 cm^{-1}, respectively.

Furthermore, in the spectrum of the CT-DNA, three peaks were observed at 1609 cm^{-1} (due to in-plane vibration of adenine), 1661 cm^{-1} (related to C=O stretch of cytosine/thymine; in-plane vibration of thymine) and 1697 cm^{-1} corresponds mainly to C=O stretch of guanine. On the other hand, the product material shows only one band at 1684 cm^{-1} mainly due to C=O stretch of cytosine and thymine base, and the pure polymer displays a band at 1682 cm^{-1} which is mainly due to C=O stretch of thymine rings.[241, 244]

CT-DNA wavenumber (cm^{-1})	DNA/poly(T-prop-Py) wavenumber (cm^{-1})	Assignment[a]
ca. 1064	1067	C-O deoxyribose stretch
1090	1087	PO_2^- symmetric stretch
1234	1227	PO_2^- asymmetric stretch
-	1274[b]	
1375	1366	C-N stretch of guanine and cytosine
1493	1472	C-N stretch, coupled with a ring vibration of guanine
1531	1527[b]	In-plane vibration of guanine and cytosine
ca. 1609	-	In-plane vibration of adenine
1661	-	C=O stretch of cytosine/thymine
1697	1684	C=O stretch of guanine

Table 6-2: Some selected peaks of CT-DNA and CT-DNA-templated poly(T-prop-Py) material and their assignment. [a] Assignments of DNA bands were made with reference to literature [16, 71, 110, 235], and [b] peak observed as a shoulder.

Therefore, based on the FTIR data which showed several spectral changes of the DNA-related bands, as well as changes in poly(T-prop-Py) related bands, it can be concluded that the product material is not a simple mixture of DNA and polymer material, but instead a supramolecular polymer of DNA/poly(T-prop-Py) material involving non-

covalent interactions such as, electrostatic interaction and hydrogen bonding interactions between the two strand types.

6.3.2 XPS studies of DNA/poly(DAP-prop-TPT) and DNA/poly(T-prop-Py) materials

In order to provide additional chemical analysis of the isolated DNA/poly(DAP-prop-TPT) material, XPS studies were undertaken. The XPS survey spectrum of DNA/poly(DAP-prop-TPT) material (figure 6.7) reveals signals related to the O, N, C, S and P elements, which originate from either DNA or poly(DAP-prop-TPT).

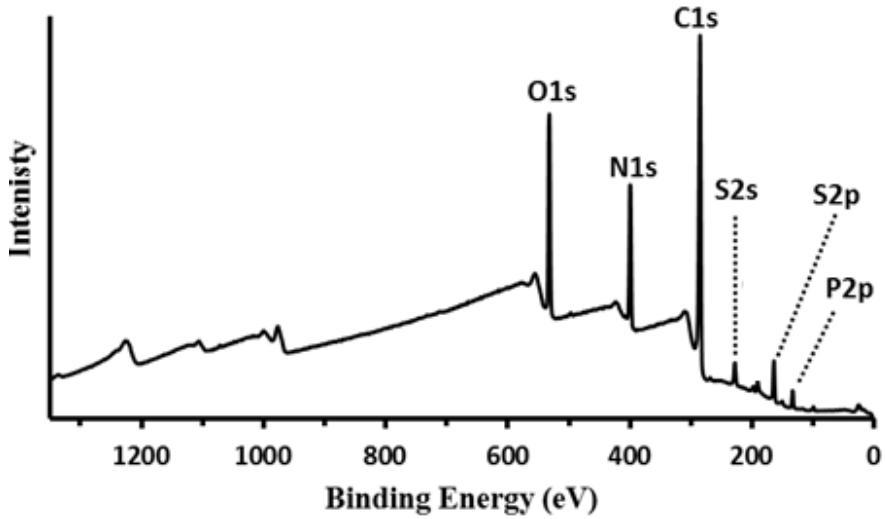

Figure 6-7: XPS survey spectrum of a sample of calf thymus DNA-templated poly(DAP-prop-TPT) material deposited upon a Si/native SiO_2 substrate.

The presence of the DNA is mainly indicated by P2p signal, whereas the S2p signal gives direct evidence of poly(DAP-prop-TPT) in the product material. Moreover, O1s signal is expected to be due to DNA, adsorbed oxygen from air and oxide layer of Si wafer. Likewise, N1s and C1s signals are originated from both DNA and poly(DAP-prop-TPT).

Examination of the S2p peak was used to confirm the presence of poly(DAP-prop-TPT) in the produced material. Figure 6.8 presents the high resolution XPS spectra of the S2p region of the isolated DNA/poly(DAP-prop-TPT) material, along with control sample of pure polyDAP-prop-TPT. Curve fitting of the S2p region (figure 6.8a) of the product material shows S2p doublets ($S2p_{3/2}$ and $S2p_{1/2}$) at binding energies of 163.9 and 165.1 eV, respectively, and the position of $S2p_{3/2}$ is consistent with the thiophene sulphur.[16, 245] Moreover, the S2p signal of the pure polyDAP-prop-TPT (figure

6.8b) also shows such an S2p doublets structure, but with a slight shift toward high binding energy, again suggesting interactions with groups on the DNA on DNA/poly(DAP-prop-TPT) nanowires formation.

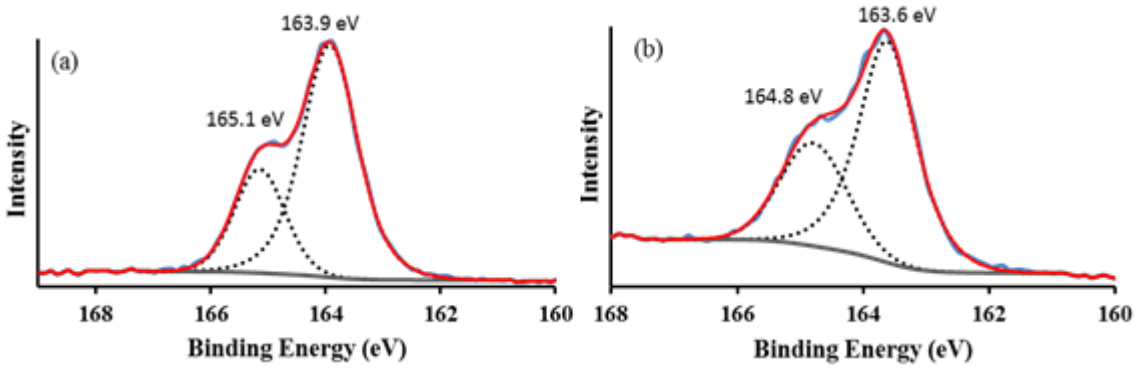

Figure 6-8: High resolution XPS spectra of S2p region of (a) calf thymus DNA-templated poly(DAP-prop-TPT) material and (b) pure poly(DAP-prop-TPT). Blue solid line represents raw data, total fits is indicated by red line and black dashed lines are for component peaks.

Further evidence for the existence of the poly(DAP-prop-TPT) along with the confirmation the presence of DNA in the produced material is provided by observation of the N1s signals (figure 6.9). Curve fitting of the N1s region of the isolated DNA/poly(DAP-prop-TPT) material (figure 6.9a), is consistent with three distinct peaks centred at 398.6, 400 and 401.5 eV, respectively. The position of these peaks is slightly shifted when comparing them with the corresponding peaks in N1s region of pure poly(DAP-prop-TPT) (figure 6.9b), which also displays three components, centred at 399.2, 400.3 and 401 eV, respectively, with a peak area ratio of ~ 4:2:1. The order of peak areas is consistent with the ratio between nitrogen atoms in the DAP-prop-TPT structure (figure 6.4).

The N1s signal of the free calf thymus DNA (figure 6.9c) was fit with only two components located at 399 and 400.2 eV, respectively. The peak at lower binding energy can be assigned to sp^2-bonded N atoms in the aromatic rings of DNA, whereas the higher energy peak due to and sp^3-bonded N atoms in exocyclic group amino group ($-NH_2$).[119, 120, 122] Therefore, in the N1s spectra of the product material, the two peaks at binding energy of 398.6 and 400 eV, respectively, can be assigned to the nitrogen atoms of the DNA molecules, as well as a contribution from neutral nitrogen atoms of polypyrrole rings in TPT units, and the nitrogen atoms of the purine fragment of the poly(DAP-prop-TPT). On the other hand, the additional lower intense peak which

is absent in the spectrum of free DNA, and has higher binding energy at 401.5 eV can be assigned to polaron structure ($C\text{-}N^{+}$) of polyTPT.[246]

In summary, the XPS spectra of the produced DNA/poly(DAP-prop-TPT) supramolecular material, have revealed a significant contributions from poly(DAP-prop-TPT), which consequently can indicate that DNA templates have a coverage of the polymer materials consistent with the AFM images presented in next section.

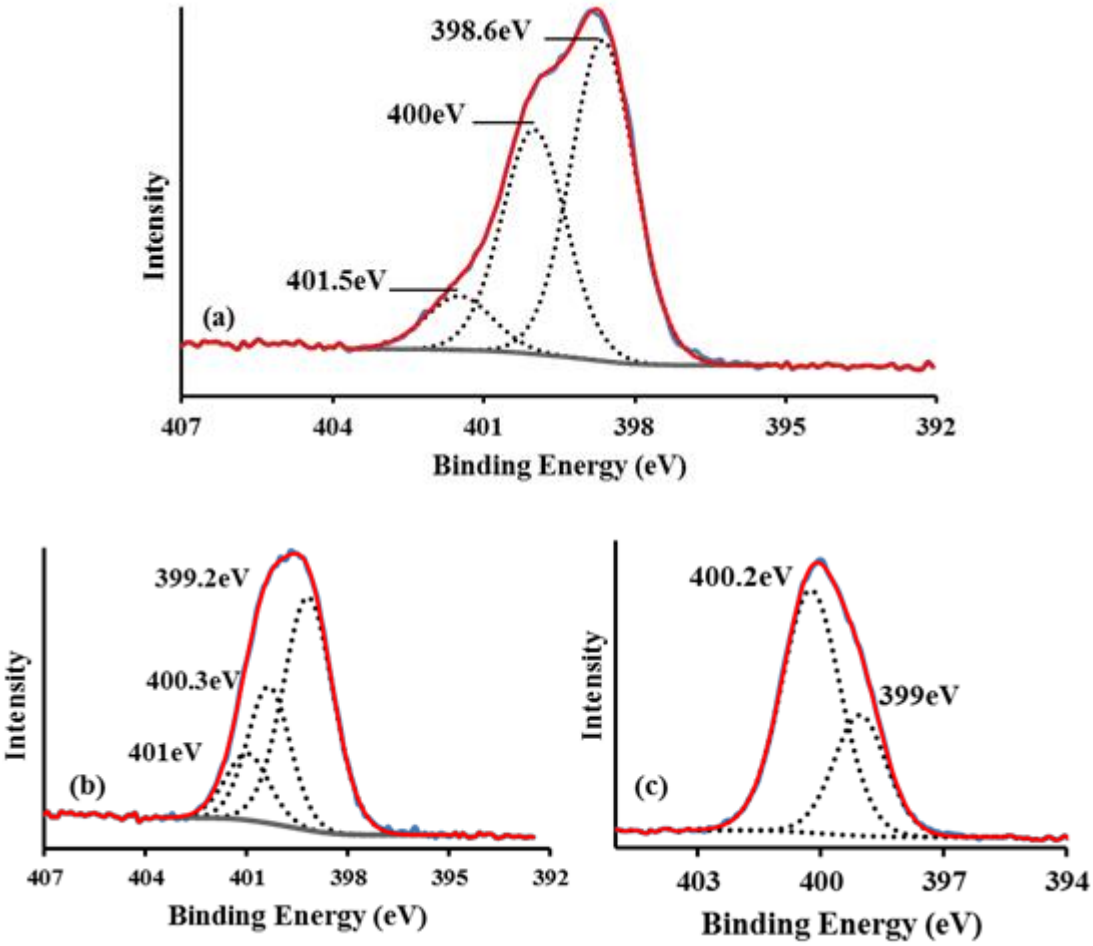

Figure 6-9: High resolution XPS spectra of N1s region of (a) calf thymus DNA-templated poly(DAP-prop-TPT) material. (b) Pure poly(DAP-prop-TPT) and (c) calf thymus DNA. Blue solid line represents raw data, total fits is indicated by red line and black dashed lines are for component peaks.

Further chemical analysis of the isolated DNA/poly(T-prop-Py) material is carried out using XPS studies. XPS survey spectrum of the product material (figure 6.10) indicates the presence of the elements O, N and C arising from DNA and poly(T-prop-Py), and P which is characteristic of DNA alone.

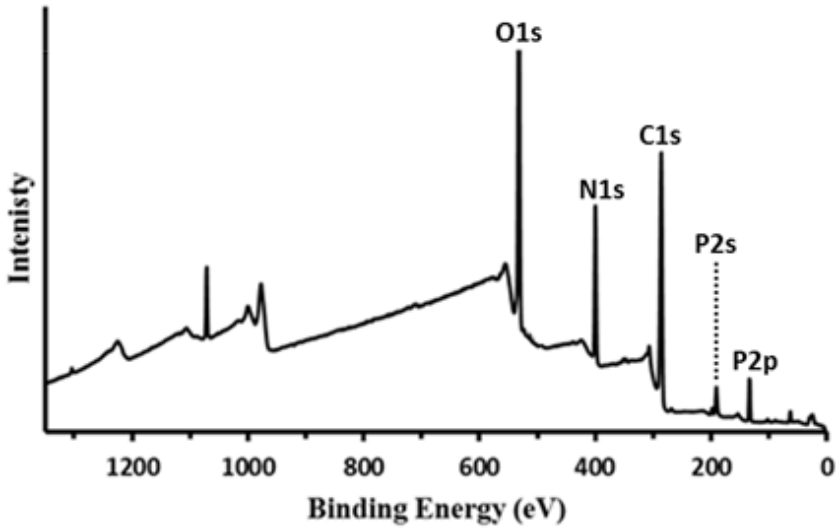

Figure 6-10: XPS survey spectrum of a sample of calf thymus DNA-templated poly(T-prop-Py) material deposited upon upon a Si/native SiO_2 substrate.

Observation of the N1s region can be used to confirm the presence of the CP and DNA in the product material. Three peaks located at binding energies of 399.1, 400.5 and 401.6 eV are resolved upon curve fitting of N1s spectrum of the DNA/poly(T-prop-Py) material (figure 6.11a). Moreover, curve fitting of the N1s region of the poly(T-prop-Py) itself (figure 6.11b) reveals also three peaks located at 399.6, 400.4 and 401.8 eV, respectively. In N1s of CP material, the most two intense peaks are at 400.4 and 399.6 eV and may be assigned to nitrogen atoms of the thymine group [247] and a contribution of the neutral nitrogen atoms of CP.[246] Contributions to a very weak peak at 401.8 eV can be assigned to cationic species (polaron) of polypyrrole units.[246] On the other hand, as discussed earlier in this section, curve fitting of the N1s region of the CT-DNA itself (figure 6.9c) was fit with only two components located at 399 and 400.2 eV, which fall in reasonable agreement with the reported binding energies of DNA.[119, 120, 122]

Therefore, in the N1s spectra of the DNA/poly(T-prop-Py) product material, a lower binding energy peak at 399.1 eV, is mainly due to the presence of DNA in the product material. The peak with binding energy of 400.5 eV, tends to dominant, arising from DNA and poly(T-prop-Py). A weak peak with binding energy of 401.6 eV can be attributed to the presence of CP. It is could be concluded that, the XPS data of the isolated DNA/(polyT-prop-Py) material, have revealed a major contributions from poly(T-prop-Py). This can consequently indicate DNA templates to be coated with polymer coverage as it will discuss in detailed in next section.

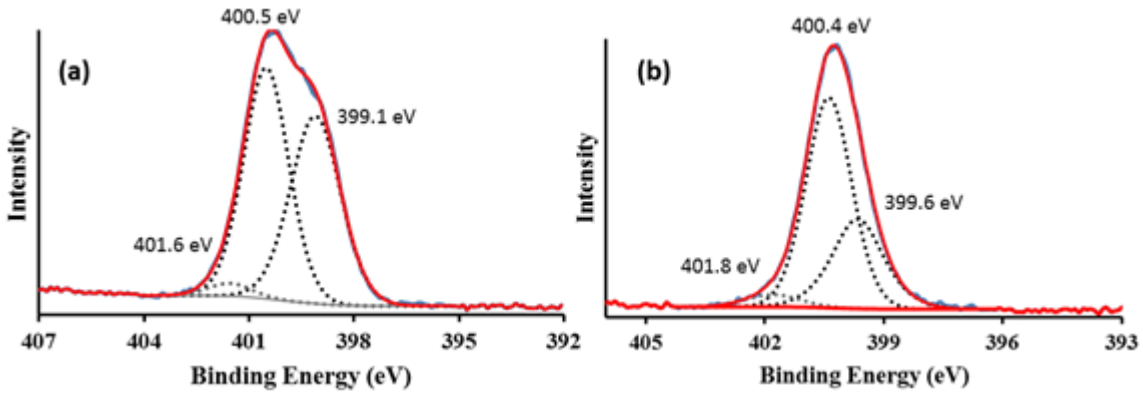

Figure 6-11: High resolution XPS spectra of N1s region of of (a) calf thymus DNA-templated poly(T-prop-Py) material, and (b) spectra of control sample of poly(T-prop-Py), immobilised upon a Si/native SiO_2. Blue solid line represents raw data, total fits is indicated by red line and black dashed lines are for component peaks.

6.3.3 Atomic force microscopy (AFM) characterisation of DNA/poly(DAP-prop-TPT) and DNA/poly(T-prop-Py) nanostructures

In order to elucidate information regarding the size and structural morphology of the produced DNA/CP material, atomic force microscopy (AFM) measurements were carried out. For AFM studies samples were prepared by aligning the DNA/CP nanostructures on TMS-modified Si/SiO_2 substrate using similar procedures as previously described in chapter 3, section 3.2.8.

Previously, AFM studies of samples of DNA-templated polypyrrole nanowires taken one hour after addition of oxidant to DNA/pyrrole containing solutions, showed individual nanowires with continuous coverage of the polymer materials along the DNA strands (figure 6.12a). However, difference in the polymer thickness along the length of DNA templates (figure 6.12b), was clearly observed.[71] Moreover, Pruneanu *et al*., have reported upon DNA-templated polypyrrole nanowires.[72] Here, the authors demonstrated that at short reaction time ~ 3 hours, thin nanowires can be prepared (figure 6.12c), but over longer incubation time the nanowires undergo a self-assembly process to produce rope-like structures (figure 6.12d). AFM studies indicated that these nanoropes are formed by twisting individual nanowires around each other. This was evident from the frayed ends of the structure where individual nanowires were observable.

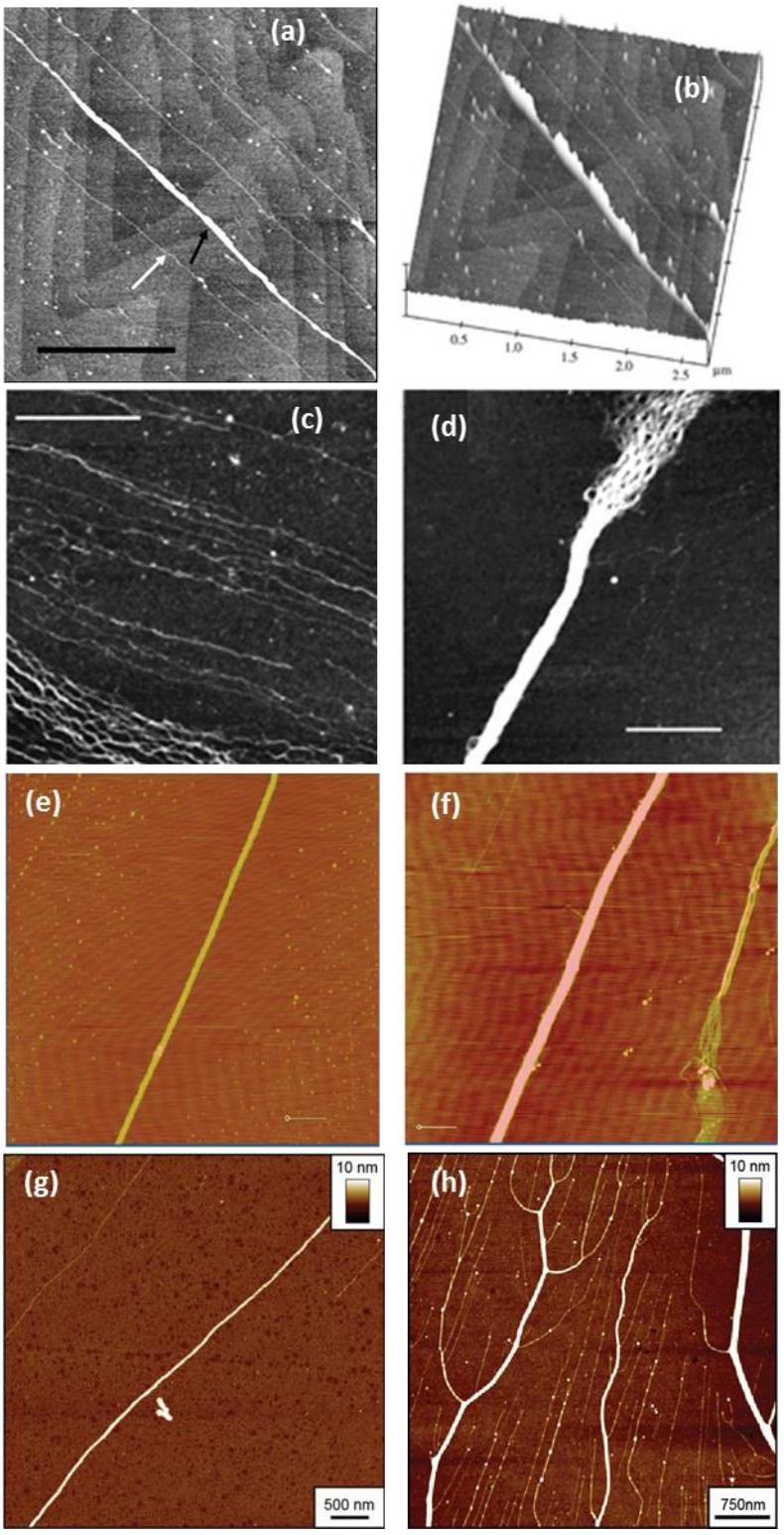

Figure 6-12: (a) AFM image of DNA/polypyrrole nanowire (scale bare is 1µm and height scale = 4 nm), and (b) the corresponding 3D image shows the height variation along a single nanowire, height scale = 7 nm.[71] (c) and (d) AFM images of DNA/polypyrrole nanowires at reaction times of 3 and 48 houres, respectively, (scale bare is 1µm and height scale = 4 nm).[72] (e and f) AFM images of DNA/Polyindole nanowires at reaction times of 24 hour and 7 days (scale bare is 1µm and height scale = 45 and 40 nm, respectively).[73] (g and h) AFM images of DNA/TPT nanowires at 24 hours reaction time.[16]

Recently, AFM images of samples of DNA/polyindole nanowires [73] showed smooth and regular structures after 24 hours reaction time (figure 6.12e). With increased reaction time to 7 days, thicker structures were observed (figure 6.12f). More recently, Watson *et al.*, (2012) have stated that after 24 hours incubation time, AFM studies showed regular and continuous coverage of the DNA templates with polyTPT material (figure 6.12g). Additionally, at the same reaction time, rope-like assemblies of nanowires (figure 6.12h) were also noted with 'branches' extended out from the main body of the nanowire.[16]

AFM measurements were carried out upon samples of DNA/poly(DAP-prop-TPT) structures, aligned upon TMS-modified silicon substrate after different reaction times, typically 5, 10 and 30 minutes and 1, 4 and 24 hours. Figure 6.13a-f depicts AFM height images of some typical examples of DNA/poly(DAP-prop-TPT) structures isolated from reaction solution at different incubation times. These images provide information regarding the formation stages of the poly(DAP-prop-TPT) at DNA templates.

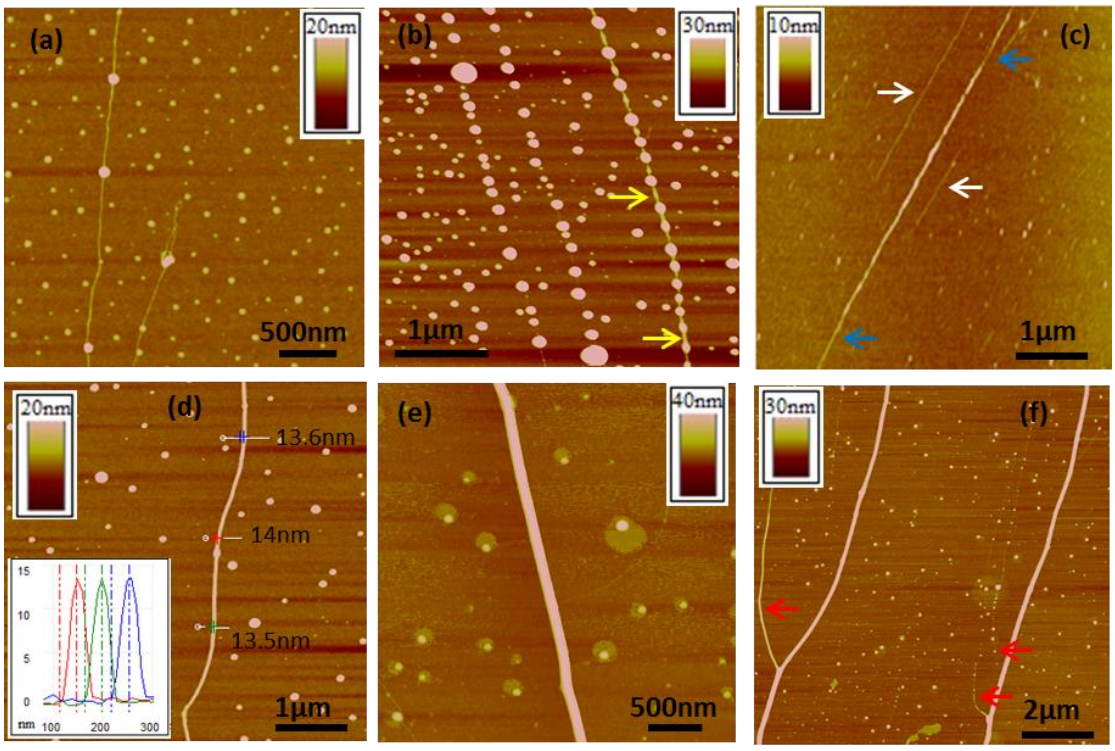

Figure 6-13: Tapping mode™ AFM height images of DNA/poly(DAP-prop-TPT) nanostructures aligned on TMS-modified Si/SiO_2 substrates after 5,10 and 30 minutes and 1, 4 and 24 hours incubation time, respectively.

AFM imaging of the sample isolated after a reaction time of 5 minutes shows evidence for the formation of CP as approximately spherical particles bound to DNA strands at random points along the duplex structures (figure 6.13a). These particles bound to the DNA at low density (~2 particles/micron) with bare DNA clearly evident between adjacent particles. A range of particle size, ranging from 18-28 nm is observed. Upon increasing the reaction time to 10 minutes, (figure 6.13b) the density and size of the polymer particles on DNA templates are noticeably increased. In this case the CP particles have a density ~ 6 particles/micron, and diameters ranging from 13-47 nm. At this incubation time, however, although the majority of the polymer particles attached to DNA still have their initial spherical shape, one can also see some which have become extended along the DNA axis (figure 6.13b, yellow arrows).

Furthermore, a sample taken after 30 minutes reaction time indicated that almost all of the isolated polymer particles have amalgamated into one another forming a continuous coverage along the template strands (figure 6.13c). However, material isolated at this time generally still has a quite irregular morphology with some regions uncoated, or at best, coated with a very thin polymer material (figure 6.13c, blue arrows). There are also some bare DNA molecules present (white arrows). After additional time (one hour), nanostructures are evident which show a regular and smooth structure with complete and continuous coverage of the duplex DNA by the polymer material (figure 6.13d). At this reaction time, the measured height of structures is consistent (~ 14 nm) along their length, see cross sections in figure 6.13d (inset).

Increasing the reaction time to 4 hours, yields nanostructures with increased diameters (~ 21 nm), see figure 6.13e. At even longer incubation time (24 hours), thicker nanostructures was observed (figure 6.13f) with structure height > 30 nm which is likely formed due to the assembly of individual "nanowires", forming rope-like structures. The formation of such rope-like structure was previously reported of polymer nanowires prepared using DNA as a template.[72] Here, the assembly of individual "nanowires" to form ropes is evident from branching (red arrows in figure 6.13f) which can be seen to extend out from the main "nanowires" structure.

Based on these finding, it could be concluded that the formation of poly(DAP-prop-TPT) on DNA takes place initially through the low density of binding spherical-shaped conducting polymer particles on the duplex DNA templates. The size and density of these polymer particles on the template increases as the reaction proceeds, producing

"bead-on-a-string" appearance. With increasing reaction time, the loading of DNA with CP is increased and the CP begins to undergo a change in shape, becoming elongated along the template axis and merge into one another, finally producing CPs nanowires with highly smooth and regular structure.

Furthermore, these studies suggested that the best incubation time for producing single "nanowires" with continuous and regular morphology was after one hour reaction time. It was also observed that the prepared DNA/poly(DAP-prop-TPT) nanostructures have shown relatively similar morphologies to other polymer nanowires prepared using DNA as a template.[16, 72, 73] Namely, the uniformity of the polymer coverage is improved as the time reaction increased, as well as longer reaction time result in the formation of rope-like structures. However, although complete, regular and smooth appearance of the DNA/poly(DAP-prop-TPT) nanowires has achieved at shorter reaction time (1 hour) in comparison with the earlier mentioned examples of polymer nanowires, a large number of agglomerated materials were also observed on the substrate surface.

Therefore, in order to prepare DNA/poly(DAP-prop-TPT) nanostructures with highly smooth and uniform structure and avoid ropes formation of these nanostructures, AFM further characterisation was carried out upon samples taken after one hour reaction time. The reaction solution (DNA/polyDAP-prop-TPT/$FeCl_3$) was also centrifuged at 6000 rpm for approximately 5 minutes. After this, the lower section of the reaction mixture, which was expected to contain mainly nanowires, was aligned upon TMS-modified Si/SiO_2 substrates for AFM analysis.

Figure 6.14a-d displays AFM height images of selected examples of the DNA/poly(DAP-prop-TPT) nanostructures aligned upon Si substrate 1 hour after the addition of $FeCl_3$ to the DNA/DAP-prop-TPT solution system. These images show 1-D nanowire-like morphology of the product material with different sizes (diameters range from 2 – 24 nm). It is therefore clear that the polymerisation growth was influenced by the DNA templates, which is evident from the height of the DNA/poly(DAP-prop-TPT) nanostructures (> 2 nm) as the height of free DNA molecules is (≤ 2nm).

Moreover, as found in the time dependent studies, samples of DNA/poly(DAP-prop-TPT) nanostructures taken after an incubation time of 1 hour showed smooth uniform morphologies with the DNA templates coated with polymer chains along the whole length. The uniformity of these coatings is similar to some previous examples of

DNA-templated polymer nanowires [16, 72, 73], from our group and present a significant enhancement to that observed in previous examples of DNA-templated iron-based nanowires (DNA/Fe_3O_4 and DNA/Fe nanowires, chapter 3 and 4) and other metal-based nanowires.[18, 64-66] Interestingly, AFM studies of the isolated DNA/poly(DAP-prop-TPT) nanostructures after the reaction solution was centrifuged showed noticeably improvements in the surface background appearance as little or no evidence for the presence of any agglomeration of non-templated material.

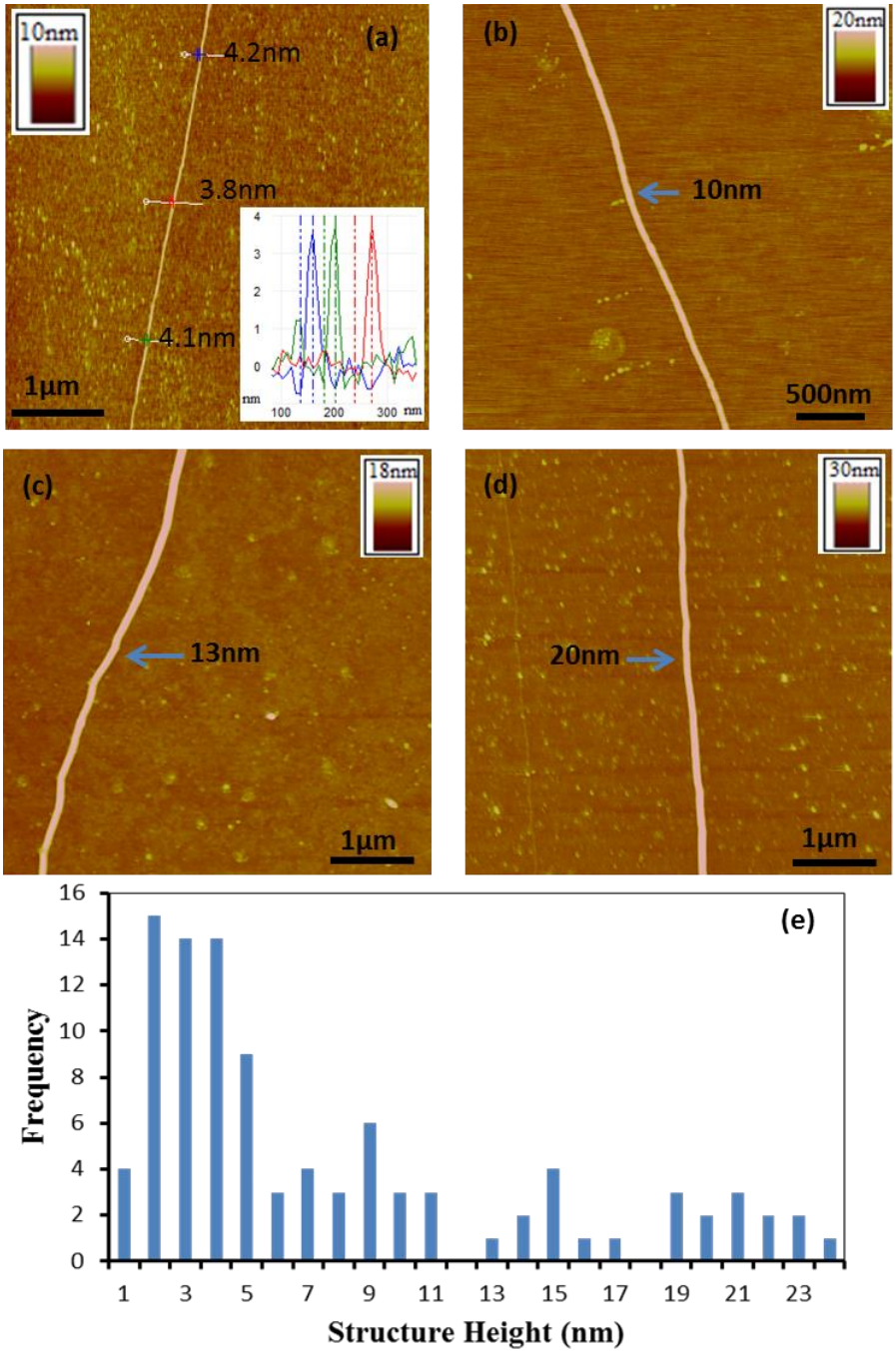

Figure 6-14: AFM studies of centrifuged samples of DNA/poly(DAP-prop-TPT) "nanowires" prepared using $FeCl_3$ as oxidant material. (a-d) AFM height images of the DNA/poly(DAP-prop-TPT) "nanowires" immobilised upon a Si/native SiO_2 substrate, after 1h, from addition of $FeCl_3$. (e) Histogram of the size distribution of the DNA/poly(DAP-prop-TPT) "nanowires".

The success of the centrifuge process for separation of the nanowires from non-templated material can be visualised by comparing the AFM images of the isolated DNA/poly(DAP-prop-TPT) nanowires in figure 6.13 and figure 6.14. Figure 6.14 shows individual "nanowires" aligned upon noticeably cleaner backgrounds. On the other hand, in figure 6.13 where there was no centrifuge process carried out, the substrate shows a number of globular features which are expected to be non-templated polymer.

Whilst the DNA templates were found to be coated with regular and smooth coatings of the polymer material, as AFM line profiles indicated, the wire diameters are consistent along their length, see figure 6.14a inset. These AFM studies revealed nanowires with a considerable variation in their heights (2-25 nm). For this reason, a statistical treatment of AFM data was carried out in order to evaluate the size distribution of the produced DNA/poly(DAP-prop-TPT) nanowires. The heights (i.e. diameter) of 100 nanowires were measured using AFM line profiles, and the frequency plotted as a function of nanowire diameter. The resulting histogram (figure 6.14e) revealed a relatively broad size distribution, with structures up to 25 nm in height. The data also showed a distinctive polymodal distribution with four modal values identified at 1–5 nm, 6–11 nm, 13–17 nm and 19–24 nm, respectively.

In summary, AFM data provide evidence for the formation of a supramolecular polymer nanowires formed through self-assembly of DNA and poly(DAP-prop-TPT) strands. Moreover, DNA is found to be a highly effective template for directing the growth of polycationic poly(DAP-prop-TPT) into organised these 1-D hybrid nanostructures.

AFM was also used to characterise the morphology of the produced DNA-templated poly(T-prop-Py) nanowires. AFM images were first recorded for samples isolated directly from the reaction solution (no centrifuge process was applied) after one hour incubation time. These images (figure 6.15a and b) show structures with different heights which are surrounded by a large number of particles on the substrate surface. These are likely to be non-templated polymer material. For this reason, the product material in reaction solution was centrifuged at 6000 rpm for ~ 5 minutes in an attempt to purify the DNA/poly(T-prop-Py) nanowires. After this, the lower section of the reaction mixture was aligned upon TMS-modified Si/SiO_2 substrates for AFM analysis.

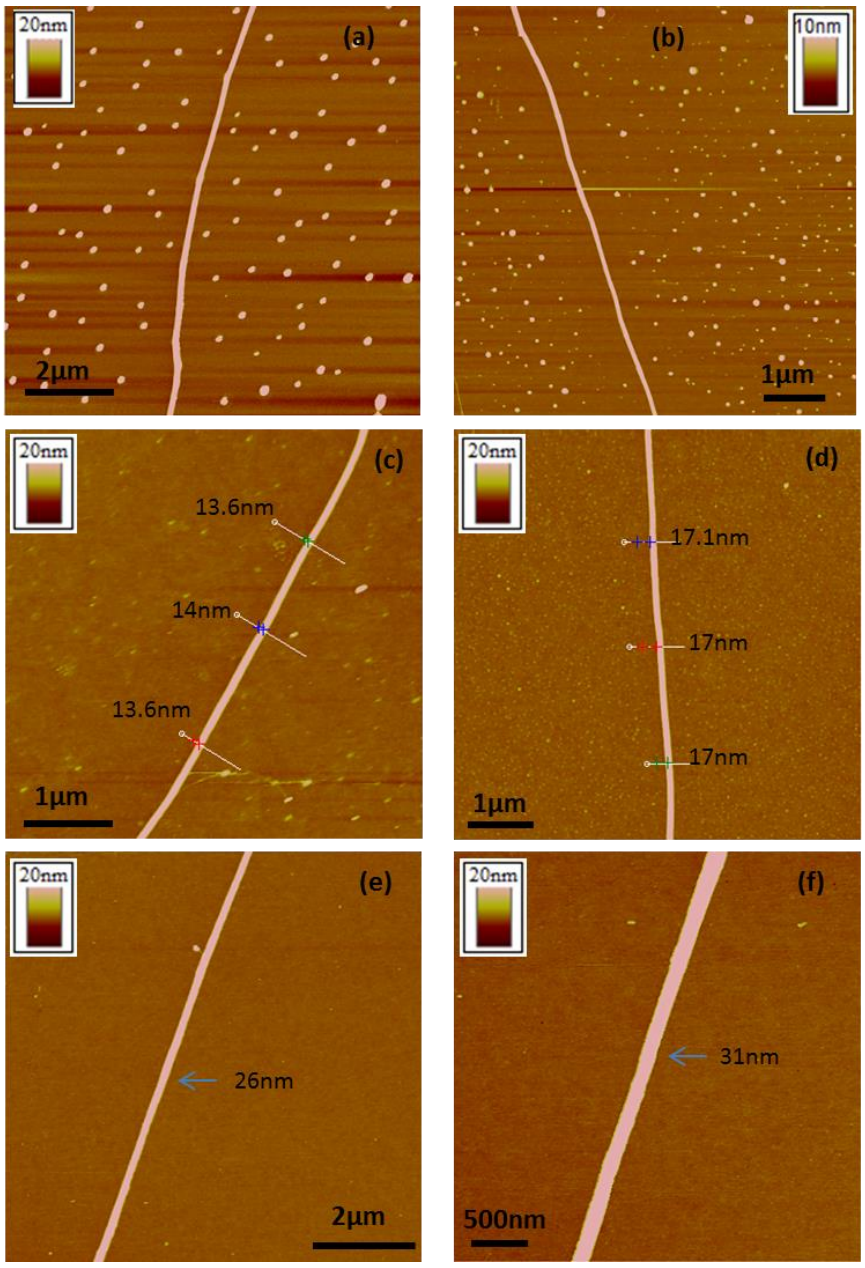

Figure 6-15: Tapping mode™ AFM height images of DNA/poly(T-prop-TPT) nanostructures aligned on TMS-modified Si/SiO_2 substrates after 1 hour incubation time. (a) and (b) AFM images of samples isolated from the reaction solution before the centrifuge process was taken place and, (c-F) AFM images of centrifuged samples.

AFM height images of material from this modified method are depicted in figure 6.15 c-f. These images show individual nanowires with different sizes (diameters range from 14 – 31 nm), to be aligned upon a significantly cleaner backgrounds. Thickening of the produced DNA/poly(T-prop-Py) nanowires with respect to the heights of bare DNA ($\leq$ 2 nm), is clearly evident, and indicates that the DNA molecules coated with the polymer material. The DNA/poly(T-prop-Py) nanowires were found to show smooth and uniform structure with continuous coverage of the DNA strands by

T-prop-Py desired polymer. The uniformity of the polymeric coverage on the DNA template molecules is similar to what was seen for DNA/poly(DAP-prop-TPT) nanowires.

It should be noted that the thicker structures isolated after 1 hour reaction time do not appear to be due to the assembly of individual nanowires. This is because there was no evidence for the presence of any branching extending out from the main body of DNA/poly(T-prop-Py) nanowires. It is therefore suggested that the variation in the structure heights of nanowires isolated after 1 hour reaction time is due to the deposition of different amount of material upon the DNA templates.

In order to evaluate the size distribution of the DNA/poly(T-prop-Py) nanowires, a statistical treatment of the average diameters recorded for 100 nanowires isolated after 1 hour incubation time was performed as described before for DNA/poly(DAP-prop-TPT) nanowires. The resulting histogram (figure 6.16) displays a broad distribution with structures up to 35 nm in height recorded. The data also shows a number of smaller structures with diameters < 3 nm, indicating not all the DNA molecules are templated with polymer material.

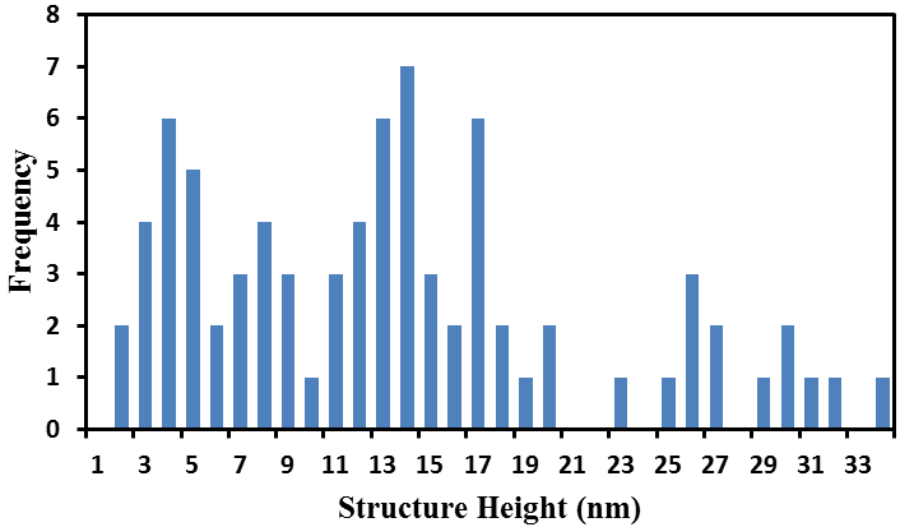

Figure 6-16: Histogram of the size distribution of the DNA/poly(T-prop-Py) nanowires.

As mentioned earlier in this section, previous AFM studies of the polymer nanowires prepared using DNA as a template [72, 73] reported changes in the structure of the polymer nanowires at longer incubation time, in which individual nanowires assemble together, forming rope-like structures. Evidence of similar nanoropes behaviour for DNA/poly(T-prop-Py) was observed for material isolated after 24 hours reaction times.

Figure 6.17 a and b, illustrate AFM images of the DNA/poly(T-prop-Py) nanowires aligned upon TMS-modified silicon substrate after 24 hours incubation times. These images showed rope-like assemblies of DNA/poly(T-prop-Py) nanowires with diameters up to 60 nm. The formation of such structures is clearly evident from the additional branches (white arrows in figure 6.17a and b) which can be seen extending out from the main body of structures.

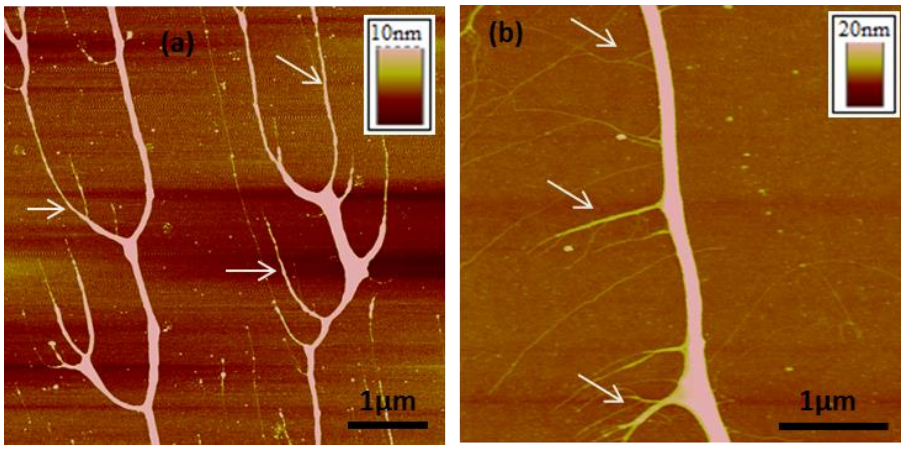

Figure 6-17: AFM height images of the DNA/poly(T-prop-Py) nanowires immobilised upon a Si/native SiO_2 substrate, after 24 hours incubation times.

6.3.4 Electrical characterization of DNA/poly(DAP-prop-TPT) and DNA/poly(T-prop-Py) nanostructures using electrostatic force microscopy (EFM)

The electrical properties of the DNA/poly(DAP-prop-TPT) "nanowires" were examined using the non-contact electric force microscopy (EFM) technique. This technique can provide straightforward method to investigate the electrical behaviour of the sample under investigation.

Figure 6.18 illustrates the EFM data of a DNA/poly(DAP-prop-TPT) nanowire aligned upon a TMS-modified silicon substrate with a thermally growth SiO_2 layer. The height image (figure 6.18a), showed the nanowire to have a diameter of 20 nm. This nanowire appears dark in the corresponding EFM phase images (figure 6.18 b-e) which were recorded at dc potentials of +9 and -9 V. The appearance of such dark contrast (negative phase shift) relative to the background at different applied bias confirms that the DNA/poly(DAP-prop-TPT) nanostructures are electrically conductive and a genuine nanowire.[16, 66, 73, 212] It was observed that the sizes of the phase shifts produced by the nanowire in the EFM phase images are wider than the actual diameter of the

nanowire as appeared in the AFM height image. This occurs because of the diffuse nature of the electric field originating from the DNA/poly(DAP-prop-TPT) sample. Additionally, the magnitude of the phase shifts associated with the DNA/poly(DAP-prop-TPT) nanowire showed a parabolic dependence upon the dc bias applied to the sample, see Figure 6.18h. This confirms that the tip-sample interactions are dominated by capacitance effects and trapped charge makes no significant contribution to the data recorded for DNA/poly(DAP-prop-TPT) nanowire.[66, 72, 73, 106] These EFM data then show that there is a continuous conduction pathway along the whole length of the produced DNA/poly(DAP-prop-TPT) nanowires. This provides further evidence for the nanowire's structure to consist of regular and continuous coating of conducting poly(DAP-prop-TPT) material around DNA templates.

In conculsion, it has been confirmed that conductive and highly uniform DNA/poly(DAP-prop-TPT) nanowires can be prepared by polymerisation of 2,6-diaminopurine-propyl-2,5-bis-dithenyl pyrrole (DAP-prop-TPT) with $FeCl_3$ in presence of DNA molecules. Moreover, the resulting nanowires with functional groups are expected to allow their use as building blocks for the construction of functional architectures.

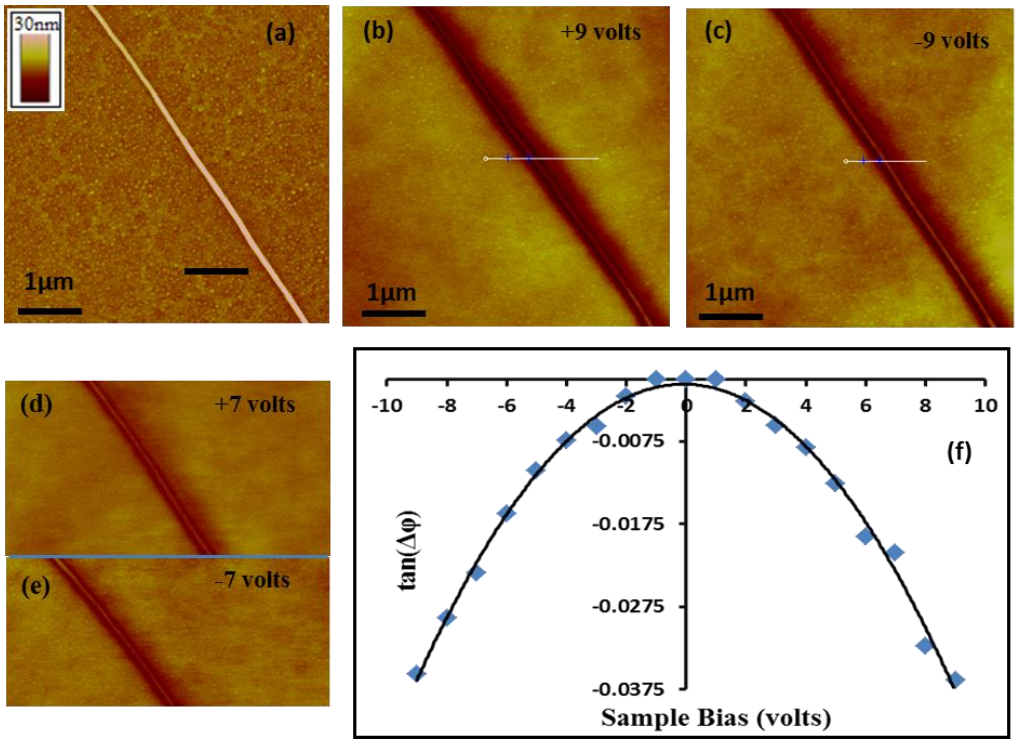

Figure 6-18: Electrostatic force microscopy data of DNA/poly(DAP-prop-TPT) nanowire aligned upon a n-Si<100>/200 nm SiO_2 wafer. (a) AFM height image of a nanowire with average diameter of 20 nm. (b, c, d and e) the EFM phase images of the nanowire in (a) at different sample biases, phase scale of 5° are. (f) Plot of the tangent of the nanowire phase shift as a function of applied voltage.

EFM was also used to probe the electronic properties of the DNA/poly(T-prop-Py) nanowires in a manner described before for DNA/poly(DAP-prop-TPT) nanowires. Figure 6.19 shows a series of EFM phase images along with the corresponding height image of the DNA/poly(T-prop-Py) nanowire. In the height image (figure 6.19a) a single 1-D wire-like structure dominants and this has an average diameter of roughly 12 nm. In the corresponding phase images (figure 6.19 b and c) which recorded at dc potentials of +7 and -7 V, respectively, the position of the nanowire can be clearly seen as a uniform dark contrast relative to background. Such dark contrast (negative phase shift) associated with the nanowire irrespective of the magnitude or sign of the applied bias, indicates DNA/poly(T-prop-Py) to be electrically conducting.[66, 72, 73, 212] Furthermore, the magnitude of the phase shifts displayed a parabolic dependence upon the dc bias applied to the sample (Figure 6.19d), confirming that the tip-sample interactions are dominated by capacitance effects.[66, 72, 73] It is worth noting here that the negative phase shift associated with the whole nanowire's structure indicates the DNA/poly(T-prop-Py) nanowires have a continuous coverage of conductive poly(T-prop-Py) material along the DNA templates.

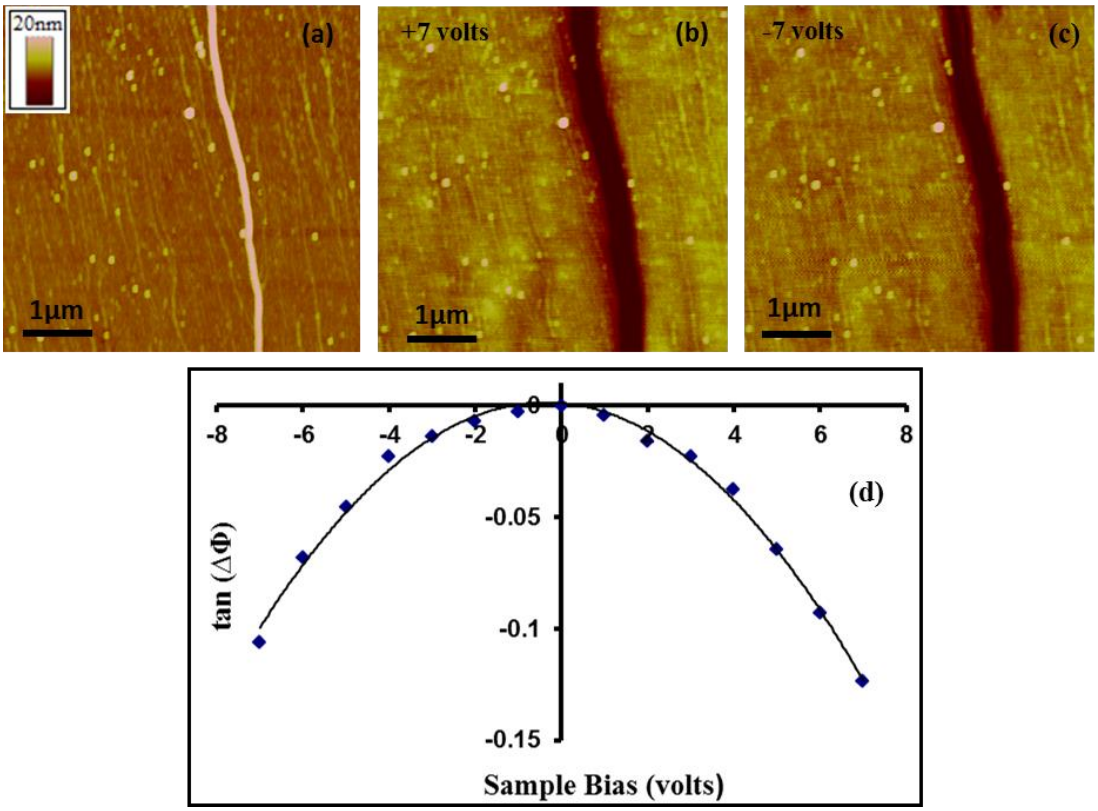

Figure 6-19: (a) Height image of DNA/poly(T-prop-Py) nanowire with average diameter of 12 nm immobilised upon Si/SiO_2 substrate diameters. (b and c) The corresponding EFM phase images at sample biases of +7 and -7 voltas, respectively, phase scale is 5°. (d) Plot of the tangent of the nanowire phase shift as a function of applied voltage

Based on spectroscopic and scanning probe microscopy, it can be concluded that two types of DNA-templated supramolecular polymer nanowire have been prepared via polymerisation of DAP-prop-TPT and T-prop-Py, respectively, with $FeCl_3$ in presence of DNA molecules. Moreover, it is expected that these two types of nanowires have potential for interaction by means of complementary hydrogen bonding between diaminopurine and thymine substituent groups of the conducting polymers. This is explored in the next section.

6.4 Atomic force microscopy (AFM) studies of a mixture of two types of DNA-templated supramolecular polymer nanowire

In order to establish changes in morphology behaviour of the produced polymer-based nanowires upon mixing them together and discover if these complementary nanowires can come together to form larger structures, AFM studies were carried out. For AFM studies, DNA/poly(DAP-prop-TPT) and DNA/poly(T-prop-Py) nanowires were first prepared and centrifuged as described earlier in sections 6.2.4. 50 µL of former nanowires was then added to 50 µL of latter and the resulting material in reaction solution was left to incubate at room temperature. The resulting material present in the reaction solution was isolated at different times and then aligned upon TMS-modified silicon substrate. In order to achieve this, 5 µL of the resulting solution was taken at different reaction times (typically 1 and 24 hours, and 22 days), and applied to the substrate surface and left to stand for approximately 1 minute before the residual solution was withdrawn from the substrate surface using micropipette. Moreover, in order to make a reliable AFM investigation, AFM measurements were also carried out upon control samples of pure DNA/poly(DAP-prop-TPT) and DNA/poly(T-prop-Py) nanowires with the same age as the samples isolated from the mixture solution.

AFM images of the material isolated from the mixture reaction along with the control samples are illustrated in figure 6.20. The first column (1a, 2a and 3a) shows AFM height images of material taken after 1 hour reaction time from the reaction solutions. AFM images (figure 6.20, 2a and 3a) of DNA/poly(DAP-prop-TPT) and DNA/poly(T-prop-Py) nanowires, respectively, displayed as expected chains of polymer-covered DNA nanowires with smooth and uniform morphology.

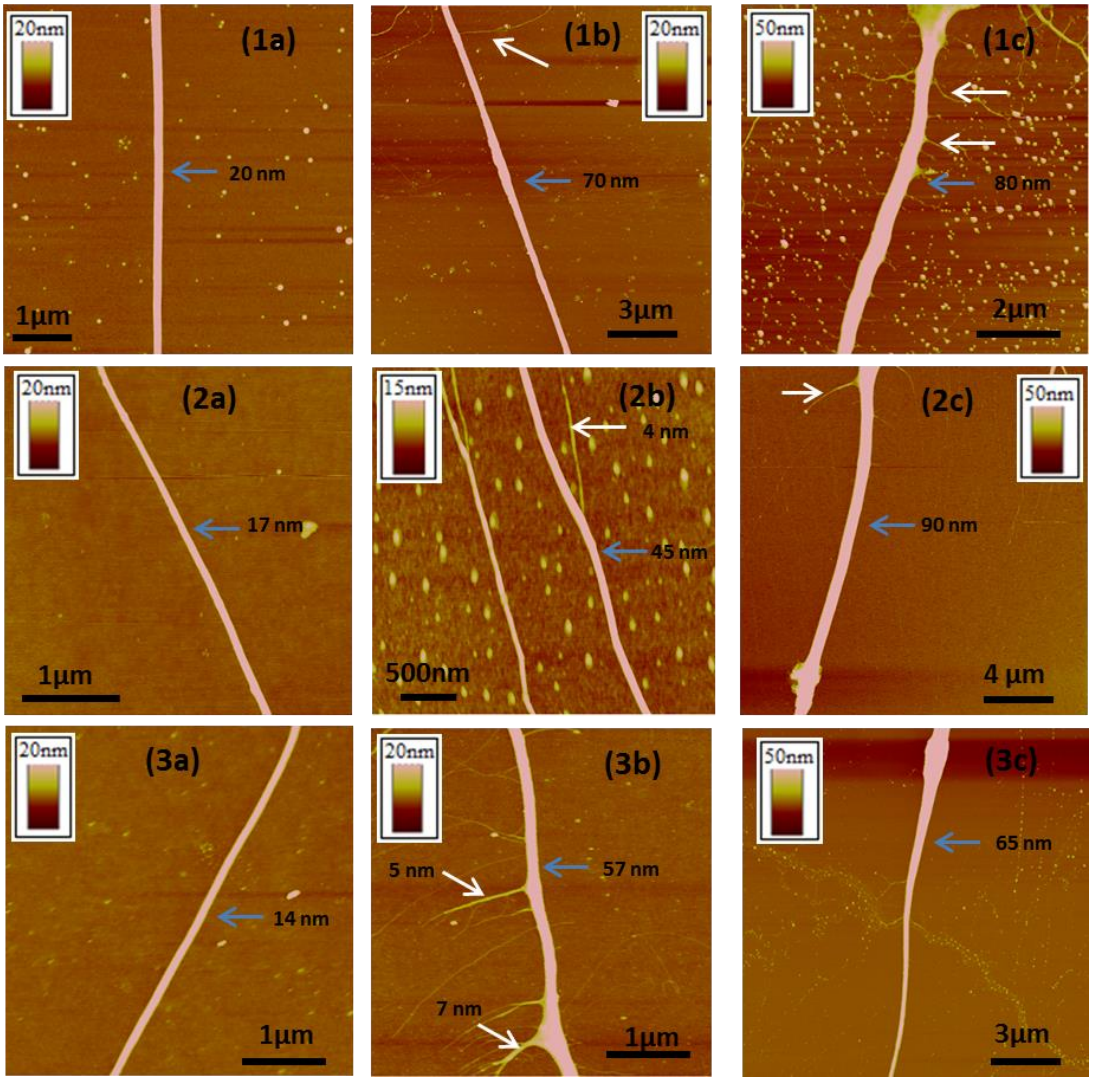

Figure 6-20: AFM height images of material isolated from a mixture of DNA/poly(DAP-prop-TPT) and DNA/poly(T-prop-Py) nanowires (row 1 a-c), along with control samples of DNA/poly(DAP-prop-TPT) nanowires (row 2 a-c), and DNA/poly(T-prop-Py) nanowires (row 3 a-c). All samples were aligned upon TMS-modified Si/SiO_2 substrates at incubation times of 1 hour (first column), 24 hours (second column) and 22 days (third column), columns are numbered from left to right.

Similarly, AFM image of material isolated from the reaction solution containing a mixture of two complementary nanowires (figure 6.20, 1a) showed 1-D wire-like structure with average diameter of 20 nm. This structure is suggested to be either DNA/poly(DAP-prop-TPT) or DNA/poly(T-prop-Py) nanowires and cannot be considered as assemblies of complementary nanowires. This is because the structure's diameter falls in reasonable agreement with the size distributions of DNA/poly(DAP-prop-TPT) nanowires (figure 6.14e) and DNA/poly(T-prop-Py) nanowires (figure 6.16). Additionally, the structure's appearance is very similar to what was seen for control samples.

Upon increasing the reaction time to 24 hours, an AFM image (figure 6.20, 1b) was recorded for the mixture sample displayed larger structure with average diameter of 70 nm. Additional thinner branches < 2 nm (denoted with white arrow) were also seen to be extending out from the body of structure. These additional branches are too thin to be nanowires, suggesting the structure to be made of polymer material around bundles of DNA. On the other hand, at this reaction time (24 hours) both of control samples (figure 6.20, 2b and 3b) showed rope-like assemblies of individual polymer nanowires with diameters of 45 and 57 nm for DNA/poly(DAP-prop-TPT) and DNA/poly(T-prop-Py) nanowires, respectively. The formation of such assemblies is indicated by further structures (figure 6.20, 2b and 3b, white arrows) which are seen as branches from the main structure's body.

At a longer incubation time (22 days), all samples revealed similar morphology behaviour, in which thicker structures were observed (figure 6.20, 1c, 2c and 3c). Although the material isolated from the mixture sample showed many branches extending out from the main structure's body, suggesting these are assemblies of individual nanowires. However, at longer incubation time previous AFM studies of polypyrrole nanowires prepared using DNA as a template showed also thicker structures with a large number of thinner branches.[72] Moreover, control samples were also displayed such morphology behaviour. Therefore, it is not convincing to consider such structures as assemblies of two types of DNA/CP nanowire.

Based on AFM data of the material isolated from the mixture of two types of DNA/CP nanowire and control samples, the applied reaction times (1 and 24 hours and 22 days) showed no evidence for a change in the observed assemblies to suggest the two complementary nanowires interact in the intended manner. This may be because the hydrogen bond sites of both poly(DAP-prop-TPT) and poly(T-prop-Py) are involved in interactions with DNA during the nanowires formation and are no longer available. However, more likely is that both thymine and diaminopurine can form self-complementary pairings (figure 6.21). Even though these form through only two hydrogen bonds, compared to three hydrogen bonds for the DAP-T interaction, the large number of groups expected on the polymer strands would allow assembly through base pairing to be occur.

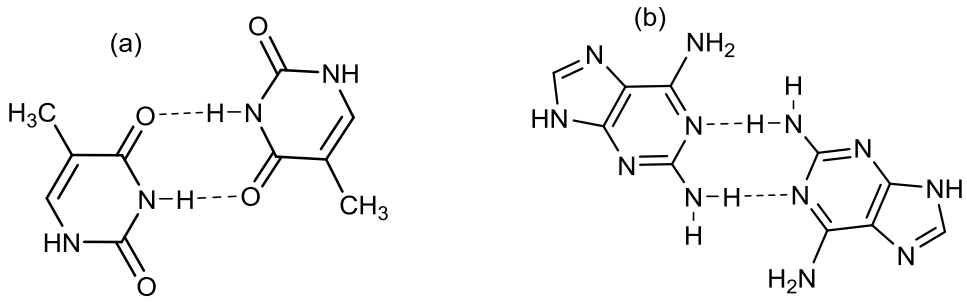

Figure 6-21: Chemical structures of (a) thymine-thymine and (b) diaminopurine-diaminopurine base pairs.

6.5 Conclusion

The preparation of hybrid supramolecular polymer nanowires was achieved by chemical oxidation of the two monomer types (DAP-prop-TPT and T-prop-Py) using $FeCl_3$ in the presence of DNA. The formation of such supramolecular materials comprising of both DNA and polymer material was confirmed by FTIR and XPS studies. AFM data of both DNA/poly(DAP-prop-TPT) and DNA/poly(T-prop-Py) nanowires showed continuous, smooth and uniform structures, whilst statistical analysis of the produced DNA/poly(DAP-prop-TPT) and DAN/poly(T-prop-Py) nanowires revealed broad size distribution with structures up to 25 and 35 nm in heights, respectively. The electronic properties of the DNA/CP nanostructures were probed using EFM, confirming that the nanostructures are nanowires, as they are electrically conducting. AFM studies of the material isolated from the mixture of two complementary nanowires did not provide reliable evidence for larger structures formation based on complementary hydrogen bonding between the purine/pyrimidine groups attached to the nanowires. This is suggested to be due to either the hydrogen bond sites attached to the monomers involved in the templating process and hence not being available, or the self-complementary nature of the based means that essentially the same processes, i.e. base pairing, can occur for pure samples of these materials, as well as mixtures.

7. Appendix

Appendix A: Abbreviations

%T	Percept transmittance
µm	Micrometre
0-D	Zero-dimensional
1-D	One-dimensional
2-D	Two-dimensional
3-D	Three-dimensional
3D-DX	Three-dimensional-double crossover
A	Adenine
Å	Angstrom
AAO	Anodic aluminium oxide
AFM	Atomic force microscopy
bcc	Body-centred cubic
C	Cytosine
c-AFM	Conductive AFM
CNC	Cellulose nanocrystals
CNT	Carbon nanotube
CPs	Conducting polymers
CT-DNA	Calf thymus DNA
CV	Cyclic voltammetry
d	Diameter of nanowire
DAP	Diaminopurine
DAP-prop-TPT	2,6-diaminopurine-propyl-2,5 bis-dithenyl pyrrole
dc	Direct current
DMF	Dimethylformamide
DMSO	Dimethylsulfoxide
DNA	Deoxyribonucleic acid
dsDNA	Double-stranded deoxyribonucleic acid
E_b	Binding energy
EDTA	Ethylenediaminetetraacetic acid
EFM	Electrostatic force microscopy

E_k	Kinetic energy
E_p	Peak potential
ESCA	Electron spectroscopy for chemical analysis
eV	Electron Volt
f_0	Resonance frequency
fcc	Face-centred cubic
FIB	Focused-ion beam
FTIR	Fourier transform infrared
G	Guanine
GMP	Guanosine monophosphate
HMM	Hybrid mesoporous materials
HRTEM	High-resolution transmission electron microscopy
HT-DNA	Herring testes DNA
I-V	Current-voltage
K	Kelvin
k	Cantilever spring constant
L	Length of nanowire
MFM	Magnetic force microscopy
mg	Milligram
mL	Millilitre
mM	Millimolar
MWNTs	Multiwalled carbon nanotubes
nm	Nanometre
PA	Polyaniline
PIn	Polyindole
PNA	Peptide nucleic acid
PPY	Polypyrrole
RNA	Ribonucleic acid
S	Siemens
SAM	Self-assembled monolayer
SCM	Scanned conductance microscopy
SEM	Scanning electron microscopy
SPM	Scanning probe microscopy
STM	Scanning tunnelling microscopy

T	Thymine
TEM	Transmission electron microscopy
TMS	Trimethylsilane
T-prop-Py	Thymine-propyl-pyrrole
TPT	Poly2,5-(bis-2-thienyl)-pyrrole
UHV	Ultra-high vacuum
XPS	X-ray photoelectron spectroscopy
XRD	X-Ray diffraction
$\Delta\phi$	Phase shift
λ	Wavelength
λ-DNA	Lambda DNA
μL	Microlitre
ϕ	Work function
Ω	Ohm

Appendix B: Further Supporting Data for the DNA/Rh nanowires

B.1 Fourier Transform Infra-Red (FTIR) spectroscopy of the DNA/Rh^{+3} system

For FTIR studies, samples were prepared as films of material upon silicon substrates. Samples for DNA/Rh^{3+} were prepared by mixing an aqueous solution of CT-DNA (30 µL; 500 µg mL^{-1}) with an aqueous solution of $RhCl_3.xH_2O$ (30 µL; 2.5 mM). The resulting DNA/Rh^{3+} solution were allowed to stand at room temperature for 20 minutes. After 20 minutes reaction time had elapsed, 80 µL of the reaction solution was deposited upon a silicon substrate, and allowing the solvent to evaporate at room temperature. Samples of bare DNA were prepared by depositing 80 µL of a CT-DNA solution (500 µg mL^{-1}) upon Si substrates and the solvent allowed to evaporate ate room temperature. FTIR spectra were performed with a Bio-Rad Excalibur FTS-40 spectrometer (Varian Inc., Palo Alto, CA, USA), and spectra were recorded over the 400–4000 cm^{-1} range, with 128 scans and at 4 cm^{-1} resolution.

In order to establish the modes of interaction between the DNA and Rh^{3+} ions during the preparation of DNA/Rh nanowires, FTIR spectroscopy was carried out upon samples of pure DNA and DNA following reaction with a solution of $RhCl_3$. xH_2O. It is known that metal cations can interact with DNA through formation of electrostatic interactions with the phosphate backbone, and/or coordinate to the DNA nucleobases. Previous FTIR studies of the DNA/metal ions interaction have reported that the metal ions attach to the DNA structure mainly at guanine (N7, O6) and adenine (N7, N1) of purines bases and at the N3 of the pyrimidine.[50] The DNA/Rh^{3+} binding have previously reported to take place at both of phosphate backbone and aromatic bases. [197, 198]

Here, FTIR spectra (figure B.1) of bare DNA and DNA/Rh^{3+} indicate that the Rh^{3+} ions bind to the DNA structure both at the nucleobase sites and to the phosphate backbone. This is evident from several noticeable changes in the position and intensity of DNA-related bands upon DNA/Rh^{3+} complex formation, (see figure B.1.1 and table B.1). These are clearly observed in the 900-1300 cm^{-1} region of spectra, thereby indicating that the Rh species are bound to DNA backbone. For example, the spectrum of bare DNA (blue curve), revealed a band located at 1097 cm^{-1} due to the symmetric PO_2^- stretches and a shoulder related to C-C deoxyribose stretch at 1033 cm^{-1}. In the DNA/Rh^{3+}, the first band is almost disappeared and the second band shifted to lower frequency (1019 cm^{-1}). Additionally, evidence for the DNA phosphate backbone/Rh^{3+}

interactions is supported with the major spectral change in region of the asymmetric PO_2^- vibrations band at 1246 cm^{-1} which is appeared as two broad bands located at 1137 and 1238 cm^{-1} in the DNA/Rh^{3+} spectrum.

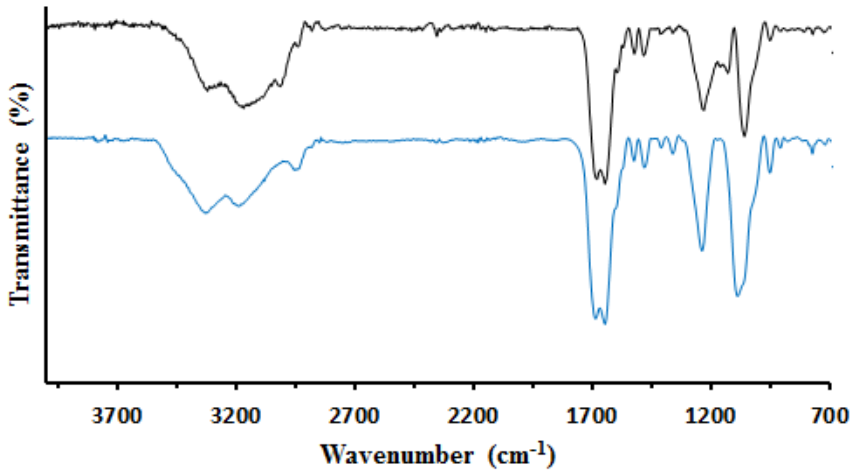

Figure B.1: FTIR data of calf thymus DNA (blue spectrum) vs DNA/Rh^{3+} system (black spectrum) in the 700-4000 cm^{-1} region.

On the other hand, the FTIR spectra in 1300-1800 cm^{-1} region show only slight changes in the intensity and position of the DNA-related bands of the DNA/Rh^{3+} complex, suggesting that DNA nucleobases may also be involved in the DNA/Rh^{3+} binding. The N-H deformation centred at 1416 cm^{-1} and the C-N stretch band of guanine and cytosine observed at 1368 cm^{-1} are reduced in their intensity. Additionally, the carbonyl stretch appeared at 1692 cm^{-1} in DNA spectrum showed slight shift to lower frequency (1688 cm^{-1}) upon DNA/Rh^{3+} complex formation. All DNA bands were assigned according to literatures.[66, 109-111, 235]

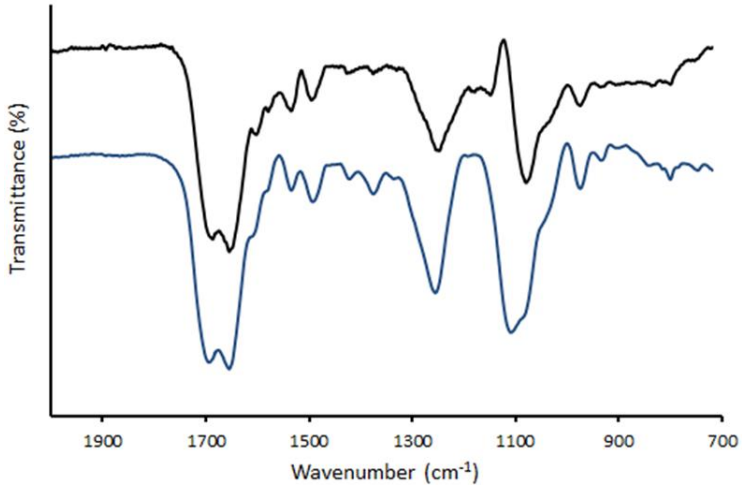

Figure B.1.1: FTIR data of calf thymus DNA (blue spectrum) vs DNA/Rh^{3+} system (black spectrum) in the 700-2000 cm^{-1} region.

Wavenumber (cm^{-1})		Assignment
CT-DNA	**CT-DNA/ Rh^{3+}**	
960	960	C-C deoxyribose stretch
1033[a]	1019 [a]	C-C deoxyribose stretch
1071	1068	P-O/C-O deoxyribose stretch
1097	-	PO_2^- symmetric stretch
-	1137	PO_2^- asymmetric stretch
1246	1238	PO_2^- asymmetric stretch
1368	1367	C-N stretch of cytosine / guanine
1416	1417	C-H / N-H deformation; C-N stretch
1488	1490	Ring vibration of cytosine / guanine
1529	1530	In-plane vibration of guanine / cytosine
1603	1600	In-plane vibration of adenine
1653	1653	C=O stretch of cytosine / thymine; In-plane vibration of thymine
1692	1688	C=O stretch of guanine / thymine; N-H thymine
2850–3500	2850–3500	C-H / N-H / O-H stretches

Table B.1. Assignment and comparison of FTIR spectra (700–4000 cm^{-1}) of calf thymus DNA, and calf thymus DNA following association of with Rh^{3+} cations in aqueous solution. [a] Peak appeared as a shoulder .

B.2 Further XPS data for samples of DNA/Rh nanostructures prepared using chemical reduction method

Evidence for the presence of the DNA in the sample material is provided by the P2p signal, expected to be presented due to the DNA phosphate backbone. XPS spectrum of P2p region detects P2p doublets ($P2p_{3/2}$ and $P2p_{1/2}$) at binding energies of 133.3 and 134.1 eV, respectively (figure B.2). These values with doublet separation of 0.8 eV are close to the binding energies of the P2p for phosphorus in the DNA backbone.[16, 119, 121]

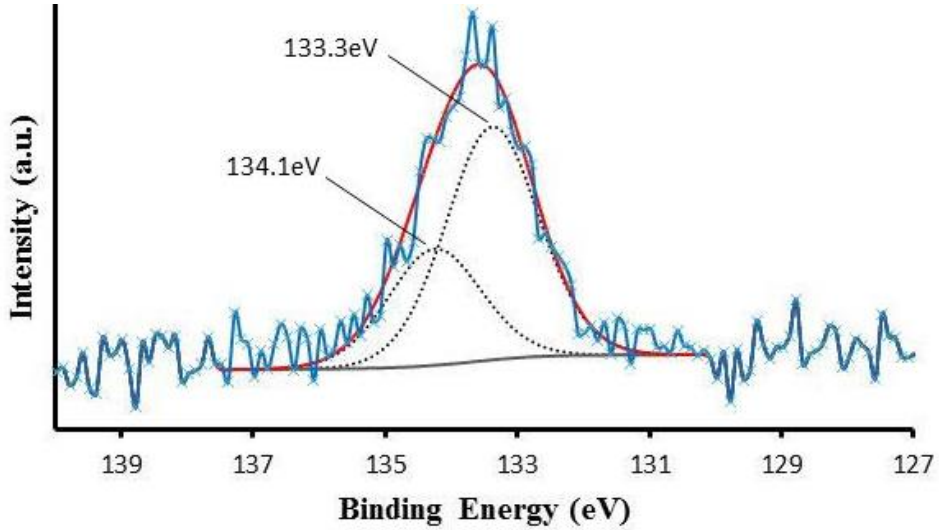

Figure B.2: High resolution XPS spectrum of P2p region of calf thymus DNA-templated Rh nanowires immobilised upon a Si/native SiO_2 substrate. Blue solid line represents raw data, total fits is represented by red line and black dashed lines is for component peak.

B.3 Further XPS data for samples of DNA/Rh nanostructures prepared using electrochemical reduction method

Curve Fitting of P2p region (figure B.3) indicates DNA is present in the product materials. This spectra show P2p doublets at binding energies of 133.3 and 134.1 eV for $P2p_{3/2}$ and $P2p_{1/2}$, respectively. These values with doublet separation of 0.8 eV can be assigned to the P2p for phosphorus in the DNA backbone.[16, 119, 121]

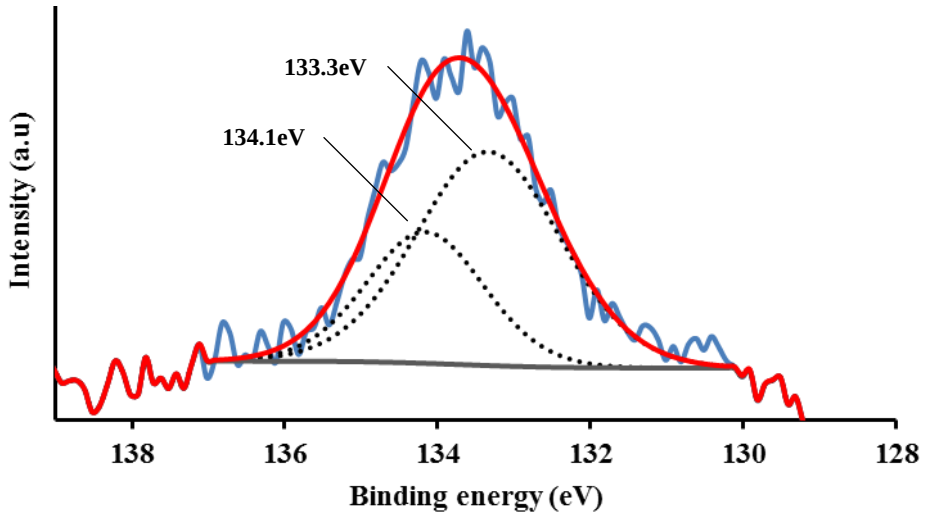

Figure B.3: High resolution XPS spectrum of P2p

Appendix C: Further Supporting Data for the DNA/poly(DAP-prop-TPT) nanowires

C.1: Further XPS data for samples of isolated DNA/poly(DAP-prop-TPT) material

For the confirmation of the presence of DNA in the product material, the XPS spectra of P2p region (figure C.1) is examined to show P2p doublets at binding energies of 133.6 and 134.4 eV for $P2p_{3/2}$ and $P2p_{1/2}$, respectively. The peak position is consistent with the P2p for phosphorus in the DNA backbone.[16, 119, 121]

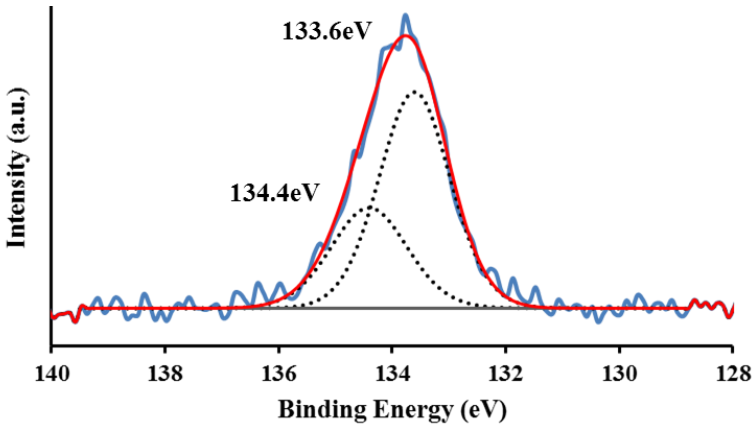

Figure C.1: High resolution XPS spectra of P2p region of calf thymus DNA-templated poly(DAP-prop-TPT) material. Blue solid line represents raw data, total fits is indicated by red line and black dashed lines are for component peaks.

C. 2: Further XPS data for samples of isolated DNA/ poly(T-prop-Py) material

Further confirmation of the presence of DNA in the product material is provided by the P2p signal, expected to be presented due to the DNA phosphate backbone. XPS spectra of P2p region (figure C.2) is examined to show P2p doublets at binding energies of 133.4 and 134.2 eV for $P2p_{3/2}$ and $P2p_{1/2}$, respectively. The peak position is consistent with the P2p for phosphorus in the DNA backbone.[16, 119, 121]

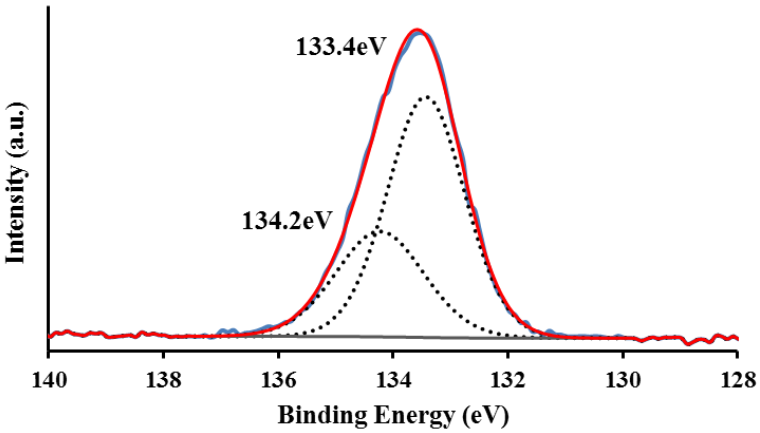

Figure C.2: High resolution XPS spectra of P2p region of calf thymus DNA-templated poly(T-prop-Py) material, immobilised upon a Si/native SiO_2. Blue solid line represents raw data, total fits is indicated by red line and black dashed lines are for component peaks.

Appendix D: Published papers

D.1 Mohamed, H.D.A., S.M.D. Watson, B.R. Horrocks, and A. Houlton, Magnetic and conductive magnetite nanowires by DNA-templating. *Nanoscale*, 2012. **4**(19): p. 5936-5945.

D.2 Watson, S.M.D, H.D.A. Mohamed, B.R. Horrocks, and A. Houlton, Electrically conductive magnetic nanowires using an electrochemical DNA-templating route. *Nanoscale*, 2013.5(12): P. 5349-5359.

8. References

1. Leydecker, S., M. Kölbel, and S. Peters, Nano Materials: *In Architecture, Interior Architecture and Design*. 2008: Birkhäuser.

2. Rao, C.N.R., A. Müller, and A.K. Cheetham, eds. *The Chemistry of Nanomaterials. Synthesis Properties and Applications*. Vol. 1. 2004, Wiley-VCH: Weinheim.

3. Mirkin, C.A., Programming the Assembly of Two- and Three-Dimensional Architectures with DNA and Nanoscale Inorganic Building Blocks. *Inorganic Chemistry*, 2000. 39(11): p. 2258-2272.

4. Eigler, D.M. and E.K. Schweizer, Positioning single atoms with a scanning tunnelling microscope. *Nature*, 1990. 344(6266): p. 524-526.

5. Kelsall, R., I.W. Hamley, and M. Geoghegan, *Nanoscale Science and Technology*. 2005: Wiley.

6. Cao, G.Z. and Y. Wang, *Nanostructures and Nanomaterials: Synthesis, Properties, and Applications* (2Nd Edition). 2011: World Scientific.

7. Roduner, E., Size matters: why nanomaterials are different. *Chemical Society Reviews*, 2006. 35(7): p. 583-592.

8. Alivisatos, A.P., Perspectives on the Physical Chemistry of Semiconductor Nanocrystals. *The Journal of Physical Chemistry*, 1996. 100(31): p. 13226-13239.

9. Rao, C.N.R., G.U. Kulkarni, P.J. Thomas, and P.P. Edwards, Size-dependent chemistry: Properties of nanocrystals. *Chemistry-A European Journal*, 2002. 8(1): p. 29-35.

10. Santra, A.K., S. Ghosh, and C.N.R. Rao, Dependence of the Strength of Interaction of Carbon Monoxide with Transition Metal Clusters on the Cluster Size. *Langmuir*, 1994. 10(11): p. 3937-3939.

11. Schodek, D.L., P. Ferreira, and M.F. Ashby, *Nanomaterials, Nanotechnologies and Design: An Introduction for Engineers and Architects*. 2009: Elsevier Science.

12. Xia, Y., P. Yang, Y. Sun, Y. Wu, B. Mayers, B. Gates, Y. Yin, F. Kim, One-Dimensional Nanostructures: Synthesis, Characterization, and Applications. *Advanced Materials*, 2003. 15(5): p. 353-389.

13. Sarkar, J., G.G. Khan, and A. Basumallick, Nanowires: properties, applications and synthesis via porous aluminium oxide template. *Bulletin of Materials Science*, 2007. 30(3): p. 271-290.

14. Hu, J.T., T.W. Odom, and C.M. Lieber, Chemistry and physics in one dimension: Synthesis and properties of nanowires and nanotubes. *Accounts of Chemical Research*, 1999. 32(5): p. 435-445.

15. Tran, H.D., D. Li, and R.B. Kaner, One-Dimensional Conducting Polymer Nanostructures: Bulk Synthesis and Applications. *Advanced Materials*, 2009. 21(14-15): p. 1487-1499.

16. Watson, S.M.D., J.H. Hedley, M.A. Galindo, S.A.F. Al-Said, N.G. Wright, B.A. Connolly, B.R. Horrocks, and A. Houlton, Synthesis, Characterisation and Electrical Properties of Supramolecular DNA-Templated Polymer Nanowires of 2,5-(Bis-2-thienyl)-pyrrole. *Chemistry – A European Journal*, 2012. 18(38): p. 12008-12019.

17. Beyer, S., P. Nickels, and F.C. Simmel, Periodic DNA nanotemplates synthesized by rolling circle amplification. *Nano Letters*, 2005. 5(4): p. 719-722.

18. Braun, E., Y. Eichen, U. Sivan, and G. Ben-Yoseph, DNA-templated assembly and electrode attachment of a conducting silver wire. *Nature*, 1998. 391(6669): p. 775-778.

19. Gu, Q., C.D. Cheng, R. Gonela, S. Suryanarayanan, S. Anabathula, K. Dai, and D.T. Haynie, DNA nanowire fabrication. *Nanotechnology*, 2006. 17(1): p. R14-R25.

20. Lu, W., P. Xie, and C.M. Lieber, Nanowire Transistor Performance Limits and Applications. *Ieee Transactions on Electron Devices*, 2008. 55(11): p. 2859-2876.

21. Cheng, C.D., R.K. Gonela, Q. Gu, and D.T. Haynie, Self-assembly of metallic nanowires from aqueous solution. *Nano Letters*, 2005. 5(1): p. 175-178.

22. Wang, Z.D., J.Q. Zhang, J.M. Ekman, P.J.A. Kenis, and Y. Lu, DNA-Mediated Control of Metal Nanoparticle Shape: One-Pot Synthesis and Cellular Uptake of Highly Stable and Functional Gold Nanoflowers. *Nano Letters*, 2010. 10(5): p. 1886-1891.

23. Yogeswaran, U. and S.M. Chen, A review on the electrochemical sensors and biosensors composed of nanowires as sensing material. *Sensors*, 2008. 8(1): p. 290-313.

24. Yu, G. and C.M. Lieber, Assembly and integration of semiconductor nanowires for functional nanosystems. *Pure and Applied Chemistry*, 2010. 82(12): p. 2295-2314.

25. Parviz, B.A., D. Ryan, and G.M. Whitesides, Using self-assembly for the fabrication of nano-scale electronic and photonic devices. *Ieee Transactions on Advanced Packaging*, 2003. 26(3): p. 233-241.

26. Becerril, H.A. and A.T. Woolley, DNA-templated nanofabrication. *Chemical Society Reviews*, 2009. 38(2): p. 329-337.

27. C. Hulteen, J. and C.R. Martin, A general template-based method for the preparation of nanomaterials. *Journal of Materials Chemistry*, 1997. 7(7): p. 1075-1087.

28. Martin, C.R., Template Synthesis of Electronically Conductive Polymer Nanostructures. *Accounts of Chemical Research*, 1995. 28(2): p. 61-68.

29. Martin, C.R., Nanomaterials: a membrane-based synthetic approach. *Science (New York, N.Y.)*, 1994. 266(5193): p. 1961-1966.

30. Zhang, Z., D. Gekhtman, M.S. Dresselhaus, and J.Y. Ying, Processing and Characterization of Single-Crystalline Ultrafine Bismuth Nanowires. *Chemistry of Materials*, 1999. 11(7): p. 1659-1665.

31. Brumlik, C.J., C.R. Martin, and K. Tokuda, Microhole array electrodes based on microporous alumina membranes. *Analytical Chemistry*, 1992. 64(10): p. 1201-1203.

32. Foss, C.A., G.L. Hornyak, J.A. Stockert, and C.R. Martin, Optical-properties of composite membranes containing arrays of nanoscopic gold cylinders. *Journal of Physical Chemistry*, 1992. 96(19): p. 7497-7499.

33. Foss, C.A., G.L. Hornyak, J.A. Stockert, and C.R. Martin, Template-Synthesized Nanoscopic Gold Particles: Optical Spectra and the Effects of Particle Size and Shape. *The Journal of Physical Chemistry*, 1994. 98(11): p. 2963-2971.

34. Parthasarathy, R.V. and C.R. Martin, Synthesis of polymeric microcapsule arrays and their use for enzyme immobilization. *Nature*, 1994. 369(6478): p. 298-301.

35. Cai, Z., J. Lei, W. Liang, V. Menon, and C.R. Martin, Molecular and supermolecular origins of enhanced electric conductivity in template-synthesized polyheterocyclic fibrils. 1. Supermolecular effects. *Chemistry of Materials*, 1991. 3(5): p. 960-967.

36. Lei, J.T., Z.H. Cai, and C.R. Martin, Effect of reagent concentrations used to synthesize polypyrrole on the chemical characteristics and optical and electronic-properties of the resulting polymer. *Synthetic Metals*, 1992. 46(1): p. 53-69.

37. Penner, R.M. and C.R. Martin, Controlling the morphology of electronically conductive polymers. *Journal of the Electrochemical Society*, 1986. 133(10): p. 2206-2207.

38. Cai, Z. and C.R. Martin, Electronically conductive polymer fibers with mesoscopic diameters show enhanced electronic conductivities. *Journal of the American Chemical Society*, 1989. 111(11): p. 4138-4139.

39. Parthasarathy, R.V. and C.R. Martin, Template-Synthesized Polyaniline Microtubules. *Chemistry of Materials*, 1994. 6(10): p. 1627-1632.

40. Padalkar, S., J.R. Capadona, S.J. Rowan, C. Weder, Y.-H. Won, L.A. Stanciu, and R.J. Moon, Natural Biopolymers: Novel Templates for the Synthesis of Nanostructures. *Langmuir*, 2010. 26(11): p. 8497-8502.

41. Flynn, C.E., S.W. Lee, B.R. Peelle, and A.M. Belcher, Viruses as vehicles for growth, organization and assembly of materials. *Acta Materialia*, 2003. 51(19): p. 5867-5880.

42. Houlton, A., A.R. Pike, M.A. Galindo, and B.R. Horrocks, DNA-based routes to semiconducting nanomaterials. *Chemical Communications*, 2009(14): p. 1797-1806.

43. Stryer, L., *Biochemistry. 3rd ed*. 1988, New York, USA: W. H Freeman & Co. 1089.

44. Houlton, A. and S.M.D. Watson, DNA-based nanowires. Towards bottom-up nanoscale electronics. *Annu. Rep. Prog. Chem. Sect. A,* 2011. 107: p. 21-42.

45. Stoltenberg, R. and A. Woolley, DNA-Templated Nanowire Fabrication. *Biomedical Microdevices*, 2004. 6(2): p. 105-111.

46. Richter, J., Metallization of DNA. *Physica E: Low-dimensional Systems and Nanostructures*, 2003. 16(2): p. 157-173.

47. Bertini, I., *Bioinorganic chemistry*. 1994: University Science Books.

48. Spiro, T.G., *Nucleic acid-metal ion interactions*. 1980: Wiley.

49. Price, C. and C. University of Newcastle upon Tyne. Dept. of, *Metal-nucleobase Complexes: Building Blocks for Supramolecular Chemistry*. 1998: University of Newcastle upon Tyne.

50. Anastassopoulou, J., Metal–DNA interactions. *Journal of Molecular Structure*, 2003. 651–653(0): p. 19-26.

51. Clever, G.H., C. Kaul, and T. Carell, DNA–Metal Base Pairs. *Angewandte Chemie International Edition*, 2007. 46(33): p. 6226-6236.

52. Miyake, Y., H. Togashi, M. Tashiro, H. Yamaguchi, S. Oda, M. Kudo, Y. Tanaka, Y. Kondo, MercuryII-Mediated Formation of Thymine−HgII−Thymine Base Pairs in DNA Duplexes. *Journal of the American Chemical Society*, 2006. 128(7): p. 2172-2173.

53. Ouameur, A.A., H. Arakawa, R. Ahmad, M. Naoui, and H.A. Tajmir-Riahi, A comparative study of Fe(II) and Fe(III) interactions with DNA duplex: Major and minor grooves bindings. *DNA and Cell Biology*, 2005. 24(6): p. 394-401.

54. Storhoff, J.J. and C.A. Mirkin, Programmed Materials Synthesis with DNA. *Chemical Reviews*, 1999. 99(7): p. 1849-1862.

55. Seeman, N.C., DNA Components for Molecular Architecture. *Accounts of Chemical Research*, 1997. 30(9): p. 357-363.

56. Chen, J.H., N.R. Kallenbach, and N.C. Seeman, A specific quadrilateral synthesized from DNA branched junctions. *Journal of the American Chemical Society*, 1989. 111(16): p. 6402-6407.

57. Zhang, Y. and N.C. Seeman, A solid-support methodology for the construction of geometrical objects from DNA. *Journal of the American Chemical Society*, 1992. 114(7): p. 2656-2663.

58. Zhang, Y. and N.C. Seeman, Construction of a DNA-Truncated Octahedron. *Journal of the American Chemical Society*, 1994. 116(5): p. 1661-1669.

59. Seeman, N.C., Nanomaterials Based on DNA. *Annual Review of Biochemistry*, 2010. 79(1): p. 65-87.

60. Zheng, J., P.E. Constantinou, C. Micheel, A.P. Alivisatos, R.A. Kiehl, and N.C. Seeman, Two-Dimensional Nanoparticle Arrays Show the Organizational Power of Robust DNA Motifs. *Nano Letters*, 2006. 6(7): p. 1502-1504.

61. Coffer, J.L., S.R. Bigham, R.F. Pinizzotto, and H. Yang, Characterization of quantum-confined CdS nanocrystallites stabilized by deoxyribonucleic acid (DNA). *Nanotechnology*, 1992. 3: p. 69-76.

62. Coffer, J.L., S.R. Bigham, X. Li, R.F. Pinizzotto, Y.G. Rho, R.M. Pirtle, and I.L. Pirtle, Dictation of the shape of mesoscale semiconductor nanoparticle assemblies by plasmid DNA. *Applied Physics Letters*, 1996. 69(25): p. 3851-3853.

63. Eichhorn, G.L. and Y.A. Shin, Interaction of metal ions with polynucleotides and related compounds. XII. The relative effect of various metal ions on DNA helicity. *Jornal of the American Chemical Society*, 1968. 90(26): p. 7323-7328.

64. Richter, J., R. Seidel, R. Kirsch, M. Mertig, W. Pompe, J. Plaschke, and H.K. Schackert, Nanoscale palladium metallization of DNA. *Advanced Materials*, 2000. 12(7): p. 507.

65. Monson, C.F. and A.T. Woolley, DNA-templated construction of copper nanowires. *Nano Letters*, 2003. 3(3): p. 359-363.

66. Watson, S.M.D., N.G. Wright, B.R. Horrocks, and A. Houlton, Preparation, Characterization and Scanned Conductance Microscopy Studies of DNA-Templated One-Dimensional Copper Nanostructures. *Langmuir*, 2010. 26(3): p. 2068-2075.

67. Dong, L., T. Hollis, B.A. Connolly, N.G. Wright, B.R. Horrocks, and A. Houlton, DNA-Templated Semiconductor Nanoparticle Chains and Wires. *Advanced Materials*, 2007. 19(13): p. 1748-1751.

68. Levina, L., V. Sukhovatkin, S. Musikhin, S. Cauchi, R. Nisman, D.P. Bazett-Jones, and E.H. Sargent, Efficient Infrared-Emitting PbS Quantum Dots Grown on DNA and Stable in Aqueous Solution and Blood Plasma. *Advanced Materials*, 2005. 17(15): p. 1854-1857.

69. Dittmer, W.U. and F.C. Simmel, Chains of semiconductor nanoparticles templated on DNA. *Applied Physics Letters*, 2004. 85(4): p. 633-635.

70. Ma, Y., J. Zhang, G. Zhang, and H. He, Polyaniline Nanowires on Si Surfaces Fabricated with DNA Templates. *Journal of the American Chemical Society*, 2004. 126(22): p. 7097-7101.

71. Dong, L., T. Hollis, S. Fishwick, B.A. Connolly, N.G. Wright, B.R. Horrocks, and A. Houlton, Synthesis, Manipulation and Conductivity of Supramolecular Polymer Nanowires. *Chemistry – A European Journal*, 2007. 13(3): p. 822-828.

72. Pruneanu, S., S.A.F. Al-Said, L.Q. Dong, T.A. Hollis, M.A. Galindo, N.G. Wright, A. Houlton, and B.R. Horrocks, Self-assembly of DNA-templated polypyrrole nanowires: Spontaneous formation of conductive nanoropes. *Advanced Functional Materials*, 2008. 18(16): p. 2444-2454.

73. Hassanien, R., M. Al-Hinai, S.A. Farha Al-Said, R. Little, L. Šiller, N.G. Wright, A. Houlton, and B.R. Horrocks, Preparation and Characterization of Conductive and Photoluminescent DNA-Templated Polyindole Nanowires. *ACS Nano*, 2010. 4(4): p. 2149-2159.

74. Vickerman, J.C., *Surface analysis : the principal techniques*. 1997, Chichester, England John Wiley. 457.

75. Smith, G.C., *Surface analysis by electron spectroscopy: measurement and interpretation*. 1994: Plenum Press.

76. Robinson, J.W., *Undergraduate instrumental analysis Sixth edition ed*. 2005, New York M. Dekker. 1079.

77. Liu, J., W. Huang, S. Chen, S. Hu, F.a. Liu, and Z. Li, Facile Electrochemical Dispersion of Bulk Rh into Hydrosols. *International Journal of Electrochemical Science*, 2009. 4(9): p. 1302-1308.

78. Rugar, D. and P. Hansma, Atomic force microscopy. *Physics Today*, 1990. 43(10): p. 23-30.

79. Yao, N. and Z.L. Wang, *Handbook of Microscopy for Nanotechnology*. 2005: Springer London, Limited.

80. Bockrath, M., N. Markovic, A. Shepard, M. Tinkham, L. Gurevich, L.P. Kouwenhoven, M.W. Wu, and L.L. Sohn, Scanned Conductance Microscopy of Carbon Nanotubes and λ-DNA. *Nano Letters*, 2002. 2(3): p. 187-190.

81. Staii, C., A.T. Johnson, and N.J. Pinto, Quantitative analysis of scanning conductance microscopy. *Nano Lett.*, 2004. 4(5): p. 859-862.

82. Zhou, Y., M. Freitag, J. Hone, C. Staii, A.T. Johnson, N.J. Pinto, and A.G. MacDiarmid, Fabrication and electrical characterization of polyaniline-based nanofibers with diameter below 30 nm. *Applied Physics Letters*, 2003. 83(18): p. 3800-3802.

83. Jespersen, T.S. and J. Nygard, Charge trapping in carbon nanotube loops demonstrated by EFM. *Nano Lett.*, 2005. 5(9): p. 1838-1841.

84. Nyffenegger, R.M., R.M. Penner, and R. Schierle, Electrostatic force microscopy of silver nanocrystals with nanometer-scale resolution. *Applied Physics Letters*, 1997. 71(13): p. 1878-1880.

85. Terris, B.D., J.E. Stern, D. Rugar, and H.J. Mamin, Contact electrification using force microscopy. *Physical Review Letters*, 1989. 63(24): p. 2669-2672.

86. Nyamjav, D., J.M. Kinsella, and A. Ivanisevic, Magnetic wires with DNA cores: a magnetic force microscopy study. *Applied Physics Letters*, 2005. 86: p. 093107.

87. Neves, C.S., P. Quaresma, P.V. Baptista, P.A. Carvalho, J.P. Araujo, E. Pereira, and P. Eaton, New insights into the use of magnetic force microscopy to discriminate between magnetic and nonmagnetic nanoparticles. *Nanotechnology*, 2010. 21(30).

88. Cornell, R.M. and U. Schwertmann, *The Iron Oxides: Structure, Properties, Reactions, Occurrences and Uses*. 2006: Wiley.

89. Greenwood N. N., a.E.A., *Chemistry of the Elements*. *Second Edition ed*. 1997, Boston, Mass. : Butterworth Heinemann. 1341.

90. Housecroft, C.E. and A.G. Sharpe, *Inorganic Chemistry*. 2008: Prentice Hall.

91. Sharpe, A.G., *Inorganic chemistry*. 1992: Longman Scientific & Technical.

92. Krehula, S. and S. Music, Formation of iron oxides in a highly alkaline medium in the presence of palladium ions. *Journal of Molecular Structure*, 2009. 924-26: p. 201-207.

93. Jia, C.-J., L.-D. Sun, F. Luo, X.-D. Han, L.J. Heyderman, Z.-G. Yan, C.-H. Yan, K. Zheng, Large-scale synthesis of single-crystalline iron oxide magnetic nanorings. *Journal of the American Chemical Society*, 2008. 130: p. 16968-16977.

94. Wolf, S.A., D.D. Awschalom, R.A. Buhrman, J.M. Daughton, S. von Molnar, M.L. Roukes, A.Y. Chtchelkanova, and D.M. Treger, Spintronics: A spin-based electronics vision for the future. *Science*, 2001. 294(5546): p. 1488-1495.

95. Sarkar, D. and M. Mandal, Static and dynamic magnetic characterization of DNA-templated chain-like magnetite nanoparticles. *The Journal of Physical Chemistry. C*, 2012. 116: p. 3227-3234.

96. Le Thi Mai, H., D. Tran Thi, D. Tran Mau, D. Nguyen Huu, and C. Dang Mau, Preparation and characterization of magnetic nanoparticles coated with polyethylene glycol, *in Apctp-Asean Workshop on Advanced Materials Science and Nanotechnology*, N. VanHieu, Editor. 2009.

97. Laurent, S., D. Forge, M. Port, A. Roch, C. Robic, L.V. Elst, and R.N. Muller, Magnetic iron oxide nanoparticles: Synthesis, stabilization, vectorization, physicochemical characterizations, and biological applications. *Chemical Reviews*, 2008. 108(6): p. 2064-2110.

98. Lee, N. and T. Hyeon, Designed synthesis of uniformly sized iron oxide nanoparticles for efficient magnetic resonance imaging contrast agents. *Chemical Society Reviews*, 2012. 41(7): p. 2575-2589.

99. Yamaguchi, K., K. Matsumoto, and T. Fujii, Magnetic-anisotropy by ferromagnetic particles alignment in a magnetic-field. *Journal of Applied Physics*, 1990. 67(9): p. 4493-4495.

100. Wang, G., X. Gou, J. Horvat, and J. Park, Facile synthesis and characterization of iron oxide semiconductor nanowires for gas sensing application. *Journal of Physical Chemistry C*, 2008. 112(39): p. 15220-15225.

101. Liao, Z.M., Y.D. Li, J. Xu, J.M. Zhang, K. Xia, and D.P. Yu, Spin-filter effect in magnetite nanowire. *Nano Letters*, 2006. 6(6): p. 1087-1091.

102. Kinsella, J.M. and A. Ivanisevic, Fabrication of ordered metallic and magnetic heterostructured DNA-nanoparticle hybrids. *Colloids and Surfaces B: Biointerfaces*, 2008. 63: p. 296-300.

103. Kinsella, J.M. and A. Ivanisevic, DNA-templated magnetic nanowires with different compositions: fabrication and analysis. *Langmuir*, 2007. 23(7): p. 3886-3890.

104. Basnar, B., Y. Weizmann, Z. Cheglakov, and I. Willner, Synthesis of nanowires using dip-pen nanolithography and biocatalytic inks. *Advanced Materials*, 2006. 18(6): p. 713.

105. Nyamjav, D. and A. Ivanisevic, Templates for DNA-tempalted Fe_3O_4 nanoparticles. *Biomaterials*, 2005. 26: p. 2749-2757.

106. Mohamed, H.D.A., S.M.D. Watson, B.R. Horrocks, and A. Houlton, Magnetic and conductive magnetite nanowires by DNA-templating. *Nanoscale*, 2012. 4(19): p. 5936-5945.

107. Guo, F., Q. Zhang, B. Zhang, H. Zhang, and L. zhang, Preparation and characterization of magnetic composite microspheres using a free radical polymerization system consisting of DPE. *Polymer*, 2009. 50: p. 1887-1894.

108. Sun, Y., B. Wang, H. Wang, and J. Jiang, Controllable preparation of magnetic polymer microspheres with different morphologies by miniemulsion polymerization. *Journal of Colloid and Interface Science*, 2007. 308(2): p. 332-336.

109. Alex, S. and P. Dupuis, FT-IR and Raman investigation of cadmium binding by DNA. *Inorganica Chimica Acta*, 1989. 157(2): p. 271-281.

110. Ouameur, A.A. and H.A. Tajmir-Riahi, Structural analysis of DNA interactions with biogenic polyamines and cobalt(III) hexamine studied by Fourier transform infrared and capillary electrophoresis. *Journal of Biological Chemistry*, 2004. 279(40): p. 42041-42054.

111. Arakawa, H., R. Ahmad, M. Naoui, and H.-A. Tajmir-Riahi, A Comparative Study of Calf Thymus DNA Binding to Cr(III) and Cr(VI) Ions. *Journal of Biological Chemistry*, 2000. 275(14): p. 10150-10153.

112. Ahmad, S., U. Riaz, A. Kaushik, and J. Alam, Soft Template Synthesis of Super Paramagnetic Fe_3O_4 Nanoparticles a Novel Technique. *Journal of Inorganic and Organometallic Polymers and Materials*, 2009. 19(3): p. 355-360.

113. Wu, W., Q. He, H. Chen, J. Tang, and L. Nie, Sonochemical synthesis, structure and magnetic properties of air-stable Fe_3O_4/Au nanoparticles. *Nanotechnology*, 2007. 18(14).

114. Tian, Y., B. Yu, X. Li, and K. Li, Facile solvothermal synthesis of monodisperse Fe_3O_4 nanocrystals with precise size control of one nanometre as potential MRI contrast agents. *Journal of Materials Chemistry*, 2011. 21(8): p. 2476-2481.

115. Qu, X.-F., G.-T. Zhou, Q.-Z. Yao, and S.-Q. Fu, Aspartic-Acid-Assisted Hydrothermal Growth and Properties of Magnetite Octahedrons. *The Journal of Physical Chemistry C*, 2009. 114(1): p. 284-289.

116. Teng, X.W. and H. Yang, Effects of surfactants and synthetic conditions on the sizes and self-assembly of monodisperse iron oxide nanoparticles. *Journal of Materials Chemistry*, 2004. 14(4): p. 774-779.

117. Pinna, N., S. Grancharov, P. Beato, P. Bonville, M. Antonietti, and M. Niederberger, Magnetite Nanocrystals: Nonaqueous Synthesis, Characterization, and Solubility. *Chemistry of Materials*, 2005. 17(11): p. 3044-3049.

118. Fujii, T., F.M.F. de Groot, G.A. Sawatzky, F.C. Voogt, T. Hibma, and K. Okada, In situ XPS analysis of various iron oxide films grwon by NO_2-assisted molecular-beam epitaxy. *Physical Review B*, 1999. 59(4): p. 3195-3202.

119. Vilar, M.R., A.M.B. do Rego, A.M. Ferraria, Y. Jugnet, C. Nogues, D. Peled, and R. Naaman, Interaction of self-assembled monolayers of DNA with electrons: HREELS and XPS studies. *Journal of Physical Chemistry B*, 2008. 112(23): p. 6957-6964.

120. Briones, C., E. Mateo-Marti, C. Gomez-Navarro, V. Parro, E. Roman, and J.A. Martin-Gago, Ordered self-assembled monolayers of peptide nucleic acids with DNA recognition capability. *Physical Review Letters*, 2004. 93(20).

121. Howell, C., J.L. Zhao, P. Koelsch, and M. Zharnikov, Hybridization in ssDNA films-a multi-technique spectroscopy study. *Physical Chemistry Chemical Physics*, 2011. 13(34): p. 15512-15522.

122. Lee, C.-Y., P. Gong, G.M. Harbers, D.W. Grainger, D.G. Castner, and L.J. Gamble, Surface coverage and structure of mixed DNA/alkylthiol monolayers on gold: Characterization by XPS, NEXAFS, and fluorescence intensity measurements. *Analytical Chemistry*, 2006. 78(10): p. 3316-3325.

123. Petrovykh, D.Y., H. Kimura-Suda, M.J. Tarlov, and L.J. Whitman, Quantitative Characterization of DNA Films by X-ray Photoelectron Spectroscopy. *Langmuir*, 2003. 20(2): p. 429-440.

124. Ballav, N., P. Koelsch, and M. Zharnikov, Orientation and Ordering in Monomolecular Films of Sulfur-Modified Homo-oligonucleotides on Gold. *The Journal of Physical Chemistry C*, 2009. 113(42): p. 18312-18320.

125. Han, Q., Liu, Xu, Chen, Wang, and H. Zhang, Growth and Properties of Single-Crystalline γ-Fe_2O_3 Nanowires. *The Journal of Physical Chemistry C*, 2007. 111(13): p. 5034-5038.

126. Daou, T.J., G. Pourroy, S. Bégin-Colin, J.M. Grenèche, C. Ulhaq-Bouillet, P. Legaré, P. Bernhardt, C. Leuvrey, Hydrothermal Synthesis of Monodisperse Magnetite Nanoparticles. *Chemistry of Materials*, 2006. 18(18): p. 4399-4404.

127. Daou, T.J., S. Begin-Colin, J.M. Grenèche, F. Thomas, A. Derory, P. Bernhardt, P. Legaré, and G. Pourroy, Phosphate adsorption preoperties of magnetite-based nanoparticles. *Chemistry of Materials*, 2007. 19: p. 4494-4505.

128. Netterfield, R.P., P.J. Martin, C.G. Pacey, W.G. Sainty, D.R. McKenzie, and G. Auchterlonie, Ion-assisted deposition of mixed TiO2-SiO2 films. *Journal of Applied Physics*, 1989. 66(4): p. 1805-1809.

129. Miller, M.L. and R.W. Linton, X-ray photoelectron spectroscopy of thermally treated SiO2 surfaces. *Analytical Chemistry*, 1985. 57(12): p. 2314-2319.

130. Shebanova, O.N. and P. Lazor, Raman spectroscopic study of magnetite ($FeFe_2O_4$): a new assignment for the vibrational spectrum. *Journal of Solid State Chemistry*, 2003. 174(2): p. 424-430.

131. DeFaria, D.L.A., S.V. Silva, and M.T. deOliveira, Raman microspectroscopy of some iron oxides and oxyhydroxides. *Journal of Raman Spectroscopy*, 1997. 28(11): p. 873-878.

132. Chourpa, I., L. Douziech-Eyrolles, L. Ngaboni-Okassa, J.F. Fouquenet, S. Cohen-Jonathan, M. Souce, H. Marchais, and P. Dubois, Molecular composition of iron oxide nanoparticles, precursors for magnetic drug targeting, as characterized by confocal Raman microspectroscopy. *Analyst*, 2005. 130(10): p. 1395-1403.

133. Li, J., C. Bai, C. Wang, C. Zhu, Z. Lin, Q. Li, and E. Cao, A convenient method of aligning large DNA molecules on bare mica surfaces for atomic force microscopy. *Nucleic Acids Research*, 1998. 26(20): p. 4785-4786.

134. Deng, Z.X. and C.D. Mao, DNA-templated fabrication of 1D parallel and 2D crossed metallic nanowire arrays. *Nano Letters*, 2003. 3(11): p. 1545-1548.

135. Kudo, H. and M. Fujihira, DNA-templated copper nanowire fabrication by a two-step process involving electroless metallization. *Nanotechnology, IEEE Transactions on*, 2006. 5(2): p. 90-92.

136. Mott, N.F., *Metal-Insulator Transitions*. 2nd ed, London: Taylor and Francis.

137. Seneor, P., A. Fert, J.L. Maurice, F. Montaigne, F. Petroff, and A. Vaures, Large magnetoresistance in tunnel junctions with an iron oxide electrode. *Applied Physics Letters*, 1999. 74(26): p. 4017-4019.

138. Li, X.W., A. Gupta, G. Xiao, and G.Q. Gong, Transport and magnetic properties of epitaxial and polycrystalline magnetite thin films. *Journal of Applied Physics*, 1998. 83(11): p. 7049-7051.

139. Colombo, M., S. Carregal-Romero, M.F. Casula, L. Gutiérrez, M.P. Morales, I.B. Böhm, J.T. Heverhagen, D. Prosperi, Biological applications of magnetic nanoparticles. *Chemical Society Reviews*, 2012. 41: p. 4306-4334.

140. Caruntu, D., G. Caruntu, and C.J. O'Connor, Magnetic properties of variable-sized Fe_3O_4 nanoparticles synthesized from non-aqueous homogeneous solutions of polyols. *Journal of Physics D-Applied Physics*, 2007. 40(19): p. 5801-5809.

141. Ma, H.-l., X.-t. Qi, Y. Maitani, and T. Nagai, Preparation and characterization of superparamagnetic iron oxide nanoparticles stabilized by alginate. *International Journal of Pharmaceutics*, 2007. 333(1-2): p. 177-186.

142. Parvin, K., J. Ma, J. Ly, X.C. Sun, D.E. Nikles, K. Sun, and L.M. Wang, Synthesis and magnetic properties of monodisperse Fe_3O_4 nanoparticles. *Journal of Applied Physics*, 2004. 95(11): p. 7121-7123.

143. Richter, J., M. Mertig, W. Pompe, I. Monch, and H.K. Schackert, Construction of highly conductive nanowires on a DNA template. *Applied Physics Letters*, 2001. 78(4): p. 536-538.

144. Silver, J., Chemistry of Iron. 1993: Blackie Academic & Professional.

145. Song, M.-M., W.-J. Song, H. Bi, J. Wang, W.-L. Wu, J. Sun, and M. Yu, Cytotoxicity and cellular uptake of iron nanowires. *Biomaterials*, 2010. 31(7): p. 1509-1517.

146. Vayssieres, L., L. Rabenberg, and A. Manthiram, Aqueous chemical route to ferromagnetic 3-d Arrays of iron nanorods. *Nano Letters*, 2002. 2(12): p. 1393-1395.

147. Tsang, S.C., V. Caps, I. Paraskevas, D. Chadwick, and D. Thompsett, Magnetically separable, carbon-supported nanocatalysts for the manufacture of fine chemicals. *Angewandte Chemie-International Edition*, 2004. 43(42): p. 5645-5649.

148. Huber, D.L., Synthesis, properties, and applications of iron nanoparticles. *Small*, 2005. 1(5): p. 482-501.

149. Mohaddes-Ardabili, L., H. Zheng, S.B. Ogale, B. Hannoyer, W. Tian, J. Wang, S.E. Lofland, S.R. Shinde, Self-assembled single-crystal ferromagnetic iron nanowires formed by decomposition. *Nature Materials*, 2004. 3(8): p. 533-538.

150. Chen, M., S. Yamamuro, D. Farrell, and S.A. Majetich, Gold-coated iron nanoparticles for biomedical applications. *Journal of Applied Physics*, 2003. 93(10): p. 7551-7553.

151. Farrell, D., S.A. Majetich, and J.P. Wilcoxon, Preparation and characterization of monodisperse Fe nanoparticles. *Journal of Physical Chemistry B*, 2003. 107(40): p. 11022-11030.

152. Hyeon, T., S.S. Lee, J. Park, Y. Chung, and H. Bin Na, Synthesis of highly crystalline and monodisperse maghemite nanocrystallites without a size-selection process. *Journal of the American Chemical Society*, 2001. 123(51): p. 12798-12801.

153. Kang, E., J. Park, Y. Hwang, M. Kang, J.G. Park, and T. Hyeon, Direct synthesis of highly crystalline and monodisperse manganese ferrite nanocrystals. *Journal of Physical Chemistry B*, 2004. 108(37): p. 13932-13935.

154. Li, F., C. Vipulanandan, and K.K. Mohanty, Microemulsion and solution approaches to nanoparticle iron production for degradation of trichloroethylene. *Colloids and Surfaces A: Physicochemical and Engineering Aspects*, 2003. 223(1-3): p. 103-112.

155. Glavee, G.N., K.J. Klabunde, C.M. Sorensen, and G.C. Hadjipanayis, Chemistry of borohydride reduction of iron(II) and iron(III) ions in aqueous and

nonaqueous media - formation of nanoscale Fe, FeB, and Fe_2B powders. *Inorganic Chemistry*, 1995. 34(1): p. 28-35.

156. Seip, C.T. and C.J. O'Connor, The fabrication and organization of self-assembled metallic nanoparticles formed in reverse micelles. *Nanostructured Materials*, 1999. 12(1-4): p. 183-186.

157. Ni, X.M., X.B. Su, H.G. Zheng, D.G. Zhang, D.D. Yang, and Q.B. Zhao, Studies on the one-step preparation of iron nanoparticles in solution. *Journal of Crystal Growth*, 2005. 275(3-4): p. 548-553.

158. Huang, K.-C. and S.H. Ehrman, Synthesis of iron nanoparticles via chemical reduction with palladium ion seeds. *Langmuir*, 2007. 23(3): p. 1419-1426.

159. Borissov, D., S. Isik-Uppenkamp, and M. Rohwerder, Fabrication of Iron Nanowire Arrays by Electrodeposition into Porous Alumina. *Journal of Physical Chemistry C*, 2009. 113(8): p. 3133-3138.

160. Wang, Q., G. Wang, B. Xu, J. Jie, X. Han, G. Li, Q. Li, and J.G. Hou, Non-aqueous cathodic electrodeposition of large-scale uniform ZnO nanowire arrays embedded in anodic alumina membrane. *Materials Letters*, 2005. 59(11): p. 1378-1382.

161. Verbeeck, J., O.I. Lebedev, G. Van Tendeloo, L. Cagnon, C. Bougerol, and G. Tourillon, Fe and Co nanowires and nanotubes synthesized by template electrodeposition. *Journal of the Electrochemical Society*, 2003. 150(10): p. E468-E471.

162. Whitney, T.M., J.S. Jiang, P.C. Searson, and C.L. Chien, Fabrication and magnetic properties of arrays of metallic nanowires. *Science*, 1993. 261: p. 1316-1319.

163. Wang, D., H.P. Jakobson, R. Kou, J. Tang, R.Z. Fineman, D. Yu, and Y. Lu, Metal and semiconductor nanowire network thin films with hierarchical pore structures. *Chemistry of Materials*, 2006. 18: p. 4231-4237.

164. Wang, D., H. Luo, R. Kou, M.P. Gil, S. Xiao, V.O. Golub, Z. Yang, C.J. Brinker, A general route to macroscopic hierarchical 3D nanowire networks. *Angewandte Chemie International Edition*, 2004. 43: p. 6169-6173.

165. Cao, Y. and T.E. Mallouk, Morphology of template-grown polyaniline nanowires and its effect on the electrochemical capacitance of nanowire arrays. *Chemistry of Materials*, 2008. 20: p. 5260-5265.

166. Martin, C.R., Membrane-based synthesis of nanomaterials. *Chemistry of Materials*, 1996. 8: p. 1739-1746.

167. Hurst, S.J., E.K. Payne, L. Qin, and C.A. Mirkin, Multisegmented one-dimensional nanorods prepared by hard-template synthetic methods. *Angewandte Chemie International Edition*, 2006. 45: p. 2672-2692.

168. Nemtoi, G., H. Chiriac, O. Dragos, M.-O. Apostu, and D. Lutic, The voltammetric characterization of the electrodeposition of cobalt, nickel and iron on gold disk electrode. *Acta Chemical Iasi*, 2009. 17(2): p. 151-168.

169. Pol, V.G., M. Motiei, A. Gedanken, J. Calderon-Moreno, and Y. Mastai, Sonochemical deposition of air-stable iron nanoparticles on monodispersed carbon spherules. *Chemistry of Materials*, 2003. 15: p. 1378-1384.

170. Gupta, R.P. and S.K. Sen, Calculation of multiplet structure of core p-vacancy levels .2. *Physical Review B*, 1975. 12(1): p. 15-19.

171. McIntyre, N.S. and D.G. Zetaruk, X-ray photoelectron spectroscopic studies of iron oxides. *Analytical Chemistry*, 1977. 49(11): p. 1521-1529.

172. Grosvenor, A.P., B.A. Kobe, M.C. Biesinger, and N.S. McIntyre, Investigation of multiplet splitting of Fe2p XPS spectra and bonding in iron compounds. *Surface and Interface Analysis*, 2004. 36: p. 1564-1574.

173. Kozakov, A.T., A.G. Kochur, K.A. Googlev, A.V. Nikolsky, I.P. Raevski, V.G. Smotrakov, and V.V. Yeremkin, X-ray photoelectron study of the valence state of iron in iron-containing single-crystal ($BiFeO_3$, $PbFe_{1/2}Nb_{1/2}O_3$), and ceramic ($BaFe_{1/2}Nb_{1/2}O_3$) multiferroics. *Journal of Electron Spectroscopy and Related Phenomena*, 2011. 184(1–2): p. 16-23.

174. Brundle, C.R., T.J. Chuang, and K. Wandelt, Core and valence level photoemission studies of iron oxide surfaces and the oxidation of iron. *Surface Science*, 1977. 68(0): p. 459-468.

175. Mills, P. and J.L. Sullivan, A study of the core level electrons in iron and its three oxides by means of X-ray photoelectron spectroscopy. *Journal of Physics D: Applied Physics*, 1983. 16: p. 723-732.

176. Lindberg, B.J., K. Hamrin, G. Johansson, U. Gelius, A. Fahlman, C. Nordling, and K. Siegbahn, Molecular spectroscopy by means of ESCA. *Physica Scripta*, 1970. 1: p. 286-298.

177. Siriwardane, R.V. and J.M. Cook, Interactions of NO and SO_2 with iron deposited on silica. J. Colloid Interf. Sci., 1985. 104(1): p. 250-257.

178. Li, X.-Q. and W.-X. Zhang, Sequestration of metal cations with zerovalent iron nanoparticles - a study with high resolution X-ray photoelectron spectroscopy (HR-XPS). *The Journal of Physical Chemistry C*, 2007. 111: p. 6939-6946.

179. Li, X.-Q. and W.-X. Zhang, Iron nanoparticles: the core-shell structure and unique properties for Ni(II) sequestration. *Langmuir*, 2006. 22: p. 4638-4642.

180. Grosvenor, A.P., B.A. Kobe, and N.S. McIntyre, Studies of the oxidation of iron by water vapour using X-ray photoelectron spectroscopy and QUASES. *Surface Science*, 2004. 572: p. 217-227.

181. Wang, C., D.R. Baer, J.E. Amonette, M.H. Engelhard, J. Antony, and Y. Qiang, Morphology and electronic structure of oxide shell on the surfacce iron nanoparticles. *Journal of the American Chemical Society*, 2009. 131: p. 8824-8832.

182. Ford, W.E., O. Harnack, A. Yasuda, and J.M. Wessels, Platinated DNA as precursors to templated chains of metal nanoparticles. *Advanced Materials*, 2001. 13(23): p. 1793-1797.

183. Watson, S.M.D., A. Houlton, and B.R. Horrocks, Equilibrium and non-equilibrium thermodynamics of templating reactions for the formation of nanowires. *Nanotechnology*, 2012. 23(50): p. 505603.

184. Jun, Y.-W., J.-W. Seo, and J. Cheon, Nanoscaling laws of magnetic nanoparticles and their applicabilities in biomedical sciences. *Account of Chemical Research*, 2008. 41(2): p. 179-189.

185. Sun, H.-L., H. Shi, F. Zhao, L. Qi, and S. Gao, Shape-dependent magnetic properties of low-dimensional nanoscale Prussian blue (PB) analogue $SmFe(CN)_6.4H_2O$. *Chemical Communications*, 2005: p. 4339-4341.

186. Song, Q. and Z.J. Zhang, Shape control and associated magnetic properties of spinel cobalt ferrite nanocrystals. *Journal of the American Chemical Society*, 2004. 126: p. 6164-6168.

187. Fukuoka, A., Y. Sakamoto, S. Guan, S. Inagaki, N. Sugimoto, Y. Fukushima, K. Hirahara, S. Iijima, Novel templating synthesis of necklace-shaped mono- and bimetallic nanowires in hybrid organic-inorganic mesoporous material. *Journal of the American Chemical Society*, 2001. 123(14): p. 3373-3374.

188. Fromen, M.C., A. Serres, D. Zitoun, M. Respaud, C. Amiens, B. Chaudret, P. Lecante, and M.J. Casanove, Structural and magnetic study of bimetallic $Co_{1-x}Rh_x$ particles. *Journal of Magnetism and Magnetic Materials*, 2002. 242–245, Part 1(0): p. 610-612.

189. Guirado-Lopez, R., P. Villasenor-Gonzalez, J. Dorantes-Davila, and G.M. Pastor, Magnetism of Rh_N clusters. *Journal of Applied Physics*, 2000. 87(9): p. 4906-4908.

190. Cox, A.J., J.G. Louderback, S.E. Apsel, and L.A. Bloomfield, Magnetism in 4d-transition metal clusters. *Physical Review B*, 1994. 49(17): p. 12295-12298.

191. Roucoux, A., J. Schulz, and H. Patin, Reduced Transition Metal Colloids: A Novel Family of Reusable Catalysts. *Chemical Reviews*, 2002. 102(10): p. 3757-3778.

192. Pradhan, M., S. Sarkar, A.K. Sinha, M. Basu, and T. Pal, High-Yield Synthesis of 1D Rh Nanostructures from Surfactant Mediated Reductive Pathway and their Shape Transformation. *The Journal of Physical Chemistry C*, 2010. 114(39): p. 16129-16142.

193. Pan, H.-B. and C.M. Wai, One-Step Synthesis of Size-Tunable Rhodium Nanoparticles on Carbon Nanotubes: A Study of Particle Size Effect on Hydrogenation of Xylene. *The Journal of Physical Chemistry C*, 2010. 114(26): p. 11364-11369.

194. Oszkó, A., G. Pótári, A. Erdőhelyi, A. Kukovecz, Z. Kónya, I. Kiricsi, and J. Kiss, Structure of the Au–Rh bimetallic system formed on titanate nanowires and nanotubes. *Vacuum*, 2011. 85(12): p. 1114-1119.

195. Li, M., T.S. Mayer, J.A. Sioss, C.D. Keating, and R.B. Bhiladvala, Template-Grown Metal Nanowires as Resonators: Performance and Characterization of Dissipative and Elastic Properties. *Nano Letters*, 2007. 7(11): p. 3281-3284.

196. Mertig, M., L.C. Ciacchi, R. Seidel, W. Pompe, and A. De Vita, DNA as a selective metallization template. *Nano Letters*, 2002. 2(8): p. 841-844.

197. Sasi, R. and U.S. Nandi, Interaction of rhodium(III) with nucleic-acids. *Current Science*, 1978. 47(20): p. 761-763.

198. Sasi, R. and U.S. Nandi, Interaction of rhodium(III) with DNA. *Biochimica et Biophysica Acta (BBA) - Nucleic Acids and Protein Synthesis*, 1979. 563(2): p. 527-533.

199. Jeon, Y.T. and G.H. Lee, Magnetism of the fcc Rh and Pd nanoparticles. *Journal of Applied Physics*, 2008. 103(Copyright (C) 2012 American Chemical Society (ACS). All Rights Reserved.): p. 094313/1-094313/5.

200. Lokesh, K.S., Y. Shivaraj, B.P. Dayananda, and S. Chandra, Synthesis of phthalocyanine stabilized rhodium nanoparticles and their application in biosensing of cytochrome c. *Bioelectrochemistry*, 2009. 75(2): p. 104-109.

201. Hoefelmeyer, J.D., K. Niesz, G.A. Somorjai, and T.D. Tilley, Radial Anisotropic Growth of Rhodium Nanoparticles. *Nano Letters*, 2005. 5(3): p. 435-438.

202. Ewers, T.D., A.K. Sra, B.C. Norris, R.E. Cable, C.-H. Cheng, D.F. Shantz, and R.E. Schaak, Spontaneous Hierarchical Assembly of Rhodium Nanoparticles into Spherical Aggregates and Superlattices. *Chemistry of Materials*, 2005. 17(3): p. 514-520.

203. Zhang, Y., M.E. Grass, S.E. Habas, F. Tao, T. Zhang, P. Yang, and G.A. Somorjai, One-step Polyol Synthesis and Langmuir−Blodgett Monolayer Formation of Size-tunable Monodisperse Rhodium Nanocrystals with Catalytically Active (111) Surface Structures. *The Journal of Physical Chemistry C*, 2007. 111(33): p. 12243-12253.

204. Abe, Y., K. Kato, M. Kawamura, and K. Sasaki, Rhodium and Rhodium Oxide Thin Films Characterized by XPS. *Surface Science Spectra*, 2001. 8: p. 117-125.

205. Cimpeanu, V., M. Kočevar, V.I. Parvulescu, and W. Leitner, Preparation of Rhodium Nanoparticles in Carbon Dioxide Induced Ionic Liquids and their Application to Selective Hydrogenation. *Angewandte Chemie International Edition*, 2009. 48(6): p. 1085-1088.

206. Contour, J.P., G. Mouvier, M. Hoogewys, and C. Leclere, X-ray photoelectron spectroscopy and electron microscopy of Pt/Rh gauzes used for catalytic oxidation of ammonia. *Journal of Catalysis*, 1977. 48(1–3): p. 217-228.

207. Nyholm, R. and N. Martensson, Core level binding-energies for the elements Zr-Te (Z = 40-52). *Journal of Physics C-Solid State Physics*, 1980. 13(11): p. L279-L284.

208. Wehner, P.S., P.N. Mercer, and G. Apai, Interaction of H_2 and CO with $Rh_4(CO)_{12}$ supported on ZnO. *Journal of Catalysis*, 1983. 84(1): p. 244-247.

209. Force, C., E. Román, J.M. Guil, and J. Sanz, XPS and 1H NMR Study of Thermally Stabilized Rh/CeO_2 Catalysts Submitted to Reduction/Oxidation Treatments. *Langmuir*, 2007. 23(8): p. 4569-4574.

210. Claessens, N., F. Demoisson, T. Dufour, A. Mansour, A. Felten, J. Guillot, J.J. Pireaux, and F. Reniers, Carbon nanotubes decorated with gold, platinum and rhodium clusters by injection of colloidal solutions into the post-discharge of an RF atmospheric plasma. *Nanotechnology*, 2010. 21(38).

211. Okamoto, Y., N. Ishida, T. Imanaka, and S. Teranishi, Active states of rhodium in rhodium exchanged Y zeolite catalysts for hydrogenation of ethylene and acetylene and dimerization of ethylene studied with X-ray photoelectron spectroscopy. *Journal of Catalysis*, 1979. 58(1): p. 82-94.

212. Yan, M. and G.H. Bernstein, A quantitative method for dual-pass electrostatic force microscopy phase measurements. *Surface and Interface Analysis*, 2007. 39(4): p. 354-358.

213. Hassanien, R., S.A.F. Al-Said, L. Siller, R. Little, N.G. Wright, A. Houlton, and B.R. Horrocks, Smooth and conductive DNA-templated Cu_2O nanowires: growth morphology, spectroscopic and electrical characterization. *Nanotechnology*, 2012. 23(7).

214. White, G.K. and S.B. Woods, Electrical and Thermal Resistivity of the Transition Elements at Low Temperatures. *Philosophical Transactions of the Royal Society of London. Series A, Mathematical and Physical Sciences*, 1959. 251(995): p. 273-302.

215. Garcia, E.Y. and D.G. Loffler, Electrical resistivities of iridium, palladium, rhodium, and tungsten at temperatures between 295 and 1100 K. *Journal of Chemical & Engineering Data*, 1985. 30(3): p. 304-305.

216. Cox, A.J., J.G. Louderback, and L.A. Bloomfield, Experimental observation of magnetism in rhodium clusters. *Physical Review Letters*, 1993. 71(6): p. 923-926.

217. Sathe, B.R., D.B. Shinde, and V.K. Pillai, Preparation and Characterization of Rhodium Nanostructures through the Evolution of Microgalvanic Cells and Their Enhanced Electrocatalytic Activity for Formaldehyde Oxidation. The *Journal of Physical Chemistry C*, 2009. 113(22): p. 9616-9622.

218. Gallaher, G., J.G. Goodwin Jr, C.-S. Huang, and M. Houalla, Thermal evolution of the support "Promoter" effect in Rh/La_2O_3. *Journal of Catalysis*, 1991. 127(2): p. 719-731.

219. Sleigh, C., A.P. Pijpers, A. Jaspers, B. Coussens, and R.J. Meier, On the determination of atomic charge via ESCA including application to organometallics. *Journal of Electron Spectroscopy and Related Phenomena*, 1996. 77(1): p. 41-57.

220. Bolto, B.A., R. McNeill, and D.E. Weiss, Electronic Conduction in Polymers. III. Electronic Properties of Polypyrrole. *Australian Journal of Chemistry*, 1963. 16(6): p. 1090-1103.

221. Chiang, C.K., C.R. Fincher, Jr., Y.W. Park, A.J. Heeger, H. Shirakawa, E.J. Louis, S.C. Gau, and A.G. MacDiarmid, Electrical Conductivity in Doped Polyacetylene. *Physical Review Letters*, 1977. 39(17): p. 1098-1101.

222. Levi, B.G., Nobel Prize in Chemistry Salutes the Discovery of Conducting Polymers. *Physics Today*, 2000. 53(12): p. 19-22.

223. Li, C., H. Bai, and G. Shi, Conducting polymer nanomaterials: electrosynthesis and applications. *Chemical Society Reviews*, 2009. 38(8): p. 2397-2409.

224. Thompson, B.C. and J.M.J. Frechet, Organic photovoltaics - Polymer-fullerene composite solar cells. *Angewandte Chemie-International Edition*, 2008. 47(1): p. 58-77.

225. Hatchett, D.W. and M. Josowicz, Composites of Intrinsically Conducting Polymers as Sensing Nanomaterials. *Chemical Reviews*, 2008. 108(2): p. 746-769.

226. Aleshin, A.N., Quasi-one-dimensional transport in conducting polymer nanowires. *Physics of the Solid State*, 2007. 49(11): p. 2015-2033.

227. Cantor, C.R. and P.R. Schimmel, *Biophysical Chemistry: Part I: The Conformation of Biological Macromolecules*. 1980: W. H. Freeman.

228. Sibghat, U., Y.-Z. Xu, and R.S. Day, Incision at Diaminopurine:Thymine Base Pairs but Not at Guanine:O4-Methylthymine Base Pairs in DNA by Extracts of Human Cells. *Biochemistry*, 1995. 34(22): p. 7438-7442.

229. Gryaznov, S. and R.G. Schultz, Stabilization of DNA:DNA and DNA:RNA duplexes by substitution of 2′-deoxyadenosine with 2′-deoxy-2-aminoadenosine. *Tetrahedron Letters*, 1994. 35(16): p. 2489-2492.

230. Haaima, G., H.F. Hansen, L. Christensen, O. Dahl, and P.E. Nielsen, Increased DNA binding and sequence discrimination of PNA oligomers containing 2,6-diaminopurine. *Nucleic Acids Research*, 1997. 25(22): p. 4639-4643.

231. Otero, T.F., J. Carrasco, A. Figueras, and E. Brillas, Electrochemical oxidation of 2,5-di-(-2-thienyl)-pyrrole in acetonitrile: cathodic stripping of the electrogenerated conducting polymer. *Journal of Electroanalytical Chemistry*, 1994. 370(1–2): p. 231-239.

232. Brillas, E., J. Carrasco, R. Oliver, F. Estrany, J. Vilar, and J.M. Morlans, Electropolymerization of 2,5-di-(-2-thienyl)-pyrrole in ethanolic medium. Effect of solution stirring on doping with perchlorate and chloride ions. *Electrochimica Acta*, 2000. 45(24): p. 4049-4057.

233. Ferraris, J.P. and T.R. Hanlon, Optical, electrical and electrochemical properties of heteroaromatic copolymers. *Polymer*, 1989. 30(7): p. 1319-1327.

234. Kofranek, M., T. Kovar, A. Karpfen, and H. Lischka, Abinitio studies on heterocyclic conjugated polymers - structure and vibrational-spectra of pyrrole, oligopyrroles, and polypyrrole. *Journal of Chemical Physics*, 1992. 96(6): p. 4464-4473.

235. Dovbeshko, G.I., N.Y. Gridina, E.B. Kruglova, and O.P. Pashchuk, FTIR spectroscopy studies of nucleic acid damage. *Talanta*, 2000. 53(1): p. 233-246.

236. Kostic, R., D. Rakovic, S.A. Stepanyan, I.E. Davidova, and L.A. Gribov, Vibrational spectroscopy of polypyrrole, theoretical study. *The Journal of Chemical Physics*, 1995. 102(8): p. 3104-3109.

237. Omastová, M., M. Trchová, J. Kovářová, and J. Stejskal, Synthesis and structural study of polypyrroles prepared in the presence of surfactants. *Synthetic Metals*, 2003. 138(3): p. 447-455.

238. Colarusso, P., K.Q. Zhang, B.J. Guo, and P.F. Bernath, The infrared spectra of uracil, thymine, and adenine in the gas phase. *Chemical Physics Letters*, 1997. 269(1-2): p. 39-48.

239. Ten, G.N., T.G. Burova, and V.I. Baranov, Analysis of hydrogen bonds by the IR spectra of thymine and N1,N3-deuterothymine. *Journal of Applied Spectroscopy*, 2005. 72(1): p. 104-110.

240. Les, A., L. Adamowicz, M.J. Nowak, and L. Lapinski, The infrared-spectra of matrix-isolated uracil and thymine - an assignment based on new theoretical calculations. *Spectrochimica Acta Part A-Molecular and Biomolecular Spectroscopy*, 1992. 48(10): p. 1385-1395.

241. Graindourze, M., J. Smets, T. Zeegers-Huyskens, and G. Maes, Fourier transform—infrared spectroscopic study of uracil derivatives and their hydrogen bonded complexes with proton donors: Part I. Monomer infrared absorptions of uracil and some methylated uracils in argon matrices. *Journal of Molecular Structure*, 1990. 222(3–4): p. 345-364.

242. Elyashevich, G.K., E.Y. Rosova, D.V. Andreeva, G.A. Polotskaya, M. Trchova, and Z. Pientka, New composite systems on the base of polyethylene porous films covered by polypyrrole and polyacrylic acid. *Journal of Applied Polymer Science*, 2005. 97(4): p. 1410-1417.

243. Omastová, M., J. Pionteck, and M. Trchová, Properties and morphology of polypyrrole containing a surfactant. *Synthetic Metals*, 2003. 135–136(0): p. 437-438.

244. Nowak, M.J., IR matrix isolation studies of nucleic acid constituents: the spectrum of monomeric thymine. *Journal of Molecular Structure*, 1989. 193(0): p. 35-49.

245. Buckel, F., F. Effenberger, C. Yan, A. Golzhauser, and M. Grunze, Influence of aromatic groups incorporated in long-chain alkanethiol self-assembled monolayers on gold. *Advanced Materials*, 2000. 12(12): p. 901-905.

246. Taouil, A.E., F. Lallemand, J.-M. Melot, J. Husson, J.-Y. Hihn, and B. Lakard, Effects of polypyrrole modified electrode functionalization on potentiometric pH responses. *Synthetic Metals*, 2010. 160(9–10): p. 1073-1080.

247. Roelfs, B., E. Bunge, C. Schröter, T. Solomun, H. Meyer, R.J. Nichols, and H. Baumgärtel, Adsorption of Thymine on Gold Single-Crystal Electrodes. *The Journal of Physical Chemistry B*, 1997. 101(5): p. 754-765.